2011

Biomechanics of the Upper Extremity in Response to Dynamic Impact Loading Indicative of a Forward Fall: An Experimental and Numerical Investigation.

Timothy Burkhart
University of Windsor

Follow this and additional works at: https://scholar.uwindsor.ca/etd

**Biomechanics of the Upper Extremity in Response to Dynamic Impact Loading
Indicative of a Forward Fall: An Experimental and Numerical Investigation.**

by

Timothy A. Burkhart

A Dissertation
Submitted to the Faculty of Graduate Studies
through Industrial and Manufacturing Systems Engineering
in Partial Fulfilment of the Requirements for
the Degree of Doctor of Philosophy at the
University of Windsor

Windsor, Ontario, Canada
2011
© 2011 Timothy A. Burkhart

Biomechanics of the Upper Extremity in Response to Dynamic Impact Loading Indicative of a Forward Fall: An Experimental and Numerical Investigation.

by

Timothy A. Burkhart

APPROVED BY:

_____
Dr. Jame Ashton-Miller, External Examiner
Department of Mechanical Engineering
University of Michigan

_____
Dr. William Altenhof
Department of Mechanical, Automotive and Materials Engineering

_____
Dr. Zbigniew Pasek
Department of Industrial and Manufacturing Systems Engineering

_____
Dr. Waguih ElMaraghy
Department of Industrial and Manufacturing Systems Engineering

_____
Dr. David M. Andrews, Advisor
Department of Kinesiology

_____
Jichang Wang, Chair of Defense
Department of Chemistry and Biochemistry

14 December, 2011

DECLARATION OF CO-AUTHORSHIP / PREVIOUS PUBLICATION

I. Co-Authorship Declaration

I hereby declare that this dissertation incorporates material that is the result of joint research, as follows: This dissertation also incorporates the outcome of joint research undertaken in collaboration with Dr. Cynthia Dunning of The University of Western Ontario. The collaboration is covered in Chapter 2 and Chapter 4 of the dissertation. In all cases, the key ideas, primary contributions, experimental designs, data analysis and interpretation, were performed by the author, and the contribution of co-authors was primarily through the provision of supervision and general editing.

I am aware of the University of Windsor Senate Policy on Authorship and I certify that I have properly acknowledged the contribution of other researchers to my dissertation, and have obtained written permission from each of the co-author(s) to include the above material(s) in my dissertation.

I certify that, with the above qualification, this dissertation, and the research to which it refers, is the product of my own work.

II. Declaration of Previous Publication

This dissertation includes 4 original papers that have been previously published/submitted for publication in peer reviewed journals, as follows:

Dissertation Chapter	Publication title/full citation	Publication status
Appendix E	Burkhart TA, Dunning CE, Andrews DM. 2011 Determining the Optimal Cut-off Frequencies for Filtering *In-vitro* Upper Extremity Impact Force and Acceleration Data through Residual Analysis. Journal of Biomechanics 44, 2728-2731.	Published
Chapter 2 Section 2.1	Burkhart TA, Andrews DM, Dunning CE. 2011 Failure Characteristics of the Distal Upper Extremity in Response to Dynamic Impact Loading. Journal of Orthopaedic Research. (DOI 10.1002/jor.22009).	Published
Chapter 2 Section 2.2	Burkhart TA, Andrews DM, Dunning CE. 2011 Multivariate Injury Risk Criteria For Fractures to the Distal Third Of the Radius and Proposed Acceptable Injury Probability Scores. Clinical Biomechanics.	Submitted
Chapter 3 Section 3.1	Burkhart TA, Clarke, D, Andrews DM. 2011. Reliability of impact forces, hip angles and velocities during simulated forward falls using a novel Propelled Upper Limb fall ARrest Impact System (PULARIS). Journal of Biomechanical Engineering.	Accepted

I certify that I have obtained a written permission from the copyright owner(s) to include the above published material(s) in my dissertation. I certify that the above

material describes work completed during my registration as graduate student at the University of Windsor.

I declare that, to the best of my knowledge, my dissertation does not infringe upon anyone's copyright nor violate any proprietary rights and that any ideas, techniques, quotations, or any other material from the work of other people included in my dissertation, published or otherwise, are fully acknowledged in accordance with the standard referencing practices. Furthermore, to the extent that I have included copyrighted material that surpasses the bounds of fair dealing within the meaning of the Canada Copyright Act, I certify that I have obtained a written permission from the copyright owner(s) to include such material(s) in my dissertation.

I declare that this is a true copy of my dissertation, including any final revisions, as approved by my dissertation committee and the Graduate Studies office, and that this dissertation has not been submitted for a higher degree to any other University or Institution.

ABSTRACT

The distal radius is one of the most common fracture sites in humans, often resulting from a forward fall with more than 60 % of all fractures to the wrist requiring some form of surgical intervention. Although there is a general consensus regarding the risk factors for distal radius fractures resulting from forward falling, prevention of these injuries requires a more thorough understanding of the injury mechanisms.

Therefore the overall purpose of this dissertation was to assess the response of the upper extremity to impact loading to improve the understanding of distal radius fracture mechanisms and the effectiveness of joint kinematic strategies for reducing the impact effects.

Three main studies were conducted that utilized *in vivo*, *in vitro* and numerical techniques. *In vitro* impact testing of the distal radius revealed that fracture will occur at a mean (SD) resultant impact force and velocity of 2142.1(1228.7) N and 3.4 (0.7) m/s, respectively. Based on the failure data, multi-variate injury criteria models were produced, highlighting the dynamic and multidirectional nature of distal radius fractures

The *in vitro* investigation was also used to develop and validate a finite element model of the distal radius. Dynamic impacts were simulated in LS-DYNA® and the resulting z-axis force validation metrics (0.23-0.54) suggest that this is a valid model. A comparison of the experimental fracture patterns to those predicted numerically (i.e. von-Mises stress criteria) shows the finite element model is capable of accurately predicting bone failure.

Finally, an *in vivo* fall simulation apparatus was designed and built that was found to reliably (Intraclass Correlation Coefficients > 0.6) apply multi-directional motion and upper extremity impacts indicative of forward falls. This study revealed that, to some extent, individuals are capable of selected an impact strategy that minimizes the significant injury variables that were outlined in the *in vitro* investigation, with very little instruction.

The body of work presented here has the potential to be used to develop distal radius fracture prevention methods in an attempt to improve the health and well being of those individuals currently at the highest risk of sustaining these injuries.

DEDICATION

To my wife Amanda and son Hudson

ACKNOWLEDGEMENTS

Western Ontario. Dr. D., Stew, Yara, Mark, and Seyward, thank you for taking me in and accepting me as your own.

Finally, thank you to my family. To my parents Lee and Donna Burkhart for instilling in me the values of respect and hard work, that have made me the person that I am. Your love and encouragement allowed me to follow my dreams. To my brother Mathew and sister in-law Carly, I am forever grateful for your support and I promise that one day I will move out. And of course, to my beautiful wife Amanda and son Hudson for being my biggest supporters and best friends. Your patience, support and love made this possible - I love you both very much, thank-you.

TABLE OF CONTENTS

LIST OF FIGURES

LIST OF TABLES

LIST OF APPENDICES

GLOSSARY

Abduction: A frontal plane motion in which a limb is moved away from the midline of the body.

Adduction: A frontal motion in which the a limb is moved toward the midline of the body

Adipose: Of, or relating to, fat tissue.

Anatomical Position: The natural position of the body in which the body is assumed to be standing, feet together, arms at the side and the head, and palms of the hands facing forward.

Barton's Fracture: A comminuted fracture of the distal radius often accompanied by dislocation of the radiocarpal joint.

Biofidelity: Ability to accurately represent natural biological properties.

Bone Mounted Accelerometer: Direct attachment of an accelerometer to the bone

Cadaveric: Of, or pertaining to, a dead body preserved for anatomical study.

Cancellous Bone: A spongy, lattice-like structure of bone. Synonymous with trabecular bone.

Cartilage: Connective tissue covering the surfaces of the bones that form a joint. Allows low-friction motion and absorbs shock.

Collagen: The primary protein in connective tissue.

Colles Fracture: A distal radius, extra articular fracture with dorsal angulation.

Comminuted: A fracture pattern in which the bone is splintered or crushed into numerous pieces.

Computed Tomography: A method of examining body organs by scanning them with x-rays and using a computer to construct a series of cross-sectional scans along a single axis.

Contractures: A permanent shortening of the muscle producing deformity or distortion.

Cortical Bone: A dense bone structure. Synonymous with compact bone.

Cyanoacrylate: A fast acting adhesive commonly used to glue bone strain gauges to bone

Diaphysis: The shaft of a long bone; a tube made of cortical bone.

Distal: Further from the point of reference, or away from the core of the body.

Dorsal Plate: A surgical instrument used to stabilize and fixate a fracture to the dorsal aspect of the radius by spanning the area of fracture. It is similar in shape to the dorsal radius surface and is held in place with surgical screws above and below the fracture

Dorsal: Pertaining to the back of the body or body segment.

Dual X-ray Absorptiometry: A diagnostic technique used to determine the bone density, often used in the diagnosis and management of osteoporosis.

Electromyography (EMG): A technique for evaluating and recording the electrical activity of a skeletal muscle.

Epidemiology: A branch of medical science that deals with the incidence, distribution, and control of disease in a population

Epiphysis: The expanded articular end of a long bone; made primarily of cancellous bone and covered with a layer of articular cartilage.

Extension: Pertaining to sagittal plane joint motion in which the angle between adjacent segments increases.

Flexion: Pertaining to sagittal plane joint motion in which the angle between adjacent segments decreases.

Frontal: A plane parallel to the long axis of the body separating the body into front and back portions.

Hounsfield Unit: The numeric information contained in each pixel of a CT image. It is related to the composition and nature of the tissue and is used to represent the density of tissue.

Hydroxyapatite: An inorganic compound composed of calcium, phosphate and hydroxide found in the bones as a crystallized lattice.

Impact: Interaction between bodies at relatively large velocities that results in a force of large magnitude or shock applied over a short duration.

Intra-cortical Pin: A medical grade stainless pin inserted into the cortical layer of a bone.

*In vitro***:** In an artificial environment outside of the body.

*In vivo***:** In a living body of a plant or animal.

Intermedullary Canal: The canal down the center of a bone filled with marrow.

Joint: The location at which two bones make contact with each other, and where relative movement occurs.

Kirschner wires (K-wires): A thin rigid wire that can be used to stabilize bone fragments.

Lateral: A position further away from the mid-line of the body.

Marrow: The soft tissue filling the cavities of bones.

Medial: A position closer to the center or mid-line of the body.

Morbidity: A diseased state or symptom.

Mortality: The state of being mortal or susceptible to death.

Osteoporosis: a condition that is characterized by decreased bone mass, decreased bone density and enlargement of bone spaces producing porosity and brittleness.

Posterior: Located towards the back of the body.

Pronation: A transverse plane motion in which the hand and forearm rotate towards the mid-line of the body.

Prone: Having the front or ventral surface of the body facing downward.

Proximal: Closer to the point of reference or closer to the core of the body.

Quasi-Static Strain Rate: Deformations that result in strain rates at or below 10^{-3}/s.

Sagittal: The plane parallel to the long axis of the body separating the body into left and right portions.

Shock: A non-periodic excitation characterized by a suddenness and severity. The measure of the magnitude of a shock wave at a specific location and instant in time.

Shock Wave: A discontinuous pressure change propagated through a medium at a velocity greater than that of sound.

Stereo lithography File Format: Describes a raw unstructured triangulated surface by the unit normal and vertices of the triangles using a three-dimensional Cartesian coordinate system.

Subcutaneous: Being, living, used or made under the skin.

Supination: A transverse plane motion in which the hand and forearm rotate away from the midline of the body.

Surface Electrode: A device composed of a metal surface (e.g., Silver/Silver-Chloride) which is placed on the skin over a muscle belly to record the electrical signal of the muscle.

Surface Mounted Accelerometer: An accelerometer attached to the skin to be used to approximate the response of the underlying bone.

Transverse: The plane perpendicular to the long axis of the body separating the body into inferior and superior portions.

Volar: Pertaining to the front of the body or body segment.

Volar Plate: A surgical instrument used to stabilize and fixate a fracture to the volar aspect of the radius by spanning the area of the fracture. It is similar in shape to the volar radius surface and is held in place with surgical screws above and below the fracture.

CHAPTER 1 – GENERAL INTRODUCTION

1.1 Epidemiology

Distal upper extremity injuries (i.e., carpal bones, radius, ulna and humerus) commonly occur as a result of fall initiated impacts, and while falls can occur in any direction, Nevitt & Cummings (1993) found that the greatest frequency of falls occur in the forward direction. As an individual falls and descends toward the ground, it is instinctive to extend the arms in front of the torso in an attempt to arrest the momentum of the body; protecting oneself from head and torso injuries (Hsiao & Robinovitch, 1998; Kim & Ashton-Miller, 2003). However, this results in a dynamically applied load to the distal upper extremity which may result in injury.

The most serious consequence of fall-related impacts to the upper extremity is fracture, and while fractures of this nature are generally non-life threatening, there are many long term sequalae. Nerve damage (Frykman, 1967), carpal tunnel syndrome (Stewart et al., 1985), osteoarthritis (Colles Frx, 2006) and missed diagnosis of scaphoid fractures (Peron et al., 2001) have been identified as injuries secondary to the fracture. Furthermore, as the strain rate approaches and exceeds physiological loading (i.e. becomes more dynamic), the fracture shifts towards a more comminuted pattern (Nordin & Frankel, 2001), increasing the likelihood of soft tissue ruptures (Wong & Pho, 1984; Stewart et al., 1985). These can lead to decreased muscle strength, contractures, and residual long term pain (Green & Gay, 1956; Colles Frx, 2006).

Despite the attention that has been given to forward fall prevention (Robitaille et al., 2005; Sleet et al., 2005; Grabiner et al., 2008; Leipzig et al., 2010) the number of
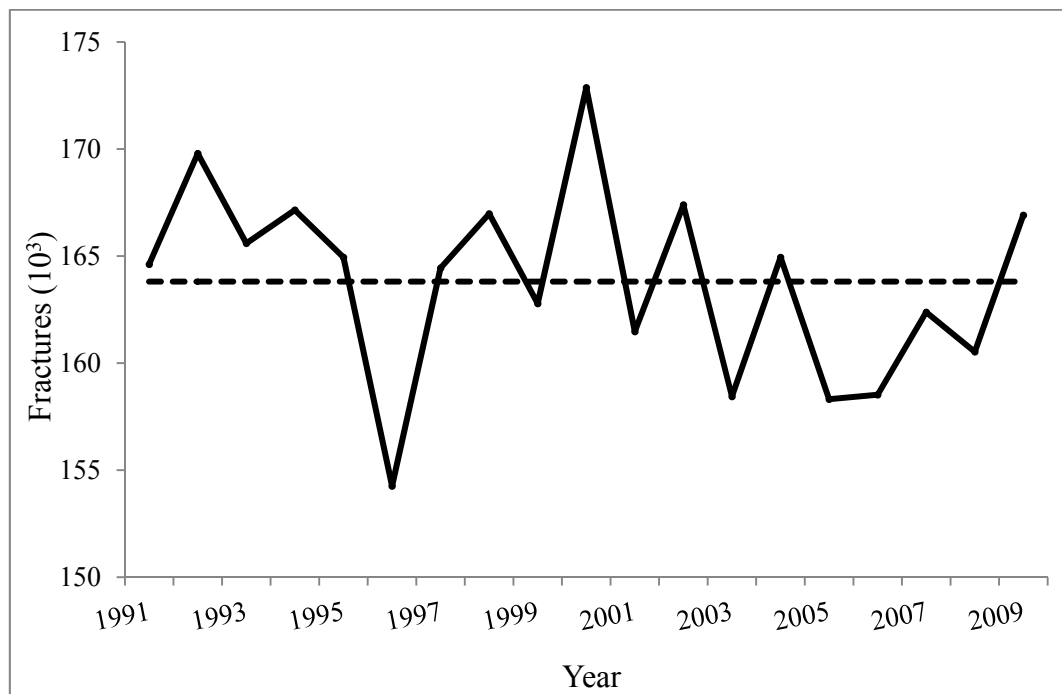
Figure 1.1: Prevalence of Upper Extremity Fractures
Data from the National Electronic Injury Surveillance Survey NEISS, 2011)
showing the ten year trend of fractures to the distal upper extremity. The dashed
line represents the national 20 year average.

fractures to the radius, as a result of falling, has remained relatively consistent over the last twenty years (USCPSC, 2010) (Figure 1.1). Given that 50 % of the Canadian population is over the age of 40 years and more than 35 % are over the age of 50 years (Statistics Canada, 2011) (the population at the greatest risk of distal radius fractures (Jones et al., 1994)) it is expected that the incidence of these injuries will continue to rise. Also, as it is estimated that these injuries currently cost the healthcare system between US $300 and $500 million annually (Burge et al., 2007), these injuries will continue to burden already stressed healthcare systems globally. Much of the research concerning forward falls and upper extremity injuries has focused its attention on three "at risk" populations: the general work force (Layne & Pollack, 2004) in-line skaters (Ellis et al., 1995) and the elderly (Blake et al, 1988).

1.1.1 General Work Force

The Workplace Safety and Insurance Board (WSIB) (2005) reported that 22.8 % of lost time injury claims were a result of a fall, with the upper extremity identified as the affected area 22.7% of the time. The associated cost of these claims has been suggested to exceed US $6 billion annually (Chang, 2002). Concerning the affected body part, 18 % of hospitalized injuries occurred to the upper extremity in the form of a non-specified fracture or sprain. As further illustrated by Courtney & Webster (1999) and Chang (2002), fall-related upper extremity injuries appear to be the most disabling of all injuries, as seen by the increase in days away from work.

1.1.2 In-line Skaters

Given the high velocities and unstable nature of the activity, in-line skaters are

also at a high risk of upper extremity injuries. Ellis et al. (1995), Houshian & Anderson (2000), and Houshian et al. (2001) found that falls associated with in-line skating resulted in a higher frequency of more serious injuries, with upwards of 50 % resulting in a fracture. Furthermore, Jaffe et al. (1997) reported that 64 % of the upper extremity injuries required some form of orthopaedic surgery. With respect to injury location, Scheiber et al. (1996), in a nationwide study, found that 32 % of the injuries occurred to the wrist, with 25 % resulting in a fracture. The elbow accounted for 9 % of the injuries with 6 % of these ending in a fracture.

1.1.3 Elderly

Arguably, the most at risk population for fractures to the upper extremity is the elderly. Age-related deficiencies have been identified by numerous authors as risk factors for falls and fall-related injuries (Nevitt & Cummings, 1993; O'Neil et al., 1994; Tinneti & Williams, 1998; Pavol et al., 1999). For example, it is estimated that osteoporosis (associated with decreased bone stiffness and strength (Seeman & Delmas, 2005)) affects over 75 million individuals worldwide. The altered bone properties associated with osteoporosis make osteoporotic fractures, the most common type in the elderly, affecting an estimated 8.9 million people each year worldwide (Fardellone, 2008). Given the high morbidity and mortality associated with osteoporotic fractures, Ray et al. (1997) and Fardellone (2008) have identified this class of injury as a public health problem and the World Health Organization has identified osteoporotic fractures as a top health priority (Fardellone, 2008). The National Academy on an Ageing Society (2003) released a report outlining the current and future health trends of the elderly and assigned a failing grade with respect to our ability to prevent fall-related

injuries and death in individuals over the age of 65 years. Furthermore, it is estimated that the financial burden of osteoporotic fracture to the distal forearm can well exceed US $385 million per year in the United States alone. Recently, Bliuc et al. (2009) found that 52 % of osteoporotic fractures that occur in individuals over the age of 60 years are fatal and the mortality rate persists for 5-10 years post-injury. These results agree with those of Donald & Bulpitt (1999) who suggest that the physical consequences of fall-related injuries to the upper extremity have profound direct and indirect costs associated with them; both monetary and in terms of quality of life.

1.2 Upper Extremity Anatomy

The upper extremity is a relatively complex system of joints and segments consisting of hard tissue, in the form of bone, and soft tissues in the form of muscles, tendons, ligaments, and subcutaneous adipose (fat). The shoulder, the elbow and the wrist are the largest joints of the upper extremity and are the joints most often involved in upper extremity injury (Figure 1.2 and Figure 1.3) (All figures in this section are modified from Tortora & Nielsen, 2011).

1.2.1 The Skeletal System

The bone that makes up the arm is referred to as the humerus (Figure 1.2) and articulates proximally with the glenoid fossa of the scapula to form the shoulder joint (Figure 1.3a). The interaction of the humeral head within the glenoid fossa (Figure 1.3a) allows the humerus to move with six degrees of freedom relative to the scapula: flexion/extension, abduction/adduction and internal/external rotation. Distally, the capitulum and trochlea of the humerus interact with the head of the radius and the

trochlear notch of the ulna, respectively, creating the elbow joint (Figure 1.3b). Technically, the elbow is a bi-articular joint allowing flexion/extension and abduction/adduction. However, abduction/adduction about the elbow is a passive movement with minimal motion and is often not included in the analysis of elbow joint kinematics (Anglin & Wyss, 2000).

The forearm (Figure 1.2) is composed of the radius and ulna bones that articulate with each other both proximally (head of radius with radial notch) and distally (head of ulna with the ulnar notch) (Figure 1.4a), allowing the radius to pivot and cross over the ulna when the forearm is pronated and supinated. An interosseous membrane confines the intermediate space between the radius and ulna and is a common site of attachment for the deep musculature of the forearm (Figure 1.4a). Protruding distally from the radius and ulna are the respective styloid processes.

The wrist joint itself is formed by the interaction of two of the carpals (scaphoid and lunate) with the distal end of the radius (Figure 1.4b). There are two additional proximal carpals, triquetrum and pisiform, while the distal portion of the wrist consists of four carpals (trapezium, trapezoid, capitate and hamate) that are responsible for forming the articulations with the metacarpals of the hand (Figure 1.4b). The articulation of the lunate and scaphoid with the radius allows the hand to move with respect to the forearm in flexion/extension as well as abduction/adduction (otherwise referred to as radial/deviation).

1.2.2 Bone Structure and Material Properties

Bone is a specialized form of connective tissue suitably adapted for its supportive and protective role (Nordin & Frankel, 2001). Bone is composed of both
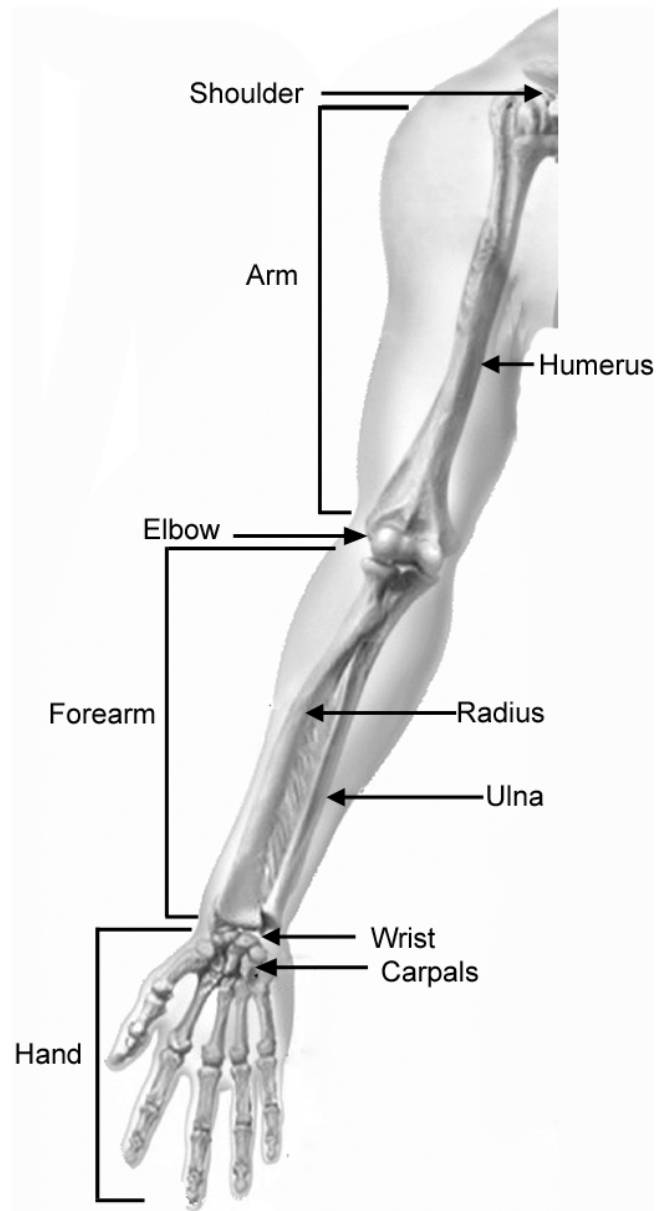
Figure 1.2: Upper Extremity Anatomy
General anatomy of the upper extremity
(Modified from Tortora, 2011).

(a)

(b)
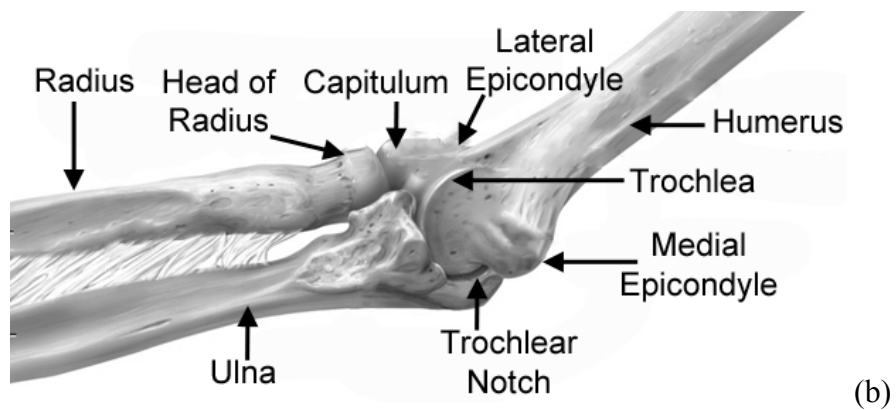
Figure 1.3: Shoulder and Elbow Anatomy
Bone anatomy of the shoulder (a) and the elbow (medial view) (b)
(Modified from Tortora, 2011).

(a)

(b)
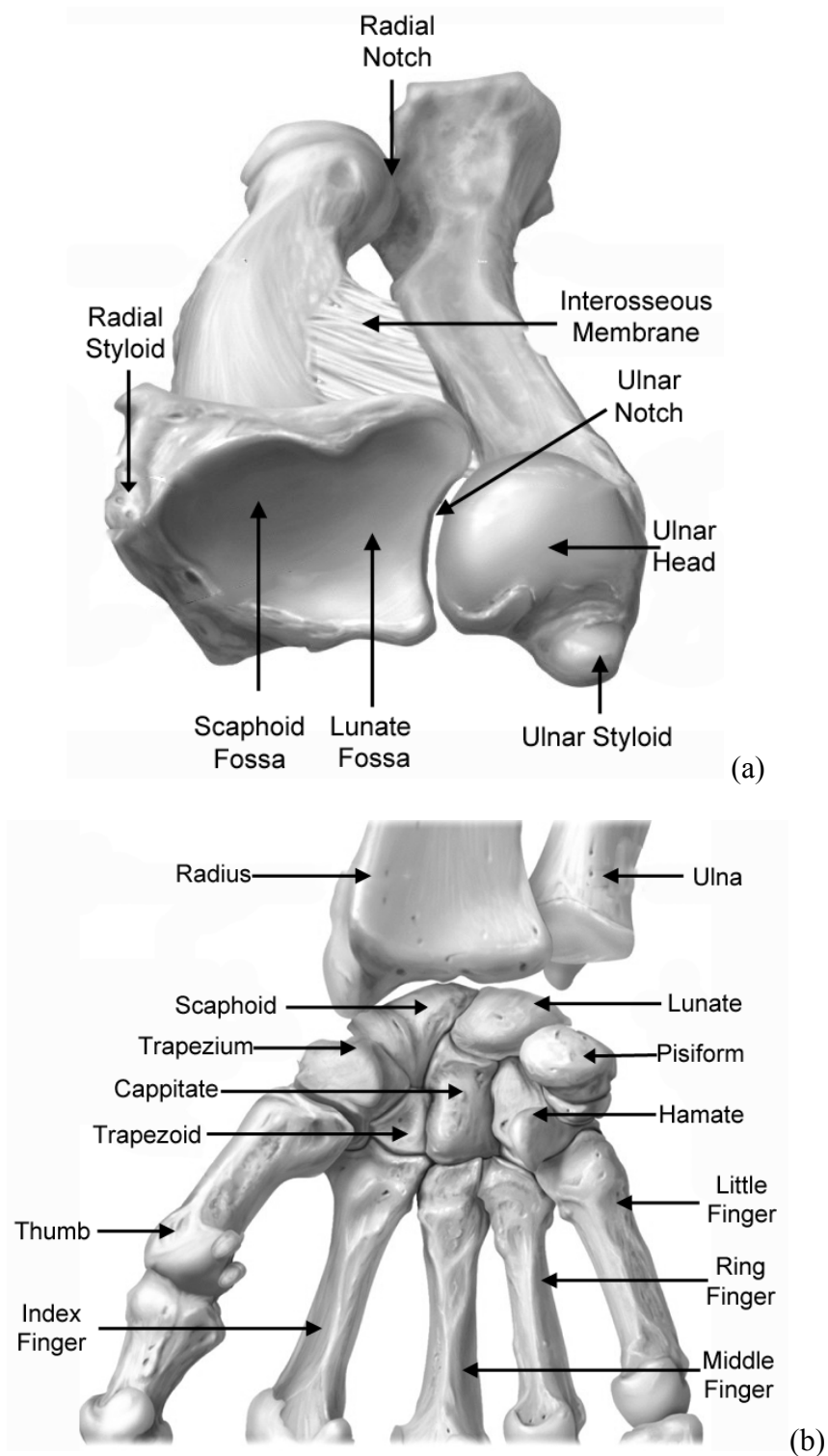
Figure 1.4: Wrist Anatomy
Bone anatomy of the radial ulnar (distal axial view) (a) wrist (volar view) (b)
joints (Modified from Tortora, 2011).

organic (water (25 %) and protein (25 %)) and inorganic materials (primarily calcium and phosphate (50 %)) (Nordin &Frankel, 2001; Li & Aspden, 1997).   It is this unique combination that allows bone to be hard and rigid (inorganic compounds) as well as flexible and resilient (organic compounds) (Nordin & Frankel, 2001).

There are two main bone microstructures: cortical and cancellous (Figure 1.5). Cortical bone is the denser of the two types and tends to form the shell of the bone, and is found primarily in the diaphyseal (shaft) region the long bones (Figure 1.5). Cortical bone consists of osteons that surround central canals (forming the main branches of the bone's circulatory network), and each osteon is made up of concentric lamellae (Figure 1.6a). The osteons are tightly packed and aligned parallel to the long axis in long bones in order to support axially directed loads. Conversely, cancellous bone is less dense, is located in the epiphyseal and metaphyseal regions (ends) of long bones (Figure 1.5) and is composed of small needle-like struts of bone called trabeculae (Figure 1.6b). The trabeculae, in turn, are composed of concentrically arranged lamelae (Figure 1.6b).

Bone is a highly complex material that is inhomogeneous, anisotropic (Figure 1.7b) and has been shown to display characteristics of an elastic-plastic material (Figure 1.7a) (Burstein et al., 1976) (Figure 1.7).   Bone is also a viscoelastic material whose modulus and strength have been shown to be proportional to the strain rate raised to the power of 0.06 (Carter & Hayes, 1977) (Figure 1.7c). In cortical bone, viscoelasticity is a result of the collagen polymer and the interfaces between the lamellae within the osteons, while cancellous bone viscoelasticity has been shown to occur as result of void collapse (Garner et al., 2000).
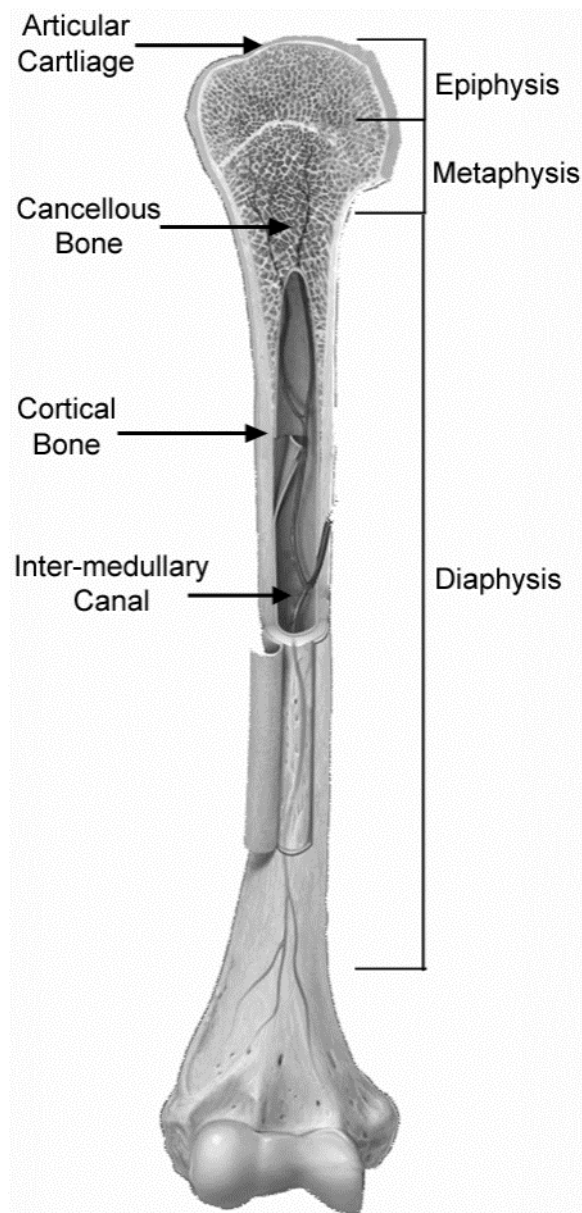
Figure 1.5: Long Bone Structure
Basic anatomy of a long bone
showing the different types of bone
and the areas unique to a long bone
(Modified from Tortora, 2011).

(a)

(b)
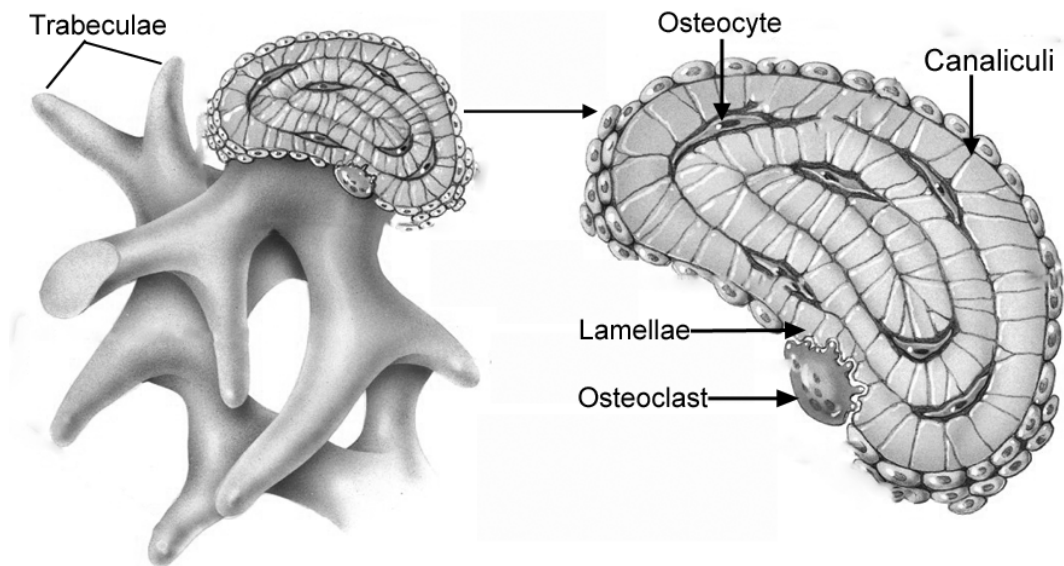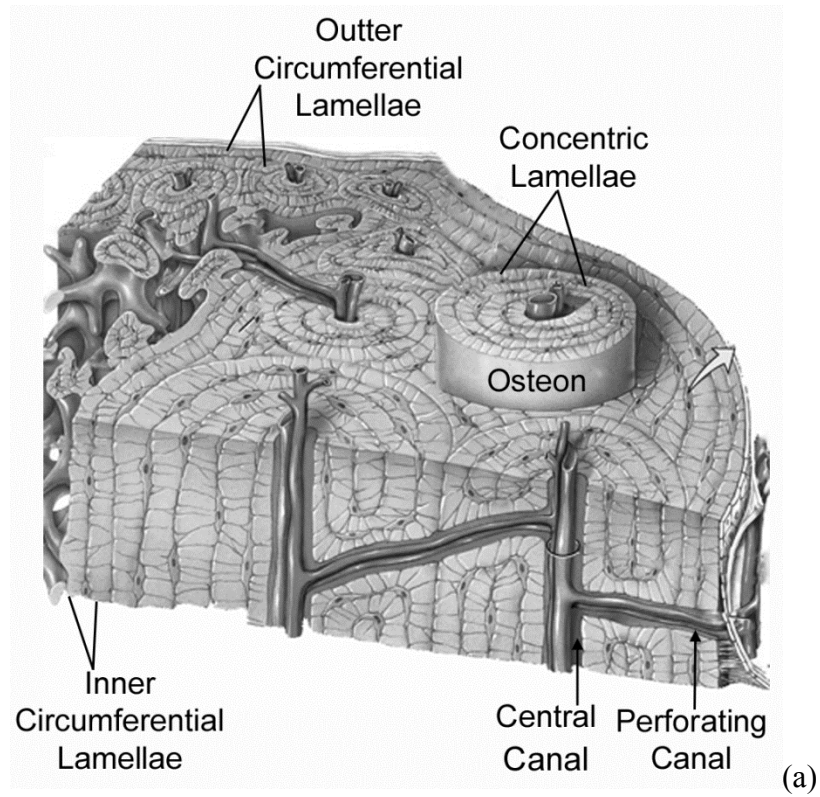
Figure 1.6: Bone Structure
Anatomy and structure of the cortical (a) and cancellous (b) bone (Modified from Tortora, 2011).
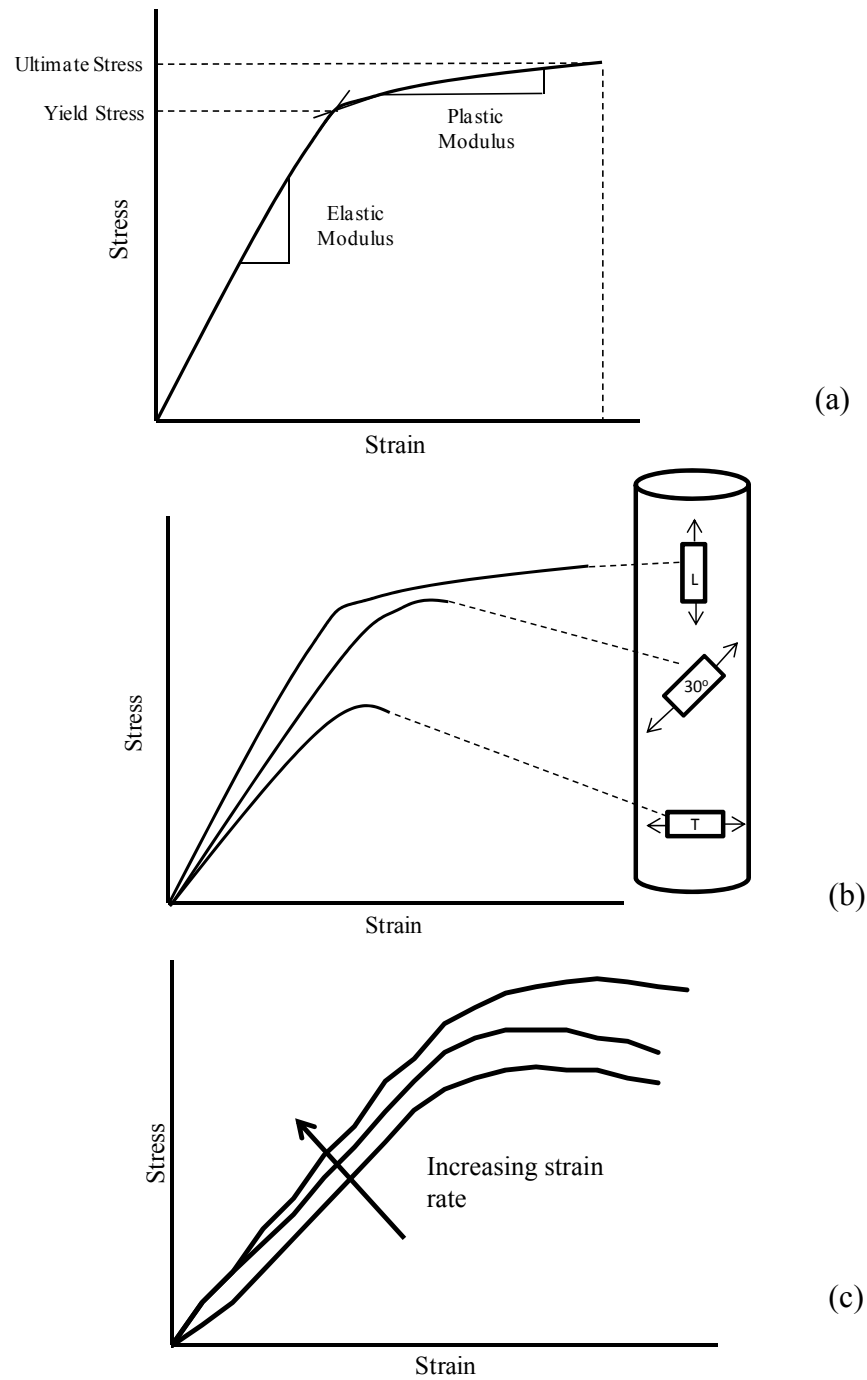
Figure 1.7: Bone Material Properties
Material properties of bone including the elastic-plastic
(a), anisotropic (L=longitudinal loading; T=transverse
loading; 30° =load applied at an angle) (b) and
viscoelastic (c) behaviours (Modified from Nordin &
Frankel, 2001).

The reported material properties of bone have varied greatly throughout the literature and are dependent on the age (Burstein et al., 1976) and sex (Khosla et al., 2006) of the donor, and the method of testing (Nordin & Frankel, 2001). For example, the elastic modulus has been found to range from 5.1 GPa to 26.4 GPa in cortical bone (Choi et al., 1990; Kaneko et al., 2003) and 0.1 GPa to 18.4 GPa in cancellous bone (Lotz et al., 1990; Turner et al., 1999) (Table 1.1). In a sample of 20-29 year olds, Burstein et al. (1976) found magnitudes of yield stress and elastic modulus of 0.1 GPa and 17.0 GPa, respectively. The yield stress was found to decrease by approximately 2.2 % per decade, while the elastic modulus decreased by more than 1.5 % per decade (Burstein et al., 1976). Furthermore, sex appears to have a large significant effect on the bone mineral density, such that males on average have approximately 27 % greater bone mineral density at the radius while females have greater spine and femoral bone mineral densities than males by more than 15 % (Kelly et al., 1990).

1.2.3 The Muscular System

Movement of the forearm with respect to the arm is achieved through contraction of the flexor and extensor muscle groups of the arm (The anatomical figures in this section have been modified from Tortora & Neilsen, 2011).

One of the main forearm flexors, located on the volar aspect of the arm, is the biceps brachii (Figure 1.8a). This muscle consists of two heads that originate superior to the glenoid fossa and on the coracoid process of the scapula and merge into a single muscle insertion onto the proximal radius. The brachioradialis originates on the lateral epicondyle of the humerus, spans the lateral aspect of the forearm and inserts onto the radial styloid (Figure 1.8a).

Table 1.1: Bone Material Properties
A summary of cortical and cancellous bone properties.

Author (Year)	Mass Density (kg/m3)	Elastic Modulus (GPa)	Yield Stress (MPa)
Cancellous Bone			
Troy et al. (2007)	976	1.8	-
Lotz et al. (1990)	200-800	0.1 - 1.0	-
Van Reiberg et al. (1995)	280	0.09 - 0.4	-
Hodkinson et al. (1992)	90-1200	1.0 - 12.0	-
Boutroy et al. (2005)	160	17.5	-
Nicholson et al. (1998)	152	-	-
Kim et al. (2005)	-	-	10
Untaroiu et al. (2005)	-	-	5
Turner et al. (1995)	-	17.5-18.1	
Cortical Bone			
Troy et al. (2007)	1392 - 2288	5.7 - 26.3	-
Louis et al. (1995)	1251	-	-
Kaneko et al. (2003)	539-1293	5.4 - 26.4	28.7 – 166.5
Boutroy et al. (2005)	902	20.0	-
Schonenau et al. (2002)	1153	-	-
Burstein et al. (1976)	-	-	-
Untaroiu et al. (2005)	-	-	134
Choi et al. (1990)	-	5.4	
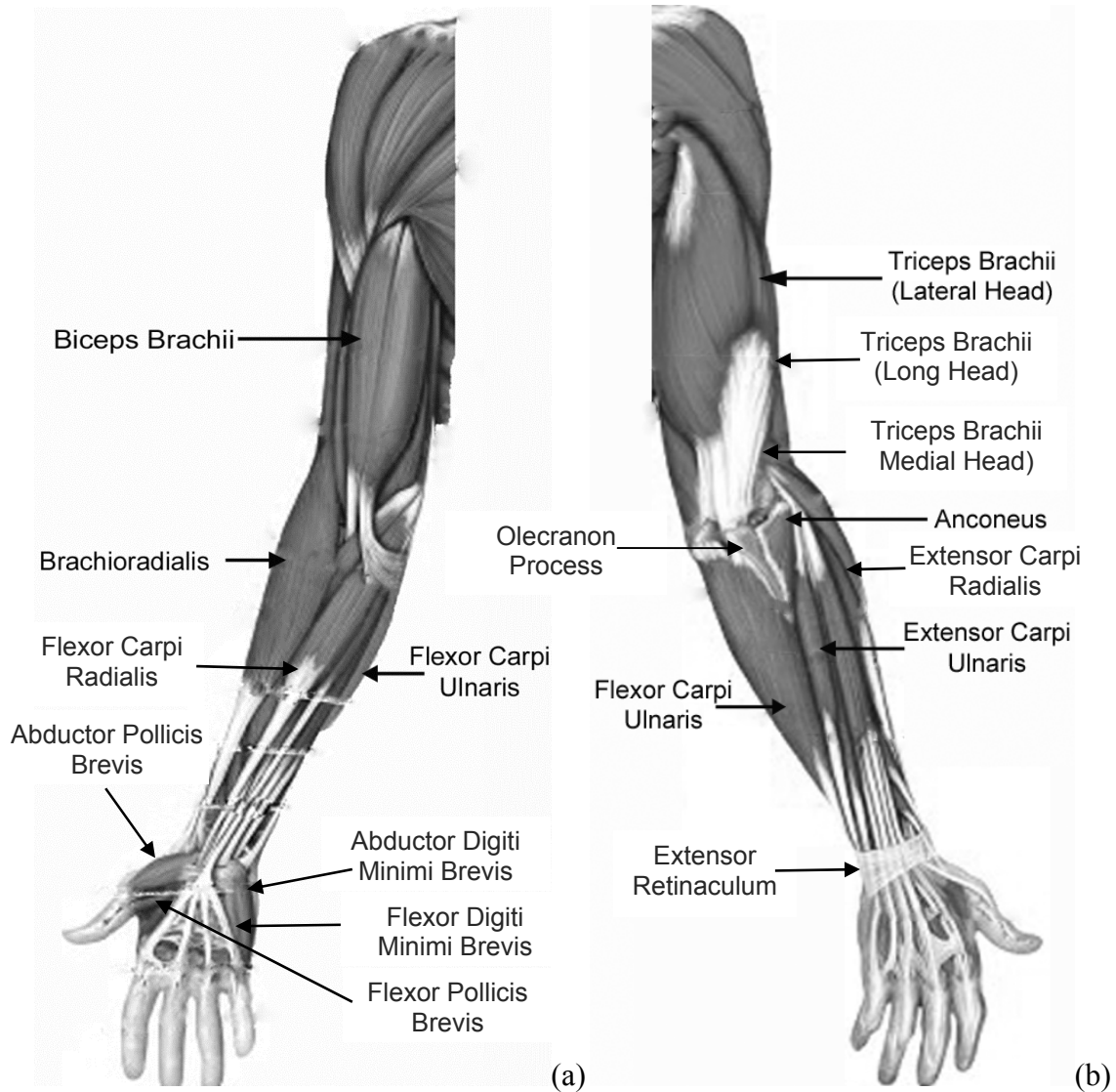
Figure 1.8: Upper Extremity Musculature
Musculature of the volar (a) and dorsal (b) upper extremity (Modified from Tortora, 2011).

While primarily a forearm flexor, brachioradialis is also involved in forearm supination and pronation. On the dorsal aspect of the arm, triceps brachii and anconeus are responsible for extending the forearm with respect to the arm (Figure 1.8b). Triceps brachii is a large muscle that originates from three locations on the scapula and humerus and inserts onto the olecranon process of the ulna (Figure 1.8b). Conversely, anconeus is relatively small, and spans a short distance from the lateral epicondyle of the humerus to the lateral aspect of the olecranon process (Figure 1.8b).

Of the approximately 50 muscles located in the upper extremity, 18 are situated in the posterior and anterior forearm and are responsible for the movement of the hand with respect to the forearm. The bulk of the muscle is situated in the proximal two-thirds of the forearm, with these muscles giving way to long tendons that extend distally to their respective insertions (Figure 1.8). Four of these muscles, flexor carpi ulnaris, flexor carpi radialis, extensor carpi ulnaris and extensor carpi radialis, are of significant importance as they are the main contributors to flexion and extension of the wrist and help to form the large superficial mass of muscle in the proximal forearm (Figure 1.8a-b). Anteriorly, the two flexor muscles share a common origin on the medial epicondyle of the humerus. Flexor carpi ulnaris travels distally where it inserts onto pisiform, hamate, and the fifth metacarpal. Flexor carpi radialis migrates diagonally to the inferior medial (radial) aspect of the forearm where it inserts onto the second and third metacarpals. Moving medio-laterally over the carpals is the flexor retinaculum, a structure responsible for ensuring that the tendons remain in close contact with the bony structures, thereby preventing the tendons from "bowing" when the muscles are activated (Figure 1.8b).

Located on the posterior aspect of the forearm (Figure 1.8a) are the extensor muscles: extensor carpi radialis and extensor carpi ulnaris. Extensor carpi radialis diverges into two divisions known as longus and brevis which continue inferiorly and laterally to insert on the second and third metacarpals, respectively. However, the extensor carpi ulnaris, moves from its origin on the lateral epicondyle of the humerus, across to the posterior forearm and inserts onto the fifth metacarpal. Similar to the flexor muscle group, the tendons of the posterior extensor muscles are held securely in place distally by the extensor retinaculum.

Abductor and flexor polices brevis are responsible for abducting and flexing the distal phalanx of the thumb, respectively (Figure 1.8a). The abductor digiti minimi causes abduction of the fifth phalanx while flexor digiti minimi brevis is responsible for flexion of the fifth phalanx (Figure 1.8a). Upon impact to the upper extremity during a forward fall, it is this mass of muscle that commonly comes into contact with the impacting surface first (Nikolic et al., 1975).

1.3 Measurement Techniques

In order to assess the injury potential of a forward fall, and to quantify the reaction of the upper extremity in response to dynamic loading, strains, forces, accelerations, kinematics and muscle activation levels need to be measured. This requires a variety of instruments, the combination of which depends on the type of testing undertaken (i.e. *in vivo* vs. *in vitro*). The following is a description of the different types of instrumentation that are utilized to assess the effect of loading, specifically dynamic loads, on the distal radius.

1.3.1 Strain Gauges

The effects of external loads on the external bone structure can be measured with strain gauges that are applied directly to the surface of the bone (Roberts, 1966). Since stress cannot be measured directly, the strain gauge measures the deformation in response to an external load, and the strain can be related to the stress if one has knowledge of the material's elastic modulus (Benham et al., 1996). The gauges must be securely fastened to the surface of the object being investigated, most commonly using a cyanoacrylate adhesive (Roberts, 1966). Cyanoacrylate is preferred as the bonding is achieved almost instantaneously (Roberts, 1966). The strain gauge foil is deformed in proportion to the deformation of the material (e.g., bone), causing the resistance in the wire to also change in proportion to the deformation.

In biomechanics the most commonly used strain gauges are foil gauges, composed of a strain sensitive pattern of wire placed securely between two insulating sheets (Figure 1.9). While strain gauges are capable of measuring the state of strain at a location on a material, they are limited by their ability to only measure the strain in one direction and cannot measure shear strain directly. To overcome this limitation, a series of strain gauges can be stacked to form a rosette (Figure 1.10), allowing the two plane strains and the shear strain to be calculated (Benham et al., 1996; Dowling, 2007). Therefore, a rosette with three gauges a,b, c at angles of α, $\alpha+\beta$, and $\alpha+\beta+\gamma$ (where α, β, γ are traditionally 45° or 60°) from the x-axis, can output strains that are related to ε_x ε_y and γ^{xy} through the following equations:

$$\varepsilon_a = \frac{\varepsilon_x + \varepsilon_y}{2} + \frac{\varepsilon_x - \varepsilon_y}{2} \cos 2\alpha + \gamma_{xy} \sin 2\alpha \qquad \text{(Eq. 1.1)}$$

$$\varepsilon_b = \frac{\varepsilon_x + \varepsilon_y}{2} + \frac{\varepsilon_x - \varepsilon_y}{2} \cos 2(\alpha + \beta) + \gamma_{xy} \sin 2(\alpha + \beta) \qquad \text{(Eq. 1.2)}$$

$$\varepsilon_b = \frac{\varepsilon_x + \varepsilon_y}{2} + \frac{\varepsilon_x - \varepsilon_y}{2} \cos 2(\alpha + \beta + \gamma) + \gamma_{xy} \sin 2(\alpha + \beta + \gamma) \qquad \text{(Eq. 1.3)}$$

When a 45° rosette is used and gauge "a" is aligned with the x-axis, these equations can be re-written as:

$$\varepsilon_x = \varepsilon_a \qquad \text{(Eq. 1.4)}$$

$$\varepsilon_y = \varepsilon_c \qquad \text{(Eq. 1.5)}$$

$$\gamma_{xy} = \varepsilon_b - \frac{\varepsilon_a + \varepsilon_c}{2} \qquad \text{(Eq. 1.6)}$$

Once calculated, these values can be used to determine the stresses (σ_x σ_y τ_{xy}) or the principal strains as below:

$$\varepsilon_{1,2} = \frac{\varepsilon_x + \varepsilon_y}{2} \pm \sqrt{\left(\frac{\varepsilon_x + \varepsilon_y}{2}\right)^2 + \left(\frac{\gamma_{xy}}{2}\right)^2} \qquad \text{(Eq. 1.7)}$$

$$\frac{\gamma_{max}}{2} = \sqrt{\left(\frac{\varepsilon_x - \varepsilon_y}{2}\right)^2 + \left(\frac{\gamma_{xy}}{2}\right)^2} \qquad \text{(Eq. 1.8)}$$

1.3.2 Load Cells and Force Platforms

Load cells and force platforms convert a force into an electrical signal and are most commonly instrumented with strain gauges. The strain gauges within a load cell or force platform can be arranged in a number of Wheatstone Bridge configurations dependent on the purpose of the instrument. This equipment works on the basis of an elastic element, to which a number of electrical strain gauges are attached. Each strain gauge responds to the local strain and the measurement of force is determined from the combination of these individual measures of strain. For example, an axial load cell would consist of four strain gauges, two aligned with the direction of loading and two perpendicularly oriented. A force platform with six degrees of freedom would
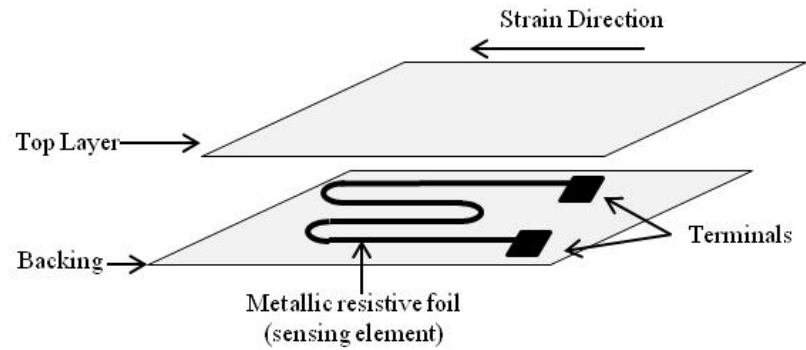
Figure 1.9: Strain Gauge Structure
General structure of a uniaxial metallic foil strain gauge.
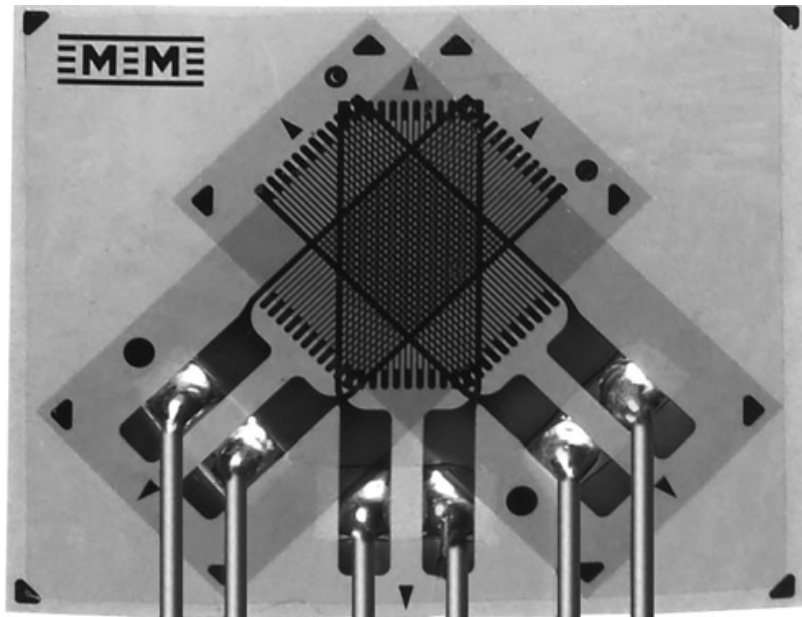
Figure 1.10: Strain Gauge Rosette
A rosette strain gauge where the gauges are arranged at 45° to one another. This arrangement allows for the measurement of the full state of strain (Vishay Micro-Measurements).

essentially consist of six axial load cells arranged to measure three force (Fx, Fy, Fz) and three moment (Mx, My, MZ) components (National Physics Laboratory, 1998).

1.3.3 Accelerometers

An accelerometer measures the accelerations that result from forces acting on a body (or anatomical segment as in this work). These forces can be static (e.g., force of gravity acting on the body) or dynamic (e.g., caused by vibrating or moving the accelerometer). For example, a piezoresistive accelerometer (strain-gauge based accelerometer) works by measuring the electrical resistance of a material when mechanical stress is applied (Figure 1.11a). Silicon capacitive accelerometers are another type of accelerometer whose small size and mass make it ideal for biological testing. These accelerometers are composed of semiconductor materials (e.g., poly silicon) and can be modelled as two stationary plates sandwiching a third moveable plate (Figure 1.11b). When subjected to acceleration (via an external force), the center plate is deflected from its initial position. This movement changes the distance between the plates, and in turn, proportionally changes each capacitor's (plate's) values (Eq.1.9).

$$C = \frac{A\varepsilon}{D} \qquad\qquad \text{(Eq. 1.9)}$$

Where C is the capacitance, A is the area of the plate, ε is the dielectric constant and D is the distance between the plates.

Strain Sensitive Resistor

Mass

(a)

Direction of Movement

Stationary Plates

Moveable Plate
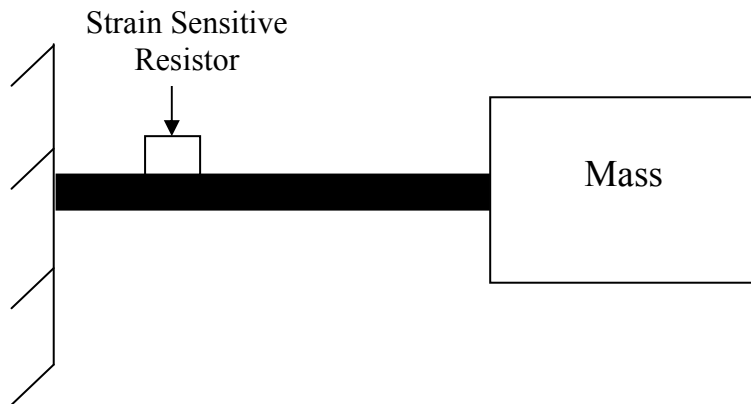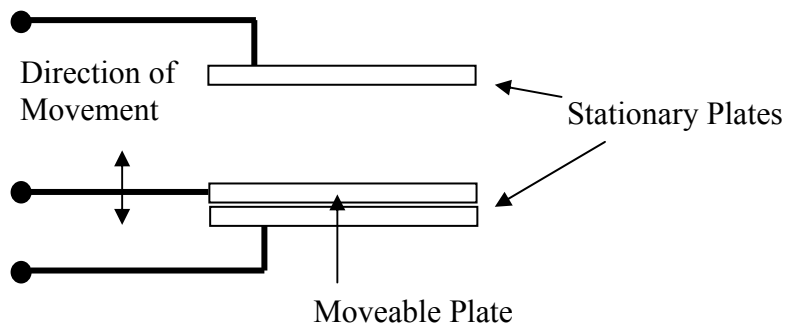
(b)

Figure 1.11: Accelerometer Structure
Schematic representations of a piezoresistive (a) and piezocapacitive (b) accelerometer.

Accelerometers are capable of measuring the shock (accelerations) produced by an impulse, at specific anatomical locations (Lafortune et al., 1995). The optimal method of collecting acceleration data of bony anatomical structures is by using bone mounted accelerometers (BMA); accelerometers that are attached directly to underlying bone via intra-cortical pins. However, bone pins can alter the microstructure of cadaveric bone and are too invasive to be used consistently in live humans for the purpose of research. Therefore, researchers must rely on less invasive techniques such as surface mounted accelerometers (SMA). Kim et al. (1993) and Lafortune et al. (1995) measured the accuracy of using SMA by comparing them directly to the outputs obtained from BMA. Their concern was that the soft tissue underlying the SMA would distort the signal and provide inaccurate measurements. However, when a proper protocol is followed, SMA are suitable surrogates for BMA for measuring the acceleration of the underlying bony structures. Kim et al. (1993) reported the most accurate results when lightweight accelerometers were pre-loaded onto the underlying bone (i.e. strapped down with approximately 45 N of force, pushing into the soft tissue).

1.3.4 Optoelectronic Measurement System

Optoelectronic systems are particularly useful for quantifying three-dimensional joint and segment kinematics when the assumption of a rigid body model is made (Andrews & Youm, 1979; Schmidt et al., 1999). These systems can be passive, in which a light is reflected off a spherical marker, or active, where the markers themselves are light emitting diodes. In either case, a camera system records the reflected or emitted light resulting in the calculation of three-dimensional position of the marker.

The Optotrak (Optotrak Certus, Northern Digital Inc, Waterloo ON, Canada) system is an active system that consists of position sensors (three cameras per sensor) that create a measurement volume (Figure 1.12) within which the markers can be registered by the cameras.

To determine the location of a marker, the Optotrak system uses a direct linear transform (DLT) (Wood & Marshall, 1986) method, whereby a relationship between the two-dimensional coordinates of the marker and the three-dimensional location in space is created during the calibration procedure. Once this relationship has been established, redundant equations are developed such that a marker can be put into an unknown position and the three-dimensional location in the global coordinate system can be calculated.

When properly placed joint markers and segment marker sets are used, the coordinate data collected from this system can be used to calculate motion about the joints. From the global position data, local joint and segment coordinate systems can be developed and joint angles determined. While the joint kinematics can be represented in a number of ways, Euler angles (Woltring, 1991) and the floating axis system (Grood & Suntay, 1983; Wu et al., 2005) are two of the more common methods. With both systems, it is required that directional cosine matrices be developed that represent the local coordinate systems of the proximal and distal segments (i.e. allowing the motion of one segment to be described with respect to the other).
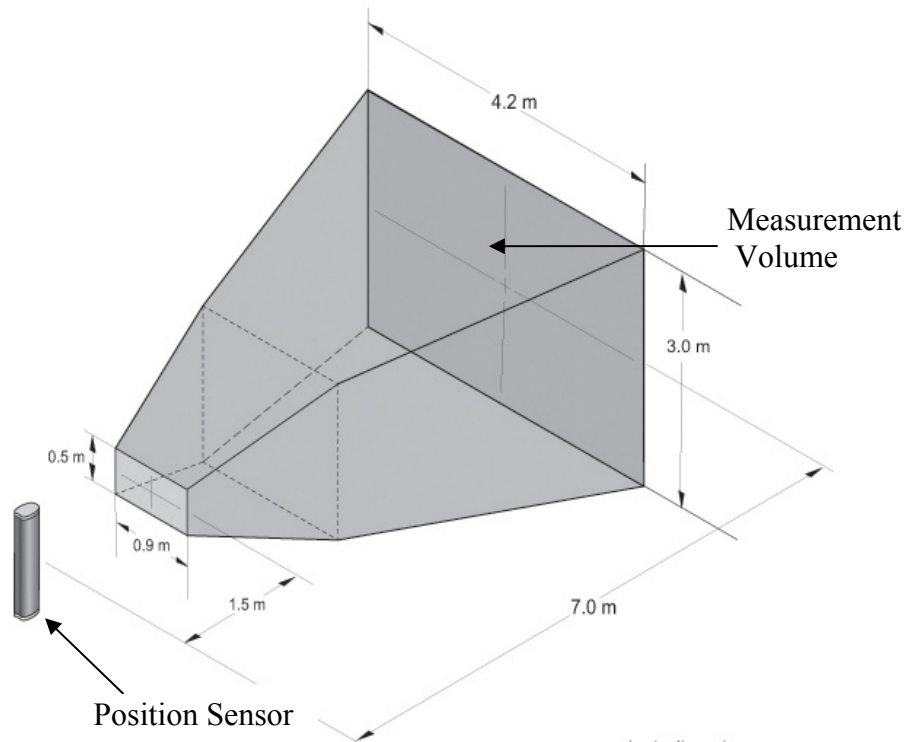
Figure 1.12: Optotrak Measurement Volume
A schematic representation of the Optotrak measurement system. One position sensor is shown here along with the associated measurement volume (grey area). Strategically placing additional position sensors can increase the size of the measurement volume (Optotrak Users Manual, 2009).

Euler angles are parameterized in terms of three component rotations that are sequence dependent (Roth, 1967; Chao, 1980) and defined by

$$r_{\alpha,\beta,\gamma} = R_x(\alpha)R_y(\beta)R_z(\gamma) \qquad \text{(Eq. 1.10)}$$

where α, β, and γ represent the rotations about the coordinate axes x, y, z (Woltring, 1991). Therefore, the component matrices are defined a

$$R_x(\alpha) = \begin{bmatrix} 1 & 0 & 0 \\ 0 & \cos\alpha & -\sin\alpha \\ 0 & \sin\alpha & \cos\alpha \end{bmatrix}$$

$$R_y(\beta) = \begin{bmatrix} \cos\beta & 0 & \sin\beta \\ 0 & 1 & 0 \\ -\sin\beta & 0 & \cos\beta \end{bmatrix}$$

$$R_z(\gamma) = \begin{bmatrix} \cos\gamma & -\sin\beta & 0 \\ \sin\beta & \cos\beta & 0 \\ 0 & 0 & 1 \end{bmatrix} \qquad \text{(Eq.1.11)}$$

The rotation matrix is determined by multiplying the above component matrices in the appropriate, sequence dependent order. For example, a rotation sequence of z, y, x (Wu et al., 2005) results in (Eq. 1.12), and the resulting Euler angles are calculated by setting the direction cosine matrix equal to the rotation matrix (Woltring, 1991; Winter, 2005).

$$\begin{bmatrix} \cos\gamma\cos\beta & \cos\gamma\sin\beta\sin\alpha - \sin\gamma\cos\alpha & \cos\gamma\sin\beta\cos\alpha + \sin\gamma\sin\alpha \\ \sin\gamma\cos\beta & \sin\gamma\sin\beta\sin\alpha + \cos\gamma\cos\alpha & \sin\gamma\sin\beta\cos\alpha - \cos\gamma\sin\alpha \\ -\sin\beta & \cos\beta\sin\alpha & \cos\beta\cos\alpha \end{bmatrix} \text{(Eq.1.12)}$$

While this method is commonly used among biomechanists and provides an accurate calculation of joint angles, the sequence dependency of this method can result in "gimbal" lock (Winter, 2005; Woltring, 1991). Furthermore, it has been suggested that Euler angles are not well understood by the clinician who might otherwise utilize such information for diagnosis and improved treatment (Grood & Suntay, 1983).

Therefore, Grood & Suntay (1983) proposed a floating axis system of calculating clinically meaningful joint angles while avoiding the problem of "gimbal" lock. The floating axes system works on the premise that there is a fixed axis in the proximal segment, a fixed axis in the distal segment and floating axis that is common to them both (Grood & Suntay, 1983; Cole et al., 1993). For example, to describe the motion of the forearm relative to the humerus, the flexion extension axis (referred to as e1) is the medial-lateral axis of the coordinate system fixed to the proximal segment (humerus); the rotation axis (referred to as e3) is the longitudinal axis of the distal (forearm) coordinate system; and the abduction-adduction axis (referred to as e2) is the common floating axis, and is perpendicular to e1 and e3 (Wu et al., 2005) (Figure 1.13). If I, J, K and i, j, k, are the unit base vectors of the humeral and forearm systems, and K is coincident with the e2 axis, j with the e3 axis, and e2 equal to the cross product of e1 and e3, the joint angles can subsequently be calculated as:

$$\alpha = -\sin^{-1}(e2 \cdot J) \qquad\qquad \text{(Eq. 1.13)}$$

$$\beta = \sin^{-1}(e1 \cdot e3) \qquad\qquad \text{(Eq. 1.14)}$$

$$\gamma = \sin^{-1}(e2 \cdot k) \qquad\qquad \text{(Eq. 1.15)}$$

1.3.5 Electromyography

When an electrical signal reaches the muscle (from a nerve), interaction of the cross bridges (thick and thin filaments) (Figure 1.14b) within the muscle occurs, causing the muscle to contract. Contraction of the muscle fibers towards the center of the muscle applies a force to the tendons, resulting in the bone at the muscle's insertion end to move towards the muscle's fixed (origin) end (Figure 1.14a).
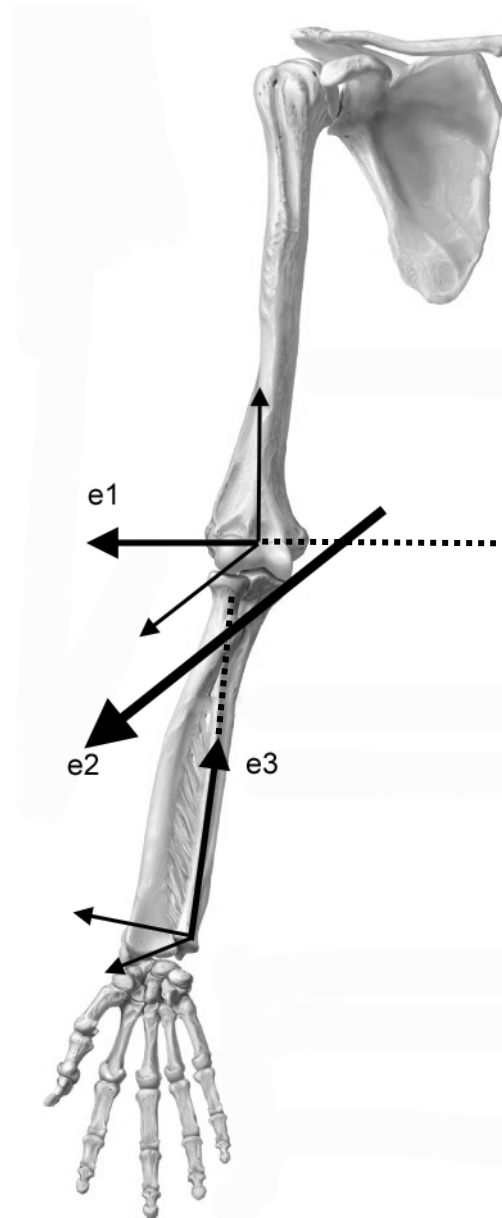
Figure 1.13: Floating Axis System
An example of the three axes
creating the floating axis joint
coordinate system (Grood &
Suntay, 1983) to describe the
motion of the forearm relative to
the humerus (right arm anterior
view).

The electrical signal, or motor unit action potential (MUAP), is caused by the movement of sodium and potassium ions across the muscle fiber (Enoka, 1996; Kamen & Gabriel 2010) and can be recorded externally by surface electrodes (Winter, 1980; Hof, 1984) (Figure 1.15). In most cases, three electrodes are used to collect the signal from a single muscle: two are placed over the muscle belly and the third, acting as ground electrode, is usually placed over a non-conductive bony prominence (Winter, 2005). This configuration produces a differentially amplified electromyographic (EMG) signal where the common ambient noise (detected by the ground electrode) has been subtracted from the EMG signal (Winter, 2005) (Figure 1.16).

There are several factors that can affect the EMG before it reaches the data acquisition equipment. The area and shape of the electrodes (De Luca 1997), spacing of the electrodes (Fuglevand et al., 1992), and presence of an electrocardiogram signal (i.e. the electrical signal from the heart) (Drake, 2006), position of the electrodes with respect to other muscles (Mogk & Keir, 2003), subcutaneous adipose tissue (Nordander et al., 2003) and skin preparation (e.g., cleaning) (Cram & Rommen, 1989).

The raw EMG signal (Figure 1.16a) is a stochastic signal with a mean of zero, making it difficult to analyze in this form (Kamen & Gabriel, 2010). Therefore, the signal is linear enveloped to transform it into a useable and more meaningful format (Potvin & Brown, 2004; Winter, 2005; Kamen & Gabriel, 2010). This involves full wave rectification of the raw signal (i.e. calculating the absolute value of each data point (Figure 1.16b) and applying a low pass Butterworth filter (Figure 1.16c). In EMG processing, the choice of filter cut-off frequency is usually a function of the purpose of
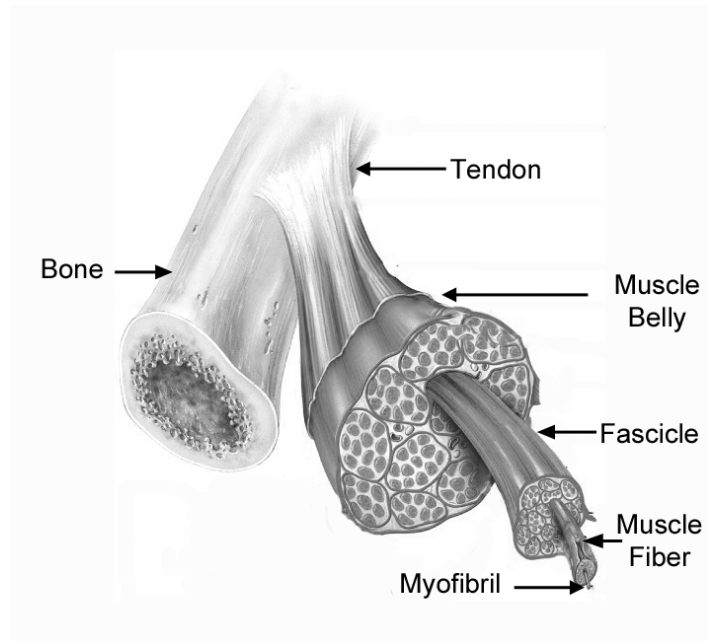
(a)
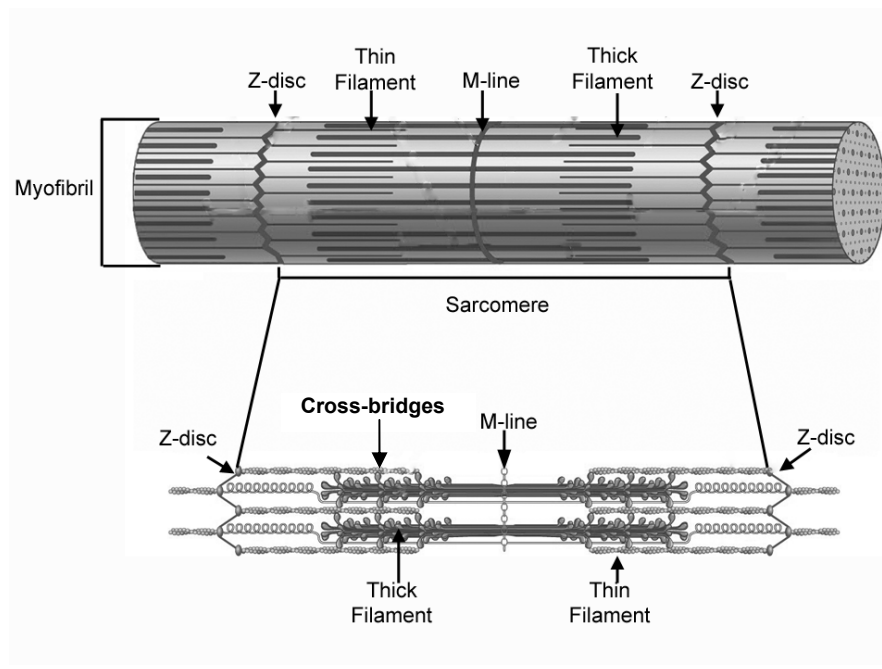
(b)

Figure 1.14: Muscle Structure
Structures of a typical skeletal muscle at the macro (a) and
microscopic (b) level (Modified from Tortora & Neilsen, 2011).
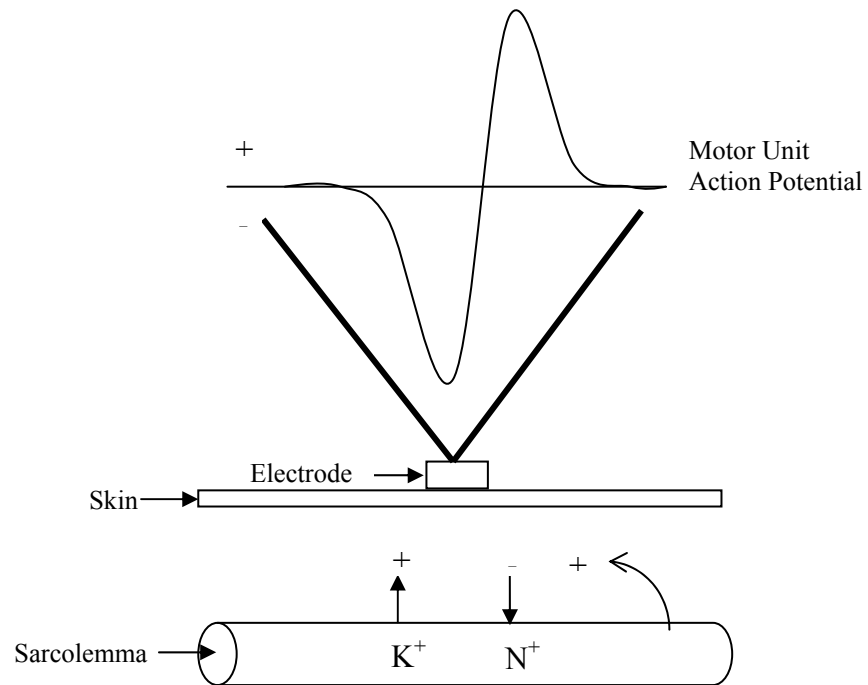
Figure 1.15: Motor Unit Action Potential Generation
Schematic representation of the events in generating a
single motor unit action potential (MUAP) and the shape
of the recorded signal (Modified from Kamen & Gabriel,
2010).

the analysis. For example, if one is interested in determining the EMG onset times, a 30-50 Hz cut-off frequency is used (Walter, 1984; Hodges & Bui, 1996) compared to a 2.5 Hz - 6 Hz frequency cut-off when the aim of the research is to estimate muscle forces (Potvin et al., 1996; Brereton & McGill, 1998).

It is important to select an appropriate mathematical method to extract meaningful information the linearly enveloped EMG. For example, the mean absolute value or root mean square error can be used to estimate the amplitude of the EMG (Clancy et al., 2006). Integration of the EMG signal can provide a measure of the muscle's total effort and the integration can occur over the entire signal or over small time intervals (Winter, 2005), while a variance ratio can be calculated that quantifies the similarity between linearly enveloped EMG signals (Hershler & Milgrom, 1978). Finally, normalization of the EMG signal to a participant's maximal voluntary contraction (MVC) (Figure 1.16d), is one of the most common and useful EMG transformations (Yang & Winter, 1984). An MVC is a procedure where an individual is placed in a standardized posture and asked to exert maximal effort (that stresses the muscle of interest) against an immovable object. Normalization of the EMG provides an estimate of the muscle forces and allows for a direct comparison of muscle activation between individuals and tasks (Mirka, 2007).

1.4 Upper Extremity Loading

There are a number of methods available (*in vitro*, *in vivo* and numerical) to measure the response of the upper extremity when loaded dynamically. Each method has its benefits and limitations in dealing with this particular load type. Within each testing method, there also exists a variety of techniques aimed at determining the force
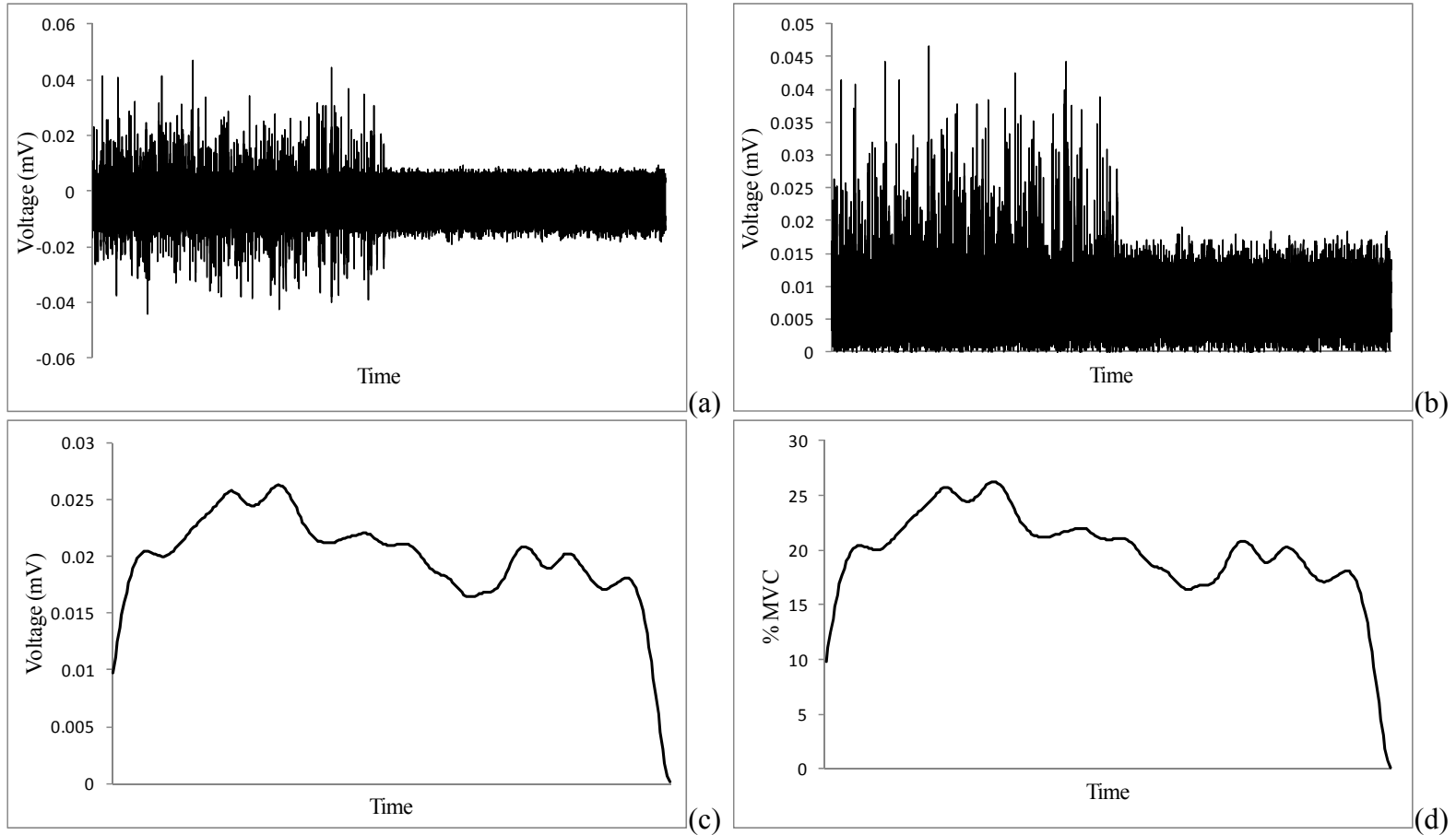
Figure 1.16: Electromyography Signal Processing
An example of the process involved in creating a linearly enveloped EMG. The raw signal (a) is full wave rectified (b) low-pass Butterworth filtered (c) and normalized to the participants' maximal voluntary contraction (d).

capacity of the upper extremity bones, the kinematics of the upper extremity joints, and the effectiveness of interventions in reducing the risk of injury to the upper extremity.

1.4.1 *In vitro* Testing

In vitro tissue mechanics can be described as the organized study of the mechanical- and structural-related properties, in an attempt to understand the force, motion and strength of animal and human tissue (muscle, bone, ligaments, cartilage) in response to system perturbations (Black, 1979; Fung, 1993). This understanding is important to injury prevention, (e.g., determining both safe and injurious loading parameters (Adams et al., 2002)), medical applications (e.g., fixation of medical implants (Dunham et al., 2005)), and to protocol and methodology development (Burkhart et al., 2011).

The ability of a tissue to withstand loading without experiencing failure is an inherent function of the tissue's structure. With respect to bone tissue, the most commonly injured tissue during impact, there are a number of factors that can have an effect on the bone's mechanical properties (e.g., ultimate strength) (Fung et al., 1993). For instance, Meyers et al. (1993) and Augat et al. (1996) found that specific geometric variables such as thickness and area of the cortical shell, and the bone mineral density, of the bone all contributed to its ultimate strength. Furthermore, as suggested by Greenwald et al. (1998), the viscoelastic properties of bone, also have an effect on the failure load of bony tissue.

Many researchers have mechanically loaded cadaver specimens to determine the maximal load strength of human forearms, specifically the distal radius (Frykman, 1967; Horseman et al., 1983; Meyers et al., 1991; Meyers et al., 1993; Augat et al.,

1996; Giacobetti, et al., 1997; Greenwald et al., 1998; Duma et al., 2003; Lubhan et al., 2005) (Table 1.2). However, a large range of strength values exists amongst these studies (1580 N – 3773 N); variation attributed to methodological inconsistencies between and within these experiments. The majority of these studies used quasi-static loading to apply forces to the forearm specimen. The quasi-static nature of these studies may not be indicative of the high energy loading of the wrist and forearm that takes place when the hand is impacted in a fall. Furthermore, Troy & Grabiner (2007) suggested that the axis of loading, and not just load magnitude, may affect both the anatomical structures that are injured as well as the ultimate failure strength. Off-axis forces (perpendicular to the long axis of the forearm) were found to initiate injury at lower magnitudes than axial forces (parallel to the long axis of the forearm), through the application of a three dimensional finite element model. Finally, of the studies that did utilize dynamic loading (e.g., McGrady et al, 2001), the impacts were relatively uncontrolled and the authors were unable to determine the true point of failure. Therefore, the fracture mechanisms of the distal radius are not well understood and it is unclear which combination of forces (Fx vs. Fy vs. Fz) and force variables (e.g., impulse, load rate) are responsible for these injuries.

1.4.2 *In vivo* Testing

While *in vivo* testing is limited to sub-maximal load applications, valuable information can be attained given that the segment is intact (i.e., contains all the viable soft tissues (muscle and fat)) that can both affect and are affected by the impact forces. Furthermore, *in vivo* testing allows for active joint kinematics to be tested. However, with respect to forward falls, it is important that the fall simulation method closely

Table 1.2: *In vitro* Loading Studies
Summary of previous *in vitro* radius loading studies.

Author (Year)	Specimen Condition	Load Conditions Displacement Rate	Failure Force (N)	Fracture location/ Severity
Greenwald et al. (1998)	Intact below elbow	2.80 m/s	2882-3808	Varied location and severity Not all specimens failed
McGrady et al. (2001)	Intact below elbow	N.S.	Non-destructive: 779 Destructive: 1093.0	Varied location and severity
Moore et al. (1997)	Intact below elbow	3.9m/s	N.S	Varied location and severity
Lubhan et al. (2005)	N.S.	N.S.	3408	Varied location and severity
Duma et al. (2003)	Intact below elbow	N.S.	2863	Varied location and severity
Meyers et al. (1993)	15 cm proximal to wrist	25mm/s	1780	Colles and Ulnar Frx patterns
Wu et al. (2000)	Distal 1/3 of radius	75 mm/s	N.S	N.S.
Augat et al. (1996)	Distal 1/3 of radius	75 mm	2698	Consistent fracture patterns
Staebler et al. (1999)	Intact below elbow	Single ramp load of 250N at 100N/s	N.S.	N.S.
Gaicobetti et al. (1997)	Intact below elbow	25mm/s	2245-2285	N.S.
Wigderowitz et al. (2000)	Distal 12 cm of radius	7 mm/s	2794	N.S.

N.S. = Authors did not state these values.

matches real world motions. Chiu & Robinovitch (1998), Chou et al. (2001), and Tsai, et al. (2003) implemented a strategy that kept the knees on the ground (creating a 30° angle between the ground and the thigh), and the fall was arrested unilaterally with one outstretched arm (15° from the vertical). These falls occurred from 1, 3, or 5 cm above the ground. DeGoede & Ashton Miller (2002) and Lo et al. (2003) used a method that took the individual off their knees and initiated a fall in a semi-upright position. Individuals were lowered and asked to flex forward so the shoulders were approximately 1m above the ground. However, unlike Chiu & Robinovitch (1998), a number of upper extremity postures were used, thus creating a variety of shoulder and elbow angle combinations. However, all falls were carried out such that only the hands contacted the ground (i.e. neither knee nor torso contact occurred).

Kim & Ashton-Miller (2003) and Tan et al. (2006) both used the same initial starting position; however, they had contradicting outcomes. Kim & Ashton-Miller (2003) varied fall distance by moving the individual backwards at intervals of 20 cm, over a range from 40-100 cm. In this case, the impact surface was located in front of the faller approximately 1.2 m off the ground, allowing subjects to fall into the platform. In comparison, Tan et al. (2006) let the individual fall from standing height to the ground, with an initial forward lean of approximately 15° to the vertical. Individuals were instructed to contact the ground with flexed knees before commissioning the upper extremity to arrest the fall (Table D.1).

Implementing another approach, DeGoede et al. (2002) used a swinging pendulum mass to initiate contact with the upper extremity while the subjects were seated in an upright position. The individuals were instructed to arrest the mass using a

variety of shoulder-elbow posture combinations, while simulating three different fall

heights. Fall height was manipulated by altering the velocity of the pendulum (1.8 m/s,

2.3 m/s and 3.0 m/s). The seated position provided adequate support to the lumbar

region of the spine while allowing adequate movement of the upper extremity. Finally,

Burkhart & Andrews (2010a, 2010b) developed a seated human pendulum to apply an

impact to the palmar soft tissues of the left and right hands (Table 1.3). The human

pendulum was pulled back a specified distance, such that the impact forces and

velocities were approximately 0.5 body weight and 1 m/s, respectively. This method

was successfully used to investigate the effect of wrist guards, elbow angles and muscle

activation levels on the acceleration experienced at the wrist and elbow. However, these

fall simulation methods are limited in that the participants start from a stationary

position and motion occurs primarily in one direction. Furthermore, the role of the

forearm and arm musculature in fall arrest is not well understood.

1.4.3 Finite Element Analysis

Finite element analysis (FEA) is a powerful tool that can be used to analyze the

response of the distal radius to impact loading computationally. The main advantage of

FEA is that multiple destructive tests can be simulated on a single model.

At its basic level, FEA consists of the discretization of a structure into a number

of simple shapes, referred to as a mesh, in order to compute the stresses and strains at

any location throughout the structure by obtaining an approximate solution to (Eq.

1.16).

$$\{F\} = [m] \cdot \{\ddot{x}\} + [c] \cdot \{\dot{x}\} + [k] \cdot \{x\} \qquad \text{(Eq. 1.16)}$$

Where: [m] = mass matrix; [c] = damping matrix; [k] = stiffness matrix; {x} = displacement; {ẋ} = velocity; {ẍ} = acceleration.

The geometric shapes used to construct the mesh are termed elements and are most commonly found in the form of hexahedrals and tetrahedrals (Figure 1.17). However, for dynamic simulations, hexahedrals are preferred as they are more stable and provide more accurate results (Benzley et al., 1999; Ramos & Simoes, 2006). Once a structure has been assigned a quality mesh, material models, material properties, contact definitions and boundary conditions are assigned to the model.

While a number of distal radius finite element models (FEM) have been developed (Table 1.3), only two have attempted to simulate the loads required to create a fracture at the distal radius (Troy & Grabiner, 2007; Buchanan & Ural, 2010). However, these two models used primarily tetrahedral elements, static loading, and did not provide a validation of their work. Therefore, the applicability of their results is limited and the need for a dynamic, validated FEM of the distal radius is highlighted.

Nodes

(a)   (b)
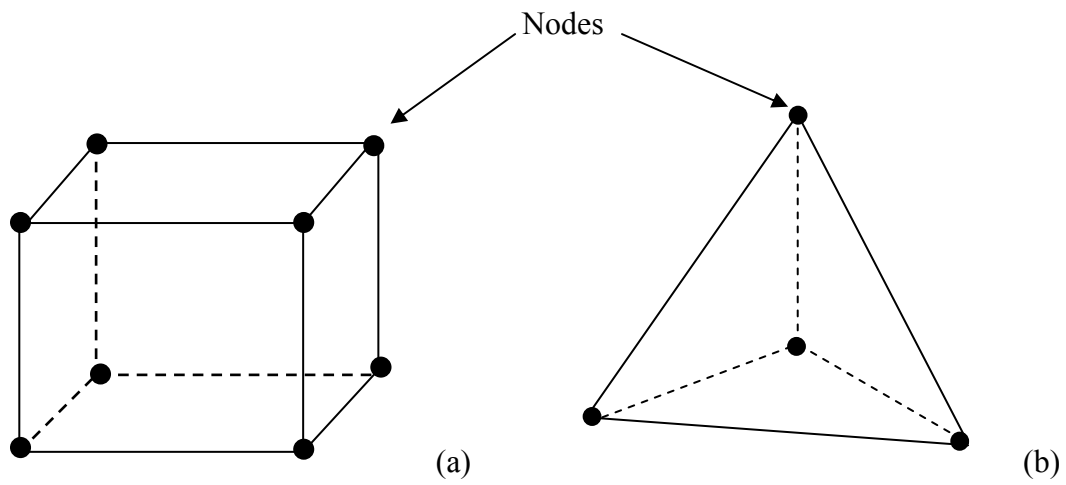
Figure 1.17: Finite Element Shapes
An example of a hexahedral (a) and tetrahedral (b) finite element used to generate a
finite element mesh. The black dots indicate the nodes

Table 1.3: Radius Finite Element Model Studies
A comparison of previous radius finite element models including types of meshes and loading protocols.

Author	Radius Section	Type of Elements	Bone Components	Mesh Diagnostics	Material Models	Load	Load Rate
Andersson et al. (2005)	Distal third	8 node brick	Cortical Cancellous	No	Linear elastic	N.S.	N.S.
Boutroy et al. (2008)	Distal 1 cm	8 node brick	Cortical Cancellous	No	Linear elastic	1000N	Static
Buchanan et al. (2010)	Distal third	Tetrahedral	NS	No	Non-linear	N.S.	Static
Carrigan et al. (2003)	Distal third	Tetrahedral	Cortical	No	NS	15 N	N.S.
MacNeil et al. (2008)	Distal 3 cm	8 node brick	Cortical Cancellous	No	Non-linear	N.S	N.S.
Pistoia et al. (2002)	Distal 2 cm	8 node brick	Cortical Cancellous	No	Non-linear	1000 N	200 mm/min
Pistoia et al. (2003)	Distal 2cm	8 node brick	Cortical Cancellous	No	NS	N.S.	N.S.
Pistoia et al. (2004)	Distal 1 cm	8 node brick	Cortical Cancellous	No	Linear	1000 N	N.S.
Rogge et al. (2002)	Distal 2 cm	8 node brick	Cortical	No	Linear elastic	5 N interval	N.S.
Troy et al. (2007)	Distal third	Mixed	Cortical Cancellous	No	Linear isotropic	3000N	Static
Ulrich et al. (1999)	N.S.	N.S.	Cortical	No	Isotropic	1000 N	N.S.

N.S. = Authors did not state these values.

1.5 Research Objectives and Hypotheses

The overarching theme of this dissertation is musculoskeletal injury and injury prevention specifically related to distal radius fractures (Figure 1.18). The overall purpose of this research is to improve the understanding of these injuries so that evidence based injury prevention interventions can successfully be designed. Although successful on their own, when used together, *in vitro*, *in vivo* and numerical research techniques provide a powerful compliment of methods capable of addressing the objectives and hypotheses of this research (Figure 1.18).

1.5.1 Research Objectives
The specific objectives of this research were:

1. To determine the *in vitro* failure characteristics of the distal radius as a result of dynamic impact loading indicative of a forward fall, and develop multivariate injury risk criteria (Sections 2.1 and 2.2).

2. To determine the effectiveness of acceleration data in predicting injury to the distal radius and validating the use of accelerometers as strain gauge surrogates to assess the response of bone to impact loading (Section 2.3).

3. To design an impact apparatus that is capable of simulating the multi-directional motion of a forward fall *in vivo* (Section 3.1).

4. To determine if the type of fall can affect the kinematics and muscle activation levels of the upper extremity *in vivo* (Section 3.2).

5. To develop and validate a finite element model of the distal radius that is capable of simulating dynamic impact loading (Sections 4.1 and 4.2).
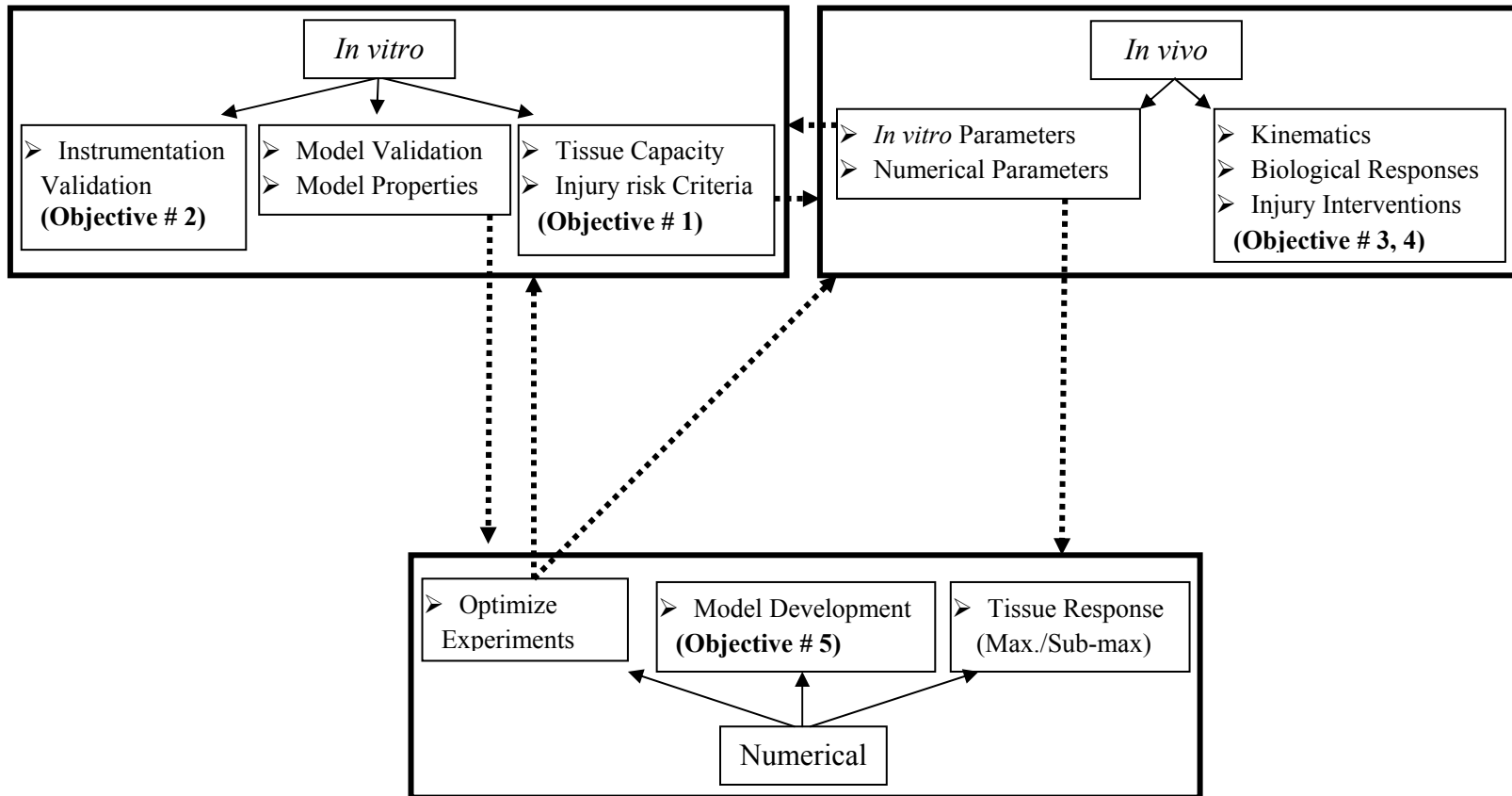
Figure 1.18: Research Methods
A schematic diagram showing the results of the individual research techniques and the interactions between them. Solid arrows show the results within each research technique while the dotted arrows highlight the relationships between research techniques.

1.5.2 Research Hypotheses

Based on the research objectives above, the corresponding hypotheses were:

1. The fracture forces of the distal radius would be lower than those previously reported for radius impact studies and the inclusion of dynamic variables such as impulse and load rate would improve the prediction of injury risk (Sections 2.1 and 2.2).

2. Accelerometers would accurately predict bone strains (measured from a strain gauge) and bone fracture (Section 2.3).

3. An impact apparatus could be developed that accurately simulates the multi-directional motion of a forward fall (Section 3.1).

4. Individuals would be capable of selecting fall kinematics that minimize the impact force variables experienced by the upper extremity (Section 3.2).

5. A valid finite element model of the distal radius could be developed that accurately predicts the bone stresses and strains, impact forces and accelerations, in response to dynamic impact loading (Section 4.1 and 4.2).

1.6 Dissertation Overview

This dissertation is written in a manuscript format. Each of the next three chapters presents a series of manuscripts that are structured to highlight the usefulness of the three fundamental testing techniques and how they complement each other. The relationship between the chapters and the studies (and objectives) included within them, are highlighted in Figure 1.18. In Chapter 2, two papers describe the *in vitro* testing of distal radius cadaveric specimens to determine the failure characteristics, injury criteria

when exposed to dynamic impact loading, while a third paper illustrates the usefulness of accelerometers in predicting bone strains. Chapter 3 outlines the development of an apparatus that applies dynamic loads to the upper extremity *in vivo*. A second manuscript in Chapter 3 describes the *in vivo* kinematics, kinetics and muscle activation levels in response to simulated forward falls using the novel fall apparatus. The development and validation of a finite element model of the distal radius is presented in Chapter 4. Finally, Chapter 5 summarizes the research and its impact, addresses the general benefits and limitations of this body of work, and suggests future work related to each of these studies.

1.7 References

Adams MA, Boduck N, Burton K, Dolan P. 2002. Biomechanics of Back Pain. London, UK: Churchill Livingstone.

Anderson DD, Deshpande BR, Daniel TE, Baratz ME. 2005. A three-dimensional finite element model of the radiocarpal joint: distal radius fracture step-off and stress transfer. The Iowa Orthopaedic Journal. 25, 108-107.

Augat P, Reeb H, Claes LE. 1996. Prediction of fracture load at different skeletal sites by geometric properties of the cortical shell. Journal of Bone and Mineral Research. 11, 1356-1363.

Andrews JG, Youm Y. 1979. A biomechanical investigation of wrist kinematics. Journal of Biomechanics. 12, 83-89

Anglin C, Wyss UP. 2000. Review of arm motion analysis. Journal of Engineering in Medicine. 214, 541-555.

Benham PP, Crawford RJ, Armstrong CG. 1996. Mechanics of engineering materials. Harlow, England: Pearson, Prentice Hall.

Benzley SE, Perry E, Merkley K, Clark B, Sjaartdama G. 1999. A comparison of all hexagonal and all tetrahedral finite element meshes for elastic and elasto-plastic analysis. Proceedings of the 4th International Meshing Roundtable. Albuquerque NM.

Black J. 1976. Dead or alive: the problem of *in vitro* tissue mechanics. Journal of Biomedical Materials Research. 10, 377-389.

Blake AJ, Morgan K, Bendall MJ, Dallosso H, Ebrahim SBJ, Arie THD, Fentem PH, Bassey EJ. 1988. Falls by the elderly at home: prevalence and associated factors. Age and Ageing*,* 17, 365-372.

Bliuc D, Nguyen N, Milch V, NguyenTV, Eisman JA, John A. 2009. Mortality risk associated with low-trauma osteoporotic fractures and subsequent fracture in men and women. Journal of the American Medical Association. 301, 513-521.

Boutroy S, van Rietbergen B, Sornay-Rendu E, Munoz F, Bouxsein ML, Delmas PD. 2008. Finite element analysis based on *in vivo* HR-pQCT images of the distal radius is associated with wrist fracture in postmenopausal women. Journal of Bone and Mineral Research. 23, 392-399.

Brereton LC, McGill SM. 1998. Frequency response of spine extensors during rapid isometric contractions: effects of muscle length and tension. Journal of Electromyography and Kinesiology. 8, 227-232.

Buchanan D, Ural A. Finite element modelling of the influence of hand position and bone properties on the Colles fracture load during a fall. 132, 081007-1 - 081007-8.

Burkhart TA, Andrews D M. 2010a. The effectiveness of wrist guards for reducing wrist and elbow accelerations resulting from simulated forward falls. Journal of Applied Biomechanics. 26, 281-289.

Burkhart TA, Andrews DM. 2010b. Activation level of extensor carpi ulnaris affects wrist and elbow acceleration responses following simulated forward falls. Journal of Electromyography and Kinesiology. 20, 1203-1210.

Burkhart TA, Dunning CE, Andrews DM. 2011. Determining the optimal system-specific cut-off frequencies for filtering *in vitro* upper extremity impact force and acceleration data through residual analysis. Journal of Biomechanics. 44, 2728-2731.

Burge R, Dawson-Hughes B, Solomon DH, Wong JB, King A, Tostenson A. 2007. Incidence and economic burden of osteoporosis-related fractures in the United States, 2005-2025.

Burstein AH, Reilly DT, Martens M, 1976. Aging of bone tissue: mechanical properties. The Journal of Bone and Joint Surgery (American Volume). 58, 82-86.

Carrigan SD, Whiteside RA, Pichora DR, Small CF. 2003. Development of a three-dimensional finite element model for carpal load transmission in a static neutral posture. Annals of Biomedical Engineering. 31, 718-725.

Carter DR, Hayes WC. 1977. The compressive behaviour of bone as a two-phase porous structure. The Journal of Bone and Joint Surgery (American Volume). 59, 954-962.

Chang WR 2002. From research to reality on slips, trips and falls. Safety Science. 40, 557-558.

Chao EYS. 1980. Justification of triaxial goniometer for the measurement of joint motion. Journal of Biomechanics. 13, 989-100.

Chiu J, Robinovitch SN. 1998. Prediction of upper extremity impact forces during falls on the outstretched hand. Journal of Biomechanics. 31, 1169-1176.

Choi K, Kuhn JL, Ciarelli MJ, Goldstein SA. 1990. The elastic moduli of human subchondral, trabecular, and cortical bone tissue and the size-dependency of cortical bone modulus. Journal of Biomechanics. 23, 1103-1113.

Chou P-H, Chou Y-L, Lin C-J, Su F-C, Lou S-Z, Lin C-F, Huang G-F. 2001. Effect of elbow flexion on upper extremity impact forces during a fall. Clinical Biomechanics. 16, 888-894.

Clancy EA, Morin EL, Merletti R. 2006. Sampling, noise-reduction and amplitude estimation issues in surface electromyography. Journal of Electromyography and Kinesiology. 12, 1-16.

Colles' Frx, (2006). Wheeless' Textbook of Orthopaedics. Duke University Orthopaedics. http://www.wheelessonline.com/ortho/colles_frx.

Cole GK, Nigg BM, Ronsky JL, Yeadon MR. 1993. Application of the joint coordinates system to three dimensional joint attitude and movement representation: a standardised proposal. Journal of Biomechanical Engineering. 115, 344-349.

Courtney TK, Webster BS. 1999. Disabling occupational morbidity in the United States: an alternative way of seeing the Bureau of Labour Statistics' data. Journal of Occupational and Environmental Medicine. 41, 60-69.

Cram JR, Rommen D. 1989. Effects of skin preparation on data collected using an EMG muscle-scanning procedure. Biofeedback and Self-Regulation. 14, 75-82.

DeGoede KM, Ashton-Miller JA, Schultz AB, Alexander NB. 2002. Biomechanical factors affecting the peak hand reaction force during the bimanual arrest of a moving mass. Journal of Biomechanical Engineering. 124, 107-112.

DeGoede KM, Ashton-Miller JA. 2002. Fall arrest strategy affects peak hand impact force in a forward fall. Journal of Biomechanics. 35, 843-848.

De Luca CJ. 1997. The use of surface electromyography in biomechanics. Journal of Applied Biomechanics, 13, 135-163.

Donald IP, Bulpitt CJ. 1999. The prognosis of falls in elderly people living at home. Age and Ageing. 28, 121-125.

Dowling N. 2007. Review of complex and principal states of stress and strain. In Mechanical Behaviour of Materials (pp. 214-249). Saddle River, NJ: Pearson, Prentice Hall.

Drake JDM, Callaghan JP. 2006. Elimination of electrocardiogram contamination from electromyogram signals: an evaluation of currently used removal techniques. Journal of Electromyography and Kinesiology. 16, 175-187.

Duma SM, Boggess BM, Crandall JR. 2003. MacMahon CB. Injury risk function for the small female wrist in axial loading. Accident Analysis and Prevention. 35, 869-875.

Dunham CE, Takaki SE, Johnson JA, Dunning CE. 2005. Mechanical properties of cancellous bone of the distal humerus. Clinical Biomechanics. 20, 834-838.

Ellis JA, Keirluf JC, Klassen TP. 1995. Injuries associated with in-line skating from the Canadian hospitals' injury reporting and prevention program database. Canadian Journal of Public Health. 86, 133-136.

Enoka R. 1996. Neuromechanical basis of kinesiology. Champaign IL: Human Kinetics.

Fardellone P. 2008. Predicting the fracture risk in 2008. Joint Bone Spine. 75, 661-664.

Frykman G. 1967. Fracture of the distal radius including sequelae-shoulder-hand-finger syndrome: disturbance in the distal radio-ulnar joint and impairment of nerve function. Acta Orthopaedica Scandinavica, 108, 1-135.

Fuglevand AJ, Winter DA, Patla AE, Stashuk, D. 1992. Detection of motor unit action potentials with surface electrodes: influence of electrode size and spacing. Biological Cybernetics. 67, 145-153.

Fung YC. (1993). Biomechanics: Mechanical properties of living tissue (2nd Ed). New York: Springer-Verlag.

Garner E, Lakes R, Lee T, Swan C, Brand R. 2000. Viscoelastic dissipation in compact bone: implications for stress induced fluid flow in bone. Journal of Biomechanical Engineering. 122, 166-172.

Giacobetti FB, Sharkey PF, Bos-Giacobetti A, Hume EL, Taras JS. 1997. Biomechanical analysis of the effectiveness of in-line skating wrist guards for preventing wrist fractures. The American Journal of Sports Medicine, 25, 223-225.

Grabiner MD, Donovan S, Bareither ML, Marone JR, Hamstra-Wright K, Gatts S, Troy KL. 2008. Trunk Kinematics and Fall Risk of Older Adults: Translating Biomechanical Results to the Clinic", Journal of Electromyography and Kinesiology. 18, 197-204.

Greenwald RM, Janes PC, Swanson SC, McDonald TR. 1998. Dynamic impact response of human cadaveric forearms using a wrist brace. The American Journal of Sports Medicine, 26, 825-830.

Green JT, Gay FH. 1956. Colles' fracture- residual disability. American Journal of Surgery. 91, 636-646.

Grood ES, Suntay WJ. 1983. A joint coordinate system for the clinical description of three-dimensional motions: application to the knee. Journal of Biomechanical Engineering. 105, 136-144.

Herschler C Milgrom M. 1978. An optimality criterion for processing electromyographic (EMG) signals relating to human locomotion. IEEE Transactions on Biomedical Engineering. 25, 413-420.

Hof AL. 1984. EMG and muscle force: an introduction. Human Movement Science. 3, 119-153.

Hodges PW, Bui BH. 1996. A comparison of computer based methods for the determination of onset of muscle contraction using electromyography. Electroencephalography and Clinical Neurophysiology. 101, 511-519.

Horseman A, Currey JD, Phil, D. 1983. Estimation of mechanical properties of the distal radius from the bone mineral content and cortical width. Clinical Orthopaedics and Related Research, 176, 298-304.

Houshian S, Andersen HM. 2000. Comparison of in-line skating and roller-skating injury. Scandinavian Journal of Medicine and Science in Sports, 10, 47-50.

Houshian S, Mehdi B, Larsen M. 2001. The epidemiology of elbow fractures in children: analysis of 355 fractures, with special reference to supracondylar humerus fractures. Journal of Orthopaedic Science 6. 312-315.

Hsiao ET, Robinovitch SN. (1998). Common protective movements govern unexpected falls from standing height. Journal of Biomechanics. 31, 1-9.

Jaffe MS, Dijkers MP, Zamentis M. 1997. A population-based survey of in-line skaters' injuries and skating practices. Archives of Physical Medicine and Rehabilitation. 78, 1352-1357.

Jones G, Nguyen PN, Sambrook PN, Kelly PJ, Gilbert C, Eisman JA. 1994. Symptomatic fracture incidence in elderly men and women: the dubbo osteoporosis epidemiology study (DOES). Osteoporosis International. 4, 277-282.

Kamen G, Gabriel D. 2010. Essentials of electromyography. Champaign IL: Human Kinetics.

Kaneko TS, Pejcic MR, Tehranzadeh J, Keyak J. 2003. Relationships between material properties and CT scan data of cortical bone with and without metastatic lesions. Medical Engineering & Physics. 25, 445-454.

Kelly PJ, Twomey L, Sambrook PN., Eisman, J. A. 1990. Sex differences in peak adult bone mineral density. Journal of Bone and Mineral Research. 5, 1169-1175.

Khosla S, Riggs BL, Atkinson EJ, Oberg AL, McDaniel LJ, Holets M, Peterson JM, Melton LJ III. 2006. Effects of sex and age on bone microstructure at the ultra distal radius: a population-based non-invasive *in vivo* assessment. Journal of Bone and Mineral Research. 21, 124-131.

Kim KY, Ashton-Miller JA 2003. Biomechanics of fall arrest using the upper extremity: age differences. Clinical Biomechanics. 18, 311-318.

Kim W, Voloshin AS, Johnson SH, Simkin A. 1993. Measurement of the impulsive bone motion by skin mounted accelerometers. Journal of Biomechanical Engineering. 115, 47-52.

Lafortune MA, Henning E, Valiant GA. 1995. Tibial shock measured with bone and skin mounted transducers. Journal of Biomechanics. 28, 989-993.

Layne LA, Pollack KM. 2004. Nonfatal occupational injuries from slips trips and falls, among older workers treated in hospital emergency departments, United States 1998. American Journal of Industrial Medicine. 46, 32-41.

Leipzig RM, Whitlock EP, Wolff TA, Barton MB, Michael YL, Harris R, Petitti D, Wilt T, Siu A. 2010. Reconsidering the approach to prevention recommendations for older adults. Annals of Internal Medicine. 153, 809-814.

Li B, Aspden RM. 1997. Mechanical and material properties of the subchondral bone plate from the femoral head of patients with osteoarthritis or osteoporosis. Annals of Rheumatic Disease. 56, 247-254.

Lotz JC, Gerhart TN, Hayes WC. 1990. Mechanical properties of trabecular bone from the proximal femur: a quantitative CT study. Journal of Computer Assisted Tomography. 14, 107-114.

Lo J, McCabe GN, DeGoede KM, Okuizumi JA, Aston-Miller JA. 2003. On reducing imoact6 force in forward falls: results of a brief intervention in young males. Clinical Biomechanics. 18, 730-736.

Lubhan J, Englund R, Trinidad G, Lyons J, Ivance D, Buczek FL. 2005. Adequacy of laboratory simulations of in-line skater falls. Journal of Hand Surgery. 30A, 283-288.

MacNeil JA, Boyd SK. 2008. Bone strength at the distal radius can be estimated from high resolution peripheral quantitative tomography and the finite element method. Bone. 42, 1203-1213.

McGrady LM, Hoepfner P, Young CC, Raasch WG, Lim T-H, Han JS. Biomechanical effect of in-line skating wrist guards on the prevention of wrist fracture. KSME International Journal. 15, 1072-1076.

Meyers ER, Hecker AT, Rooks DS, Hipp JA, Hayes WC. 1993. Geometric variables from DXA of the radius predict forearm fracture load *in vitro*. Calcified Tissue International. 52, 199-204.

Meyers ER, Sebeny EA, Hecker AT, Corcoran TA, Hipp JA, Greenspan S. Hayes WC. 1991. Correlations between photon absorption properties and failure load of the distal radius *in vitro*. Calcified Tissue International. 52, 292-297.

Mirka GA. 1991. The quantification of EMG normalization error. Ergonomics. 34, 343-352.

Mogk JPM, Keir PJ. 2003. Crosstalk in surface electromyography of the proximal forearm during gripping tasks. Journal of Electromyography and Kinesiology. 13, 63-71.

Moore MS, Popvic NA, Daniel JN, Boyea SR, Polly DW. 1997. The effect of a wrist brace ion injury patterns in experimentally produced distal radius fractures in a cadaveric model. The American Journal of Sports Medicine. 25, 394-401.

National Physics Laboratory. 1998. Guide to the measurement of Force. London, England: Institute of Measurement and Control.

National Academy on an Ageing Society. 2003. State of ageing and health in America. http://www.agingsociety.org/agingsociety/pdf/state_of_aging_report.pdf;

Nevitt MC, Cummings SR. 1993. Type of fall and risk of hip and wrist fractures: the study of osteoporotic fractures. Journal of the American Geriatrics Society. 41, 1226-1234.

Nikolic V, Hancevic J, Hudec M, Banovic B. 1975. Absorption of the impact energy in the palmar soft tissue. *Anatomical Embryology,* 148, 215-221.

Nordander C, Wilner J, Hansson G-A, Larsson B, Unge J, Granquist L, Skerfving. 2003. Influence if the subcutaneous fat layer, as measured by ultrasound, skinfold callipers and BMI, on the EMG amplitude. European Journal of Physiology. 89, 514-519.

Nordin M, Frankel VH. 2001. Biomechanics of bone. In Basic Biomechanics of the Musculoskeletal System (pp 27-58). Baltimore MD: Lippincott Williams & Wilkins.

O'Neil TW, Varlow J, Silman AJ, Reeve J, Todd C, Woolf AD. 1994. Age and sex influences on fall characteristics. Annals of Rheumatic Disease. 53, 773-775.

Pavol MJ, Owings TM, Foley KT, Grabiner MD. 1999. The sex and age of older adults influences the outcome of induced trips. The Journals of Gerontology. 56, M428-M437.

Perron AD, Brady WJ, Keats TE, Hersh RE. 2001. Orthopedic pitfalls in the ED: scaphoid fracture. American Journal of Emergency Medicine. 19, 310-316.

Pistoia W, van Rietbergen B, Lochmuller E-M, Lill CA, Eckstein F, Ruegsegger P. 2004. Image-based micro-finite-element modeling for improved distal radius strength diagnosis: moving from "bench" to "bedside". Journal of Clinical Densitometry. 7, 153-160.

Pistoia W, van Rietbergen B, Lochmuller E-M, Lill CA, Eckstein F, Ruegsegger P. 2002. Estimation of distal radius failure load with micro-finite element analysis models based on the three-dimensional peripheral quantitative computed tomography images. Bone. 30, 842-848.

Pistoia W, van Rietbergen B, Ruegsegger P. 2003. Mechanical consequences of different scenarios for simulated bone atrophy and recovery in the distal radius. Bone. 33, 937-945.

Potvin JT, Norman RW, McGill SM. 1996. Mechanically corrected EMG for the continuous estimation of erector spinae muscle loading during repetitive lifting. European Journal of Applied Physiology. 74, 119-132.

Potvin JR, Brown SHM. 2004. Less is more: high pass filtering, to remove up to 99% of the surface EMG signal power, improves EMG-based biceps brachii muscle force estimates. Journal of Electromyography and Kinesiology. 14, 389-399.

Ray NF, Chan JK, Thamer M, Melton LJ- III. 1997. Medical expenditures for the treatment of osteoporotic fractures in the United States in 1995: Report from the national osteoporosis foundation. Journal of Bone and Mineral Research. 12, 24-35.

Ramos A, Simoes JA. 2006. Tetrahedral versus hexahedral finite elements in numerical modelling of the proximal femur. Medical Engineering & Physics. 916-924.

Roberts VL. 1966. Strain gauge techniques in biomechanics. Experimental Mechanics. 6, 19A-22A.

Robitaille Y, Laforest S, Fournier M, Gauvin L, Parisien M, Corriveau H, Trickey F, Damestoy N. 2005. Moving forward in fall prevention: an intervention to improve balance among older adults in real world settings. American Journal of Public Health. 95, 2049-2056.

Rogge RD, Adams BD, Goel VK. 2002. An analysis of bone stresses and fixation stability using a finite element model of simulated distal radius fractures. Journal of Hand Surgery. 27A, 86-92.

Roth B, 1967. Finite position theory applied to mechanism synthesis. Journal of Applied Mechanics. 34, 599-606.

Scheiber RA, Branche-Dorsey CM, Ryan GW, Rutherford GW, Stevens JA, O'Neil J. 1996. Risk factors for injuries from in-line skating and the effectiveness of safety gear. New England Journal of Medicine. 335, 1630-1635.

Seeman E, Delmas P. 2005. Bone quality-the material and structural basis of bone strength and fragility. New England Journal of Medicine. 354, 2250-2261.

Schmidt R, Diesselhorst-Klug C, Silny J, Rau G. 1999. A marker-based measurement protocol for unconstrained wrist and elbow motions. Journal of Biomechanics. 32, 615-621.

Sleet DA, Moffett DB, Stevens J. 2008. CDCs research portfolio in older adult fall prevention: a review of progress, 1985-2005, and future research directions. Journal of Safety Research. 39, 259-267.

Staebler MP, Moore DC, Akelman E, Weiss A-PC, Fadale PD, Crisco JJ. 1999. The effect of wrist guards in bone strain in the distal forearm. The American Journal of Sports Medicine. 27, 500-506.

Statistics Canada. 2011. Population by sex and age group. CANSIM table 051-0001 available from http://www40.statcan.gc.ca/l01/cst01/demo10a-eng.htm

Stewart HD, Innes AR, Burke FD. 1985. The hand complications of Colles' fractures. The Journal of Hand Surgery. 10-B, 103-106.

Tan JS, Eng JJ, Robinovitch S N, Warrick B. 2006. Wrist impact velocities are smaller in forward falls than backward falls from standing. Journal of Biomechanics. 39, 1804-1811.

Tinetti ME, Williams CS. 1998. The effect of falls and fall injuries on functioning in community-dwelling older persons. Journal of Gerontology. 53, M112-M119.

Tortora GJ, Nielsen M. 2011. Principles of Human Anatomy, 12 ed. Hoboken NJ: Wiley.

Troy KL, Grabiner MD. 2007. Off-axis loads cause failure of the distal radius at lower magnitudes than axial loads: A finite element analysis. Journal of Biomechanics. 40, 1670-1675.

Tsai M-C, Chou P-H, Chou Y-L, Lin T-S. 2003. Energy analysis of different trunk tilting angles in joint loading during fall on an outstretched hand. Biomedical Engineering- Applications Basis and Communication. 15, 217-222.

Turner CH, Rho J, Takano Y, Tsui TY, Pharr GM. 1999. The elastic properties of trabecular and cortical bone tissues are similar: results from two microscopic measurement techniques. Journal of Biomechanics. 32, 437-441.

Ulrich D, van Rietbergen B, Laib A, Ruegsegger P. 1999. Load transfer analysis of the distal radius from *in vivo* high resolution CT-imaging. Journal of Biomechanics. 32, 821-828.

United States Consumer Product Safety Commission. 2011. National Electronic Injury Surveillance System on-line data base. Retrieved from https://www.cpsc.gov/cgibin/NEISSQuery/home.aspx

Walter CB. 1984. Temporal quantification of electromyography with reference to motor control research. Human Movement Science. 3, 155-162.

Wigderowitchm CA, Paterson CR, Dashti H, McGurty D, Rowley DI. 2000. Prediction of bone strength from cancellous structure of the distal radius: can we improve on DXA. Osteoporosis International. 11, 840-846.

Winter DA, Rau G, Kadefors R, Broman H, De Luca CJ. 1980. Units, terms and standards in the reporting of EMG research. A report by the International Society of Biomechanics

Winter DA. 2005. Biomechanics and Motor Control of Human Movement. Hoboken, NJ: John Wiley & Sons, Inc.

Woltring HJ. 1991. Representation and calculation of 3-D joint movement. Human Movement Science. 10, 603-616.

Wong FYH, Pho RWH. 1984. Median nerve compression with tendon ruptures, after Colles' fracture. Journal of Hand Surgery European. 9, 139-141.

Wood GA, Marshall RN. 1986. The accuracy of DLT extrapolation in three-dimensional film analysis. Journal of Biomechanics. 19, 781-785.

Workplace Safety and Insurance Board (2005). Workplace safety and insurance board statistical supplement. http://www.wsib.on.ca/wsib/wsibobj.nsf/LookupFiles/DownloadableFile2005Statistical Supplement/$File/2278A_StatSup.pdf.

Wu C, Hans Y, He Y, Fan B, Njeh CF, Augat P, et al. 2000. Prediction of bone strength of distal forearm using radius bone mineral density and phalangeal speed of sound. Bone. 26, 529-533.

Wu G, van der Helm FCT, Veeger HEJ, Makhsous M, Van Roy P, Anglin C, Nagels J, Karduna AR, McQuade K, Wang X, Werner FW, Bucholz B. 2005. ISB recommendations on definitions of joint coordinate systems of various joints for the reporting of human joint motion - part II: shoulder, elbow, wrist and hand. Journal of Biomechanics. 38, 981-992.

Yang J, Winter DA. 1984. Electromyographic amplitude normalization methods: improving their sensitivity as diagnostic tools in gait analysis. Archives of Physical Medicine and Rehabilitation. 65, 517-521.

CHAPTER 2 – *IN VITRO* INVESTIGATION OF FRACTURES TO THE DISTAL RADIUS

2.1 Failure Characteristics of the Isolated Distal Radius in Response to Dynamic Impact Loading.[1]

2.1.1 Introduction

The distal radius is one of the most common fracture sites following a forward fall. Nevitt & Cummings (1993) reported that, of 337 forward falls, 39 % resulted in a wrist fracture with more than 60 % of all fractures to the wrist requiring some form of surgical intervention (Jaffe et al., 1997; Hill et al., 1998). This has lead to these injuries being identified as a major health problem (Ray et al. 1997) and the World Health Organization (WHO) to list fracture prevention among healthcare priorities (Fardellone, 2008). Despite this, fracture frequency has remained high and researchers have been unable to determine the optimal treatment strategies for various patterns and severities of wrist fractures (Henry, 2008). For example, from 1991-2009, the average number of emergency room reported wrist fractures remained relatively constant at approximately 164,000 per year in the United States alone (United States Consumer Product Safety Commission, 2011).

Although there is a general consensus regarding the risk factors for distal radius fractures resulting from forward falling (DeGoede, et al., 2003) prevention of these injuries requires a more thorough understanding of the injury mechanisms. Also, as stated by Henry (2008), the injury mechanism is one of the most important elements of

---

[1]A version of this work has been accepted for publication: Burkhart TA, Andrews DM, Dunning CE. In-press. Failure Characteristics of the Isolated Distal Radius in Response to Dynamic Impact Loading. Journal of Orthopaedic Research. This work is also the result of joint research between the University of Windsor and The University of Western Ontario and was presented at the Canadian Orthopaedic Research Association Conference, 2011.

the injury history, as this information can help discern the degree of damage, not only to the bone, but to the surrounding tissue as well. For example, Beardsley et al. (2005) identified the importance of understanding the energy involved in a fracture, as it generally determines the degree of comminution, thus affecting the treatment protocol. An accurate understanding of the injury mechanism (e.g., kinetic energy involved and direction of loading) can be accomplished by improving our knowledge of both the input parameters and the bones' response to dynamic loading through valid laboratory studies (Lubhan et al., 2005). While many researchers have mechanically loaded human cadaver specimens to determine the maximal external load strength of the distal radius (Frykman, 1967; Horseman et al., 1983; Meyers et al., 1991; Meyers et al., 1993; Augat et al., 1996; Giacobetti et al., 1997; Lewis et al., 1997; Moore et al., 1997; Greenwald et al., 1998; Staebler et al., 1999; McGrady et al., 2001; Duma et al., 2003; Lubhan et al., 2005), methodological inconsistencies, such as static or uncontrolled loading protocols, have lead to variability in results.   Researchers have studied the response to dynamic impact loads (Lewis et al., 1997; Moore et al., 1997; Greenwald et al., 1998; Lubhan et al., 2005) to better simulate real-world conditions, but their loading protocols have consisted of either high energy impacts that caused unrealistic fracture patterns throughout the specimen (Lubhan et al., 2005), or specimens were only impacted one time at a uniform load or load rate and were only classified as either having a fracture or not (Duma et al., 2003).

Therefore, the purpose of this study was to determine the mechanical properties of the distal radius, pre-fracture and at fracture, in response to dynamic, energy controlled, impact loading consistent with a forward fall arrest.

2.1.2 Methods

Eight (4 male, 4 female; 5 left, 3 right; mean (SD) age 61.0 (9.7) years) fresh-frozen human cadaveric radius specimens from donors that were free of metabolic bone diseases, metastatic cancers, diabetes, renal failure and pre-existing trauma, were procured. The distal articular surface of the radius was kept intact, while the remainder was cleaned of all soft tissues. Specimens were cemented into sections of 8.89 cm (3.5 inch) diameter PVC tubing, leaving the distal third of the radius exposed. Care was taken during potting to ensure the specimen alignment maintained a 75° angle in the sagittal plane (Greenwald et al., 1998) (Figure 2.1a), with no frontal plane tilt (Staebler et al., 1999), thereby mimicking the position of the radius *in vivo* during a forward fall (Figure 2.1b). To isolate fractures to the distal radius and to avoid potential lunate and scaphoid fractures, which also commonly occur after a fall (Leslie & Dickson, 1981), a high density polyethylene scaphoid and lunate model (SawBones®, Pacific Research Laboratories Inc., Vashon Washington) was used to impact the articular surface of the distal radius. The model was attached to a load cell, which in turn was attached to the impact plate (Figure 2.1a). To accommodate the *in vivo* 45° wrist extension angle during a fall (Troy & Grabiner, 2007a), the radio-carpal angle was set at approximately 42° using a custom jig, based on the mean angle between the radius and proximal row of carpal bones being 93 % of the global wrist angle (Werner et al., 1997) (Appendix A).

Impulsive impacts were applied with a custom designed pneumatic impact system (Quenneville et al., 2010) (Figure 2.2). A 6.8 kg projectile was propelled through an acceleration tube by pressurized air.

(a)

(b)
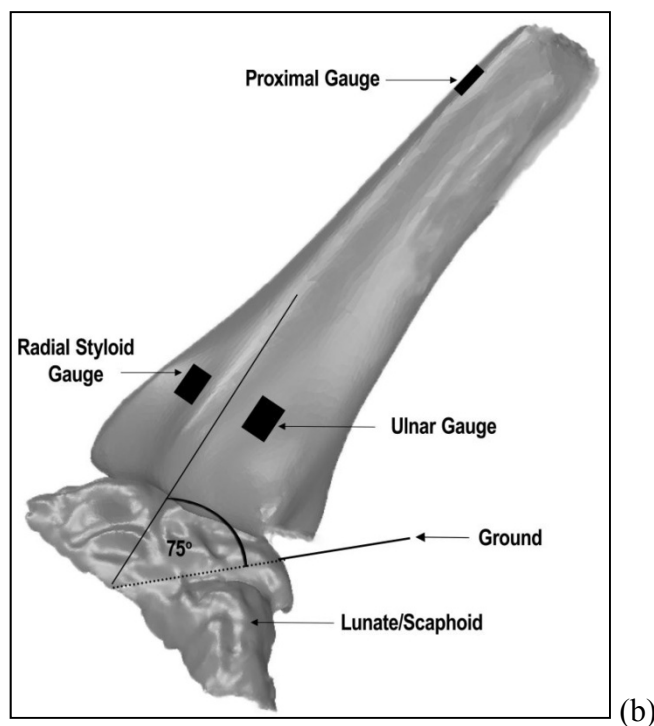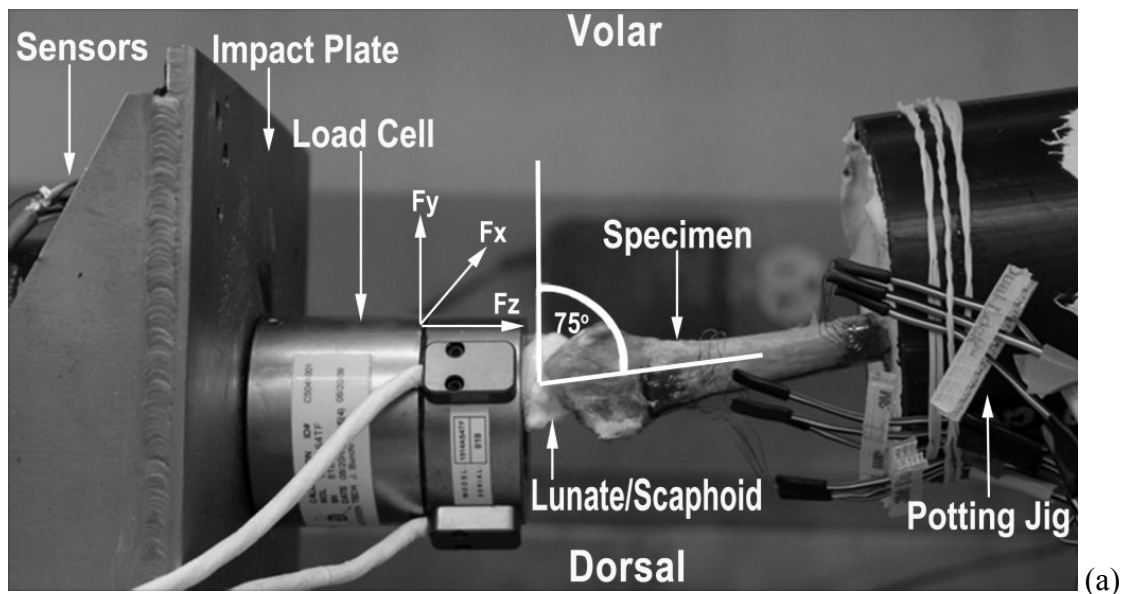
Figure 2.1: *In vitro* **Experimental Set-up.**
Experimental set-up: (a) a 3D schematic of the distal radius shown in a position consistent with the upper extremity during a forward fall; (b) the specimen within the impact device against the model lunate and scaphoid. The 75° angle is representative of the angle between the ground and the volar aspect of the radius. The specimen and potting jig are free to move towards the right following impact (Reproduced with permission from Journal of Orthopaedic Research, Wiley Publishing).
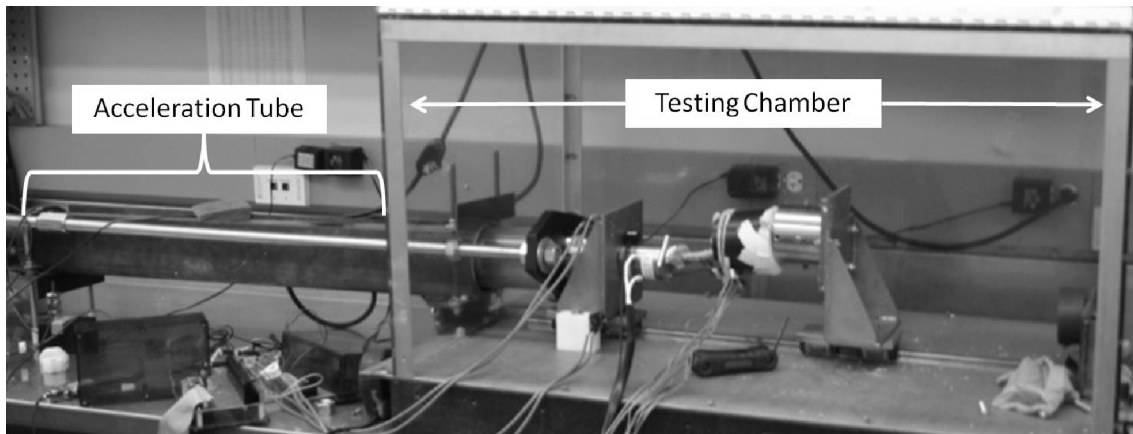
Figure 2.2: Impactor Set-up
The impact apparatus: the 6.8 kg mass projectile travels through the acceleration tube and exits within the testing chamber, applying an impact to the specimen.

Air pressure within the tube was proportional to an input voltage and was released via a fast acting solenoid valve (VXR2380, SMC Corporation, Tokyo, Japan). The potted end of the specimen was attached to a bracket that moved freely along a linear rail and ball bearing system following impact. The mass of the specimen (with cement), bracket and potting jig (~ 7 kg) provided enough resistance to allow for adequate impulse duration. Prior to testing, a pressure-velocity relationship was determined to allow fine control over the projectile's exit velocity. Impacts were energy controlled; the projectile mass was kept constant and the velocity was incrementally increased. The impact plate was instrumented with a 6 degree of freedom strain gauge based load cell (Denton Femur load cell, Model # 1914A, Robert A. Denton Inc., Rochester Hills MI; natural frequency 6kHz), and optical sensors (TCRT100 Vishay semiconductors, Malvern PA.) to measure impact force, and velocity, respectively (Figure 2.3).

Three 45° stacked strain gauge rosettes (Vishay Micro-Measurements, Vishay Precision Group Malvern PA; grid resistance=350 Ω; gauge factor= +1.3%) were glued (M-bond 200; Vishay Micro-Measurements) dorsally along the length of the radius following previously developed procedures (Staebler et al., 1999; Austman et al., 2007). Two gauges were located distally, one just proximal to the radial styloid (gauge 1) and one on the ulnar side of the radius (gauge 2), medial to the radial styloid gauge (Figure 2.3). The third gauge was placed on the lateral aspect of the proximal diaphysis (gauge 3), close to the specimen-cement interface (Figure 2.3). The middle gauge of each
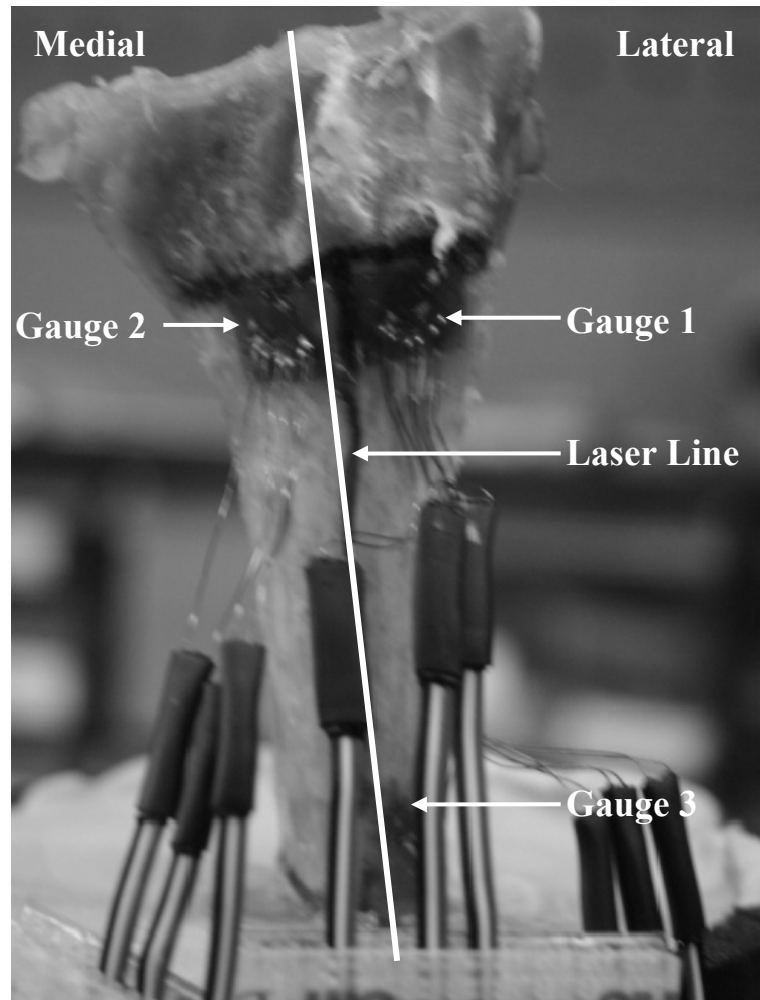
Figure 2.3: *In vitro* **Strain Gauge Locations**
Locations of the strain gauges along the length of the
radius. The middle gauge was aligned with the long axis
of the radius, which was identified by a laser (shown here
as the vertical white line) (Reproduced with permission
from Journal of Orthopaedic Research, Wiley Publishing).

rosette configuration was aligned with the longitudinal axis of the radius, denoted by a laser line (Figure 2.3). Each gauge was wired independently into a quarter bridge completion circuit (SCXI 1314, National Instruments, Austin TX). Velocity, force and strain data were acquired at 15 kHz (National Instruments NI-PXI 1050, and SCXI 1010) by a customized LabView (LabView 2008, National Instruments, Austin TX) data collection program.

Force data were filtered with a phase-less 4th order Butterworth filter and the optimal cut-off frequencies were calculated via residual analysis (Winter, 2005; Burkhart et al., 2011). Optimal cut-off frequencies were different between the pre-fracture and fracture events and between channels. Therefore, unique cut-off frequencies were used across all force channels for pre-fracture (Fx: 500 Hz; Fy: 600 Hz; Fz: 400 Hz) and fracture (Fx: 600 Hz; Fy: 700 Hz; Fz: 500 Hz) trials (Burkhart et al., 2011) (Appendix E).

Pilot testing determined that an initial target impact energy of 20 J was low enough not to cause any visible specimen damage; subsequent impacts occurred in 10 J increments until failure occurred. Failure was defined as specimens being fractured into two distinct segments. Specimens were visually inspected following each impact to determine if signs of external trauma were present. When failure occurred, the specimens were removed from the testing apparatus and the injury location, type, pattern and severity were noted and classified using the Frykman (Frykman, 1967) and AO (Mueller et al., 1990) fracture classification systems (Appendix B).

Force-time curves were used to calculate the peak force, impulse, impulse duration and load rate, for the three force components (Fx, Fy, Fz), as well as the

resultant impact reaction force (IRF$_r$). The peak principal strains were calculated from the strain gauge rosettes (Benham et al., 1996), such that positive and negative principal strains ($\mu\epsilon$) were indicative of tensile and compressive strains, respectively (Bozkus et al., 2004).

Data were classified into three impact events: i) Pre-fracture-the first non-damaging impact at a 20 J target; ii) a crack event when damage was noted on the articular surface of the radius, but with no visual propagation beyond the surface; iii) the fracture event-the impact at which failure of the specimen occurred as described above.

One-way (3 impact events) repeated measures ANOVAs were conducted for each dependent variable. A two-way (2 hand x 3 impact event) mixed repeated measures ANOVA, with hand as the between subject factor, was conducted to determine if the mean differences in the [i, j, k,] vector components were significant. Finally, a two-way (3 impact events x 2 strain components) repeated measures ANOVA was used to determine if differences existed in the absolute values of the tensile and compressive strains. All statistics were performed with SPSS 19 (IBM SPSS statistics, IBM Corporation, Somers NY). Tukey's HSD was used to post hoc significant effects and alpha was set at 0.05 for all statistical tests.

2.1.3 Results

An average of four impact trials were required to reach fracture and the fracture event trial always followed the crack event trial. Mean (SD) velocities of 2.1 (0.04) m/s, 3.2 (0.7) m/s and 3.4 (0.7) m/s were recorded for the pre-fracture, crack and fracture events. These corresponded to increasing impact energy levels of 15.3 (0.5) J, 36.0

(14.9) J, and 45.5 (12.9) J, respectively. Mean impact velocity (p=0.01) and energy (p=0.01) increased significantly between events. The coefficients of variation for velocity and energy measures during the pre-fracture trials were 2 % and 3 %, respectively.

The IRF_r increased significantly from 1286.6 (171.1) N to 2285.1 (1155.9) N for the pre-fracture and crack impacts (p=0.02), but decreased between the crack and fracture (2142.1 (1228.7) N) impacts (Table 2.1). Similarly, loading rates increased significantly (p=0.01) from the pre-fracture (374.4 (153.8) kN/s) to the crack events (1134.9 (685.0) kN/s), and then decreased to 804.6 (0.8) kN/s at fracture (Table 2.1). The mean (SD) IRFr pre-fracture impulse of 9.1 (0.5) N·s increased significantly to 13.9 (4.2) N·s at the crack event and 14.2 (5.4) N·s at fracture (p=0.01). At fracture, the impulse was applied for 31.4 (13.6) ms, which was significantly longer than the mean duration of 19.3 (4.2) ms measured at pre-fracture (p=0.03) (Table 2.1).

There was a consistent pattern in the directional loading of the distal radius, as indicated by the IRFr vector components between left and right hand specimens. There was a significant difference (p=0.01) in the i (Fx) vector component between the left (0.15 (0.03)) and right (-0.21 (0.02)) specimens across all impact events, suggesting that the load was directed towards the ulnar side of the radius in both left and right specimens (Table 2.2). The force was directed more towards the dorsal aspect of the radius in the left compared to the right specimens, with j (Fy) vector components of -0.19 (0.03) and -0.03 (0.05), respectively (p=0.01) (Table 2.2). The k (Fz) vector component dominated the IRFr with an average of 0.96 (0.01) directed along the radius long axis, with no significant side differences (Table 2.2). Finally, there were no

Table 2.1: Impact Force Variables
Mean (SD) impact force parameters across the three impact events (Reproduced with permission from Journal of Orthopaedic Research, Wiley Publishing).

	Pre-Fracture	Crack	Fracture
Peak Forces (N)			
IRFr	1286.6 (171.1)	2285.1 (115.9)*	2142.1 (1228.7)
IRFx	255.3 (50.0)	436.1 (283.8)	431.4 (304.3)
IRFy	189.6 (78.0)	315.1 (120.1)*	332.3 (144.1)*
IRFz	1247.5 (169.5)	2231.0 (1135.9)*	2088.1 (1198.6)
Impulse (Ns)			
IRFr	9.1 (0.5)	13.9 (4.2)*	14.2 (5.5)*
IRFx	1.7(0.2)	2.7 (1.1)	3.2 (2.0)
IRFy	1.1 (0.6)	1.8 (0.7)*	2.4 (1.4)*
IRFz	8.7 (0.5)	13.2 (3.8)*	12.5 (4.9)
Load Rate (kN/s)			
IRFr	374.4 (153.8)	1134.9 (685.0)*	1028.8 (804.6)
IRFx	0.01 (0.004)	0.01 (0.006)	0.01 (0.008)
IRFy	91.2 (3.8)	132.5 (12.1)	284.6 (260.6)
IRFz	359.9 (148.6)	1102.3 (674.5)*	988.8 (788.0)
Impulse Duration (ms)			
IRFr	19.4 (4.2)	22.6 (10.4)	31.4 (13.7)*
IRFx	14.3 (1.6)	20.8 (9.9)	23.0 (9.0)
IRFy	10.1 (32)	17.9 (7.3)*	24.0 (12.4)*
IRFz	19.0 (4.2)	18.0 (4.3)	25.0 (13.3)

*Represents a significant difference between the pre-fracture and fracture impact event ($p < 0.05$).

Table 2.2: Force Vector Components
Mean (SD) vector components of the resultant impact reaction force (N). The vector components are with reference to the load cell co-ordinate system such that positive i is directed towards the right; positive j is in the volar direction; and positive k is directed proximally (Reproduced with permission from Journal of Orthopaedic Research, Wiley Publishing).

	Pre-Fracture			Crack			Fracture		
	i	j	k	i	j	k	i	j	k
Left	0.15*	-0.19*	0.97	0.11*	-0.21*	0.97	0.09*	-0.19*	0.97
	(0.037)	(0.03)	(0.01)	(0.03)	(0.02)	(0.02)	(0.09)	(0.04)	(0.01)
Right	-0.21*	-0.04*	0.98	-0.17*	-0.03*	0.98	-0.21*	-0.01*	0.98
	(0.02)	(0.06)	(0.01)	(0.05)	(0.04)	(0.01)	(0.03)	(0.04)	(0.01)

*Represents a significant difference between left and right specimens ($p < 0.05$).

significant vector component differences across the three impact events for either the right or left specimens.

The compressive strains increased significantly (average of 92 %) between pre-fracture and fracture events at all gauge locations (gauge 1: p=0.01; gauge 2: p=0.03; gauge 3: p=0.01) (Figure 2.4).

The largest strain increase from initial impact to failure occurred at site of gauge 2, from a mean (SD) of -1213.2 (660.9) με to 2717.8 (1697.8) με. However, the largest overall mean compressive strains at fracture occurred at gauge 3 (-3664.2 (1889.5) με). Across all impact events, no significant tensile strain differences were found at any of the gauge locations (Figure 2.4). The largest tensile strains also occurred at gauge 2 an average (SD) magnitude of 1224.8 (1171.6) με.

Overall, the absolute magnitudes of the compressive strains were larger than the tensile strains across all impact events and at each gauge location. At the site of gauge 2 a significant difference between the absolute tensile and compressive strains (1309.3 με) occurred at fracture only (p=0.029). The same interaction occurred at gauge 2 with a significant difference of 1492.9 με between the absolute values of the tensile and compressive strains at fracture (p=0.01). However, at gauge 3, there was a significant difference in the absolute magnitude between tension and compression at all three events (p=0.04) by an average of 2009.3 με, with the greatest difference occurring at fracture (2538.2 με) (Figure 2.4).

The severity, location and pattern of fractures were relatively consistent between specimens (Figure 2.5). All specimens experienced intra-articular damage to the ulnar side of the
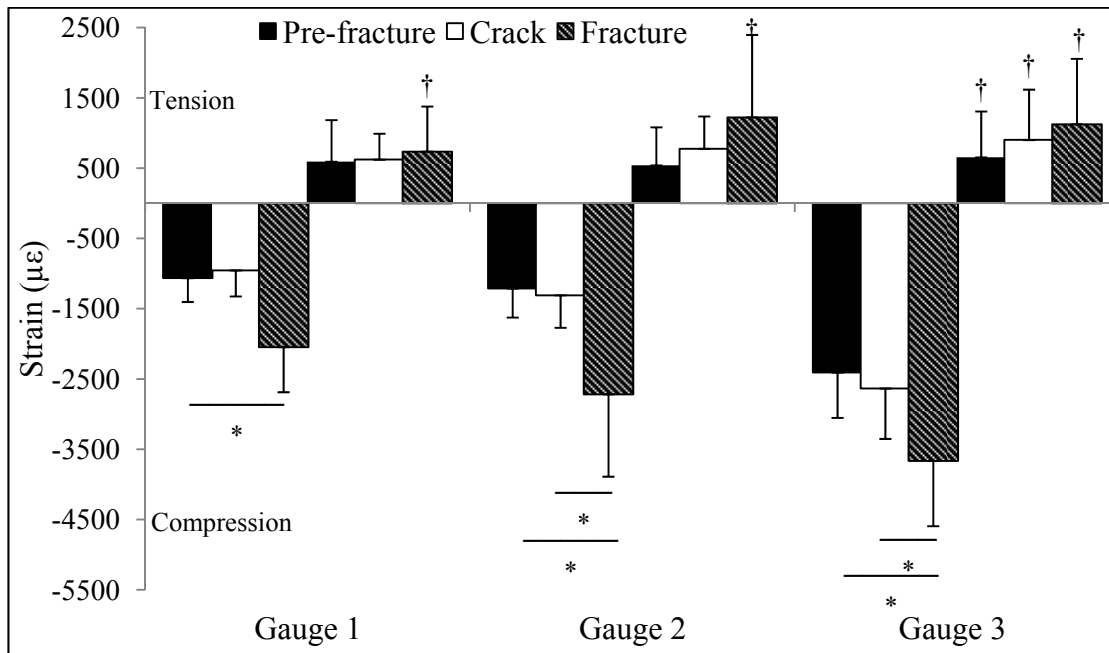
Figure 2.4: Radius Strains
Mean (SD) of the tension (positive) and compression (negative) strain components across the pre-fracture, crack, and fracture events. ([†] represents a significant difference between the mean absolute magnitude of the tension and compression strains at the specified fracture event ($p<0.05$); * represents a significant difference across the specified fracture events for compression and tension, respectively ($p<0.05$)) (Reproduced with permission from Journal of Orthopaedic Research, Wiley Publishing).
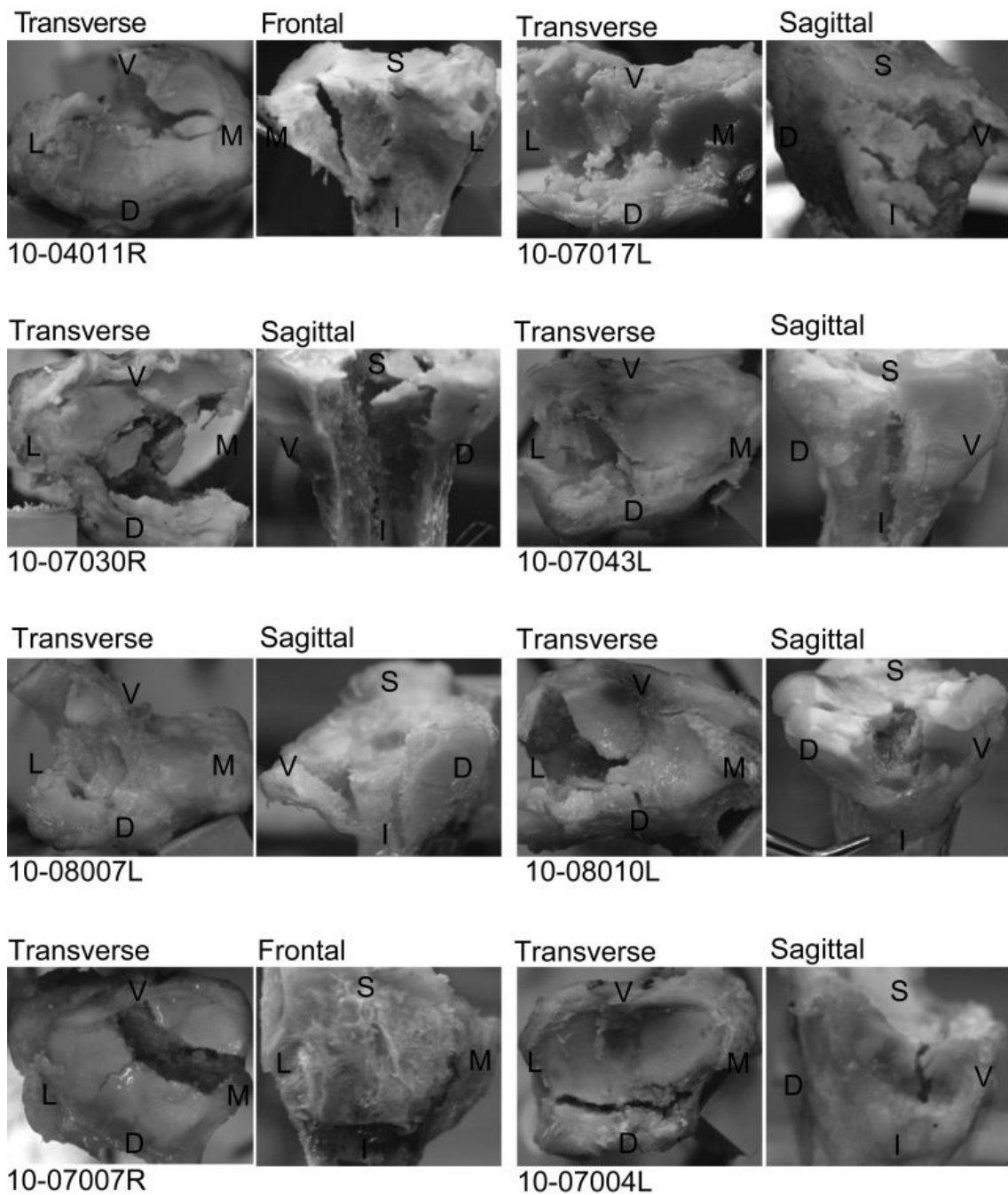
Figure 2.5: Radius Fracture Patterns
One specimen representing typical fracture patterns in the transverse (a) and sagittal (b) plane. The pictures are labelled to orient the specimens with respect to the medial (M), lateral (L), volar (V) and dorsal (D) directions (Reproduced with permission from Journal of Orthopaedic Research, Wiley Publishing).

radius, six incurred damage into the sigmoid fossa (Figure 2.5), two specimens failed with classic Colles fracture patterns (10-08010L and 10-07007R), and one with a Barton's volar fracture pattern (10-04011R) (Figure 2.5). Two specimens were classified as type III (10-04011R and 10-07007R) Frykman fractures and six were classified as type VII. With respect to the AO classification system, there were two B2 (10-07043L and 10-07004L), three B3 (10-04011R, 01-07017L and 10-08007L), two C1 (10-08010L and 10-07007R) and one C3 (10-07030R) (Figure 2.5).

2.1.4 Discussion

To the authors' knowledge, this is the first study to systematically impact the distal radius dynamically to failure, by controlling impact energy through incremental increases in velocity. While this approach was used successfully for the tibia (Quenneville et al., 2010, 2011), this is the first time it has been applied to simulate impacts to the distal radius that are consistent with forward fall arrest. The significant differences between, and relatively small variability (coefficients of variation) about the mean velocities and energies across all impact events (pre-fracture, crack and fracture), suggest that this is a reliable method for this purpose. This is further supported by the consistent, clinically relevant fracture patterns reported between specimens (Figure 2.5). A large range of fracture forces have been reported previously, resulting primarily from uncontrolled impact applications or from static, as opposed to dynamic loading conditions. The mean crack (2285.5 N) and fracture (2142.1 N) forces reported here are slightly smaller in magnitude than the average fracture forces of 2798.6 N and 2352.3 N reported for previous dynamic (Greenwald et al., 1998; McGrady et al., 2001; Duma et

al., 2003;Lubhan et al., 2005;) and static (Meyers et al., 1993; Augat et al., 1996; Troy & Grabiner, 2007a) evaluations.

The dynamic nature of the loading used in the current study is highlighted by comparing the high mean loading rate (1028.8 kN/s) with that reported by Duma et al. (2003) (735.8 kN/s), who simulated airbag/radius impacts. Loading the distal radius dynamically, as it would be during real-world forward fall arrest, is an important and necessary consideration, given the highly rate dependant (viscoelastic) properties of bone (McElhaney, 1966; Greenwald et al., 1998; Hansen et al., 2008). The impacts in the current study were also applied in a controlled and systematic fashion which isolated the fracture primarily to the distal radius; a result consistent with clinical findings.

Furthermore, the direction of the applied loading was found to be mostly characteristic of a forward fall onto an outstretched hand (Troy & Grabiner, 2007b). However, the versatility of the impact system is such that numerous radius postures could be tested, which would allow researchers to study a range of fracture patterns that have clinical relevance. A notable exception was that differences in impact force directions were found along the x-axis (i vector component), between left and right specimens. This identified a tendency to load towards the ulnar side of the radius. It is assumed that the articular surface of the radius and how it interacted with the scaphoid and lunate may have contributed to the loading documented in this direction. Johnson & Szabo (1993) reported that the average radial angle (the slope of the radial intra-articular surface) was approximately 25° (towards the ulna). In combination with

previous findings, this may help to explain why upwards of 58 % of distal radius fractures also involve the distal ulna to some degree (May et al., 2002).

Resultant impact reaction forces and loading rates increased significantly between the pre-fracture and crack events, followed by a non-significant decrease at fracture. This was despite an increase in the impact energy, impulse, and impulse duration between crack and fracture. Although post-crack damage was classified as insignificant from a visual standpoint, it may have been enough to decrease the strength and stiffness of the specimens to some degree. Both tensile and compressive strains increased in magnitude from crack to fracture events, which may be indicative of underlying micro-damage and decreased specimen stiffness (Behiri & Bonfield, 1980).

Structural changes to the bone such as these have decreased the work to fracture, represented in the current study as the fracture force (Reilly & Currey, 2000). Martin et al. (1997), who measured work directly, found that the work to fracture decreased as a result of micro-damage, and continued to decline into the post yield region. The damage identified during the crack event may also have transitioned the bone into the elastic-continuum domain (Gupta & Zioupos, 2008). If so, the bone, although still structurally sound, would tend to absorb energy at the expense of stiffness and strength (i.e. the general architecture of the bone remains intact but the material properties are weakening). This implies that the true point of failure may have occurred at energies somewhere between those measured at the crack and fracture events, but also that the repeated impacts had a limited cumulative effect. Furthermore, the mean fracture energies reported in the current study also resulted in a level of comminution that is consistent with the findings of Beardsley et al. (2005), and individually, those

specimens that fractured at a higher energy (e.g., specimen 07030R, 62 J) tended to sustain a higher degree of damage than those fractured at lower energy levels (e.g., 07004, 30 J). Knowing the energy absorbed at fracture can aid the clinician in their treatment of the fracture and can alert them to other, soft tissue damages (Beardsley et al., 2005).

The strain data reported here confirmed that the dorsal radius experiences a high degree of compressive strain during fractures consistent with forward fall arrest. The pre-fracture compressive strains agree well with those of Staebler et al. (1999) who compared distal radius strains between conditions with and without wrist guards under sub-maximal loading (mean of 750 $\mu\varepsilon$). However, the tri-axial strain gauges used here provide a better description of the true state of strain. The strain data also support the patterns and severity of injuries reported; the compressive strains were consistently higher on the ulnar side of the radius (gauge 2), which corresponded to the documented damage. This helps to explain why almost 60 % of distal radius fractures are accompanied by some form of ulnar involvement, most commonly the ulnar styloid process (May, et al., 2002).

The radii were tested in isolation of the ulna and surrounding soft tissues that would normally help align the bones of the radio-carpal joint and provide support to the radius. Potting the specimen up to the distal third provided some structural support, which would otherwise be taken up by the surrounding tissues. This helped prevent large bending moments, and radial diaphysis fractures that would result. In an attempt to localize the fractures to the distal radius, a model lunate and scaphoid were utilized consistently for all impacts. The properties of the model lunate and scaphoid (provided

by the manufacturer) showed that the model was stiffer than actual lunate and scaphoid bones (1860 MPa vs. 360 MPa) (Lo et al., 1998), but the density (1.06 g/cm^3 vs. 1.67 g/cm^3) and shore hardness (80 vs. 85) compared well (McCalister et al., 2003; Kincaid et al., 2007).

The repeated impact methodology utilized in this study may have induced non-visible cumulative micro-traumas that could have changed the material properties of the bones and altered their failure characteristics. The comparison of the force data to previous work (Martin et al., 1997) suggests that the cumulative damage between the pre-fracture and crack events was minimal and had little effect on the outcome. With this said, it is highly likely that the bone was damaged after the crack event enough to change the mechanical properties, and the true failure point most likely resides between the crack and fracture trials described herein. This would have resulted in more conservative estimates of the actual failure characteristics (i.e. worst case scenario).

It has previously been shown that the forces produced by the musculature during rapid loading can alter the strength of the bones that the muscles attach to (Nordsletten & Ekeland, 1993). Therefore it is possible that the lower fracture forces reported in the current study are partially related to the lack of muscle forces resulting from the use of isolated radius specimens. The limited number of specimens combined with the testing of only one radius/impact surface angle and one simulated wrist angle suggest that the generalizability and application of the findings may be limited. Although this is the most commonly reported configuration of the upper extremity during forward falls, the results presented here may not be generalizable to other fall configurations.

The current study was successful in providing kinetic data that describes the behaviour of the distal radius in response to dynamic loading that is consistent with what would be experienced during a forward fall onto an outstretched hand. An accurate description of the distal radius injury mechanisms provides the necessary information for the implementation of successful injury prevention interventions. such as better designed wrist guards (Burkhart et al., 2010), fall training (Lo et al., 2003), improving the attenuation of various floor materials (Robinovitch & Chiu, 1998), and changes to the materials and mechanisms of automobile airbags (Duma et al., 2003). The impact device described here will allow researchers to test a series of impact angles and different effective masses with the potential to create a variety of fracture patterns, further advancing our understanding of distal radius fractures.

2.1.5 References

Augat P, Reeb H, Claes LE. 1996. Prediction of fracture load at different skeletal sites by geometric properties of the cortical shell. Journal of Bone Mineral Research 11. 1356-1363.

Austman RL, Beaton BJB, Quenneville CE, King GJW, Gordon KD, Dunning CE. 2007. The effect of distal ulnar implant stems material and length on bone strains. Journal of Hand Surgery [American Edition]. 32A, 848-854.

Beardsley CL, Anderson DD, Marsh JL, Brown TD. 2005. Interfragmentary surface area as an index of comminution severity in cortical bone impact. J Orthopaedic Research. 23, 686-690.

Behiri JC, Bonfield W. 1980. Crack velocity dependence of longitudinal fracture in bone. Journal of Material Science. 15, 1841-1849.

Benham PP, Crawford RJ, Armstrong CG. 1996. Stress and strain transformations. In Mechanics of Engineering Materials (pp 292-3339). Harlow England: Pearson Prentice Hall.

Bozkus H, Bozdag E, Sunbuloglu E, Tanyeli E, Sarioglu AC, Hanci M. 2004. Surface strain and stress analysis of the mid-cervical vertebrae bone compartments: A biomechanical pilot study. Turkish Neurosurgery. 14, 1-11.

Burkhart TA, Andrews DM. 2010. The effectiveness of wrist guards for reducing wrist and elbow acceleration responses following simulated forward falls. Journal of Applied Biomechanics. 26, 281-289.

Burkhart TA, Dunning CE, Andrews DM, 2011. Quantifying the optimal system specific filter frequency cut-offs through residual analysis. Journal of Biomechanics. 44, 2728-2731.

DeGoede KM, Ashton-Miller JA, Schultz AB. 2003. Fall-related upper body injuries in the older adult: a review of the biomechanical issues. Journal of Biomechanics. 36, 1043-1053.

Duma SM, Boggess BM, Crandall JR, MacMahon CB. 2003. Injury risk function for the small female wrist in axial loading. Accident Analysis Prevention. 35, 869-875.

Fardellone P. 2008. Predicting the fracture risk in 2008. Joint Bone Spine. 75, 661-664.

Frykman G. 1967. Fracture of the distal radius including sequelae-shoulder-hand-finger syndrome: disturbance in the distal radio-ulnar joint and impairment of nerve function. Acta Orthopaedica Scandinavia. 108, 1-135.

Giacobetti FB, Sharkey PF, Bos-Giacobetti MA, Hume EL, Taras JS. 1997. Biomechanical analysis of the effectiveness of in-line skating wrist guards for preventing wrist fractures. The American Journal of Sports Medicine. 25, 223-225.

Greenwald RM, Janes PC, Swanson SC, McDonald TR. 1998. Dynamic impact response of human cadaveric forearms using a wrist brace. The American Journal of Sports Medicine. 26, 825-830.

Gupta HS, Zioupos P. 2008. Fracture of bone tissue: the 'hows' and 'whys'. Medical Engineering and Physics. 30, 1209-1226.

Hansen U, Zioupos P, Simpson R, Currey JD, Hynd D. 2008. The effect of strain rate on the mechanical properties of human cortical bone. Journal of Biomechanical Engineering 130; 011011-1 - 011011-8.

Henry MH. 2008. Distal radius fractures: current concepts. Journal of Hand Surgery [American Edition]. 33A, 1215-1227.

Hill C, Riaz M, Mozzam A, Brenne, MD. 1998. A regional audit of hand and wrist injuries: a study of 4873 injuries. Journal of Hand Surgery [British-European Edition]. 23, 196-200.

Horseman A, Currey JD, Phil D. 1983. Estimation of mechanical properties of the distal radius form the bone mineral content and cortical width. Clinical Orthopaedics. 176, 298-304.

Jaffe MS, Dijkers MP, Zamentis M. 1997. A population-based survey of in-line skaters' injuries and skating practices. Archives of Physical Medicine and Rehabilitation. 78, 1352-1357.

Johnson PG, Szabo MD. 1993. Angle measurements of the distal radius: a cadaver study. Skeletal Radiology. 22, 243-246.

Kincaid B, Schroder L, Mason J. 2007. Measurement of orthopaedic cortical bone screw insertion performance in cadaver bone and model materials. Experimental Mechanics. 47, 595-607.

Leslie IJ, Dickson RA. 1981. The fractured carpal scaphoid: natural history and factors influencing outcome. Journal of Bone and Joint Surgery. 63B, 225-230.

Lewis LM, West O'C, Standeven J, Jarvis HE. 1997. Do wrist guards protect against fractures? Annals of Emergency Medicine. 29, 766-769.

Lo IKY, King GJW, Milne AD, Johnson JA, Chess DC. 1998. A biomechanical analysis of the intra scaphoid compression using the Herbert scaphoid screw system. Journal of Hand Surgery [British-European Edition]. 23B, 209-213.

Lo J, McCabe GN, DeGoede KM, Okuizumi H, Ashton-Miller, JA. 2003. On Reducing impact force in forward falls: results of a brief intervention in young males. Clinical Biomechanics. 18, 730-736.

Lubhan J, Englund R, Trinidad G, Lyons J, Ivance D, Buczek FL. 2005. Adequacy of laboratory simulation of in-line skater falls. Journal of Hand Surgery [American Edition] 30A, 283-288.

Martin RB, Gibson VA, Stover SM, Gibeling JC, Griffin LV. 1997. Residual strength of equine bone in not reduced by intense fatigue loading: implications for stress fracture. Journal of Biomechanics. 30, 109-114.

May MM, Lawton JN, Blazar PE. 2002. Ulnar styloid fractures associated with distal radius fractures: incidence and implications for distal radioulnar joint instability. Journal of Hand Surgery [American Edition]. 27A, 965-971.

McCalister WV, Knight J, Kaliappan R, Trumble TE. 2003. Central placement of the screw in simulated fractures of the scaphoid waist. Journal of Bone and Joint Surgery. 85A; 72-77.

McElhaney JH. 1966. Dynamic response of bone. Journal of Applied Physiology. 21, 1231-1236.

McGrady LM, Hoepfner P, Young CC, Raasch WG, Lim T-H, Han JS. 2001. Biomechanical effect of in-line skating wrist guards on the prevention of wrist fracture. KSME International Journal. 15, 1072-1076.

Meyers ER, Sebeny EA, Hecker AT, Corcoran TA, Hipp JA, Greenspan SL, Hayes WC. 1991 Correlations between photon absorption properties and failure load of the distal radius *in vitro*. Calcified Tissue International. 52, 292-297

Meyers ER, Hecker AT, Rooks DS, Hipp JA, Hayes WC. 1993. Geometric variables from DXA of the radius predict forearm fracture load *in vitro*. Calcified Tissue International. 52,199-204.

Moore MS, Popovic NA, Daniel JN. 1997. The effect of a wrist brace on injury patterns in experimentally produced distal radius fractures in a cadaveric model. The American Journal of Sports Medicine. 25, 394-401.

Mueller ME, Nazarian S, Koch P, Schatzker J. 1990. The AO classification of fractures of long bones. Berlin, Germany: Springer-Verlag.

Nevitt MC, Cummings SR. 1993. Type of fall and risk of hip and wrist fracture: the study of osteoporotic fractures. Journal of the American Geriatrics Society. 41, 1226-1234.

Nordsletten L, Ekeland A. 1993. Muscle contributions to tibial fracture strength in rats. Acta Orthopaedica Scandinavia. 64, 157-160.

Quenneville CE, Fraser GS, Dunning CE. 2010. Development of an apparatus to produce fractures from short-duration high-impulse loading with an application in the lower leg. Journal of Biomechanical Engineering. 32, 014502-1 – 014502-4.

Quenneville CE, McLachlin SD, Greeley GS, Dunning CE. 2011. Injury tolerance criteria for shirt-duration axial impulse loading of the isolated tibia. Journal of Trauma. 70, E13-E18.

Ray NF, Chan JK, Thamer M. Melton LJ III. 1997. Medical expenditures for the treatment of osteoporotic fractures in the United States in 1995: report from the national osteoporosis foundation. Journal of Bone and Mineral Research. 12, 24-35.

Reilly GC, Currey JD. 2000. The effects of damage and micro-cracking on the impact strength of bone. Journal of Biomechanics. 33, 337-343.

Robinovitch SN, Chiu J. 1998. Surface stiffness affects impact force during a fall on an outstretch hand. Journal of Orthopaedic Research. 16, 309-313.

Staebler MP, Moore DC, Akelman E, Weiss AP, Fadale PD, Crisco JJ III. 1999. The effect of wrist guards on bone strain in the distal forearm. The American Journal of Sports Medicine. 27, 500-506.

Troy KL, Grabiner, MD. 2007a. Off-axis loads cause failure of the distal radius at lower magnitudes than axial loads: a finite element analysis. Journal of Biomechanics. 40, 1670-1675.

Troy KL, Grabiner MD. 2007b. Asymmetrical ground impact of the hands after a trip-induced fall: experimental kinematics and kinetics. Clinical Biomechanics. 22, 1088-1095.

United States Consumer Product Safety Commission. 2011. National Electronic Injury Surveillance System on-line data base. Retrieved from https://www.cpsc.gov/cgibin/NEISSQuery/home.aspx

Werner FW, Short WH, Fortino MD, Palmer AK. 1997. The relative contribution of selected carpal bones to global wrist motion during simulated planar motion and out-of-plane wrist motion. Journal of Hand Surgery [American Edition]. 22A, 708-713.

Winter DA. 2005. In: Biomechanics and Motor Control of Human Movement. Hoboken, New Jersey: John Wiley and Sons Inc.

2.2 Multivariate Injury Risk Criteria and Proposed Acceptable Injury Probability Scores for Fractures to the Distal Radius[2].

2.2.1 Introduction

Fractures to the forearm have been estimated to comprise almost 20 % of all reported fractures worldwide, with the distal radius being the most commonly injured site (Johnell & Kannis, 2006). While distal radius fractures have numerous aetiologies, as many as 39 % of forward falls result in a fracture (Nevitt & Cummings, 1993). Numerous studies have attempted to determine the forces and mechanics associated with these types of fractures (Frykman, 1967; Meyers et al., 1991; Augat et al., 1996; Duma et al., 2003; Lubhan et al., 2005). However, many of their loading protocols limit the application of their findings. For example, some researchers have used a quasi-static loading protocol (Augat et al., 1996; Meyers et al., 1991), which is not indicative of the dynamic loading that occurs to the radius during a fall. Of those studies that have made use of dynamic loading protocols (Frykman 1967; Lubhan et al., 2005), there has been little control over the applied loads, which have often been excessively high in magnitude, and have consequently created damage to all of the surrounding structures. This can make it difficult to accurately identify the true fracture forces and relevant fracture patterns.

Duma et al. (2003) systematically applied impacts to the distal forearm to determine the wrist fracture forces and, based on their results, developed an injury risk criterion or model for wrist fractures. They considered variables such as bone mineral density, donor age and height, but did not explore force components (i.e. axial and off-

---

[2]A version of this work has been submitted for publication: Burkhart TA, Andrews DM, Dunning CE. Clinical Biomechanics, October 7th, 2011. This work was also a result of joint research between the University of Windsor and The Univeristy of Western Ontario.

axis forces and moments) or dynamic variables of impact such as velocity and impulse. This resulted in an injury risk criterion based on the force in the axial direction only. Given that the behaviour of bones at failure is highly dependent on loading rate and loading direction, Duma et al.'s (2003) model may not be sufficiently comprehensive to assess injury risk. Accurate failure probability models are needed to assess the effectiveness of injury prevention strategies such as wrist guards, protective flooring and fall prevention training. For example, although Burkhart & Andrews (2010) found that wrist guards were capable of reducing off-axis wrist accelerations during simulated forward fall arrest, it is unclear whether these reductions are sufficient to lower the overall risk of injury to a significant proportion of the population. Developing a multivariate injury prediction model, such as the one described herein, will improve such estimates and provide a basis by which different intervention strategies can be assessed.

Choosing the correct statistical distribution is critical to providing the most accurate injury prediction models. While logistic regression is a powerful statistical tool for developing prediction models, it requires a larger number of samples (Peduzzi et al., 1996) to produce valid results. Large samples are not always possible or economically feasible in *in vitro* testing, particularly with human specimens. A Weibull analysis is an alternate method that was designed specifically for the assessment of failure and survivability data (Abernathy, 2006). This method provides graphical, easily interpretable results that can offer direct evidence of the underlying failure mechanism (Abernathy, 2006). Finally, this type of analysis is robust to small sample sizes, which makes it an ideal method for analyzing failure data of human specimens.

Therefore, the purpose of the current study was two-fold: First, to systematically produce distal fractures to cadaveric human radii, with the aim of developing a multivariate distal radius injury risk prediction model that incorporates dynamic loading variables in multiple directions. It is anticipated that including such variables will provide more robust injury risk prediction models compared to those currently available. The second purpose was to utilize the Weibull distribution to interpret the failure data and establish distal radius injury probability thresholds.

2.2.2 Methods

This study consists of a secondary analysis of the data that were collected using the methodology described in section 2.1, where eight (4 male, 4 female; 5 left, 3 right; mean (SD) age 61.0 (9.7) years) fresh-frozen human cadaveric radius specimens were tested. Specimens were screened to ensure that they were free of metabolic bone diseases, metastatic cancers, diabetes renal failure and pre-existing trauma. The articular surface of the distal radius was kept intact, while the remainder was cleaned of all soft tissues. Specimens were cemented into sections of 8.89 cm (3.5 inch) diameter PVC tubing (distal third of radius exposed), and were arranged to mimic the position of the radius, *in vivo*, during a forward fall (i.e. specimens were potted at a 75° angle in the sagittal plane (Figure 2.1) (Greenwald et al., 1998) with no frontal plane tilt (Staebler et al., 1999), and oriented with the dorsal surface facing down (Burkhart et al., 2011). To isolate injury to the distal radius and to avoid potential lunate and scaphoid fractures, which also commonly occur after forward falls (Leslie & Dickson, 1981), a high density polyethylene scaphoid and lunate model (SawBones®, Pacific Research Laboratories Inc., Vashon Washington) was used to impact the articular surface of the distal radius

(Figure 2.1). The model was attached to a load cell, which in turn was attached to the impact plate of a pneumatic impact system (Figure 2.1) (described below). To accommodate the *in vivo* 45° wrist extension angle during a fall (Troy & Grabiner, 2007), the radio-carpal angle was set at approximately 42° using a custom potting jig. This was in accordance with the findings of Werner et al. (1997), who found that the mean angle between the radius and proximal row of carpals is approximately 93 % of the global wrist angle.

Impulsive impacts were applied with a custom designed pneumatic impact system (Burkhart et al., 2011; Quenneville et al., 2010) (Figure 2.2). A 6.8 kg projectile was propelled through an acceleration tube by pressurized air. Air pressure within the tube was proportional to an input voltage and was released via a fast acting solenoid valve (VXR2380, SMC Corporation, Tokyo, Japan). The potted end of the specimen was attached to a bracket that moved freely along a linear rail and ball bearing system following impact. The mass of the specimen (with cement), bracket and potting jig (~ 7 kg) provided enough resistance to allow for adequate impulse duration (~ 20 ms) (Burkhart et al., 2011). Prior to testing, a pressure-velocity relationship was determined to allow fine control over the projectile's exit velocity. Impacts were energy controlled; the projectile mass was kept constant and the velocity was incrementally increased. The impact plate was instrumented with a 6 degree of freedom strain gauge based load cell (Denton Femur load cell, Model # 1914A, Robert A. Denton Inc., Rochester Hills MI; Natural frequency of 6kHz), and optical sensors (TCRT100 Vishay Semiconductors, Germany) to measure impact force, and velocity, respectively. Velocity, and force data were acquired at 15 kHz (National Instruments NI-PXI 1050, and SCXI 1010) by a

custom LabView (LabView 2008, National Instruments, Austin TX) data collection program. Force data were filtered with a dual pass 4th order Butterworth filter and the optimal cut-off frequencies were calculated via residual analysis (Burkhart et al., 2011) (Appendix E).

Potted specimens were securely clamped into the testing system and positioned such that the carpals and radius were properly aligned. Pilot testing determined that initial target impact energy of 20 J was low enough not to cause any visible specimen damage; subsequent impacts occurred in 10 J increments until failure occurred. Failure was defined as specimens being fractured into two distinct segments. Specimens were visually inspected following each impact to determine if signs of external trauma were present and the energy at which the first crack event occurred was also recorded.

Force-time curves were used to calculate the peak force, impulse, impulse duration and load rate, for the three force components (Fx-medial/lateral direction; Fy-volar/dorsal direction; Fz-axial direction (Figure 2.1), and the resultant impact reaction force (IRF_r). Data were classified into three impact events: i) Pre-fracture or the first non-damaging impact at a 20 J target; ii) the crack event, when damage was noted on the articular surface of the radius but with no visual propagation beyond the surface and iii) the fracture event, corresponding to the impact at which failure of the specimen occurred as described above.

Best subsets regression analysis (SigmaPlot 12.0, Systat Software Inc. Chicago IL) was carried out to determine which combination of variables best predicted each injury event (crack and fracture) including: all force variables (i.e. Fx, Fy, Fz, the resultant, and the moments about the x and y axes), velocity, energy, ultra distal radius

bone mineral density, donor height, weight and age. The natural logarithm of Fz was also included in the analysis as it has previously been shown to be a significant impact injury predictor in the lower extremity (Funk et al., 2002; Quenneville et al., 2011). The model that best represented each event was chosen based on the combination of the highest R^2, the lowest Variance Inflation Factors (<5 to ensure no multicollinearity) and the significance of each variable that was included (p<0.05), such that the final models accounted for the highest explained variance in injury with the fewest variables. To compare the multivariate models to the more traditional method of using only axial force as an injury predictor, linear regression analysis was used to create injury risk models that included only Fz for both the crack and fracture events.

Weibull plots (Figure 2.6 a-f) were created by plotting Eq. (2.1) versus Eq. (2.2) (Appendix G),

$$y = \ln\left(ln\left[\frac{1}{1-P_f}\right]\right) \tag{Eq. 2.1}$$

$$x = \ln(x) \tag{Eq. 2.2}$$

where, P_f is the median rank of each data point and x is the Fz or the risk score for the force-only and multivariate models, respectively. For each plot a best-fit line was determined. Following the linear least squares method (Faucher & Tyson, 1988; Vallo, 2002) the slope of the line is the Weibull parameter beta (β). The y-intercept of this line is used to find the Weibull alpha (α) parameter according to Eq. (2.3):

$$\alpha = e^{-\left(\frac{b}{\beta}\right)} \tag{Eq. 2.3}$$

Cumulative distribution functions (CDF) were produced, the shape of which are dependent on the alpha and beta coefficients. The Fz and risk scores at 10 %, 25 %, 50

% 75 % and 90 % probability of injury were also determined. Finally, the data

presented by Duma et al. (2003) (including the actual specimen failure data as well as

specimen failure data that they scaled to a 5th percentile female) were also analyzed

with the Weibull methods so that their data could be directly compared to the force-only

data presented here.

2.2.3 Results

The mean (SD) pre-fracture, crack and fracture event forces were 1286.6 (171.1

N), 2285.1 (115.9 N), 2142.1 (1228.7 N), respectively. The mean (SD) pre-fracture

velocity was 2.1 (0.04) m/s, which increased significantly to 3.2 (0.7) m/s for the crack

event and again to 3.4 (0.7) m/s at fracture. The damage incurred by the distal radius

was consistent and clinically relevant in terms of the severity, type and location of the

fracture patterns. All of the specimens experienced damage to the intra-articular surface

on the ulnar side of the radius. Seventy-five percent of the specimens had damage that

extended into the sigmoid fossa while two displayed a classic Colles type fracture

pattern.

The best subsets analyses resulted in 17 and 14 different models for the crack

and fracture events, respectively (Appendix F). The model that best represented the

crack event (Adj. R^2 = 0.698) included Fy Impulse (p=0.007), Fz Load rate (p=0.013),

velocity (p=0.02) and ln(Fz) (p=0.047) (Figure 2.8a), while the best predictive model of

the fracture event (Adj. R^2=0.815) included Peak Fz (p=0.015), Fy Impulse (p=0.005)

and velocity (p<0.001). In contrast, Fz alone accounted for only 55 % and 29 % of the

variance in the crack (p=0.03) or fracture (p=0.07) outcomes, respectively. The

linearity of the Weibull distributions (Adj. R^2 0.75-0.96) suggests that this was an

appropriate method of fitting the data (Figure 2.6 a-f). Beta coefficients for the current study's force only models were 1.7 and 1.5 for the crack and fracture events, respectively (Figure 2.6 a-b). Comparatively, the beta coefficients for the force-only Duma et al. (2003) data were found to be 2.9 (scaled: Figure 2.6 c) and 2.5 (un-scaled: Figure 2.6d). However, the beta coefficients for the multivariate measure of failure risk (crack: 3.4; fracture: 3.7), were approximately twice those reported for the force-only crack event and more than 14 % greater than those for all of the force-only fracture models (Figure 2.6 e-f).

When axial force was considered exclusively, a 700 N Fz force was associated with a 10 % probability of a crack event, while the 10 % probability of fracture was shown to be approximately 550 N (Figure 2.7 and Table 2.3). In comparison, the data presented by Duma et al. (2003), when reanalyzed with the Weibull method, showed a 10% probability of failure at approximately 1200 N and 1300 N when scaled to the 5th percentile female and when un-scaled, respectively (Figure 2.7 and Table 2.3). Finally, the multivariate survivability curves, calculated from the parameters of the Weibull analyses, suggest that there is a 10 % probability of crack (Figure 2.8a and Table 2.3) and fracture (Figure 2.8b and Table 2.3) failure events at a risk factor score of approximately 0.5 and 0.6, respectively.

2.2.4 Discussion

The impact velocities reported here compare well with those interpolated from Chiu & Robinovitch (1998), suggesting that they are indicative of those that would occur from a fall from approximately standing height. Furthermore, the relatively low variability in impact velocities and the consistent, clinically relevant, fracture patterns
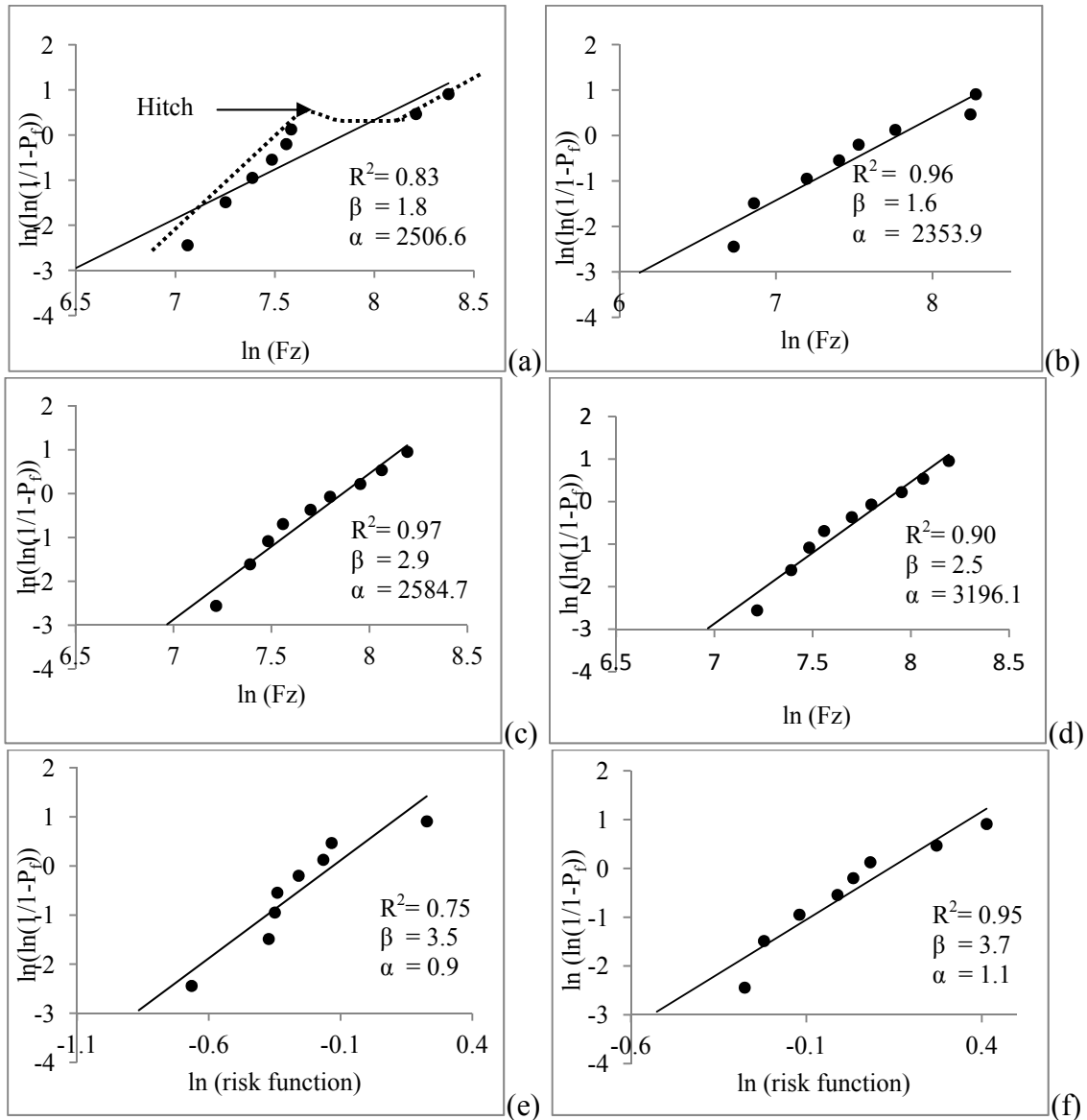
Figure 2.6: Weibull Plots
Weibull plots showing the lines of best fit for the current study's force-only (a) and the current study's crack (b) events; the force-only Duma et al. (2003) scaled (c) and un-scaled (d) data; and the current study's multivariate crack (e) and fracture (f) events. R^2 is the proportion of variance in y explained by x; α and β are the Weibull parameters calculated from the properties of the regression line and determine the shape of cumulative distribution functions. The dotted line in part (a) is an example of a "hitch" in the data, as described by Abernathy et al. (1983).
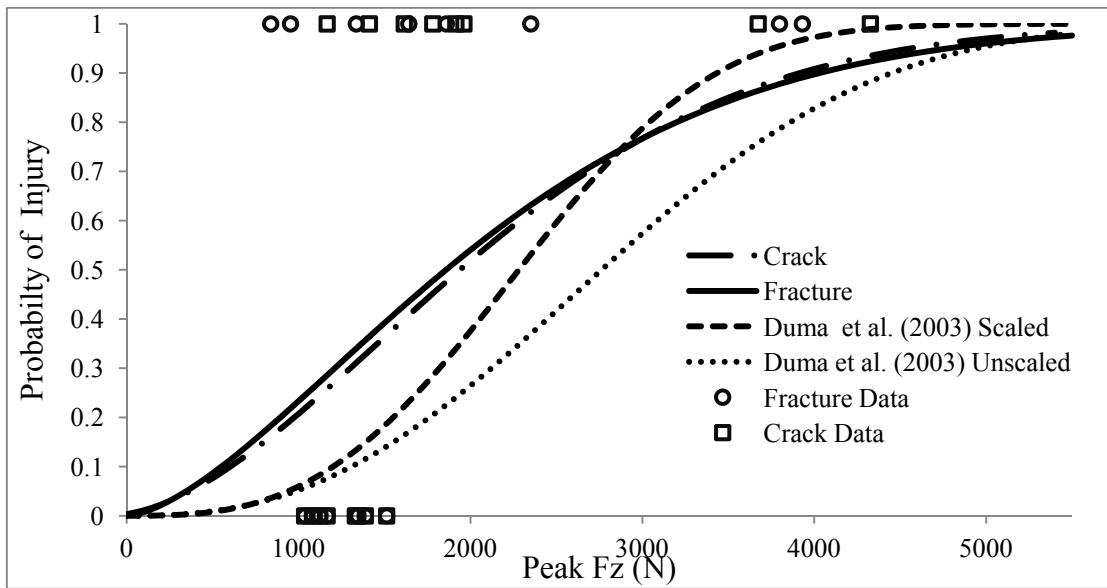
Figure 2.7: Force-Only Cumulative Distribution
Cumulative distribution functions for the peak force (N) measured along the z-axis
(Fz), based on the parameters calculated from the Weibull analysis. The forces used
in the scaled Duma et al. (2003) curve were scaled to a 5th percentile female.

Table 2.3: Injury Risk Scores and Failure Probabilities
Axial force (Fz) and multivariate risk score values across a range of failure
probabilities. Also included are the Weibull coefficients for all models.

Models	Probability of Injury					Weibull Coefficients	
	0.1	0.25	0.5	0.75	0.9	Beta	Alpha
Force-only							
Crack	703.3	1240.3	2038.2	3014.8	4015.3	1.8	2506.9
Fracture	551.0	1053.6	1858.2	2906.2	4031.8	1.6	2353.9
Duma Scaled[a]	1201.0	1690.9	2281.3	2888.8	3433.7	2.9	2584.7
Duma Un-scaled	1307.6	1948.7	2763.2	3638.8	4451.2	2.5	3196.1
Multivariate							
Crack	0.4	0.6	0.8	1.0	1.1	3.5	0.9
Fracture	0.6	0.8	1.0	1.2	1.4	3.7	1.1

[a] Duma Scaled and Duma Un-scaled values refer to data from Duma *et al.* (2003). Un-scaled values are the actual data from their failure tests, while the scaled represent the actual values scaled to the 5th percentile female.
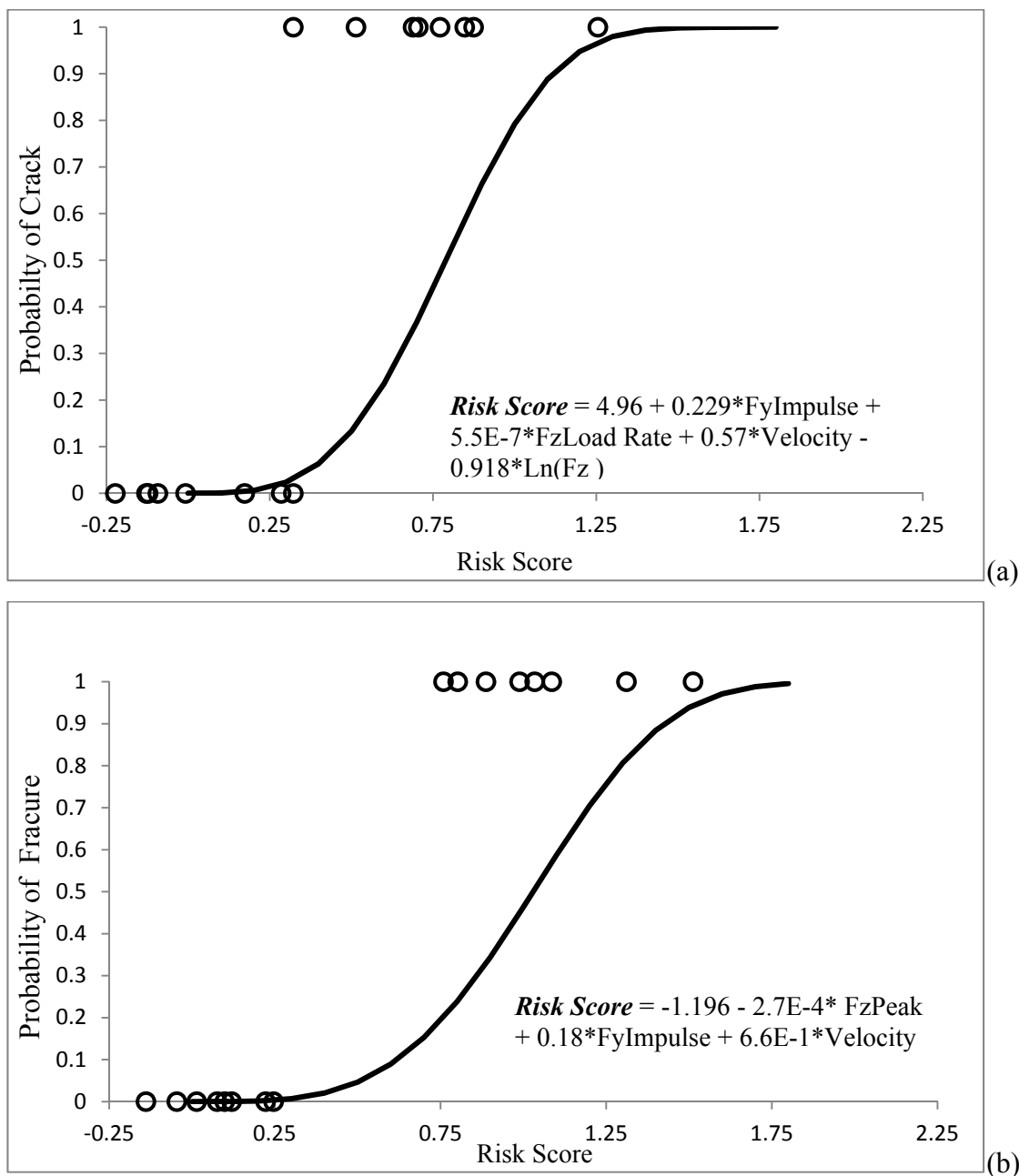
Figure 2.8: Multi-Variate Cumulative Distributions
Cumulative distribution functions for the multivariate crack (a) and fracture (b) injury
risk scores, based on the parameters of the Weibull analysis risk models. The respective
injury risk score equations are also included with the graphs.

suggest that this is a viable method of simulating forward fall-induced loads to the distal

radius (Burkhart et al., 2011). From this, two multivariate injury criteria models and

distal radius injury probability thresholds were developed.

A best subsets analysis was chosen as the method to determine the multivariate

model that best predicts the risk of a crack and fracture event, as it allowed the selection

of the best model based both on statistics as well as relevant biomechanical criteria

(Hosmer et al., 1989). Overall, the multivariate models provided better failure

predictions (based on Adj. R^2) compared to the models that only incorporated the axial

(Fz) force, both from this study and those of Duma et al. (2003). The inclusion of

impulse along the y-axis (medial-lateral) and velocity in both crack and fracture models,

and Fz Load rate in the crack model, underscore the dynamic nature of these events and

highlight the visco-elastic and anisotropic behaviour of bone during failure. In

addition, the results suggest that force directions and rates must be considered, along

with force magnitudes when attempting to predict the risk of distal radius fractures. The

inclusion of off-axis (i.e. Fy) force variables further supports the "off-axis" findings of

Troy & Grabiner (2007). Using finite element analysis of the distal radius, they found

that the failure forces decreased as the applied force was directed away from the long-

axis of the radius.

Surprisingly, the bone mineral density of the distal (BMD) radius was not

included in either of the multivariate models presented here. While Troy & Grabiner

(2007) were able to show an effect of BMD on the failure strength of their model

radius, the results presented here are consistent with the findings of Meyers et al. (1993)

and Duma et al. (2003). In both of these *in vitro* studies, no significant bone mineral

density relationship with failure load or fracture risk was found. The omission of bone mineral density here may have been a result of the strict control over the quality of the specimens, which essentially reduced the variance in these data.

The Weibull distribution is a popular tool for analysing survival and failure data (Faucher & Tyson, 1988; Smith, 1991; Abernathy, 2006). The main advantages of the Weibull distribution are that it provides graphical and easily interpretable results (i.e. coefficients). For example, an analysis of the beta coefficient and the Weibull distributions (Figure 3.6a-f) provides the researcher with an indication of the injury mechanisms, while the cumulative distribution functions (whose shape is dictated by the alpha and beta coefficients) enables the instantaneous probability of injury to be determined (Abernathy, 2006). Furthermore, the Weibull distribution is reasonably accurate with small sample sizes, as often happens when testing human specimens to failure. However, the slopes of the crack and fracture CDFs (Figure 2.8a-b) do not appear to fit the data accurately. While this is a common fit of the Weibull distribution among analyses performed on bone failure (Yoganandan et al., 1996; Funk et al., 2002; Quenneville et al., 2011) future work should investigate alternate distributions (e.g., Kaplan-Meier survivability functions) that more accurately represent this type of bone failure data.

The values of the force-only beta coefficients presented here are suggestive of a "constant failure rate" mechanism at lower force levels, compared to the beta coefficients of the multivariate risk functions, which are more representative of a "wear out" failure mechanism (Abernathy et al., 1983). The beta coefficient of the multivariate risk function (i.e. the slope of the Weibull distribution becomes more steep)

is also indicative of a normal distribution, and thus, the onset of failure becomes more predictable (Abernathy, 2006). While beta coefficients provide a general idea of distal radius injury mechanisms, further research is needed to assign Weibull shape parameters that are more specific to bone failure. Finally, the crack event data, in both the force-only and multivariate models, revealed a "dogleg" or "hitch" in the Weibull distribution data (Figure 3.6a and Figure 3.6e) that may be indicative of multiple failure mechanisms (Abernathy, 2006). The fact that the fracture event plots do not exhibit this type of abnormality may be a function of the damage that occurred during the crack event, which may have decreased the strength of all specimens proportionally. This finding also implies that the true point of fracture lies somewhere between the crack and fracture events.

The probability of risk values determined from the cumulative distribution functions are important parameters when establishing exposure limits for the prevention of injury. A range of risk probabilities were explored to accurately describe the spectrum of failure forces and risk scores obtained. The authors would suggest considering a risk on the order of 10 % - 25 % as design guidelines, as has been recommended by previous authors (Yoganandan et al., 1996; Quenneville et al., 2011).

Previous *in vitro* biomechanical studies interested in developing distal radius injury risk prediction models have focused almost exclusively on fracture forces presented axially to the specimens and have mostly utilized quasi-static loading protocols that are not indicative of radius loading that occurs during fall arrest. The current study highlights the importance of considering all impact force components as well as other dynamic variables that play a significant role in predicting the risk of

distal radius fracture. Injury probability thresholds in the range of 10 % - 25 % have

been presented and should assist researchers in the assessment and development of

injury prevention interventions.

2.3.5 References

Abernathy B, Breneman JE, Medlin CH, Reinman GL. 1983. Weibull Analysis Handbook. Technical Report available from: http://www.dtic.mil/cgi-bin/GetTRDoc?AD=ADA143100&Location=U2&doc=GetTRDoc.pdf

Abernathy B, 2006. The new Weibull handbook (5th ed.) Abernathy: North Palm Beach, Florida.

Augat P, Reeb H, Claes LE, 1996. Prediction of fracture load at different skeletal sites by geometric properties of the cortical shell. Journal of Bone and Mineral Research. 11, 1356-1363.

Burkhart TA, Andrews DM, 2010. The effectiveness of wrist guards for reducing wrist and elbow accelerations resulting from simulated forward falls. Journal of Applied Biomechanics. 26, 281-289.

Burkhart TA, Dunning CE, Andrews DM, 2011. Determining the optimal system specific cut-off frequencies for filtering *in vitro* upper extremity impact force and acceleration data by residual analysis. Journal of Biomechanics. 44, 2728-2731.

Chiu J, Robinovitch SN, 1998. Prediction of upper extremity impact forces during falls on the outstretched hand. Journal of Biomechanics. 31, 1169-1176.

Duma SM, Boggess BM, Crandall JR, MacMahon CB, 2003. Injury risk function for the small female wrist in axial loading. Accident Analysis and Prevention. 35, 869-875.

Faucher B, Tyson WR, 1988. On the determination of Weibull parameters, Journal of Material Sciences. 7, 1199-1203.

Frykman, G, 1967. Fracture of the distal radius including sequelae-shoulder-hand-finger syndrome: disturbance in the distal radio-ulnar joint and impairment of nerve function. Acta Orthopaedica Scandinavia 108, 1-135.

Funk JR, Crandall JR, Tourett LJ, MacMahon CB, Bass CR, Patrie J, et al. 2002. The axial injury tolerance of the human foot/ankle complex and the effect of Achilles tendon tension. Journal of Biomechanical Engineering. 124, 750-757.

Greenwald RM, Janes PC, Swanson SC, McDonald TR, 1998. Dynamic impact response of human cadaveric forearms using a wrist brace. American Journal of Sports Medicine. 26, 825-830.

Johnell O, Kannis JA, 2006An estimate of the worldwide prevalence and disability associated with osteoporotic fractures. Osteoporosis International. 17, 1726-173.

Hosmer DW, Jovanovic B, Lemeshow S, 1989. Best subsets logistic regression. Biometrics. 45, 1265-1270.

Leslie IJ, Dickson RA, 1981. The fractured carpal scaphoid: natural history and factors influencing outcome. Journal of Bone and Joint Surgery. 63B, 225-230.

Lubhan J, Englund R, Trinidad G, Lyons J, Ivance D, Buczek FL, 2005. Adequacy of laboratory simulation of in-line skater falls. Journal of Hand Surgery. 30A, 283-288.

Meyers ER, Hecker AT, Rook, DS, Hipp JA, Hayes WC. 1993. Geometric variables from DXA of the radius predict forearm fracture load *in vitro*. Calcified Tissue International. 52, 199-204.

Meyers ER, Sebeny EA, Hecker AT, Corcoran TA, Hipp JA, Greenspan SL, et al. 1991. Correlations between photon absorption properties and failure load of the distal radius *in vitro*. Calcified Tissue International. 52, 292-297.

Nevitt MC, Cummings SR. 1993. Type of fall and risk of hip and wrist fracture: the study of osteoporotic fractures. Journal of the American Geriatric Society. 41, 1226-1234.

Peduzzi P, Concato J, Kemoer E, Holford TR, Feinstein AR, 1996. A simulation study of the number of events per variable in logistic regression analysis. Journal of Clinical Epidemiology. 12, 1372-1379.

Quenneville CE, Fraser GS, Dunning CE. 2010. Development of an apparatus to produce fractures from short-duration high-impulse loading with an application in the lower leg. Journal of Biomechanical Engineering. 32, 014502-1 – 014502-4.

Quenneville CE, McLachlin SD, Greeley GS, Dunning CE, 2011. Injury tolerance criteria for short duration axial impulse loading of the isolated tibia. Journal of Trauma, Injury and Care. 70, E13-E18

Smith, R.L., 1991. Weibull regression models for reliability data. Reliability Engineering and System Safety. 34, 55-77.

Staebler MP, Moore DC, Akelman E, Weiss A-PC, Fadale PD, Crisco JJ, 1999. The effect of wrist guards on bone strain in the distal forearm. The American Journal of Sports Medicine. 27, 500-506.

Troy KL, Grabiner MD, 2007. Off-axis loads cause failure of the distal radius at lower magnitudes than axial loads: a finite element analysis. Journal of Biomechanics. 40, 1670-1675.

Vallo CI, 2002. Influence of load type on flexural strength of a bone cement based on PMMA. Polymer Testing. 21, 793-800.

Werner FW, Short WH, Fortino MD, Palmer AK, 1997. The relative contribution of selected carpal bones to global wrist motion during simulated planar motion and out-of-plane wrist motion. Journal of Hand Surgery. 22-A, 708-713.

Yoganandan N, Pintar FA, Boynton M, Begeman P, Prasad P, Kuppa SM, et al., 1996. Dynamic axial tolerance of the human foot-ankle complex. Society of Automotive Engineering. 962426, 207-218.

2.3 Predicting Distal Radius Bone Strains and Injury in Response to Impulsive Impacts to Failure Using Multi-axial Accelerometers.

2.3.1 Introduction

Impacts that occur as a result of activities such as landing during running or arresting the body's momentum with the upper limbs following a forward fall, can produce relatively large loads at the impact interface. These loads result in shock waves that travel through, and can have potentially injurious effects on the underlying anatomical tissues, including bone (Radin et al., 1973). Changes in the properties of shock waves resulting from impact (e.g., velocity) have been shown to accurately describe changes to bone, such as fractures and the progress of fracture healing (Pelker & Saha, 1983; Folma et al., 1993). Measuring a bone's response to impact and the properties of shock waves that are generated by the impact have generally been conducted *in vitro* via strain gauges (Pelker & Saha, 1983) glued to the bone. However, in addition to being invasive (*in vivo*), strain gauges are expensive, are generally used only once, and can be difficult to assemble and attach to the specimens being tested. While these limitations apply to *in vitro* strain gauge applications, they hold especially true for *in vivo* work (Milgrom et al., 2004).

Accelerometers have been used widely both *in vivo* and *in vitro* for measuring impact initiated shock waves (Boyer & Nigg, 2004; Burkhart & Andrews 2010a, 2010b; Burkhart et al., 2011). They can be relatively low mass (i.e. a few grams), inexpensive, reusable, easy to attach, and can be used non-invasively. Accelerometers have been used to measure the overall intensity of an impact and to study the shock wave as it travels through various regions of the body. For example, numerous studies of the

lower extremity have highlighted the shock attenuating effects of soft tissues (e.g., muscle) (Schinkel-Ivy et al., 2011) and modifying joint angles (Lafortune et al., 1996), by analyzing the peak accelerations at different anatomical locations.

Compared to the lower extremity, the upper extremity has received little attention in this regard. Hwang & Kim (2004) and Kim et al. (2006) measured accelerations at the hand in response to different fall heights and wrist guard materials. Furthering this work, Burkhart & Andrews (2010a, 2010b) presented accelerations at the wrist and elbow and along multiple axes as a function of wrist guard use (Burkhart & Andrews, 2010a), changing elbow angles (Burkhart & Andrews, 2010a) and different levels of forearm muscle activation (Burkhart & Andrews, 2010b). While this research has provided good information regarding the shock attenuating ability of the upper extremity in different impact conditions, there is little to no data available that shows that simply lowering the magnitude of the resultant segment acceleration variables (e.g., peaks, times to peak, acceleration rates) is enough to prevent an injury from occurring. Furthermore, with the exception of Edwards et al. (2009), limited work has been done relating surface acceleration signals to underlying strains during impact. While Edwards et al. (2009) present good bone strain prediction models using accelerometers, their data were limited to sub-maximal impacts and they measured accelerations along a single axis of the tibia only.

Therefore, the purposes of the current work were to: i) determine the efficacy of multi-axial accelerometers for predicting injury (crack and fracture events) to bone (radius) in response to impacts, and; ii) assess the relationship between signals measured from multi-axial accelerometers and strain gauges along the length of the

radius. If bone accelerations can predict injury well following dynamic impacts, and the relationship between bone acceleration and strain is sufficiently strong, then considerable cost and time savings could be realized for *in vitro* testing protocols.

2.3.2 Methods

This study consists of a secondary analysis of the data that was collected using the methodology described in Section 2.1, where eight (4 male, 4 female; 5 left, 3 right; mean (SD) age 61.0 (9.7) years) fresh-frozen human cadaveric radius specimens were tested. Specimens were free of metabolic bone diseases, metastatic cancers, diabetes, renal failure and pre-existing trauma. The articular surface of each radius was kept intact, while the remainder was cleaned of all soft tissues. Specimens were cemented into sections of 8.89 cm (3.5 inch) diameter PVC tubing (distal third of radius exposed), and were arranged to mimic the position of the radius, *in vivo*, during a forward fall (i.e. specimens were potted at a 75° angle in the sagital plane (Greenwald et al., 1998), with no frontal plane tilt (Staebler et al., 1999) (Figure 2.1). The specimens were oriented with the dorsal surface facing down. To isolate fractures to the distal radius and to avoid potential lunate and scaphoid fractures, which also commonly occur after a fall (Leslie & Dickson, 1981), a high density polyethylene scaphoid and lunate model (SawBones®, Pacific Research Laboratories Inc., Vashon Washington) was used to impact the articular surface of the distal radius (Figure 2.2). The model was attached to a load cell, which in turn was attached to the impact plate. The mean angle between the radius and proximal row of carpal bones is approximately 93 % of the global wrist angle (Werner et al., 1997). Therefore, to accommodate the *in vivo* 45° wrist extension

angle during a fall (Troy & Grabiner, 2007), the radio-carpal angle was set at approximately 42° using a custom jig.

Impulsive impacts were applied with a custom designed pneumatic impact system (Quenneville et al., 2010). A 6.8 kg projectile was propelled through an acceleration tube by pressurized air. Prior to testing, a psi-velocity relationship was determined to allow fine control over the projectile's exit velocity. Impacts were energy controlled; the projectile mass was kept constant and the velocity was incrementally increased. The projectile collided with an impact plate that was instrumented with a 6 degree of freedom strain gauge based load cell (Denton Femur load cell, Model # 1914A, Robert A. Denton Inc., Rochester Hills MI; natural frequency 6 kHz), and optical sensors (TCRT100 Vishay Semiconductors, Malvern, PA) to measure impact force, and velocity, respectively. This system effectively transferred the impact force through the load cell and onto the distal end of the radius. The potted end of the specimen was attached to a bracket that moved freely along a linear rail and ball bearing system following impact. Three 45° stacked strain gauge rosettes (Vishay Micro-Measurements, Vishay Precision Group Malvern PA; grid resistance=350 Ω; gauge factor= +1.3%) were glued (M-bond 200; Vishay Micro-Measurements) dorsally along the length of the radius following previously developed procedures (Staebler et al., 1999; Austman et al., 2007). Two gauges were located distally, one just proximal to the radial styloid (gauge 1) and one on the ulnar side of the radius (gauge 2), medial to the radial styloid gauge (Figure 2.9). The third gauge was placed on the lateral aspect of the proximal diaphysis (gauge 3) at the specimen-cement interface (Figure 2.9). The middle gauge of each rosette configuration was aligned with the longitudinal axis of the

radius, denoted by a line projected onto the bone by a laser level. Each gauge was wired independently into a quarter bridge completion circuit (SCXI 1314, National Instruments, Austin TX). Two micro electro-mechanical (MEM) 100 g tri-axial accelerometers (Freescale semiconductor, MMA220KEG (x and y axes); MMA1210 (z axis); Ottawa ON, Canada) were glued to the bone following the same protocol for gluing the strain gauges. The distal accelerometer was placed dorsally just medial to the radial styloid process and just proximal to the intra-articular surface (Figure 2.9). Due to the position of the proximal strain gauge, the proximal accelerometer was glued to the volar aspect of the diaphysis at the bone-cement interface (Figure 2.9). As a result of sampling capacity limitations with the instrumentation, accelerations were only collected along two of the three axes: parallel with the long axis of the radius (axial) and at a right angle to the long axis of the radius (off-axis) in the volar-dorsal direction. These axes were chosen based on previous work (Burkhart & Andrews, 2010a, 2010b) that showed negligible accelerations in the medial-lateral direction.

Potted specimens were securely clamped into the testing system and positioned such that the carpals and radius were properly aligned. Pilot testing determined that initial target impact energy of 20 J was low enough not to cause any visible specimen damage; subsequent impacts occurred in 10 J increments until failure occurred. Failure was defined as specimens being fractured into two distinct segments. Specimens were visually inspected following each impact to determine if signs of external trauma were present. While data at all impacts were recorded, the response of the radius at three specific impact events were noted: i) Pre-fracture-the first non-damaging impact at a 20 J target; ii) a crack event-when damage was noted on the articular surface of the radius,
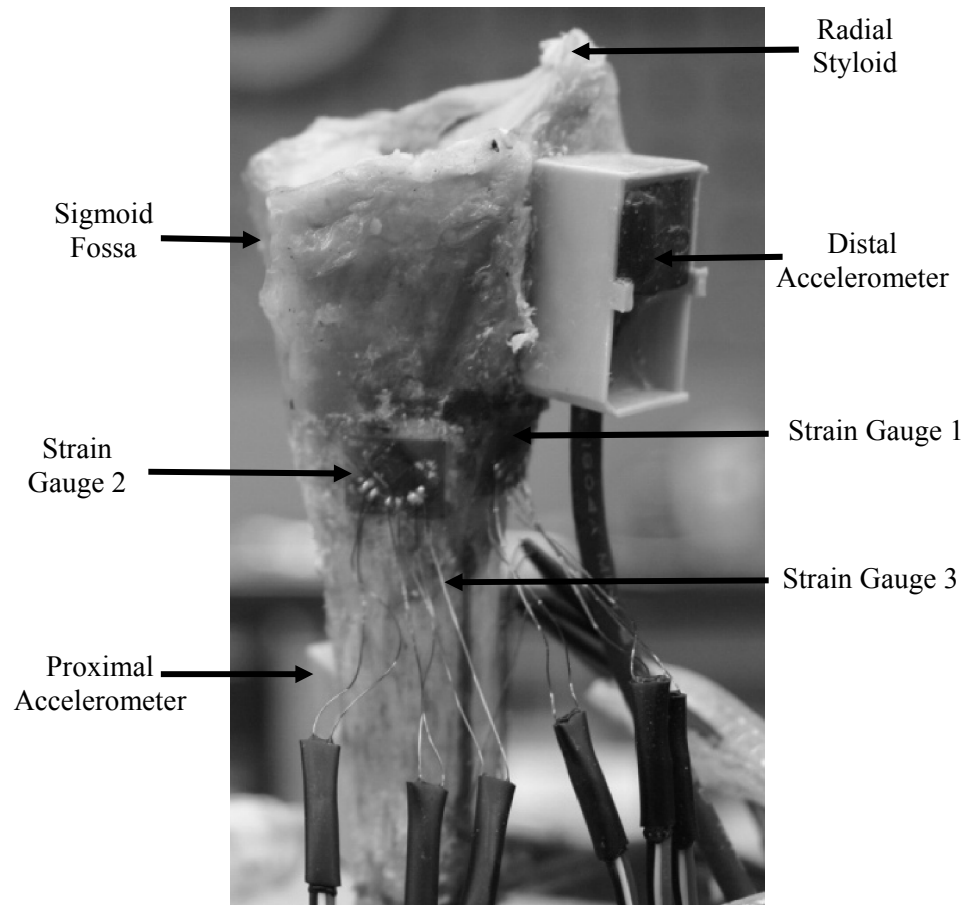
Figure 2.9: Strain Gauge and Accelerometer Positions
A distal radius specimen showing the locations of
the three strain gauges and the two accelerometers.
The locations of the sigmoid fossa and the radial
styloid have been included to orient the position of
the radius.

but with no visual propagation beyond the surface; iii) the fracture event-the impact at which failure of the specimen occurred, as described above.

Velocity, force, acceleration (Figure 2.10a) and strain (Figure 2.10b) data were acquired at 15 kHz (National Instruments NI-PXI 1050, and SCXI 1010) by a customized LabView (LabView 2008, National Instruments, Austin TX) data collection program. Force and acceleration data were filtered with a phase-less 4th order Butterworth filter and the optimal cut-off frequencies were calculated via residual analysis (Burkhart et al., 2011). The optimal cut-off frequencies for the force variables were different between the pre-fracture and fracture events and between channels, and therefore, unique cut-off frequencies were used across all force channels for pre-fracture (Fx: 500 Hz; Fy: 600 Hz; Fz: 400 Hz) and fracture (Fx: 600 Hz; Fy: 700 Hz; Fz: 500 Hz) trials. Residual analysis also determined that all acceleration channels should be filtered at 700 Hz (Burkhart et al., 2011) (Appendix E).

The peak principal strains were calculated from the strain gauge rosettes (Benham et al., 1996), such that positive and negative principal strains (με) were indicative of tensile and compressive strains, respectively (Bozkus et al., 2004). Strain rate was calculated from the strain-time curves as the rate of the linear portion of the curve between 30 % and 70 % of the peak strain. Peak axial, off-axis and resultant accelerations were calculated, along with axial and off-axis acceleration rates (also calculated between 30 % and 70 % of the peak (Duquette & Andrews, 2010)). The mean velocity of the shock wave through the bone was calculated from the strain and acceleration data separately. Shock wave velocity was defined as the distance between
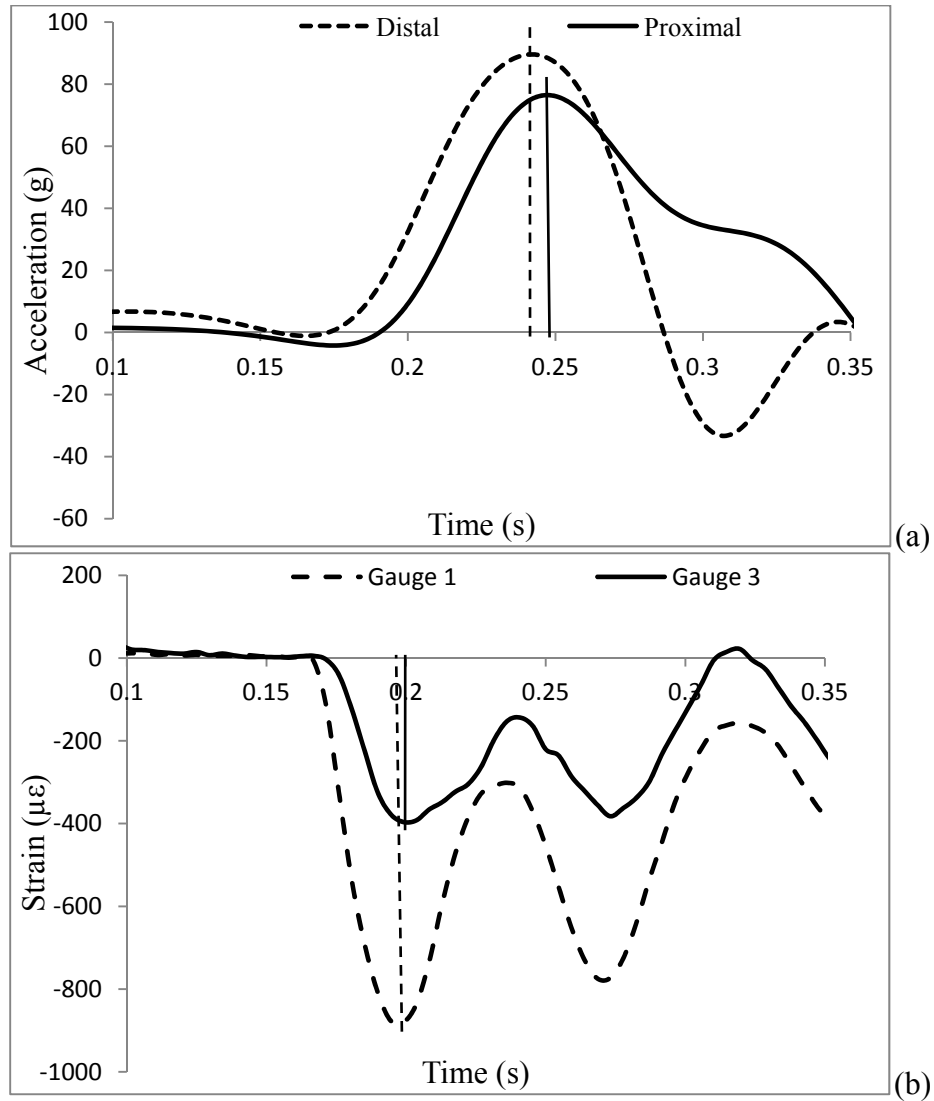
Figure 2.10: Acceleration and Strain Curves
Typical distal and proximal axial acceleration (a) and gauge 1 and
gauge 3 compressive strain (b) curves for a pre-fracture impact event.
The vertical lines represent the times to peak for each respective curve.

the respective sensors, divided by the difference in the time between the peaks at the distal and proximal sensors. The center of each strain gauge was digitized (Microscribe® G2X, Immersion corporation San Jose, CA) and the length of the resultant vector was used as the distance value in the velocity calculation.

Injury prediction equations were created where the pre-fracture trial defined no injury and the fracture trial defined injury. The multi-impact method adopted here means that the dependant variables are inherently correlated and traditional binary logistic regression was not an appropriate statistical method to use. Instead, generalized estimating equations were utilized (Pan, 2001). Models were first developed to determine the predictive value of the acceleration and strain variables on their own, followed by an analysis of multi-variate equations. The multi-variate equations were created by first including all variables and systematically eliminating those that were not significant ($p>0.05$) and running subsequent tests until all variables in the model were significant. The individual models were assessed according to the Quasi-Likelihood under Independence model Criterion (QIC) which is computed using the full log quasi-likelihood function (Pan, 2001; Ballinger, 2004). This criterion operates such that the smaller the value the better the model. A baseline model was also created, including only the intercept, to determine the effectiveness of the uni- and multi-variate models in predicting injury (i.e. models that had smaller QICs compared to the intercept model would be considered an effective injury prediction model).

To assess the relationship between the acceleration variables and the measured strains, linear generalized estimating equations were developed and the best models

were selected based on the same criteria as the logistic models. Marginal R^2 values were also calculated using Eq. (2.1) (Ballinger, 2004; Zheng, 2000).

$$R^2 = 1 - \frac{\sum_{i=1}^{n}(Y_i - \hat{Y}_i)^2}{\sum_{i=1}^{n}(Y_i - \bar{Y}_i)^2} \qquad\qquad (Eq. 2.4)$$

Where $\hat{Y}_i$ are the values predicted from the model after it is estimated, and $\bar{Y}_i$ is the estimated marginal mean across all impacts.

Pearson correlation coefficients were used to analyse the relationship between the impact velocity and the peak accelerations. Repeated measures ANOVAs were conducted to determine if significant mean differences existed in the strain and acceleration variables across the three impact events (pre-fracture, crack and fracture). Finally, a 2x3 (2 velocity calculation methods x 3 impact events) repeated measures ANOVA was used to establish if significant mean differences existed in the shock wave velocity when calculated by strain gauges compared to accelerometers. All statistical tests were performed in SPSS 19 (IBM SPSS 19, IBM, Armonk New York, USA) and alpha was set at 0.05 for all analyses.

2.3.3 Results

Peak accelerations in both the axial (r=0.73) and off-axis (r=0.72) directions correlated well with the increase in impact velocity across all impacts (2.1 m/s – 3.4 m/s). Peak axial and off-axis accelerations also increased significantly from the pre-fracture to the crack event, as well as between the pre-fracture and fracture impact events. Peak accelerations were 56 % and 60 % greater during the fracture event

compared to the pre-fracture event in the axial and off-axis directions, respectively

(Figure 2.11a). Acceleration rates increased significantly between the pre-fracture

 (26260.4 (16442.6) g/s) and crack (73625.6 (43671.4) g/s) events in the off-axis

direction only (Figure 2.11b).

Mean (SD) peak compressive strains of -2046.5 (-878.5) and -2717.7 (-1697.8)

were recorded during fracture from gauge 1 and gauge 2, respectively, and both were

significantly different than the strains recorded during the pre-fracture event (Figure

2.12a). There were no significant differences in the strain rates across any of the

fracture events or at either gauge (Figure 2.12b).

While peak distal axial, off-axis and resultant accelerations were found to be

better predictors of injury on their own, compared to the intercept-only model, resultant

acceleration was the best predictive acceleration variable (QIC=15.61; p<0.001) (Table

2.4). However, the prediction was improved when a multi-variate model (QIC=9.42)

was considered, specifically the combination of peak resultant acceleration (p<0.001)

and donor body mass index (BMI) (p<0.001). With respect to the strain-only models,

those that included only compressive strain at gauge 1(QIC=21.07; p < 0.001) and

gauge 2 (QIC=21.99; p<0.001) were shown to improve the prediction of injury

compared to the intercept-only model (Table 2.5), Similar to the multi-variate

acceleration models, the strain models were improved (QIC=19.60) when other

variables were considered; the best injury prediction model included peak compressive

strain (p<0.001) and compressive strain rate (p=0.039) at gauge 2 (Table 2.5).

Linear models that contained peak axial acceleration (QIC=1.4E7; p<0.001;

R^2=0.80) and peak resultant acceleration (QIC=1.5E7; p<0.001; R^2=0.80) were found to
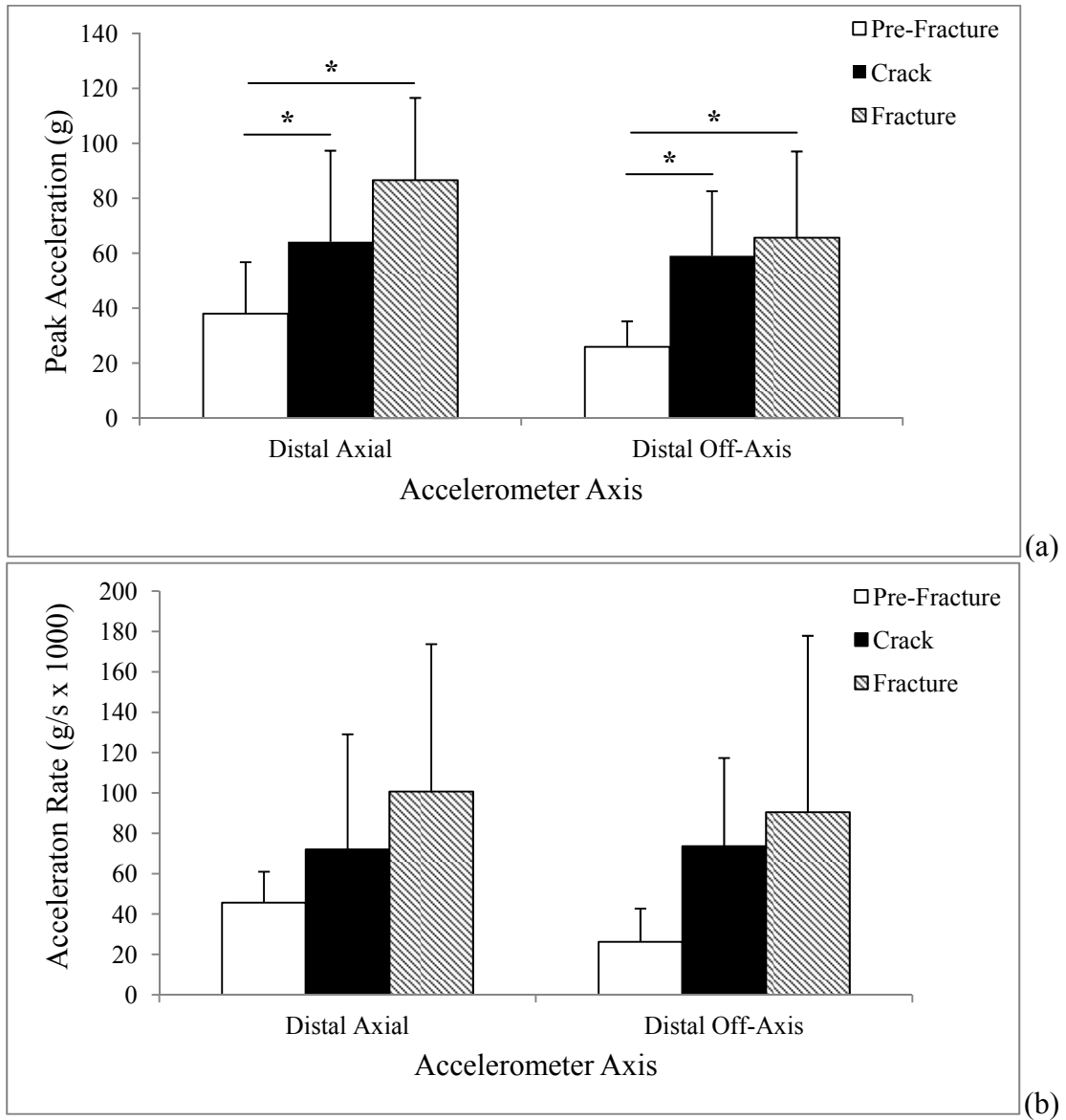
Figure 2.11: Radius Acceleration and Acceleration Rate
Comparison of the mean (SD) peak accelerations (a) and acceleration rates (b)
between the pre-fracture, crack and fracture events (*p<0.05).
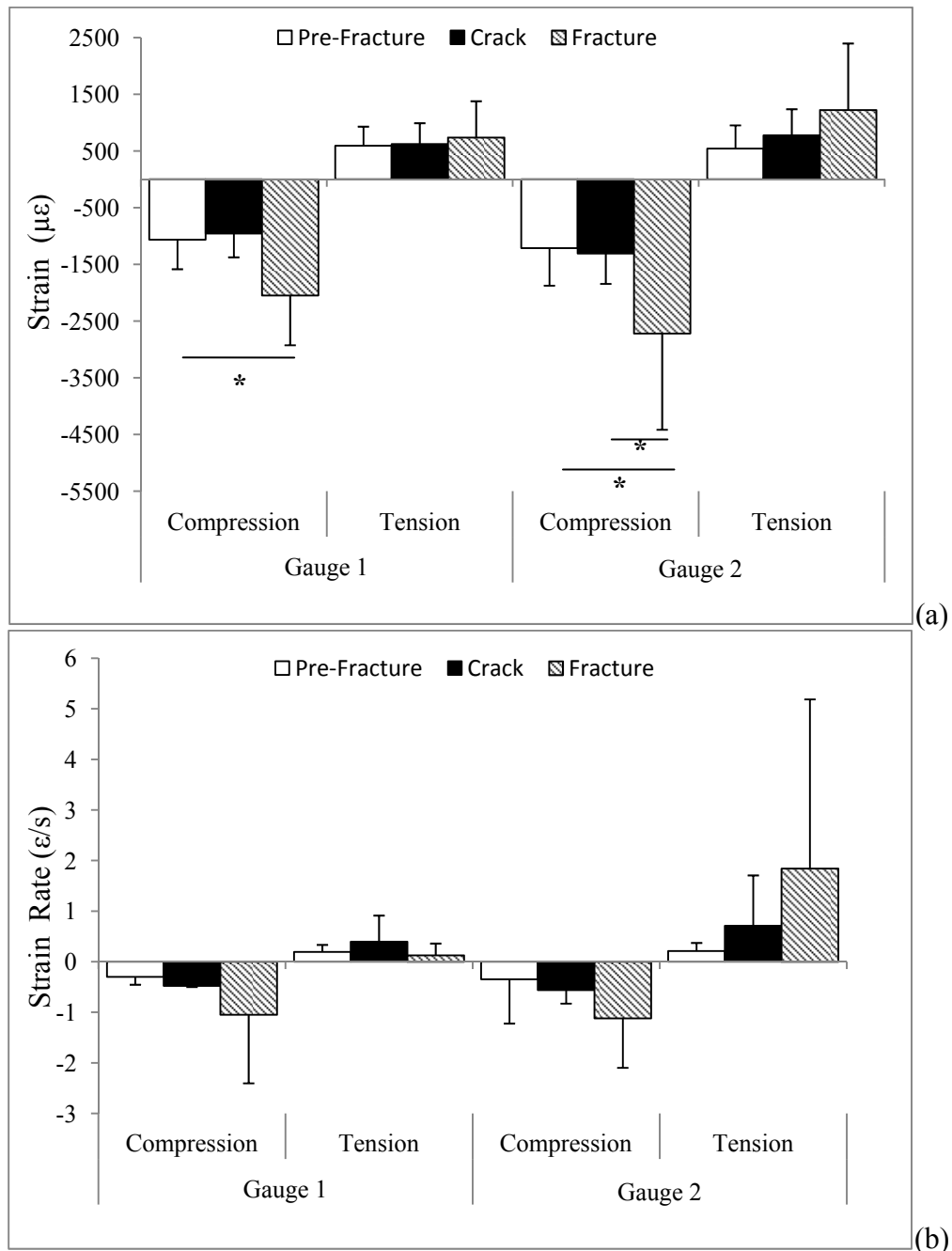
Figure 2.12: Radius Strain and Strain Rate
Comparison of the mean (SD) peak strains (a) and strain rates (b) for gauges 1 and 2, between the pre-fracture, crack and fracture events (*p<0.05)

Table 2.4: Acceleration and Strain Based Injury Models
Summary of the uni-variate and multi-variate logistic injury prediction models. The models predict the probability of injury by calculating a value between 0 (no injury) and 1 (injury).

Model	Goodness of Fit[*]	Intercept	Beta	p-value
Intercept-only Model	22.18			
Uni-variate Acceleration				
Peak Distal Axial	17.25	-3.44	0.03	0.001
Peak Distal Off-Axis	19.14	-2.57	0.03	0.001
Peak Distal Resultant	15.62	-3.54	0.02	0.001
Distal Axial rate	23.16	-1.94	1.07E-5	0.001
Distal Off-Axis rate	23.83	-1.66	8.51E-6	0.001
Multi-variate Acceleration				
Distal Resultant	9.43	-9.39	-0.01	0.001
BMI (kg/m^2)			-0.05	0.001
Uni-variate Strain				
Gauge 1 Compression	21.07	-2.80	-0.001	0.001
Gauge 1 Tension	27.54	-1.38	0	0.246
Gauge 2 Compression	21.99	-2.41	-0.001	0.001
Gauge 2 Tension	25.48	-1.86	0.001	0.052
Gauge 1 Compression Rate	25.23	-1.43	-4.4E-7	0.001
Gauge 1 Tension Rate	29.46	-0.88	-1.47E-6	0.611
Gauge 2 Compression Rate	26.98	-0.98	7.01E-8	0.19
Gauge 2 Tension Rate	25.66	-1.30	1.63E-8	0.001
Multi-variate Strain				
Gauge 2 Compression	19.60	-2.35	-0.001	0.001
Gauge 2 Compression Rate			1.82E-7	0.039

[*] Goodness of fit is assessed based on the Quasi-Likelihood under Independence model Criterion (QIC) value, such that smaller values represent better models.
Note: Gauge 1 = Distal radial styloid, Gauge 2 = distal ulnar side of radius.

Table 2.5: Uni-variate Strain Predictors

Summary of the uni-variate strain predictors

Model	Goodness of Fit	Intercept	Beta	p-value	R^2
Gauge 1 Compression					
Peak Axial	14644084.89	-675.88	-9.63	<0.001	0.80
Peak Off-Axis	17272607.14	-1041.02	-5.31	0.34	0.80
Peak Resultant	15276602.79	-700.64	-7.20	<0.001	0.79
Gauge 1 Tension					
Peak Axial	5412631.53	500.27	2.06	0.44	0.71
Peak Off-Axis	5178869.29	833.95	-3.95	0.01	0.72
Peak Resultant	5556529.33	635.44	0.00	1.00	0.79
Gauge 2 Compression					
Peak Axial	27882454.42	-1045.55	-8.56	0.14	0.75
Peak Off-Axis	30436456.25	-1693.99	1.17	0.74	0.73
Peak Resultant	29506475.25	-1236.58	-4.40	0.28	0.74
Gauge 2 Tension					
Peak Axial	7437087.33	393.88	5.55	0.05	0.79
Peak Off-Axis	8461803.66	667.20	1.81	0.58	0.76
Peak Resultant	7887769.47	458.81	3.55	0.12	0.77

be the best models for predicting compressive strains measured from gauge 1, while the peak off-axis acceleration was a significant predictor of the tensile strain at gauge 1 (Table 2.5). There were no significant uni-variate strain prediction models for either of the strain components at gauge 2. Similarly, no significant multi-variate strain prediction models were found (Table 2.5).

The overall mean (SD) shock wave velocity decreased significantly (p=0.004) from the pre-fracture (101.7 (62.3) m/s) to the fracture event (18.0 (9.2) m/s) (Figure 2.13). Peak accelerations were found to overestimate the calculation of the shock wave velocity by approximately 14 m/s, compared to the peak compressive strains. However, these differences were not significant (Figure 2.13).

2.3.4 Discussion

To the author's knowledge, this is the first study to investigate the efficacy of accelerometers for predicting distal radius fracture from impulsive impacts and describing the general behaviour of the underlying bone. Overall, peak compressive strains and peak accelerations increased significantly in response to an increase in the intensity of the impact event at both distal strain gauge locations and along all axes, respectively. Furthermore, peak compressive strains and resultant accelerations were shown to be good predictors of distal radius fracture, and in turn, the resultant acceleration associated well with the compressive strains that were recorded at the same location.

The strong correlations between the peak accelerations and the input velocities (mean r=0.72) further indicates that accelerometers are capable of responding to, and
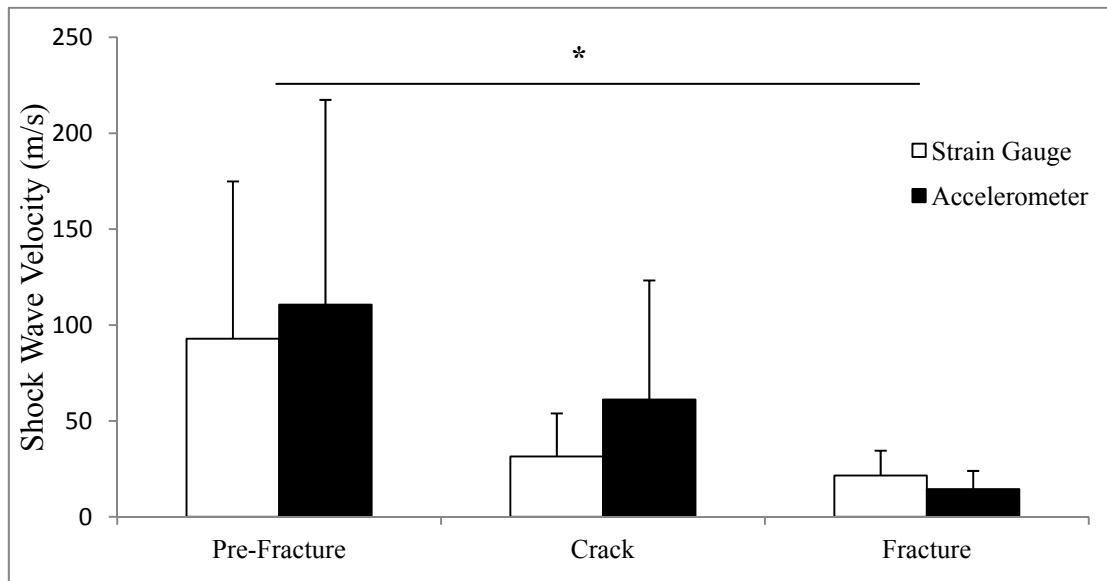
Figure 2.13: Shock Wave Velocities
Mean (SD) shock wave velocities calculated from the times of the peak strains and the peak accelerations (*Represents a significant difference between the pre-fracture and fracture shock wave velocity across measurement type at $p < 0.05$).

indicating a change in the intensity of the impact. These data agree well with previously

reported impact accelerations from drop heights between 25 cm and 38 cm (Kim et al.,

2006). However, in this study (Kim et al., 2006), a surrogate hand model was used and

it was not possible to conclude whether these impact accelerations resulted in failure.

The mean peak axial acceleration of approximately 90 g reported in the current study

was found to correspond well with the fracture event. In addition, the current study

presented the accelerations in the off-axis direction (normal to the long axis of the

radius). This appears to be an important measure in assessing the potential for injury to

the distal radius as it has been suggested that the distal radius becomes more susceptible

to fracture as the impact force becomes directed less axially (Troy & Grabiner, 2007).

Binary logistic (no fracture vs. fracture) generalized estimating equations where

utilized to assess the association of the acceleration and strain variables with injury. On

their own, each of the acceleration variables, along each of the axes, was a significant

predictor of injury, while peak distal axial, off-axis and resultant acceleration improved

the predictability of injury when compared to the baseline model. However, a multi-

variate model combining the resultant acceleration with donor BMI produced a better

model. It has repeatedly been shown that BMI is a significant indicator of fracture,

such that increasing one's BMI tends to decrease the fracture risk (DeLaet et al., 2000).

While the compressive strain measures at both gauges (with the exception of

compressive strain rate at gauge 2) were all significant uni-variate predictors of injury,

the best model was multi-variate and included both the peak compressive strain and

compressive strain rate at the second gauge site. The inclusion of these site-specific

variables is supported by the widely accepted view that the failure of bone is highly

dependent on the direction and rate of loading (Nordin & Frankel, 2001). This model also suggests that the gauge measurements are more equipped to predict the failure when it occurs in the vicinity of the gauge itself. The majority of the specimens failed at or near the ulnar side of the radius, coinciding with the site of strain gauge 2, with very little damage occurring on the radial styloid side, in line with gauge 1. Overall, the strain gauges and accelerometers performed equally well at predicting the onset of distal radius failure, and in some of the uni-variate models, the accelerometers were better predictors of injury than the strain gauges.

Three of the strain prediction models presented here provide a good estimate of the strains experienced at the distal radius. Peak axial and resultant accelerations were found to be good predictors of the compressive strains, while the peak off-axis accelerations were better at predicting the tensile strains. However, these accelerations were only associated with the strains measured from gauge 1 (distal radial styloid), and were not significantly associated with the strain components from strain gauge 2 (distal ulnar side of radius). As the accelerometer was placed just distal to strain gauge 1, this indicates that, although a strong relationship exists between the bone strains and accelerations, the accelerations can only provide a reasonably good estimate of the strains at the site of the accelerometer.

Aside from providing valuable information with regards to the mechanical properties of the bone in response to increasing impacts, the information from strain gauges can also be used to quantify the velocity and magnitude of the shock wave as it travels through the bone (Pelker & Saha, 1983; Folma et al., 1993; Cheng et al., 1995). Pelker and Saha (1983) were able to show that changes occurred to the behaviour of the

shock wave, when the bone through which it travelled, was altered (e.g., changes in bone density and porosity). While strain gauges likely provide a more accurate measure of shock wave velocity than accelerometers, since they are attached directly to the bone, their invasiveness, cost, single use, and difficult mounting makes strain gauges virtually unusable for *in vivo* applications (Folma et al., 1993). The absence of significant differences between the shock wave velocities calculated with the strain gauges and the accelerometers indicates that the accelerometers used here are a viable method for measuring the velocity of the shock wave at different impact intensities, through the bone to which they are attached. While significance was only found between the pre-fracture and fracture events, the shock wave velocity decreased significantly across all increasing impact velocities. Similar to past work (Pelker & Saha, 1983; Folma et al., 1993), this result suggests that repetitive impacts are leading to underlying changes in the bone that may have an effect on the mechanical properties.

It is important to address the limitations of this work to ensure an accurate analysis of the accelerometer signals. A major limitation is the absence of the surrounding soft tissues that may have an effect on the accelerometer signal. *In vivo*, accelerometers would be susceptible to the passive and active movement of the underlying tissues, essentially altering the shock wave as it travels proximally through anatomical structures (Burkhart & Andrews, 2010a, 2010b, Holmes & Andrews, 2006). Therefore, the relationship between the accelerations and strains may differ in the presence of soft tissues. However, a comparison of surface-mounted and bone-mounted accelerometers showed that the peaks and times to peaks are minimally affected by the underlying soft tissues with differences of approximately 2.1 g and 5 ms, respectively

(Lafortune et al., 1995). Furthermore, in the upper extremity, common sites of accelerometer attachment are the radial styloid and the olecranon process (Burkhart & Andrews, 2010a, 2010b), both of which have minimal overlaying soft tissue. The effect of any underlying tissue is also limited considerably *in vivo*, by pre-loading the accelerometers so that they are pushed into the soft tissues as close to the underlying bone as possible (Burkhart & Andrews, 2010a, 2010b). Another notable limitation is the lack of acceleration data along the third (medial-lateral) axis. The strain data and fracture patterns suggest that there may be a significant medial-lateral component contributing to failure. The inclusion of medial-lateral accelerations may improve the already good strain prediction models and provide an even better description of the true state of strain. Future work needs to be conducted on the acceleration response of intact specimens (with soft tissues in place), along all three axes.

In the current study, signals from accelerometers were used to predict the response of bone to impacts of increasing intensity until failure. The results suggest that multi-axial accelerometers that are bone-mounted are a viable option for predicting the risk of distal radius injury in *in vitro* applications. They are also able to describe the general state of strain of the underlying bone and are good strain gauge surrogates for measuring the characteristics of the shock wave.

2.3.5 References

Austman RL, Beaton BJB, Quenneville CE, King GJW, Gordon KD, Dunning CE. 2007. The effect of distal ulnar implant stem material and length on bone strains, Journal of Hand Surgery. [American], 32-A, 848-854.

Ballinger GA. 2004. Using generalized estimating equations for longitudinal data analysis. Organizational Research Methods. 7, 127-150.

Benham PP, Crawford RJ, Armstrong CG. 1996. Mechanics of Engineering Materials. Harlow England: Pearson Prentice Hall, Ch. 11.

Bozkus H, Bozdag E, Sunbuloglu E, Tanyeli E, Sarioglu AC, Hanci M. 2004. Surface strain and stress analysis of the mid-cervical vertebrae bone compartments: A biomechanical pilot study. Turkish Journal of Neurosurgery. 14: 1-11.

Burkhart TA, Andrews DM. 2010a. The effectiveness of wrist guards for reducing wrist and elbow accelerations resulting from simulated forward falls. Journal of Applied Biomechanics. 26, 281-289.

Burkhart TA, Andrews DM. 2010b. Activation level of extensor carpi ulnaris affects wrist and elbow acceleration response following simulated forward falls Journal of Electromyography and Kinesiology. 20, 1203-1210.

Burkhart TA, Dunning CE, Andrews DM. 2011. Determining the optimal system specific cut-off frequencies for filtering *in vitro* upper extremity impact force and acceleration data by residual analysis. Journal of Biomechanics. 44, 2725-2755.

Boyer KA, Nigg BM. 2004. Muscle Activity in the leg is tuned in response to impact force characteristics. Journal of Biomechanics. 37, 1583-1588.

Cheng S, Timonen J, Suominen H. 1995. Elastic wave propagation in bone *in vivo*: methodology. Journal of Biomechanics. 28, 471-478.

De Laet C, Kanis JA, Oden A, Johanson H, Johnell O, Delmas P, Eisman JA, Kroger H, Fujiwara S, Garnero P, McCloskey EV, Mellstrom D, Melton LJ III, Meunier PJ, Pols HAP, Reeve J, Silman A, Tenenhouse A. 2005. Body mass index as a predictor of fracture risk: A meta-analysis. Osteoporosis International. 16, 1330-1338.

Duquette AM, Andrews DM. 2010. Comparing methods of quantifying tibial acceleration slope. Journal of Applied Biomechanics. 2, 229-233.

Edwards WB, Ward ED. Meardo, SA, Derrick TR. 2009. The use of external transducers for estimating bone strain at the distal tibia during impact activity. Journal of Biomechanical Engineering. 131, 051009-1 – 0501009-6.

Folma Y, Goshen E, Gepstein R, Sevi R, Libert S. 1993. Acceleration assessment of osseous union. Archives of Orthopaedic Trauma and Surgery. 112, 193-197.

Greenwald RM, Janes PC, Swanson SC, McDonald TR. 1998. Dynamic impact response of human cadaveric forearms using a wrist brace. The American Journal of Sports Medicine. 26, 825-830.

Holmes AM, Andrews DM. 2006. The effect of leg muscle activation state and localized muscle fatigue on tibial response during impact. Journal of Applied Biomechanics. 22, 275-284.

Hwang I-K, Kim K-J. 2004. Shock-absorbing effects of various padding conditions in improving efficacy of wrist guards. Journal of Sports Science and Medicine. 3, 23-29.

Kim K-J, Alian AM, Morris WS, Lee Y-H. 2006. Shock attenuation of various protective devices for prevention of fall related injuries of the forearm/hand complex. The American Journal of Sports Medicine. 34, 637-643.

Lafortune MA, Henning E, Valiant GA. 1995. Tibial shock measured with bone and skin mounted transducers. Journal of Biomechanics. 28, 989-993.

Lafortune MA, Lake MJ, Henning EM. 1996. Differential shock transmission response of the human body to impact severity and lower limb posture. Journal of Biomechanics. 29, 1531-1537.

Leslie IJ, Dickson RA. 1981. The fractured carpal scaphoid: natural history and factors influencing outcome. Journal of Bone and Joint Surgery. 63-B, 225-230.

Milgrom C, Fineston A, Hamel A, Mandes V, Burr D, Sharkey N. 2004. A comparison of bone strain measurements at anatomically relevant sites using surface gauges versus strain gauged bone staples. Journal of Biomechanics. 37, 947-952.

Nordin M, Frankel VH. 2001. Basic Biomechanics of the musculoskeletal system. Baltimore MD: Lippincott Williams and Williams.

Pan W. 2001. Akaike's information criterion in Generalized Estimating Equations. Biometrics. 57, 120-125

Pelker RR, Saha S. 1983. Stress wave propagation in bone. Journal of Biomechanics. 16, 481-489.

Quenneville CE, Fraser GS, Dunning CE. 2010. Development of an apparatus to produce fractures from short-duration high-impulse loading with an application in the lower leg. Journal of Biomechanical Engineering. 32, 014502-1 – 014502-4.

Radin EL, Parker HG, Pugh JW, Steinberg RS, Paul IL, Rose RM. 1973 Response of the joints to impact loading-III. Journal of Biomechanics. 6, 51-57.

Schinkel-Ivey A, Burkhart TA, Andrews DM. 2011 (in press). Leg tissue mass composition affects tibial acceleration response following impact. Journal of Applied Biomechanics.

Staebler MP, Moore DC, Akelman, Weiss A-PC, Fadale PD, Crisco JJ. 1999. The effect of wrist guards on bone strain in the distal forearm. The American Journal of Sports Medicine. 27, 500-506.

Troy KL, Grabiner MD. 2007. Off-axis loads cause failure of the distal radius at lower magnitudes than axial loads: a finite element analysis. Journal of Biomechanics. 40, 1670-1675

Werner FW, Short WH, Fortino MD, Palmer AK. 1997. The relative contribution of selected carpal bones to global wrist motion during simulated planar motion and out-of-plane wrist motion. Journal of Hand Surgery. 22A, 708-713.

Zheng B. 2000. Summarizing the goodness of fit of generalized linear models for longitudinal data. Statistics in Medicine. 19, 1265-1275.

CHAPTER 3 – *IN VIVO* RESPONSE OF THE UPPER EXTREMITY TO DYNAMIC SUB-MAXIMAL IMPACT LOADING

3.1 Reliability of Impact Forces, Hip Angles and Velocities During Simulated Forward Falls Using a Novel Propelled Upper Limb Fall Arrest Impact System (PULARIS)[3].

3.1.1 Introduction

Despite the attention given to injuries caused by forward falls (Grabiner et al., 2008), and the World Health Organization making their prevention a key priority (Fardellone, 2008), these injuries continue to be some of the most prevalent preventable injuries worldwide (National Academy on an Aging Society, 2003; Grabiner et al., 2008). One of the most commonly injured anatomical sites is the distal upper extremity (Statistics Canada, 2011) and the demographic at the highest risk for a fall event and subsequent injury are those over the age of 65 years (Statistics Canada, 2011). Considering that the number of individuals over the age of 65 years is expected to grow exponentially over the next two decades (National Academy on an Aging Society, 2003), distal upper extremity injuries will continue to stress healthcare systems globally (Kakarlapudi et al., 2000). It has also been suggested that upwards of 80 % of sport-related distal radius fractures are a result of fall onto the upper extremity (Lawson et al., 1995). With respect to in-line skating, it has been suggested that more than a third of all injuries occur to the distal radius with two-thirds of these being fractures or dislocations (Schieber et al., 1994).

Acquiring an accurate understanding of the kinematics and kinetics of *in vivo* forward falls is limited in the field due to the infrequent and unpredictable

---

[3]A version of this work has been accepted for publication: Burkhart TA, Clarke D, Andrews DM. Reliability of Impact Forces, Hip Angles and Velocities During Simulated Forward Falls Using a Novel Propelled Upper Limb fall Arrest Impact System (PULARIS). Journal of Biomechanical Engineering.

nature of these events. To date, numerous forward fall simulation methods designed to impact the distal upper extremity have been tested in the laboratory, but have generally been limited by the need to perform impacts safely for participants. To keep impact force severity to a reasonable level, Chiu & Robinovitch (1998) and Troy & Grabiner (2007) had participant's lean forward from a kneeling position until their hands contacted a force platform. Robinovitch and Chiu (1998) and Chou et al. (2009) also used a kneeling start position, but supported participants' torsos using a strap, which when released, resulted in participants impacting a force platform with the hands. Forward falls have also been simulated by having participants start from a stationary, upright standing position and impacting their hands against a vertically mounted force platform (Kim & Ashton-Miller, 2003) or starting from a position where their shoulders began 1 m off the ground, followed by impacts to horizontally mounted force platforms after being released (DeGoede & Ashton-Miller, 2002; Lo et al., 2003). Using a weighted pendulum, DeGoede et al. (2002) impacted the hands of stationary seated participants to study the effect of different elbow angles in reducing the impact force to the upper extremity. Lastly, Burkhart & Andrews (2010a, 2010b) adopted a seated human pendulum method where participants impacted vertically mounted force platforms with their hands after being released from a resting position a known distance from the platforms.

The above methods have provided good kinematic and kinetic data of simulated forward falls and have contributed significantly to the understanding of forward fall arrest mechanisms and injury prevention strategies. However, they are all limited in a few ways that may affect their validity compared to real world events. First, starting the

simulated falls from a stationary position does not replicate the dynamic movements

(e.g., walking and running) typical at the initiation of many fall events (Berg et al.,

1997). Second, due to the fairly restricted uni-directional motion of most of the

laboratory methods, the subsequent impact forces have been mainly constrained to the

axial direction. Lastly, the hip and extremity postures utilized prior to impact (e.g.,

seated and kneeling positions) are not entirely representative of the body positions

adopted when falling unexpectedly in the field (Pavol et al., 2001). Developing a

method that enables researchers to consistently apply impacts to the upper extremities in

different upper extremity orientations and from dynamic initial positions, might help to

improve our understanding of the mechanisms of injury to the distal upper extremity

that are associated with forward fall arrest.

Therefore, this section describes a novel impact method that has been developed

to accurately simulate the kinematics of forward falls and the resultant impacts onto

outstretched hands. The repeatability of impact forces and velocities resulting from the

Propelled Upper Limb fall ARrest Impact System (PULARIS) method is presented for

several upper extremity positions and fall heights to demonstrate its effectiveness for

simulating forward falls in the laboratory.

3.1.2 Methods

3.1.2.1 Development of PULARIS
The physical structure of PULARIS consists of four (two top and two bottom)

2.3 m x 0.05 m x 0.005 m steel tubing crossbars in a scissor-like arrangement (Figure

3.1) that are each attached to one of four (two top and two bottom) metal trolleys

(Unistrut, Wayne, MI; Model # P2950) (Figure 3.1). Three of the trolleys (two top and

the bottom posterior) have four 0.03 m diameter bearings that sit within c-channel tracks; the top track is rigidly attached to the laboratory ceiling grid work and the bottom track (2.3 m) connects the two bottom crossbars. The bottom forward trolley is fixed in place to the forward edge of the bottom track. The system can be lifted and lowered while the participant is suspended from the bottom track (i.e. to control the height of the fall) via a steel cable attached to the bottom posterior trolley and to a 900 kg capacity winch (Posi-lock Puller Inc. Cooperstown ND. Model # 5312). The winch is securely fastened to the rear end of the bottom track, which enables approximately 1.5 m of vertical movement of the bottom track above the ground when the trolley is pulled backwards towards the winch (Figure 3.1). A consistent between-trial height was achieved by marking the position of the lower posterior trolley for the 0.05 m and 0.10 m falls separately.

Two idler sprockets are attached to each of the top crossbars and subsequently connected to a 12 m section of chain (Figure 3.1). The chain also interfaces with two additional idler sprockets: one rigidly connected to the upper, most posterior aspect of the upper track; and the second fastened anteriorly to a speed reducer (Iron Horse™ Worm Gearboxes, Automation Direct, Atlanta GA, Model # WG-175-010-D) and 0.25 horse power electric motor (Marathon Electric Motors, Wausau WI. Model # 56H17T2011) (Figure 3.1), which provides the forward-rear thrust. Mounted to the bottom track is another 1.8 m section of c-channel track that is inverted to make it capable of housing two (forward and rear) solenoid-controlled (Guardian Electric
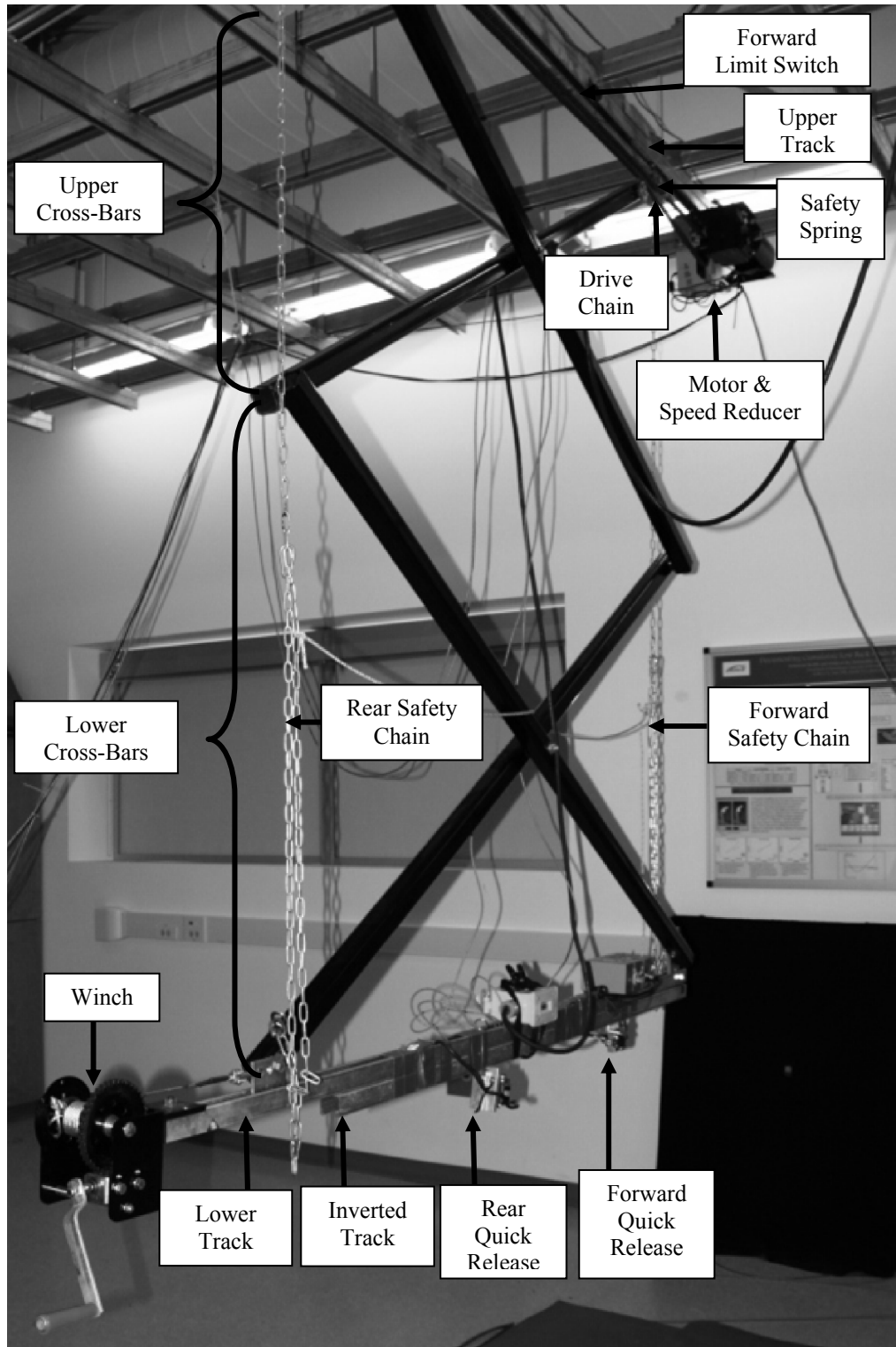
Figure 3.1: PULARIS Structure
The major structural components of the Propelled Upper Limb fall ARrest Impact System (PULARIS). Forward motion of the PULARIS would occur from the left to the right.

Manufacturing, Woodstock, IL. Model # 18-P) quick releases (Sea Catch quick release,
McMillian Design Inc. Gig Harbor WA. Model # TR3; 0.65 ton capacity) (Figure 3.2).
The jaws of each quick release open when the solenoid is activated, causing a pin
attached to the solenoid's plunger to push the internal lever of the quick release (Figure
3.2). This releases a shackle linked to a metal ring which is attached directly to the torso
and leg straps. These straps support the participant's hip and legs, respectively while
suspended.

During testing, the solenoids were controlled by solid state relays (Tyco
Electronics Corporation Berwyn, PA Model # R10) that were programmed (LabVIEW
2009, National Instruments, Austin TX) such that the forward quick release was
activated approximately 150 ms before the posterior quick release. This delay ensured
that the hands impacted the force platforms (described below) prior to the legs coming
into contact with the ground (this was confirmed visually during testing and also during
video analysis). A slotted optical switch with a light emitting diode (LED) (Honeywell
Sensing and Control, Golden Valley, MN. Model# HOA1877-003) sandwiched the
upper forward sprocket and was used to count the number of sprocket teeth that passed
as PULARIS was moved backwards between the release point (close to the force
platforms) and start point (away from the force platforms), prior to each trial (Figure
3.3). The participant was released automatically from PULARIS when it passed the
release point as it moved forward away from the start point after the optical switch
counted the set number of teeth. Distance and velocity were determined knowing that
the space between each tooth was 12.7 mm.
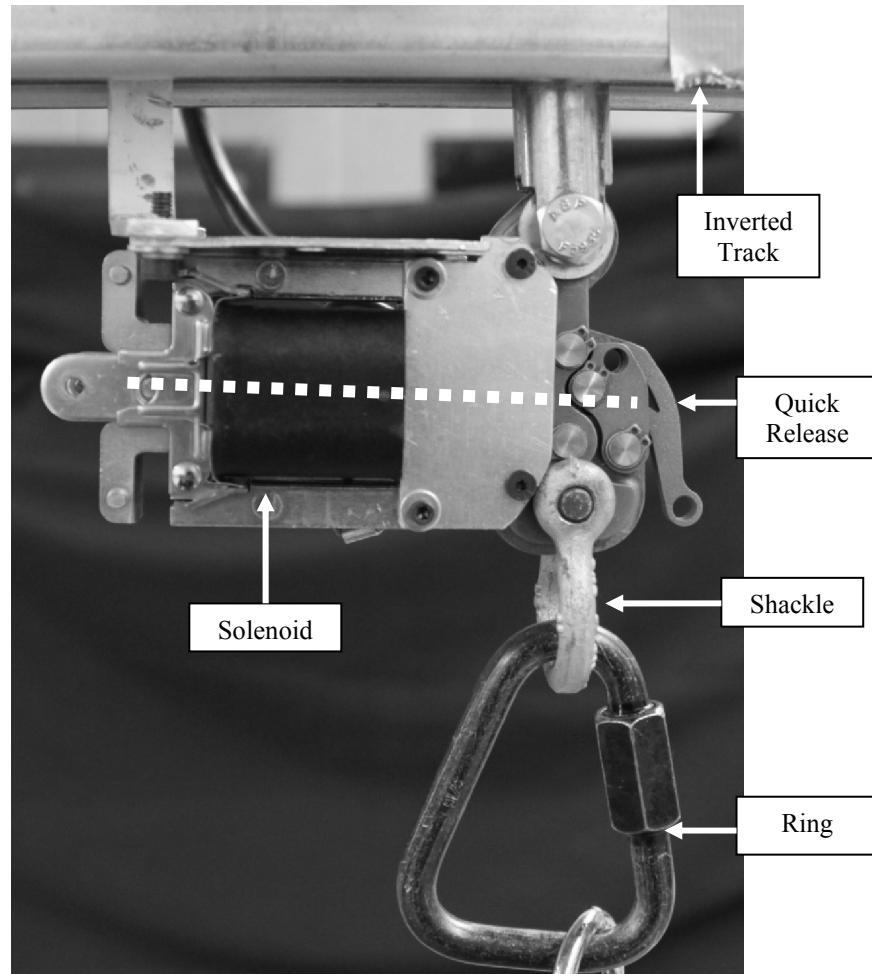
Figure 3.2: Quick Release Structure
Example of a quick release mechanism used to suspend and
release participants from the inverted lower track of PULARIS.
The quick release is engaged by an electrical impulse from the
computer to release the shackle (thereby dropping the
participant) via an internal plunger of the solenoid that acts in
the direction of the dashed line.
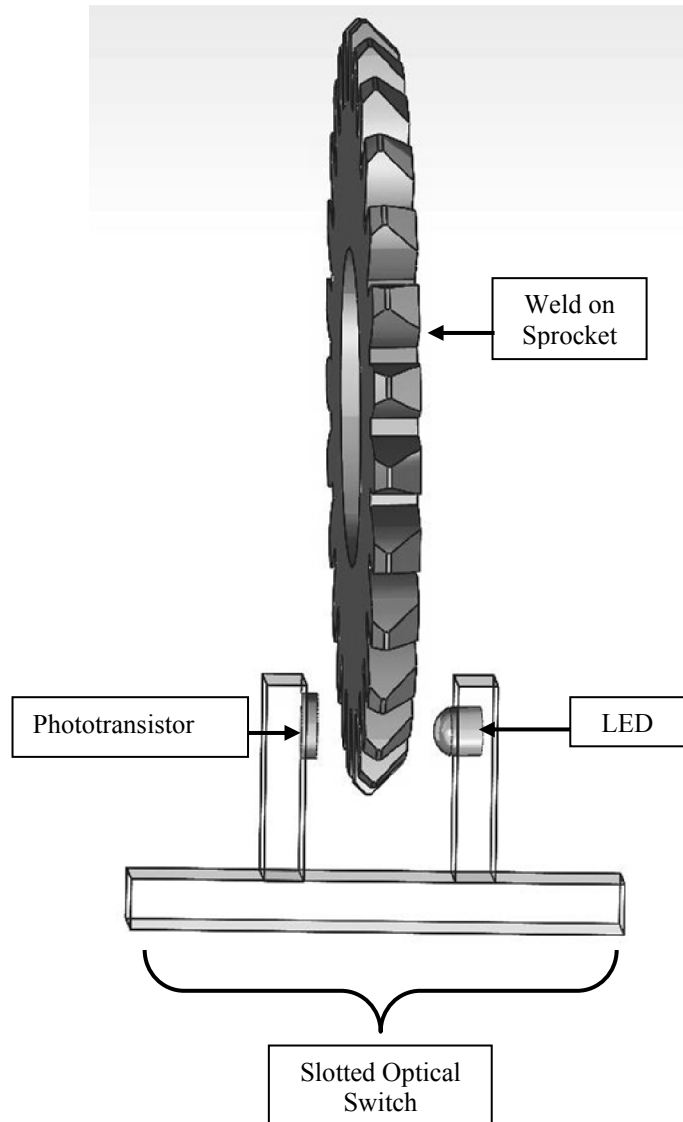
Figure 3.3: Slotted Optical Switch Mechanism
A top view schematic (SolidWorks, Dassault Systemes
SolidWorks Corp. Concord, MA) of the optical switch
used to determine the start and release points and distance
and velocity of PULARIS.

An AC drive (Automation Direct, Atlanta GA. Model # GS2-1-0P5) allowed for adjustment and control of the motor's velocity and acceleration, creating the forward-rear kinematic characteristics of the PULARIS structure. Two types of movement were possible with this set-up: i) a jog function, in which slow intermittent movements could be achieved, the distance of which depended on how long the function was activated; and ii) a run function, allowing for faster continuous distances to be covered with a single activation of the function. Generally, the jog function was used to set the start and release points for each trial, while the run function was used to propel the PULARIS and participant between the start and release points.

A number of mechanisms have been implemented within the system to ensure the safety of the participants. Two limit switches (Honeywell Sensing and Control, Golden Valley MN, USA; Model Number: BZ-2RW84-A2) were positioned at either end of the upper tracking and, when activated (i.e. PULARIS runs past the switches) movement of the system is immediately terminated. The forward limit switch was positioned such that, in the event of a quick release malfunction, the participant would not experience any further forward motion. The PULARIS control box was equipped with an emergency stop. Also, at each end of the upper tracking were two stiff springs (k=25 kN/m), capable of preventing PULARIS from impacting the motor or the sprocket at the forward and rear ends, respectively. Two safety chains were also implemented to prevent the cross-bars from falling should a failure in any of the links

occur. Finally, the area underneath PULARIS, from the start point and beyond the force platforms was covered with protective foam padding (Figure 3.4).

3.1.2.2 Experimental Set-up

To test the effectiveness of PULARIS in simulating the flight and impact phases of forward falls with outstretched upper extremities, 10 participants (5 male, 5 female; mean (SD) age: 23.2 (3.1) years; height: 1.7 (0.12) m; body mass: 71.2 (17.4) kg; BMI: 23.4 (3.7 kg/m^2)) with no history of upper extremity trauma consented to testing. All participants provided written informed consent and all procedures were approved by the University of Windsor Research Ethics Board (Appendix K).

Prior to being attached to PULARIS, spherical markers were placed on the right knee joint center, the right greater trochanter and to a fin attached to the participant's back at the level of the C7-T1 vertebrae using double sided tape. These markers were used to track the motion of the hip and to calculate the hip angle prior to and during the impact event. The participants were supported by a wooden box (not shown) while they were fitted into the torso sling, and the torso and leg straps were hooked into the rings of the forward and rear quick releases (Figure 3.4). The distance between the forward and rear quick releases remained constant for all tests within each participant such that, the forward quick release was positioned over the center of the participant's back while the rear quick release was placed over the mid-calf region. These positions ensured that the participant was balanced within the torso sling and leg straps. The ratio of the length of the leg strap to the length of the torso straps was set at 2:1, ensuring a consistent angle of each of the participants' bodies relative to the ground. PULARIS was elevated using the winch system (thereby lifting the participant off the wooden box so it could be
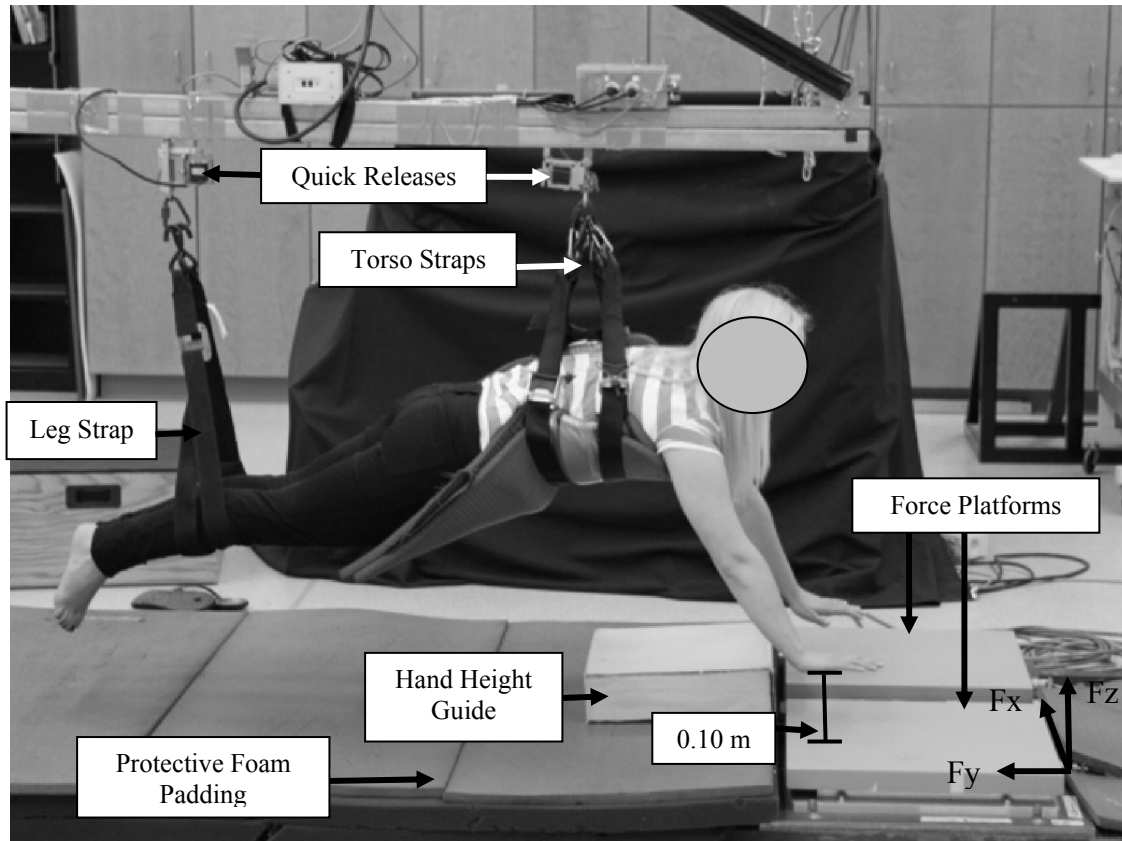
Figure 3.4: PULARIS Experimental Set-up
Experimental set-up of a straight arm 0.10 m fall of an un-instrumented participant just prior to release. The directions of the hand force components Fx, Fy and Fz are included for reference.

removed) and participants were moved forward toward two strain gauge based force

platforms (Advanced Mechanical Technology Inc. Watertown MA. Model #OR6-7;

2200 N capacity; natural frequency of 1 kHz), that were rigidly secured to the floor

beside one another (Figure 3.4). Participants were instructed to extend their arms so

that the backs of their arms were just touching the torso sling, with forearms extended at

the elbows. The height of the hands above the force platforms was adjusted by raising

or lowering PULARIS so that shoulder, elbow and wrist angles did not change from the

initial position. All other upper extremity conditions occurred with respect to this initial

straight arm posture and the height of PULARIS. The palms were lined up with the

near edges of the force platforms and this was set as the release point. Setting this point

based on the position of the hands relative to the edge of the force platforms accounted

for the continued forward movement of the participant during the flight phase once

released from PULARIS, such that the hands would impact them close to their centers.

Participants were then moved backwards (i.e. the entire PULARIS moves backwards

within the upper tracking) to the start point (approximately 1.95 m from the force

platforms). Once the start point was set, PULARIS was propelled forward towards the

force platforms at a velocity of approximately 1.0 m/s. The participant was dropped at

the release point and an impact was applied to the palm of each hand as they arrested

their fall. A 0.36 m x 0.36 m x 0.10 m piece of foam was placed in front of the force

platforms for participants to use as a height guide for their hands (Figure 3.4). For

example, participants were instructed to align their hands at the middle and the top of

the foam block for a 0.05 m and 0.10 m high fall, respectively. In addition, a thick bed

of foam was provided under PULARIS' full runway leading up to the force platforms to

cushion the impact of the participants' torsos and legs with the ground upon release.

These impacts were described by participants to be consistent with those experienced

when landing on the mattress of a bed after jumping on it from a standing height.

Each participant experienced three repetitions of three different fall types

(related to upper extremity posture: straight-arm, self-selected and bent-arm) at impact

and two different fall heights (0.05 m and 0.10 m). The straight-arm posture was

included to act as a worst-case scenario fall, whereas the self-selected posture was

included to allow participants to choose the posture that they felt would minimize the

impact. For the bent-arm falls, a 20° flexion angle about the elbow was set once

participants were moved to the start point, using an analog goniometer (Lafayette

Instruments Co., Inc. Lafayette IN. Model # 01135). Participants were instructed to

maintain the respective upper extremity postures throughout the duration of the impact

to the best of their ability including, shoulder elbow and wrist postures.

All trials were recorded from the right side with a digital video camera (Sony

Handycam, Sony Corporation, Tokyo Japan, Model # DCR-SX43) at 30 frames/s. The

videos were manually digitized (ProAnalyst Professional Edition, Xcitex Inc.

Cambridge MA.) in two dimensions to determine the horizontal and vertical position of

the knee, hip and fin markers. Fifteen frames before and after the impact (determined

visually where the right hand first made contact with the force platform) were analyzed

from each video. The hip angle (calculated as the torso relative to the thigh) pre-impact

and at impact were calculated within the ProAnalyst software such that positive and

negative angles represented flexion and extension, respectively. The peak hip

horizontal and vertical velocities prior to impact and the horizontal and vertical hip

velocities at impact were calculated by taking the first derivative of the position data in both the horizontal and vertical directions. The peak hip angular velocity and hip angular velocity at impact were also calculated within the same intervals as the linear velocity components. Video data were filtered with a 4th order zero-lag Butterworth filter at 5 Hz (Wu, 2000). The maximum PULARIS velocity was also collected (calculated by dividing the chain pitch (12.7mm) by the time elapsed between passing sprocket teeth, measured via the optical switch).

Peak vertical (Fz), medio-lateral (Fx) and anterior-posterior (Fy) impact forces were determined from the force-time curves for both the left and right hands. The force data were sampled at 4000 Hz and filtered with a 4th order, zero-lag, low pass Butterworth filter. The Fy and Fz force data were filtered at 80 Hz, while the Fx force data were filtered at 65 Hz, as determined via residual analysis (Burkhart et al., 2011).

3.1.2.3 Statistics

A 2 x 2 x 3 (2 velocities (PULARIS vs. video) x 2 fall heights x 3 fall types) repeated measures ANOVA was used to determine if significant differences existed in the mean PULARIS and horizontal hip velocities. Since the PULARIS velocity was in the horizontal direction only, the vertical hip velocity was not included in this factorial analysis. A 2 x 3 (2 height x 3 fall types) repeated measures ANOVA was used to analyze the mean differences in the peak left and right hand forces separately. Lastly, to determine if significant mean hip angle differences existed, a 2 x 2 x 3 (2 phase (pre-impact vs. impact) x 2 fall height x 3 fall types) repeated measures ANOVA was conducted. Lastly a 2 x 3 (2 fall height x 3 fall type) repeated measures ANOVA was used to determine if significant differences existed in peak hip angular velocity and the

hip angular velocity at impact. The mean values across each of the three respective trials were used in all of the ANOVAs, alpha was set at 0.05, and post-hoc testing was conducted with Tukey's HSD.

To assess the repeatability of this method, two different Intra-class Correlation Coefficient (ICC) analyses were performed on the velocity data. The first was concerned with the reliability across the three trials (two-way random for absolute agreement, single measures (ICC 2, 1)) and the second analysed the reliability between the fall types (two-way random for absolute agreement, average measures (ICC 2, k)) (Shrout & Fleiss, 1979). The repeatability of the hand force measurements between the three trials of each fall type were also determined for the left and right hands separately (two-way random for absolute agreement, single measures (ICC, 2,1)) (Shrout & Fleiss, 1979). The repeatability of the hip angle was assessed separately for each phase, and fall type (two-way random for absolute agreement, single measures (ICC, 2,1)) (Shrout & Fleiss, 1979). ICCs for all force, velocity and angle variables were calculated independently for the 0.05 m and 0.10 m falls and the following ICC intervals where used to define the magnitude of reliability (Fleiss et al., 2003): ICC<0.4 = poor; 0.4>ICC<0.59 = fair; 0.60>ICC<0.74 = good; ICC>0.74 = excellent. Finally, the minimal differences for the error to be real were calculated according to Weir (2005).

3.1.3 Results

Overall, PULARIS was capable of attaining an overall mean (SD) horizontal velocity of 1.00 (0.10) m/s (0.73 m/s - 1.1 m/s), resulting in mean (SD) maximum horizontal and vertical hip velocities of 1.2 (0.30) m/s and 1.9 (0.4) m/s, respectively. Although small (0.24 m/s), a significant difference existed between the mean horizontal

PULARIS velocity and the peak horizontal hip velocity ($p < 0.001$). At impact males were found to have a significantly lower horizontal hip velocity component (0.78 m/s vs. 0.96 m/s) but a greater vertical hip velocity component (1.8 m/s vs. 1.1 m/s) compared to females. The height or type of fall did not significantly affect any of the velocity measurements (Table 3.1). The overall mean (SD) peak angular hip velocity and angular velocity at impact were found to be 3.0 (0.55) rad/s and 2.1 (0.48) rad/s and both were significantly affected by fall height (Table 3.1).

Overall, the angle of the hip changed significantly ($p < 0.001$) from a relatively neutral position (0.89 (3.2) $^\circ$) pre-impact to an extended posture (-10.3 (1.5) $^\circ$) at the time of impact (Table 3.2). However, the hip angle was not affected by either the fall height, type of fall or sex.

The height of the fall significantly affected the right Fz impact forces ($p=0.02$) such that the force increased from 325.7 (29.0) N at 0.05 m to 379.1 (20.8) N during the 0.10 m falls (Table 3.3). A significant fall height by fall type interaction was found for the left Fz impact forces whereby they increased by 100.4 N from the 0.05 m falls to the 0.10 m falls during the straight-arm conditions (Table 3.3). The left and right Fx impact forces increased significantly by more than 10 N when the height of the fall was increased from 0.05 m to 0.10 m (Table 3.3). Finally, males experienced significantly greater Fx (54.4 N vs. 33.4 N) and Fy (170.4 N vs. 113.5 N) impact forces for both the left and right hands compared to females.

Good to excellent reliability was found for 83 % of the PULARIS and peak horizontal and vertical hip velocities at both the 0.05 m and 0.10 m heights across fall

Table 3.1: PULARIS and Hip Velocities
Summary of the mean (SD) PULARIS and hip velocities (m/s), Intra-class Correlation Coefficients (ICCs) and the between trial differences (m/s) at the 0.05 m and 0.10 m heights. The minimal differences for the error to be real (MD) are shown in the brackets next to the mean trial differences.

| Velocities | 0.05 m Height | | | 0.10 m Height | | |
	Mean (SD)	ICC	Mean Trial Difference (MD)	Mean (SD)	ICC	Mean Trial Difference (MD)
PULARIS						
Across Fall Type	1.0 (0.2)	0.76	0.01 (0.18)	1.0 (0.16)	0.98	0.002 (0.03)
Between Trials	1.0 (0.1)	0.70	0.01 (0.13)	1.0 (0.01)	0.73	0.003 (0.09)
Peak Horizontal Hip[a]						
Across Fall Type	1.2 (0.7)	0.52	0.02 (0.85)	1.2 (0.19)	0.66	0.04 (1.8)
Between Trials	1.2 (0.03)	0.60	0.03 (0.97)	1.6 (0.70)	0.71	0.03 (1.2)
Peak Vertical Hip						
Across Fall Type	1.6 (0.46)	0.97	0.09 (1.7)	1.7 (0.48)	0.98	0.02 (1.4)
Between Trials	1.9 (0.06)	0.83	0.06 (2.3)	1.9 (0.05)	0.61	0.11 (4.1)
Horizontal Hip at Impact[a,b]						
Between Trials	0.76 (0.03)	0.76	0.08 (1.8)	0.79 (0.06)	0.64	0.08 (2.8)
Vertical Hip at Impact[b]						
Between Trials	1.3 (0.12)	0.60	0.07 (3.5)	1.5 (0.20)	0.77	0.13 (4.6)
Angular Velocity						
Peak[c]	2.8 (0.51)	0.92	0.08 (2.1)	3.1 (0.65)	0.90	0.03 (2.6)
At Impact[c]	1.9 (0.32)	0.73	0.07 (2.7)	2.3 (0.13)	0.93	0.08 (2.4)

[a] Significant difference from the overall PULARIS velocity (p<0.05).

Table 3.2: Hip Angles
Summary of the mean (SD) hip angles (degrees), Intra-class Correlation Coefficients (ICCs) and the between trial differences (degrees) at the 0.05 m and 0.10 m heights and between the pre-impact and impact phases. Positive and negative angles represent hip flexion and extension, respectively. The minimal differences for the error to be real (MD) are shown in the brackets next the mean trial differences.

	0.05 m Height			0.10 m Height		
	Mean (SD)	ICC	Mean Trial Difference (MD)	Mean (SD)	ICC	Mean Trial Difference (MD)
Pre-Impact[a]	0.15 (3.2)			1.6 (3.0)		
Straight-arm	-2.9 (1.9)	0.83	2.3 (64.5)	2.4 (1.9)	0.92	2.4 (56.2)
Self-selected	-0.11 (31.6)	0.90	2.1 (53.6)	4.2 (3.2)	0.74	4.1 (88.6)
Bent-arm	3.5 (1.7)	0.92	2.2 (69.3)	-1.7 (3.1)	0.88	0.99 (45.1)
Impact	-9.6 (1.7)			-10.9 (1.04)		
Straight-arm	-11.0 (2.7)	0.74	3.3 (82.4)	-10.8 (3.1)	0.87	4.1 (72.7)
Self-selected	-10.4 (0.82)	0.91	1.1 (220.2)	-9.9 (2.6)	0.84	3.3 (74.2)
Bent-arm	-7.7 (2.4)	0.91	3.0 (65.6)	-12.0 (0.54)	0.90	0.71 (49.7)

[a] Significant difference in hip angles between the pre-impact and impact phases.

Table 3.3: Force Reliability
Summary of the mean (SD) left and right hand impact forces (N), Intra-class
Correlation Coefficients (ICCs) and between trial differences. The minimal differences
for the error to be real (MD) are shown in the brackets next the mean trial differences.

	0.05 m Height			0.10 m Height		
	Mean (SD)	ICC	Mean Trial Difference (MD)	Mean (SD)	ICC	Mean Trial Difference (MD)
Overall						
Right						
Fx	39.4 (12.5)[a,b]	0.66	2.8 (137.7)	50.4 (8.5)[b]	0.64	8.4 (122.5)
Fy	138.8 (21.1)[b]	0.82	5.3 (217.1)	137.6 (24.1)[b]	0.65	6.7 (268.2)
Fz	325.7 (29.0)[a]	0.68	1.4 (768.3)	379.1 (20.8)	0.64	18.6 (526.0)
Left						
Fx	39.2 (13.2)[a,b]	0.81	5.2 (115.6)	50.8 (11.5)[b]	0.66	4.5 (139.0
Fy	145.8 (21.4)[b]	0.71	8.4 (282.9)	145.6 (9.6)[b]	0.69	7.8 (289.3)
Fz	323.9 (27.7)	0.70	33.6 (783.7)	383.7 (25.4)	0.70	23.6 (636.1)
Straight-Arm						
Right						
Fx	39.7 (1.7)	0.67	2.2 (122.0)	55.1 (4.3)	0.72	5.8 (126.2)
Fy	148.1 (40.4)	0.89	2.8 (183.3)	165.0 (69.5)	0.76	6.7 (222.2)
Fz	327.8 (27.2)	0.57	31.6 (950.6)	404.1 (15.5)	0.40	20.6 (442.6)
Left						
Fx	36.0 (5.8)	0.81	7.8 (103.2)	54.0 (1.8)	0.68	2.4 (119.6)
Fy	158.2 (53.3)	0.72	7.3 (324.6)	173.6 (50.3)	0.81	11.9 (357.7)
Fz	312.6 (20.8)	0.73	25.1 (710.1)	413.0 (3.6)	0.76	4.8 (501.4)
Self-Selected						
Right						
Fx	37.8 (0.6)	0.55	0.71 (130.6)	41.9 (11.2)	0.52	13.5 (88.0)
Fy	140.2 (41.5)	0.74	3.4 (255.7)	119.8 (26.8)	0.53	4.6 (300.1)
Fz	314.8 (15.2)	0.80	19.5 (637.1)	380.8 (22.6)	0.84	26.9 (535.4)
Left						
Fx	38.2 (4.0)	0.82	4.5 (101.6)	47.6 (5.1)	0.40	6.6 (146.4)
Fy	145.1 (49.1)	0.75	11.4 (297.8)	131.4 (27.5)	0.52	6.5 (252.2)
Fz	331.4 (36.6)	0.72	45.1 (848.9)	376.5 (23.4)	0.70	27.1 (710.8)
Bent- Arm						
Right						
Fx	41.8 (4.3)	0.75	5.5 (146.0)	47.9 (4.9)	0.68	6.1 (153.3)
Fy	128.0 (29.8)	0.85	9.6 (212.2)	128.1 (43.9)	0.66	8.8 (282.2)
Fz	334.6 (18.9)	0.67	24.6 (717.2)	362.2 (6.5)	0.68	8.4 (599.9)
Left						
Fx	41.6 (2.7)	0.80	3.4 (141.3)	53.8 (3.4)	0.88	4.4 (151.0)
Fy	134.1 (32.5)	0.67	6.6 (226.4)	131.8 (33.9)	0.75	4.9 (258.2)
Fz	323.7 (23.0)	0.66	30.6 (791.9)	372.8 (30.0)	0.65	39.0 (696.2)

[a]Significant difference between fall heights (p<0.05).
[b]Significant sex effect (males are greater than females at p<0.05).

types (ICCs = 0.52 - 0.98). Good to excellent reliability was also found for all of the

between trial velocities (ICCs = 0.60 - 0.83) (Table 3.1).

Furthermore, all hip angular velocity variables showed good to excellent

reliability with ICCs that ranged from 0.73 - 0.93. Finally, the mean between trial

differences in velocity were relatively small, ranging from 0.002 m/s to 0.13 m/s, and

were all smaller than the minimal differences for the error to be real.

The ICCs for between trial hip angles were all classified as good to excellent

(ICCs = 0.74 - 0.92) across all fall heights, types and phases (Table 3.2). Furthermore,

the mean between trial differences in hip angles were small (0.71^{o} - 4.1^{o}) and were all

less than the minimal differences for the error to be real (Table 3.2).

Good to excellent reliability was achieved in 80 % of the hand force variables

with 14 exceeding 0.75 (Table 3.3). Overall, the self-selected falls exhibited the lowest

ICCs with approximately 42 % falling below the good to excellent reliability cut-off of

0.6 (Table 3.3). Similar to the velocities, and hip angles, the between trial differences in

hand forces were all relatively small with a range between 0.71 N (0.05 m height, right

hand Fx, self-selected trials) and 45.1 N (0.05 m height, left hand Fz, self-selected

trials) and fell below the minimal differences for the error to be real (Table 3.3).

3.1.4 Discussion

Previous laboratory studies interested in fall-related impacts have generally

restricted motion of simulated falls to one primary direction (horizontal or vertical),

have started falls from stationary positions, or have not evaluated these types of falls

with participants in fully extended hip, and lower and upper extremity postures. The

PULARIS system described here is a novel fall simulation method which addresses the

limitations of previous methods by providing a significant horizontal and vertical velocity component during the free fall portion of the fall, prior to impact. Participant movement and body postures consistent with forward falls before impact (determined from previous laboratory studies (Troy & Grabiner, 2007)) can also be more closely matched using PULARIS, compared to other impact simulation methods.

The peak vertical hip velocities reported in this study are approximately 25 % - 50 % less than those reported previously for falls from standing height (van den Kroonberg et al., 1996; Hsiao & Robinovitch, 1998; Wu, 2000; Bourke et al., 2008), but correspond well with those that have been recorded from kneeling (Weerdesteyn et al., 2008). Wu (2000) presented both the vertical (2.5 m/s) and horizontal (2.0 m/s) components of hip velocity associated with standing height falls. Although these falls resulted in greater peak velocity magnitudes than those measured in the current study, the ratio of horizontal to vertical velocities reported here (~ 0.75) agree well those from Wu (2002) (~ 0.80). Furthermore, while the peak angular hip velocities during a forward fall reported by Bourke & Lyons (2008) are approximately three times greater than those reported here; their falls occurred from a stationary standing height. When adjusting for the location of the hip above the impact surface during standing (~ 1.0 m, Bourke & Lyons (2008); ~ 0.4 m current study), the hip angular velocities agree relatively well. Finally, although they measured the hip angular velocity during fall catch trials, the hip angular velocity reported by Grabiner et al. (1996), are similar to those reported here.

Vertical and horizontal hip velocities at impact showed the lowest ICCs and the greatest error, both between trials and fall types. This most likely occurred as a result of

defining impact as the point at which the hands contacted the force platforms as opposed to when the hip impacted the ground. The difficulty in visually identifying hand contact in a single frame (Pain et al., 2005) has been linked to errors in the resulting kinematic measurements. Improving the ability to detect the instant at which the hand contacts the force platform may be achieved through further video processing methods (Li et al., 2008) or by increasing the frame rate of video collection (Li et al., 2008; Davis et al., 2009; Salisbury et al., 2010). Small differences in velocities between trials could also be a function of errors in the positioning of the participants when determining the release and start points. Finally, the PULARIS velocity was found to be significantly less than the peak horizontal hip velocity by approximately 0.21 m/s. For this study, the movement of PULARIS was programmed to reach a maximum velocity prior to the quick releases being activated, at which point it quickly decelerated and stopped. However, following quick release, the participant would have continued to accelerate until the moment the hands came into contact with the force platform, resulting in a greater peak velocity compared with PULARIS.

The pre-impact hip flexion angles reported here are approximately 75 % less than the forward fall hip flexion angles reported by Grabiner et al. (1996) and Pavol et al. (2001). However, as a result of recovering from the trip or being caught by a safety harness, the participants in these studies did not fully transition into the flight phase characteristic of a forward fall. Had the participants been allowed to complete the fall, it is likely that the torso would have begun to extend about the hip, resulting in hip angle values more agreeable with those presented here. This is seen, briefly, in the data presented by Grabiner et al. (1996), where the angle about the hip begins to show a

pattern of extension just prior to the end of the trial, when recovery occurs. Despite differences in the pre-impact hip angles reported here compared to previous work, they were found to be very repeatable and unaffected by changes in the upper extremity posture. Furthermore, with simple adjustments to the ratio of the leg straps to the torso straps, and with the timing of the quick releases (front vs. back), it would be possible to test the effects of different hip postures and landing scenarios (e.g., knee first impacts) on the kinematics and kinetics of the upper extremity using PULARIS.

The mean overall Fz impact forces from the right and left hands (~352.7 N) in this study were less than the average of those reported previously (~600 N) (Chiu & Robinovitch, 1998; Robinovitch & Chiu, 1998; Troy & Grabiner, 2007; DeGoede & Ashton-Miller, 2002; Kim & Ashton-Miller, 2003; Lo et al., 2003; Chou et al., 2009; Burkhart & Andrews, 2010a, 2010b). As discussed earlier, the majority of past methods for simulating impacts from forward falls have primarily restricted the fall to a single direction of motion and the impact forces have been directed mainly parallel to the long axis of the upper extremity. However, as a result of the forward and sometimes sideways motion that individuals might experience during a forward fall, it is highly likely that sizable upper extremity forces in the medial-lateral and anterior-posterior directions would also occur. The motion of the body achieved by being able to apply velocities in the horizontal and vertical directions with PULARIS did in fact result in medial-lateral and anterior-posterior impact force components, and would explain the smaller vertical forces in this study compared to previous work. These results, combined with the velocity data, suggest that PULARIS is capable of simulating the multi-directional non-stationary movement of the start and flight phases of an actual

forward fall. However, it should be noted that during the 0.05 cm falls, the hands may have impacted the force platform a few milliseconds prior to the legs being released (as determined via projectile motion calculations). This could not be confirmed visually because of the relatively low sampling rate of the video. Therefore, at the instant of impact, the hands may have counteracted the momentum of the body and PULARIS for a very short time. While this would not have affected the reliability analysis, it may account for the lack of significant differences in the Fy hand forces between the 0.05 m and 0.1 m falls. Regardless, the timing between torso and leg release can be easily adjusted with the current system in order to establish a true flight phase, without having to increase the participant drop height.

Although a significant height effect was found for the right Fz impact forces, the mean overall vertical impact forces increased by only 16 %, despite a twofold increase in hand height. This may partly be explained by the relative closeness of the hands to the force platforms during the 0.05 m falls. Slight adjustments of the hand towards the top surface of the force platforms as participants approach the release point, could result in lower than expected impact forces. The lowest ICCs and greatest errors occurred mainly during the self-selected falls, and although small, these errors are most likely a result of the participants selecting inconsistent fall strategies between trials.

While the majority of the force and velocity ICCs suggested good to excellent reliability, there were five ICCs that exhibited poor reliability that warrant further explanation. The ICC statistic is highly dependent on the version of the ICC that is used and the heterogeneity of the sample (Weir, 2005). Therefore, it is important to consider the standard error of the measurement (SEM), reflected here as the minimal difference

needed for the errors to be considered real (i.e. the MD), when interpreting both the high and low ICCs (Weir, 2005). The mean between trial differences were all relatively small and less than the calculated minimal differences for the error to be real, suggesting that the differences reported here are all within an acceptable range of error and not a result of the different trials themselves (van den Kroonberg et al., 1996; Weir, 2005). Despite the low ICCs in these few cases, PULARIS is capable of replicating horizontal and vertical velocities that result in repeatable three-dimensional hand forces from trial to trial.

Overall, the results presented here suggest that this novel method is an appropriate approach to studying the response of the distal upper extremity to impact loading during non-stationary, multi-directional movements indicative of a forward fall. The consistent velocities of the system itself resulted in participant hip velocities in both the horizontal and vertical directions and impact forces in both hands that had fairly good reliability overall. This system performed well at different fall heights, and is designed with flexibility of testing in mind. By modifying the timing of the trunk and leg quick releases and by adjusting the relative lengths of straps supporting the trunk and legs, PULARIS allows for a variety of upper and lower extremity, and hip postures to be tested that are consistent with different elderly and sport-related fall scenarios.

3.1.5 References

Berg WP, Alessio HM, Mills EM, Ton, C. 1997. Circumstances and consequences of falls in independent community-dwelling older adults. Age and Ageing. 26, 261-268.

Bourke AK, O'Donovan KJ, O'Laigh G, 2008. The identification of vertical velocity profiles using an inertial sensor to investigate pre-impact detection of falls. Medical Engineering and Physics. 30, 937-946.

Burkhart TA, Andrew, DM. 2010a. The effectiveness of wrist guards for reducing wrist and elbow accelerations resulting from simulated forward falls. Journal of Applied Biomechanics. 26, 281-289.

Burkhart TA, Andrews DM. 2010b. Activation level of extensor carpi ulnaris affects wrist and elbow acceleration responses following simulated forward falls. Journal of Electromyography and Kinesiology. 20, 1203-1210.

Burkhart TA, Dunning CE, Andrews DM. 2011. Determining the optimal system-specific cut-off frequencies for filtering *in vitro* upper extremity impact force and acceleration data by residual analysis. Journal of Biomechanics. 44, 2728-2731.

Chiu J, Robinovitch SN, 1998. Prediction of upper extremity impact forces during falls on the outstretched hand. Journal of Biomechanics. 31, 1169-1176.

Chou P-H, Lo, S-Z, Chen H-C, Chiu C-F, Chou Y-L, 2009. Effects of forearm axially rotated postures on elbow load and elbow flexion angle in one one-armed arrest of a forward fall. Clinical Biomechanics. 24, 632-636.

Davis JT, Limpisvasti O, Fluhme D, Mohr KJ, Yocum LA, ElAttrache NS, Jobe FW. 2009. The effect of pitching biomechanics on the upper extremity in youth adolescent baseball pitchers. The American Journal of Sports Medicine. 37, 1484-1491.

DeGoede KM, Ashton-Miller JA, Schultz AB, Alexander NB, 2002. Biomechanical factors affecting the peak hand reaction force during the bimanual arrest of a moving mass. Journal of Biomechanical Engineering. 24, 107-112.

DeGoede KM, Ashton-Mille, JA, 2002. Fall arrest strategy affects peak hand impact force in a forward fall. Journal of Biomechanics. 35, 843-848.

Fardellone P, 2008. Predicting the fracture risk in 2008. Joint Bone Spine. 75, 661-664.
Fleiss JL, Levin B, Paik MC, 2003, Statistical methods for rates and proportions, New York, NY (pp. 604-605): John Wiley & Sons.

Grabiner MD, Donovan S, Bareither ML, Marone JR, Hamstra-Wright K, Gatts S, Troy KL, 2008. Trunk kinematics and fall risk of older adults: translating biomechanical results to the clinic. Journal of Electromyography and Kinesiology. 18, 197-204.

Grabiner MD, Feuerbac JW, Jahingen DW. 1996. Measures of paraspinal muscle performance do not predict initial trunk kinematics after tripping. Journal of Biomechanics. 29, 735-744.

Hsiao ET, Robinovitch SN, 1998. Common protective movements govern unexpected falls from standing height. Journal of Biomechanics. 31, 1-9.

Kakarlapudi TK, Santini A, Shahane SA, Douglas D, 2000. The cost of treatment of distal radius fractures. Injury. 31, 229-232.

Kim K-J, Ashton-Miller JA, 2003. Biomechanics of fall arrest using the upper extremity: age differences. Clinical Biomechanics. 18, 311-318.

Lawson GM, Hajducka C, McQueen MM. 1995. Sports Fractures of the Distal Radius-Epidemiology and Outcome. Injury. 26, 33-36.

Li Y, Ai H, Yamashita T, Lao S, Kawade M, 2008. Tracking in low frame rate video: a cascade particle filter with discriminative observers of difference life spans.   IEEE Transactions on Pattern Analysis and Machine Intelligence. 30, 1728-1735.

Lo J, McCabe GN, DeGoede KM, Okuizumi H, Ashton-Miller JA, 2003. On reducing hand impact force in forward falls: results of a brief intervention in young males. Clinical Biomechanics. 18, 730-736.

National Academy on an Aging Society. 2003. State of aging and health in America, Retrieved from http://www.agingsociety.org/agingsociety/pdf/state_of_aging_report.pdf.

Pain MTG, Mills C, Yeadon MR. 2005. Video analysis of the deformation and effective mass of gymnastic landing mats. Medicine and Science in Sport and Exercise. 37, 1754-1760.

Pavol MJ, Owings TM, Foley KT, Grabiner MD, 2001. Mechanisms leading to a fall from an induced trip in healthy older adults. Journal of Gerontology, 56A, M428-M437.

Robinovitch SN, Chiu J, 1998. Surface stiffness affects impact force during a fall on the outstretched hand. Journal of Orthopaedic Research. 16, 309-313.

Schieber RA, Branche-Dorsey CM, Ryan GW. 1994. Comparison of In-line Skating Injuries with Roller-skating and Skateboarding Injuries. Journal of the American Medical Association. 271, 1856-1858.

Shrout PE, Fleiss JL. 1979. Intraclass correlations: uses in assessing rater reliability. Psychological Bulletins. 2, 420-428.

Salisbury SM, Martin GG, Kier WM, Schulz JR, 2010. Venom kinematics during prey capture in conus: the biomechanics of a rapid injection system. Journal of Experimental Biology. 213, 673-682.

Statistics Canada. 2011. Activity limiting injuries, Retrieved From Http://Www.Statcan.Gc.Ca/Pub/82-221-X/2011002/Tblstructure/1hs/1hc/Hc1ixx-Eng.Htm.

Troy KL, Grabiner MD, 2007. Asymmetrical ground reaction impact of the hands after a trip-induced fall: experimental kinematics and kinetics, Clinical Biomechanics, 2, 1088-1095.

United States Consumer Product Safety Commission. 2011. National Electronic Injury Surveillance System On-Line Data Base, Retrieved from https://www.cpsc.gov/ cgibin/NEISSQuery/home.aspx.

van den Kroonberg AJ, Hayes WC, McMahon TA. 1996. Hip impact velocities and body configurations for voluntary falls from standing height. Journal of Biomechanics. 29, 807-811.

Weerdesteyn V, Groen BE, van Swingchem R, Duysens J. 2008. Martial arts falls reduce hip impact forces in naive subjects after a brief period of training. Journal of Electromyography and Kinesiology. 18, 235-242.

Weir JP, 2005. Quantifying test-retest reliability using the intraclass correlation coefficient and the SEM. Journal of Strength and Conditioning Research. 19, 231-240.

 Wu G. 2000. Distinguishing fall activities from normal activities by velocity characteristics. Journal of Biomechanics. 33, 1497-1500.

3.2 Kinematics, Kinetics and Muscle Activation Patterns of the Upper Extremity During Simulated Forward Falls.

3.2.1 Introduction

During a forward fall, the distal upper extremity is often used to arrest the body's forward momentum (Troy & Grabiner, 2007). This impact initiates a shock wave that travels through the tissues, such as bone, fat, muscle, tendons and ligaments, moving away from the initial area of impact (Light et al., 1980; Wosk & Voloshin, 1981; Chu et al., 1986). The soft tissues, collectively regarded as wobbling mass (Gruber et al., 1998), are responsible for the passive and active attenuation of the shock wave. Authors agree that muscle is the most important force attenuating structure given its ability to passively deform, thereby absorbing the impact energy, while simultaneously possessing the ability to actively adjust the amount of shock attenuation through eccentric contractions about the joints (Elftman 1939; Derrick et al., 1998; Pain & Challis, 2001). An example of the passive attenuating capabilities of muscle was presented by Schinkel et al. (2011) who, while controlling for muscle activation, found a significant negative relationship between the amounts of shank soft tissue, specifically muscle, and the tibial acceleration response.

Changes in muscle activation, potentially leading to a change in muscular stiffness, play a key role in the attenuation of force and the dissipation of energy within and between body segments. Santello (2005) highlights the importance of the proper modulation of muscle forces to ensure optimal control of joint angles during impact. Also, it is hypothesized that the muscles undergo a preparatory level of muscle activation in an attempt to adequately respond to unknown forces and force durations

that are common among accidental falls (Dietz et al., 1981; Santello, 2005). When a muscle's level of activation is increased, it is representative of the increase in the tension generated in the muscle tissue itself. It is this tension increase that is responsible for the subsequent changes in structural stiffness (Nigg & Liu, 1999), and numerous researchers have supported this claim as it relates to the lower extremity (Nigg & Liu, 1999; Flynn, et al., 2004; Holmes & Andrews, 2006). With respect to the upper extremity, Burkhart & Andrews (2010a) found that, as muscle activation was increased in the extensor carpi ulnaris (ECU) from 12 % maximal voluntary contraction (MVC) to 48 % MVC, the acceleration responses at the wrist and elbow were also increased, agreeing well with results of previous lower extremity studies. Burkhart & Andrews (2010a) also found that the muscle activation of the flexor carpi ulnaris (FCU), a primary antagonist of the ECU, increased in proportion to the ECU. Furthermore, Dietz et al. (1981) were able to show that pre-impact preparatory muscle activation was present in the triceps brachii, such that the level of muscle activation began to increase approximately 30 ms prior to impact and peaked after the occurrence of the peak force.

Finally, it has also been suggested that changes in upper extremity joint angles can have an effect on the forces that result from impacts (DeGoede & Ashton-Miller, 2002; DeGoede et al., 2002; DeGoede & Ashton-Miller, 2003; Chou et al., 2009; Burkhart & Andrews 2010b; Hsu et al., 2011). For example, DeGoede & Ashton-Miller (2002) and DeGoede et al. (2002) found that the impact forces were significantly less during impacts that occurred when participants were instructed to land as safely as possible, compared to falls that occurred with straight-arms. Chou et al. (2009) and Hsu

et al. (2011) also found that medial-lateral impact forces and elbow and shoulder loads were significantly greater when the arm was externally rotated. Conversely, Burkhart & Andrews (2010b) reported that elbow flexion angle at impact did not lower the impact effect at the wrist or elbow.

While the above investigations have been useful in providing insight into the effects of joint kinematics and muscle activation on the impact and joint loads, these studies have generally been limited by the fall simulation methods utilized. In the past, simulated falls have been limited to a single direction of motion and have generally been anticipated falls (i.e. mainly horizontal or vertical and participants were aware of when the fall would occur). Furthermore, while DeGeoede & Ashton-Miller (2002) provided information regarding both joint angles and muscle activation, they did so only for the triceps brachii and biceps brachii and only reported muscle activation levels for the 50 ms prior to impact. In the previous section (Section 3.2), a novel Propelled Upper Limb fall ARest Impact System (PULARIS) was presented that accurately and reliably simulates forwards falls. The PULARIS system applies multi-directional motion to participants and allows for un-anticipated falls to be simulated, addressing the limitations of past fall methods.

Therefore, the purpose of this study was to explore the effects of different fall types and fall heights on the kinematics, kinetics, and muscle activation of the upper extremity using a fall simulation method that more accurately represents the multi-directional motion of an actual forward fall using the PULARIS fall simulation method.

3.2.2 Methods

3.2.2.1 Participants

A novel Propelled Upper Limb fall ARrest Impact System (PULARIS) (Section 3.2) was used to simulate the impact phase of a forward fall on twenty (10 male; 10 female) participants (mean (SD) age: 23.6 (3.0) years; height: 1.72 (0.11) m; body mass: 68.6 (15.2) kg; BMI: 23.0 (3.5) kg/m^2) with no history of upper extremity trauma. All participants provided written informed consent prior to testing and all procedures were approved by the University of Windsor's Research Ethics Board (Appendix K).

3.2.2.2 Instrumentation

The PULARIS system was used to propel the participants towards two strain gauge based force platforms (Advanced Mechanical Technology Inc. Watertown MA, model # OR6-7; 2200N capacity; natural frequency of 1kHz) rigidly mounted to the laboratory floor; forces were collected along the three force axes: Fx: medio-lateral; Fy: anterior-posterior; Fz: inferior-superior (Figure 3.8). Two tri-axial accelerometers (MMA1213D and MMA3201D, Freescale Semiconductor, Inc, Ottawa ON, Canada; range of +/- 50 G and +/- 40 G, respectively) were firmly attached to the skin using double sided tape and a normal pre-load of approximately 45 N, which was applied using an elastic Velcro™ strap, to measure the response of the distal and proximal forearm. The distal accelerometer was attached to the posterior surface of the forearm just medial to the radial styloid, while the proximal accelerometer was attached to the olecranon process of the ulna (Burkhart et al., 2010a, 2010b) (Figure 3.5). A residual analysis was performed for all force and acceleration signals to determine the optimal filter cut-off frequencies (Burkhart et al., 2011) (Table 3.4).
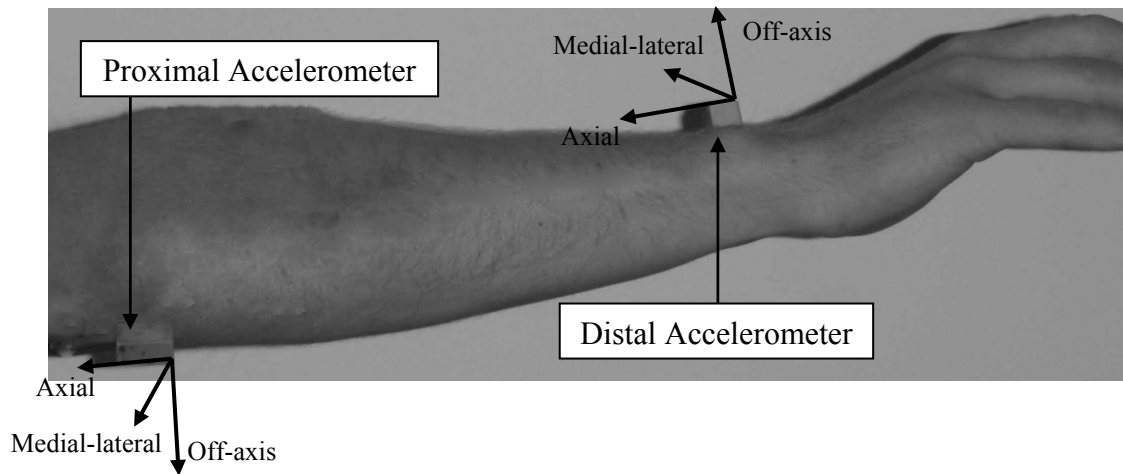
Figure 3.5: Experimental Accelerometer Placement
Location of the distal and proximal accelerometers and the corresponding accelerometer axes. The Velcro® straps used to preload the accelerometers are not shown here.

Table 3.4: *In vivo* Filter Cut-off Frequencies
Results of the residual analysis (mean (SD); n=5) to
determine the optimal filter cut-off frequencies for the
right and left hand impact forces and proximal and distal
forearm accelerations. The cut-off frequencies from the
residual analysis were rounded to the nearest 5 Hz to
determine the actual values used.

Variable	Calculated From Residual Analysis (Hz)	Actual Value Used (Hz)
Fx Right	64.3 (3.5)	65
Fy Right	82.3 (2.7)	80
Fz Right	76.8 (4.0)	80
Fx Left	61.2 (4.4)	60
Fy Left	76.4 (1.8)	80
Fz Left	89.3 (2.4)	90
Distal Axial	66.9 (5.7)	70
Distal Medial-lateral	74.0 (1.8)	75
Distal Off-axis	83.8 (2.3)	85
Proximal Axial	86.2 (2.0)	90
Proximal Medial-lateral	82.4 (2.0)	80
Proximal Off-axis	75.1 (6.0)	75

All force and acceleration signals were filtered with a 2nd order, dual pass Butterworth filter at the respective cut-off frequencies.

Muscle activation levels were collected from six muscles of the upper extremity including: Biceps Brachii (BB), Brachioradialis (BR), Triceps Brachii (lateral head) (TrLa), Anconeus (AN), Extensor Carpi Ulnaris (ECU), and Flexor Carpi Ulnaris (FCU). Six pairs of Kendall Ag/Ag-Cl rectangular (23 mm x 33 mm) surface electrodes (Tyco Healthcare Group LP, Mansfield MA; ES40076-H59P) were placed over the muscle bellies of each respective muscle in the direction of their lines of actions (2 cm inter-electrode distance) (Figure 3.6). The skin underlying the electrodes was shaved, when necessary, and cleaned with 70 % isopropyl alcohol. The EMG signals were differentially amplified (± 2.5V; AMT-8 Bortec Calgary Canada; Bandwidth 10 Hz-1000 Hz, CMRR =115 dB at 60 Hz, input impedance =10 GΩ), full wave rectified and filtered with a dual pass 2nd order Butterworth filter (cut-off frequency of 2.5 Hz) and normalized to the participants' maximal voluntary contractions (see Section 3.2.2.3 below).

The six muscles that were used for this study were selected based on the results of pilot work where data from an initial eleven muscles were analysed. Briefly, a cross-correlation analysis was used to compare the signals of the initial eleven muscles to determine the magnitude of shared signal between muscles with similar functions (Table 3.5). The cross-correlation analysis produced the cross-correlation coefficient (Rxy), the cross correlation coefficient squared (Rxy^2, representing the proportion of shared signal) and the phase lag between the signals. The six muscles, from the original
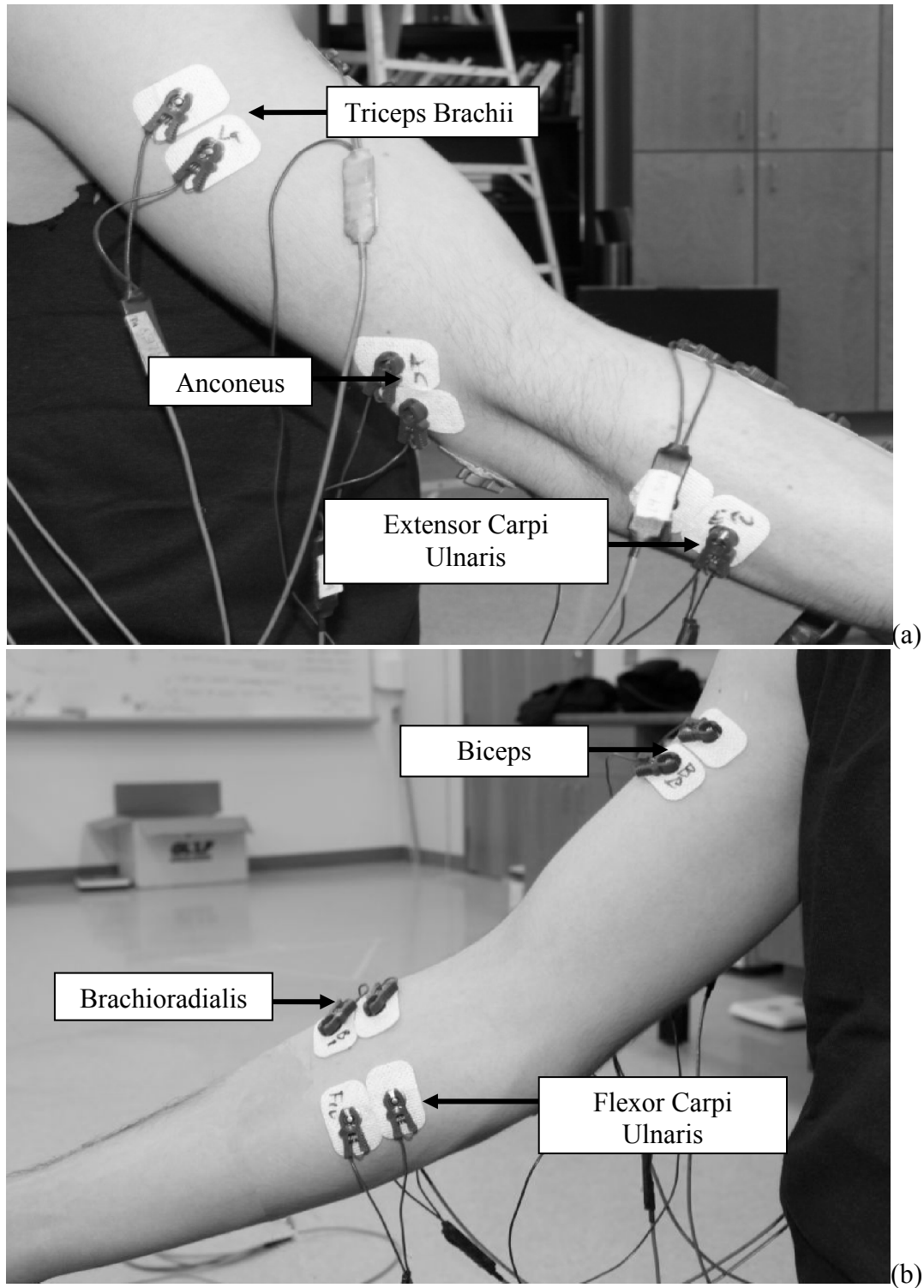
Figure 3.6: EMG Electrode Placement
Placement of the bi-polar electrodes on the dorsal (a) and volar (b) aspects of the
upper extremity.

Table 3.5: EMG Cross-Correlation Results
Mean (SD) peak cross-correlation coefficients (Rxy), phase (lag) between signals (ms) and shared common signal (Rxy^2) for each specified combination of muscles and at each drop height (N = 5). The selection of the six muscles to use for the current study (bolded below table) was based on the Rxy^2 and the phase lag.

	Overall			5 cm drop			10 cm drop		
	Rxy	Lag	Rxy^2	Rxy	Lag	Rxy^2	Rxy	Lag	Rxy^2
BBxBR	0.96	20.0	0.93	0.97	18.5	0.95	0.96	19.2	0.93
	(0.04)	(38.0)	(0.07)	(0.02)	(34.4)	(0.04)	(0.02)	(24.8)	(0.4)
TrLoxTrLa	0.94	1.0	0.89	0.89	1.0	0.83	0.95	2.7	0.90
	(0.03)	(5.0)	(0.05)	(0.13)	(15.7)	(0.2)	(0.04)	(21.4)	(0.08)
TrLoxAN	0.92	-4.0	0.85	0.90	-15.5	0.83	0.89	11.4	0.81
	(0.03)	(5.0)	(0.05)	(0.14)	(20.1)	(0.2)	(0.1)	(17.0)	(0.1)
TrLaxAN	0.95	4.0	0.92	0.96	-5.0	0.93	0.93	11.6	0.88
	(0.01)	(3.0)	(0.02)	(0.04)	(14.7)	(0.1)	(0.1)	(15.5)	(0.1)
ECUxECR	0.98	-7.0	0.97	0.97	-10.0	0.94	0.98	-9.9	0.96
	(0.01)	(4.0)	(0.02)	(0.03)	(10.0)	(0.1)	(0.02)	(20.1)	(0.05)
ECUxEDC	0.97	8.02	0.94	0.96	8.2	0.93	0.96	1.6	0.92
	(0.01)	(4.0)	(0.02)	(0.04)	(10.0)	(0.1)	(0.04)	(14.2)	(0.8)
ECRxEDC	0.94	14.0	0.88	0.91	19.8	0.84	0.92	10.1	0.86
	(0.03)	(8.6)	(0.05)	(0.09)	(19.2)	(0.2)	(0.1)	(31.0)	(0.1)
FCUxFCR	0.94	16.0	0.83	0.98	14.6	0.95	0.94	50.0	0.88
	(0.01)	(25.6)	(0.01)	(0.02)	(41.1)	(0.4)	(0.05)	(67.2)	(0.1)
FCUxFDS	0.94	34.0	0.89	0.96	24.9	0.93	0.93	62.8	0.88
	(0.01)	(17.9)	(0.02)	(0.02)	(32.7)	(0.04)	(0.05)	(73.0)	(0.08)
FCRxFDS	0.97	71.0	0.94	0.98	9.7	0.96	0.98	5.8	0.95
	(0.01)	(78.5)	(0.03)	(0.03)	(24.9)	(0.1)	(0.02)	(0.9)	(0.04)

Note: **BB**=biceps brachii; **BR**=brachioradialis; TrLo=triceps brachii (long head); **TrLa**=Triceps brachii (lateral head); **AN**=anconeus; **ECU**=extensor carpi ulnaris; ECR=extensor carpi radialis; **FCU**=flexor carpi ulnaris; FCR=flexor carpi radialis; EDC=extensor digitorum communis; FDS=flexor digitorum superficialis.

eleven, used in this study were selected based on both Rxy^2 and the phase lag. For example, 89 % of the signals from the lateral head and long head of triceps brachii were common, and the phase lag was small (approximately 5 ms). Therefore, only one of these muscles (lateral head of triceps brachii) was selected to be included in the larger study.

A three position sensor Optotrak system (Optotrak Certus, Northern Digital Inc., Waterloo ON, Canada) was used to track upper extremity motions and to calculate joint angles. Individual markers (1 cm diameter) were placed on the radial and ulnar styloid processes, the lateral and medial epicondyles and the acromion process on the right upper extremity of each participant. Three rigid four-marker cluster sets were also used to track the motion of the segments of the right upper extremity and were placed on the dorsal aspect of the hand, the distal forearm, and the arm (van Andel et al., 2008) (Figure 3.7). The forearm marker cluster was placed as close to the wrist as possible as this is where the majority of pronation/supination takes place (Scmidt et al., 1999; van Andel et al, 2008). A fourth marker cluster, in the form of a fin, was placed on the torso above the C7-T1 vertebrae (Howarth & Callaghan, 2010) (Figure 3.7). While it is more common to represent the torso with a marker cluster on the sternum, the prone posture of the participants during testing did not afford this configuration. All markers were sampled at 100 Hz, and filtered with a dual pass 2nd order Butterworth filter at 6 Hz (van der Woude et al., 1989; Howarth & Callaghan, 2010). While the segment marker sets were positioned to ensure that complete data sets were completed, there were instances when a marker was lost or became obscured for a period of time. Missing data were replaced using cubic spline interpolation (Coburn & Crisco, 2005;
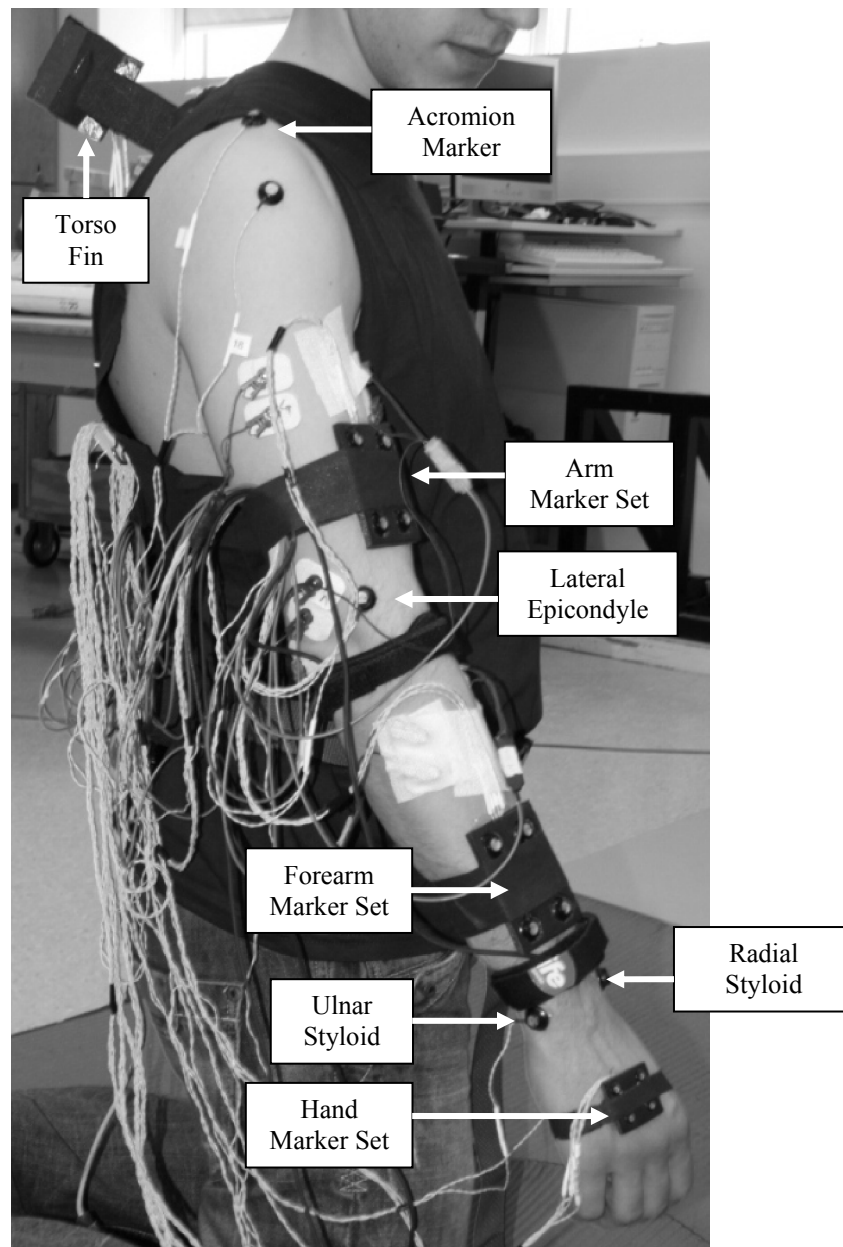
Figure 3.7: Joint and Segment Marker Placement
Location and placement of the joint markers and the
segment marker sets.

Howarth & Callaghan, 2010), where 10 points were used on either side of the missing data gap. Only the right upper extremity was instrumented due to sampling limitations.

3.2.2.3 Experimental Protocol

Following the application of instrumentation, a series of maximal voluntary contractions (MVCs) of each muscle were performed. Table 3.6 displays the method used to collect each muscle's MVC and the associated reliability (Intraclass Correlation Coefficient (ICC)). The MVC trials for each muscle were performed three times with a one minute rest between each trial to avoid muscle fatigue. The maximum EMG signal from the three trials was used to normalize the EMG signals from the experimental trials.

A static marker calibration procedure was performed to measure the locations of the joint markers with respect to the segment marker sets. The participants were positioned within the measurement volume with the arm vertical, the forearm flexed at 90° about the elbow and the wrist in the neutral position (0° flexion/extension) (Schmidt et al., 1999). Data were collected for 25 s while the participant maintained this standardized posture.

Participants lied prone on a torso sling that rested on a box (0.30 m high) with the dorsal aspect of their arms in contact with the torso sling (Figure 3.8). The PULARIS structure was lowered and the two quick releases were positioned such that the forward quick release was located approximately above the C7/T1 vertebrae and the rear quick release above the mid-calf. The straps of the torso and leg slings were hooked into the quick releases and the lengths of the straps were adjusted to achieve a

Table 3.6: MVC Postures and Methods
The postures, methods and reliability (ICC) associated with the collection of each muscle's maximal voluntary contraction (MVC). Each muscle's MVC was collected three times with a one minute rest between trials to avoid muscle fatigue.

| Muscle | MVC Collection Method | | ICC[a] |
	Posture	Action	
Biceps Brachii (BB)	Arm flexed at 90°, forearm pronated 90°	Participant flexed their forearm about the elbow against a manual resistance	0.96
Brachioradialis (BR)	Same as Biceps Brachii	Same as Biceps Brachii	0.94
Triceps Brachii (lateral head) (TrLa)	Same as Biceps Brachii	Participant extended the forearm about the elbow against a manual resistance	0.80
Anconeus (AN)	Same as Biceps Brachii	Same as Triceps Brachii	0.97
Extensor Carpi Ulnaris (ECU)	Arm flexed at 90°, Forearm fully pronated and supported by a table	Participant instructed to attempt to touch their third digit to the dorsal aspect of their forearm	0.94
Flexor Carpi Ulnaris (FCU)	Arm flexed at 90°, forearm fully pronated and supported by a table, the hand extended over the edge	Participant instructed to attempt to flex the hand about the wrist against a manual resistance	0.97

[a]A random effects for absolute agreement single measures ICC (ICC 2,1) (Shrout & Fleiss, 1979) was used.
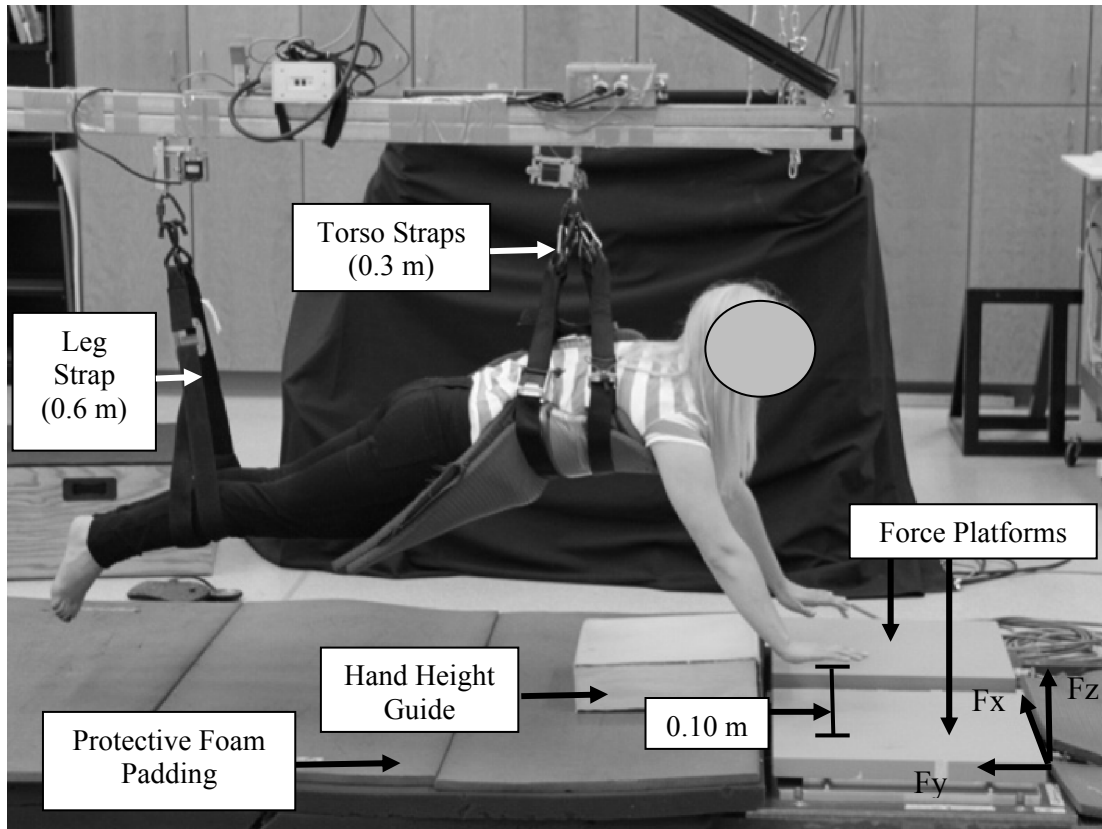
Figure 3.8: Kinematic Study Experimental Set-up
Experimental set-up for a straight arm 0.10 m fall of an un-instrumented participant just prior to release. The directions of the hand force components Fx, Fy and Fz are included for reference.

leg strap length to torso strap length ratio of 2:1 to ensure that the angle the body made with the ground was consistent between participants (Figure 3.8). Once attached to the quick releases, PULARIS was raised, the box removed and the participants were moved towards the force platforms, where the height of the hands was adjusted so that they were 0.05 m or 0.10 m above the ground, depending on the condition being tested. The left and right hands were aligned with the back edge of the respective force platform and this was set as the release point. Setting the release point at the edge of the force platforms ensured that the hands impacted the center of the platform, given the continued forward motion of the participants following release. Participants were then moved backwards to a start point (approximately 1.9 m from the force platform). Once the start point was set, PULARIS was propelled forward towards the force platforms at a velocity of approximately 1.0 m/s, and as PULARIS passed the release point, the participants were dropped (the torso quick release was set to drop 150 ms prior to the legs to ensure that the hands impacted before the legs impacted the ground), such that an impact was applied to the palm of each hand as they arrested their fall.

A 0.36 m x 0.36 m x 0.10 m piece of foam was placed in front of the force platforms for participants to use as a height guide for their hands (Figure 3.8). For example, participants were instructed to align their hands at the middle and the top of the foam block for a 0.05 m and 0.10 m high fall, respectively.

Each participant experienced three repetitions of three different fall types at impact (related to upper extremity posture: straight-arm, self-selected and bent-arm) and two different fall heights (0.05 m and 0.10 m). The straight-arm posture was included to act as a worst-case scenario fall, whereas the self-selected posture was included to

allow participants to choose the posture that they felt would minimize the impact consequences. For the bent arm falls, a 20° flexion angle about the elbow was set once participants were moved to the start point, using an analog goniometer (Lafayette Instruments Co., Inc. Lafayette IN. Model # 01135). Participants were instructed to maintain the respective upper extremity postures throughout the duration of the impact to the best of their ability (including shoulder elbow and wrist postures). Finally, "no-fall" trials were randomly included throughout the testing protocol such that the participants were set-up like a normal trial but were not dropped when they passed the release point. One no-fall trial was performed during each combination of fall height and fall type (six no-fall trials in total). The "no-fall" trials were included to prevent the participants from anticipating the drops, thereby attempting to maintain the unpredictability of actual forward fall events.

3.2.2.4 Data Analysis

Peak vertical (Fz), medio-lateral (Fx) and anterior-posterior (Fy) impact forces (Figure 3.8) were determined from the force-time curves for both the left and right hands along with the impulse, impulse duration and loading rate (measured as the slope of the line between 30 % and 70 % of the peak (Burkhart & Andrews 2010a, 2010b)). Peak accelerations (PA) and acceleration rates (AR) (also measured between 30 % and 70 % of the peak (Burkhart & Andrews, 2010a, 2010b)), were measured along all three accelerometer axes for both accelerometers (axial: parallel with the long axis of the forearm; off-axis: normal to the long axis of the forearm in the inferior-superior direction, and medio-lateral direction (Figure 3.5)).

The peak and time of peak normalized linearly enveloped EMG signals were determined for each muscle. The average EMG (AEMG) was calculated over four separate fall phases including: i) start-release: defined as the phase from the start of data collection to quick release; ii) release-impact: the phase from the time of quick release to the initiation of the Fz impulse. The impulse along the z-axis was used here as Fz was the dominant force component; iii) impact-peak: the period from the initiation of the impulse to the time of the peak Fz; and iv) peak-end: defined from the peak Fz to the cessation of the Fz impulse (Figure 3.9). While it is customary to average the EMG over a constant window (e.g., 50 ms), processing the EMG over the previously defined fall phases allows for the EMG to be averaged over windows that are more meaningful with respect to the signals of interest.

The peak velocity and the velocity at impact (in x, y, z, and resultant directions) of the wrist joint center was calculated from the ulnar and radial styloid markers as the first derivative of the position data. Carpal, forearm, radius, and humeral coordinate systems were constructed based on the relationship between the joint and segment marker systems during the static calibration trial (Schmidt et al., 1999; Winter, 2005) according to the International Society of Biomechanics (ISB) recommendations (Wu et al., 2005). Joint angles were calculated using the floating axis joint coordinate system method presented by Grood & Suntay (1983) (Table 3.7). Therefore, flexion/extension (flexion is positive) and ulnar/radial deviation (radial deviation is positive) about the wrist, flexion/extension (flexion is positive), pronation/supination (supination is positive) about the elbow, and plane of elevation (frontal plane = 0° and sagittal plane = 90°), elevation angle (flexion is positive), and rotation (internal rotation is positive)
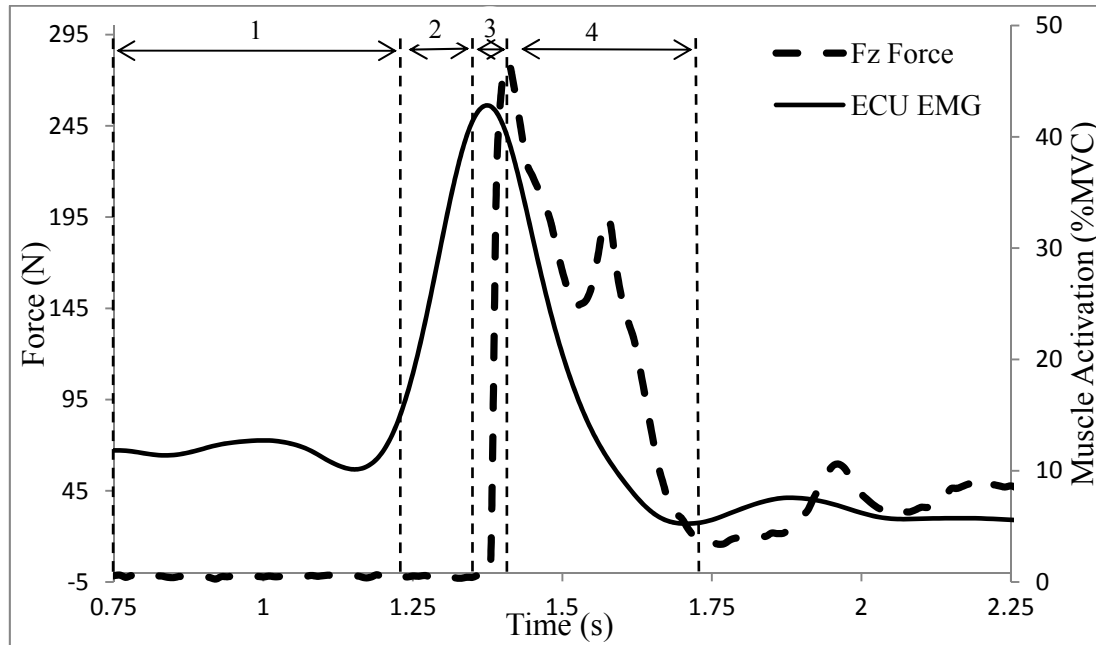
Figure 3.9: Fall Phases
Typical 0.05 m straight arm Fz force and extensor carpi ulnaris (ECU) EMG curves
showing the four impact phases: 1) start-release; 2) release-impact; 3) impact-peak 4)
peak-end. The EMG signals were averaged across the four phases for all muscles.

Table 3.7: Floating Axis Joint Coordinate Systems
Definition of the joint coordinate systems used to define the wrist, elbow and shoulder joint motion.

| Motion | Joint coordinate system axes [a,b] | | |
	Flexion/extension (e1)	Pronation/Supination (e3)	Abduction/Adduction (e2)
Hand relative to radius	Medial-lateral axis fixed to the radius	Longitudinal axis fixed to the carpals	Common axis perpendicular to e1 and e3
Forearm relative to humerus	Medial-lateral axis fixed to the humerus	Longitudinal axis fixed to the forearm	Common axis perpendicular to e1 and e3[c]
Humerus relative to torso	Longitudinal axis fixed to the torso	Longitudinal axis fixed to the humerus	Anterior-posterior axis fixed to the humerus

[a]Wu et al. (2005)
[b]Grood & Suntay (1983)
[c]Motion about this axis is referred to as the carrying angle (Anglin & Weiss, 2000). This is a passive motion that is rarely reported, and therefore, is not reported here.

about the shoulder were calculated. While pronation/supination generally describes the axial rotation of the radius with respect to the ulna, as a simplification, pronation/supination in the current study describes the rotation of the distal forearm about the longitudinal axis of the proximal (arm) segment (Schmidt et al., 1999). The joint angles were averaged over the same fall phase windows described for the EMG.

3.2.2.5 Statistics

Three-way 2 x 3 x 2 (2 fall height x 3 fall types x 2 sex) mixed repeated measures ANOVAs, with sex as the between subject factor, were performed on all of the force and acceleration variables discussed above. Four-way 2 x 4 x 2 x 4 (2 fall heights x 3 fall types x 2 sex x 4 fall phases) mixed repeated measures ANOVAs were used to analyse the EMG and joint angle data. The means of the three trials for each combination of fall height and fall type were used for all statistical analysis. Fall type main effects were post-hoc tested with a Bonferroni adjustment, while significant interactions were analysed with Tukey's HSD post hoc test. Alpha was set at 0.05 and all statistical tests were conducted with IBM SPSS 19 (IBM SPSS statistics, IBM Corporation, Somers NY).

3.2.3 Results

The overall mean (SD) peak resultant right wrist velocity was 1.5 (0.4) m/s (Figure 3.10a), corresponding to mean (SD) peak resultant impact forces of 345.1 (17.8) N and 347.4 (128.75) N to the right and left hands, respectively. No significant differences were found between the right and left hand for any of the force variables. Therefore, only force data for the right hand will be presented.

(a)

(b)
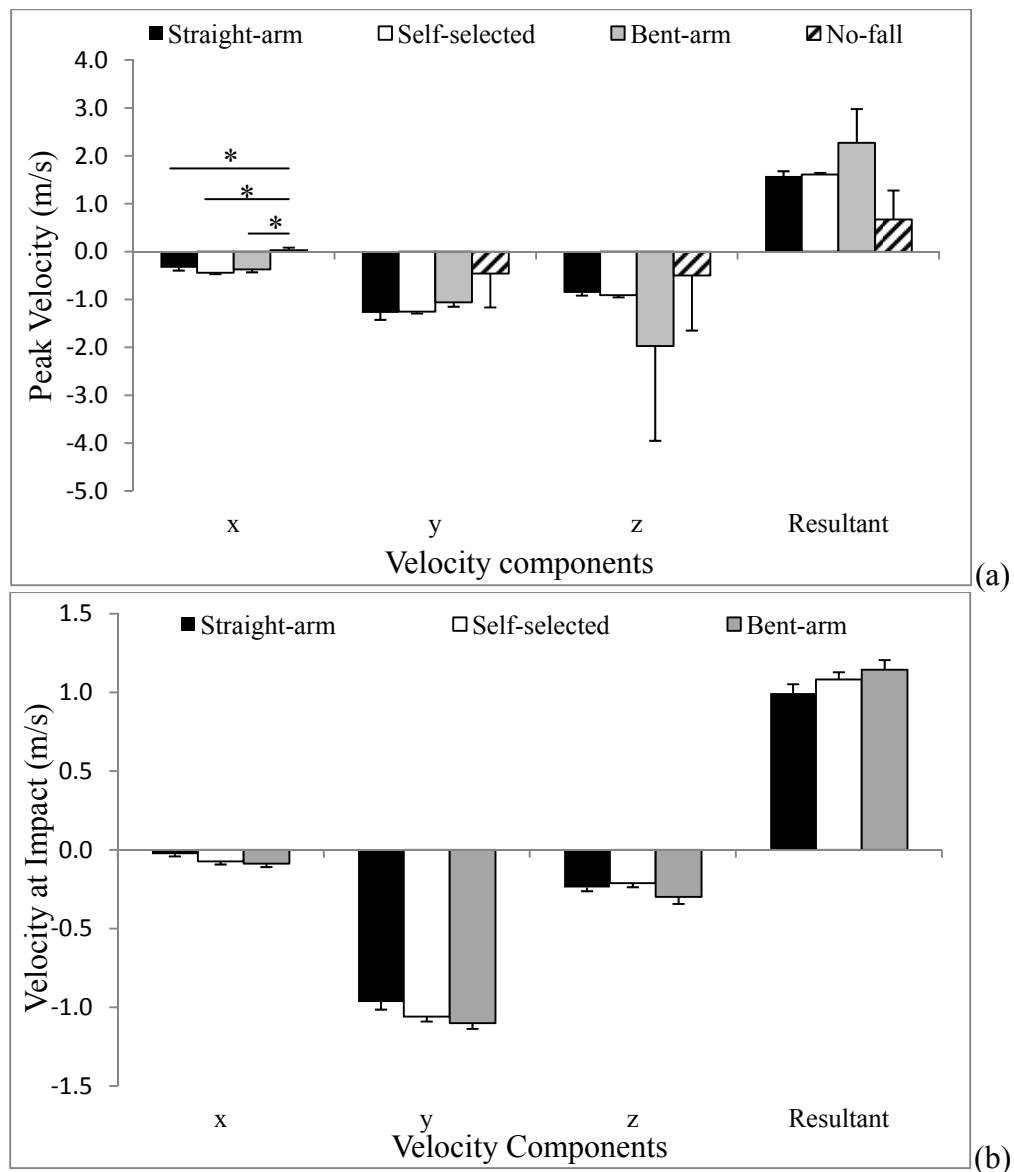
Figure 3.10: Wrist Velocity Components
Comparison of the mean (SD) x (medial-lateral), y (anterior-posterior) and z
(inferior-superior) peak wrist velocity components (a) and the wrist velocity
at impact (b) across fall types (* $p < 0.05$). Positive x velocity is towards the
body's midline, positive y velocity is backwards away from the force
platforms, and positive z is upwards away from the force platforms.

Peak wrist velocity in the x-direction was significantly less during the no-fall trials

compared to all other trials by a mean of 0.42 m/s, while the y, z and resultant velocities

were not significantly affected by the height or type of the fall (Figure 3.10a). Finally,

neither the type of fall nor the fall height significantly affected any of the wrist

velocities at impact (Figure 3.10b).

A significant main effect of sex was found for the peak force, impulse and

impulse duration, such that males experienced a greater force and impulse and shorter

impulse duration, compared to females (Table 3.8). However, when normalized to body

weight, these significant sex differences did not exist (body weight normalized forces

are not shown here). The mean (SD) Fx force was significantly less during the 0.05 m

fall (31.6 (20.5) N), compared to the 0.10 m fall (40.1 (22.1) N). However, no other

peak forces were affected by fall height. A significant fall height main effect was also

found for the Fr, Fx, and Fz load rate, with all three load rates increasing from the low

to high fall heights. Finally, fall type main effects were found for Fy impulse, Fx

impulse duration, Fy load rate, and Fz load rate. The straight-arm falls produced greater

impulses and load rates and shorter impulse durations than the self-selected or bent-arm

falls (Table 3.8).

A significant fall type by fall height interaction was found for the peak Fy force,

whereby the mean (SD) straight-arm Fy force (163.6 (68.2) N) was significantly greater

than the self-selected (124.0 (32.5) N) and bent-arm (126.8 (39.7) N) forces during the

0.10 m falls, but not the 0.05 m falls. The Fr load rate was also affected by a significant

fall type by fall height interaction where the mean (SD) load rate increased by

approximately 12.5 kN/s and 9.0 kN/s between the 0.05 m and 0.10 m falls during the

Table 3.8: Fall Height and Fall Type Force Variables
Comparison of the mean (SD) force variables across sex, fall height and fall type conditions. Statistical significance was achieved at $p < 0.05$.

	Sex		Fall Height		Fall Type		
	Female	Male	0.05 m	0.10 m	Straight-Arm	Self-Selected	Bent-Arm
Peak (N)							
Fr	265.2[a]	425.0	341.0	349.1	364.0	332.9	338.3
	(11.2)	(30.4)	(3.3)	(30.3)	(28.1)	(6.6)	(4.3)
Fx	27.8[a]	43.9	31.6[b]	40.1	36.5	35.6	35.5
	(16.2)	(22.8)	(20.5)	(22.1)	(30.1)	(20.3)	(24.4)
Fy	111.2[a]	160.1	133.2	138.1	152.4[e]	127.6	127.0
	(36.0)	(39.6)	(43.0)	(46.8)	(56.6)	(38.4)	(39.7)
Fz	243.5[a]	396.3	316.4	323.4	331.5	309.7	318.5
	(69.5)	(103.7)	(125.0)	(110.0)	(331.5)	(113.3)	(136.3)
Impulse (N·s)							
Fr	43.8[a]	87.7	65.4	66.1	65.5	69.1	62.7
	(2.6)	(4.5)	(4.5)	(2.2)	(1.1)	(0.6)	(3.0)
Fx	4.1[a]	7.3	5.5	5.9	5.6	5.8	5.7
	(1.8)	(3.9)	(3.3)	(3.4)	(4.1)	(3.5)	(4.0)
Fy	15.6[a]	29.9	22.3	23.2	25.6[d]	21.3	21.3
	(6.4)	(9.7)	(10.6)	(11.4)	(12.0)	(10.8)	(10.2)
Fz	39.7[a]	79.5	59.0	60.2	58.1	63.6	57.2
	(10.4)	(32.2)	(29.5)	(32.7)	(43.9)	(33.6)	(30.2)
Impulse Duration (s)							
Fr	0.38	0.44	0.42	0.42	0.40	0.43	0.41
	(0.10)	(0.06)	(0.07)	(0.08)	(0.07)	(0.08)	(0.08)
Fx	0.35	0.42	0.37	0.41	0.37[c]	0.40[c]	0.40
	(0.13)	(0.08)	(0.15)	(0.08)	(0.25)	(0.02)	(0.08)
Fy	0.38[a]	0.44	0.41	0.41	0.40	0.44[e]	0.40
	(0.08)	(0.06)	(0.07)	(0.08)	(0.07)	(0.08)	(0.08)
Fz	0.39[a]	0.44	0.42	0.41	0.40	0.44[e]	0.40
	(0.08)	(0.06)	(0.07)	(0.08)	(0.23)	(0.08)	(0.08)
Load Rate (kN/s)							
Fr	12.9	17.6	11.6[b]	18.8	17.7[c]	13.4[c]	14.6
	(1.5)	(4.3)	(2.9)	(4.8)	(8.8)	(6.5)	(2.7)
Fx	1.0	1.2	0.78[b]	1.5	1.2	1.1	1.2
	(0.9)	(1.3)	(0.77)	(1.5)	(1.2)	(1.0)	(1.2)
Fy	3.4	5.2	3.7	4.9	6.3[c]	4.0	2.5[c]
	(3.4)	(4.0)	(2.9)	(4.7)	(5.3)	(3.7)	(2.5)
Fz	13.2	16.9	12.0[b]	18.1	17.1[c]	13.1[c]	15.0
	(8.4)	(10.0)	(9.0)	(10.0)	(9.4)	(9.2)	(9.8)

[a] Significant sex main effect
[b] Significant fall height main effect
[c] Significant difference between two fall types
[d] Significantly different than all other fall type conditions
[e] Significant fall height by fall type interaction

straight-arm and self-selected fall types, while a 9.0 kN/s decrease was noted between the straight- and bent-arm fall types at 0.10 m.

In contrast to the force results, only two of the acceleration variables were significantly affected by sex; peak proximal medial-lateral acceleration and proximal medial-lateral acceleration rate. Both variables were greater in males compared to females (Table 3.9). All of the peak acceleration variables increased significantly between the 0.05 m to 0.10 m fall height by an average of 3.2 g. Similarly, fall height also had a significant effect on all of the acceleration rate variables, increasing from a mean (SD) of 353.4 (155.1) g/s during the 0.05 m falls to 579.2 (242.4) g/s during the 0.10 m falls. Peak accelerations were generally greater during the bent-arm falls compared to the straight-arm and self-selected falls, with significance found along all three axes at the distal accelerometer and the off-axis direction at the proximal accelerometer. The greatest differences were found at the distal accelerometer along the off-axis, such that the bent arm acceleration was 5.2 g and 4.4 g greater than the straight-arm or self- selected falls (Table 3.9). A fall type main effect was also found for four of the six acceleration rate variables. The acceleration rates associated with the bent-arm falls were, on average, 30.1 % greater for the distal axial and off-axis acceleration rates and 29.8 % greater for the proximal axial and off-axis acceleration rates.

Overall, TrLa and ECU exhibited the highest mean (SD) peak muscle activation level at 40.2 (21.9) % MVC, and 46.0 (18.8) % MVC, respectively (Figure 3.11). A fall type main effect was found across all muscles with the peak normalized muscle activation being significantly less during the no-fall trials compared to all other fall

Table 3.9: Fall Height and Fall Type Acceleration Variables

Comparison of the mean (SD) acceleration variables across sex, fall height and fall type conditions. Statistical significance was achieved at $p < 0.05$.

	Overall		Fall Height		Fall Type		
	Female	Male	0.05 m	0.10 m	Straight-arm	Self-selected	Bent-arm
Acceleration Peak (g)							
Distal Axial	9.5	8.9	7.6 [b]	10.8	7.8	8.7	11.2[d]
	(3.2)	(2.7)	(3.2)	(3.0)	(2.8)	(3.0)	(3.3)
Distal Off-axis	9.3	10.4	7.4[b]	12.3	7.5	8.8	13.2[d]
	(3.6)	(5.2)	(3.8)	(5.2)	(3.2)	(4.8)	(5.4)
Distal Medial-lateral	3.2	3.8	2.8[b]	4.2	3.2	2.8[c]	4.6[c]
	(2.3)	(2.6)	(2.1)	(2.9)	(2.4)	(2.1)	(2.9)
Proximal Axial	6.7	6.1	5.1[b]	7.7	5.7	6.2	7.3
	(3.1)	(2.6)	(2.8)	(2.9)	(2.5)	(2.9)	(3.1)
Proximal Off-axis	9.4	10.5	7.5[b]	12.4	7.6	9.0	13.2[d]
	(3.2)	(5.2)	(3.6)	(5.0)	(3.0)	(4.4)	(5.5)
Proximal Medial- lateral	4.2[a]	7.2	4.4[b]	7.0	5.3	5.5	6.2
	(3.3)	(3.2)	(3.4)	(3.9)	(3.0)	(3.3)	(4.6)
Acceleration Rate (g/s)							
Distal Axial	833.7	746.7	650.5 [b]	929.8	679.7	743.1	947.8 [d]
	(368.7)	(312.1)	(347.2)	(352.5)	(317.8)	(347.2)	(348.8)
Distal Off-axis	1145.8	1268.6	918.1[b]	1496.3	915.5	1130.2	1575.9[d]
	(394.7)	(643.7)	(422.8)	(649.5)	(391.8)	(566.4)	(650.0)
Distal Medial-lateral	351.3	416.3	315.3[b]	452.2	351.5	334.4	465.4
	(247.1)	(325.1)	(249.8)	(340.9)	(295.9)	(269.9)	(320.4)
Proximal Axial	543.8	538.4	432.5[b]	649.7	454.2	519.2	649.9[d]
	(268.8)	(251.1)	(240.0)	(277.8)	(205.4)	(247.8)	(323.6)
Proximal Off-axis	1154.3	1269.1	918.5[b]	1504.8	915.5	1142.9	1576.6[d]
	(377.5)	(642.7)	(421.5)	(630.6)	(391.8)	(538.1)	(648.2)
Proximal Medial-lateral	347.8[a]	542.8	309.9[b]	580.8	460.4	390.5	485.0
	(249.0)	(292.9)	(261.9)	(327.5)	(237.3)	(267.2)	(379.5)

[a] Significant sex main effect
[b] Significant fall height main effect
[c] Significant difference between two fall types
[d] Significantly different than all other fall type conditions
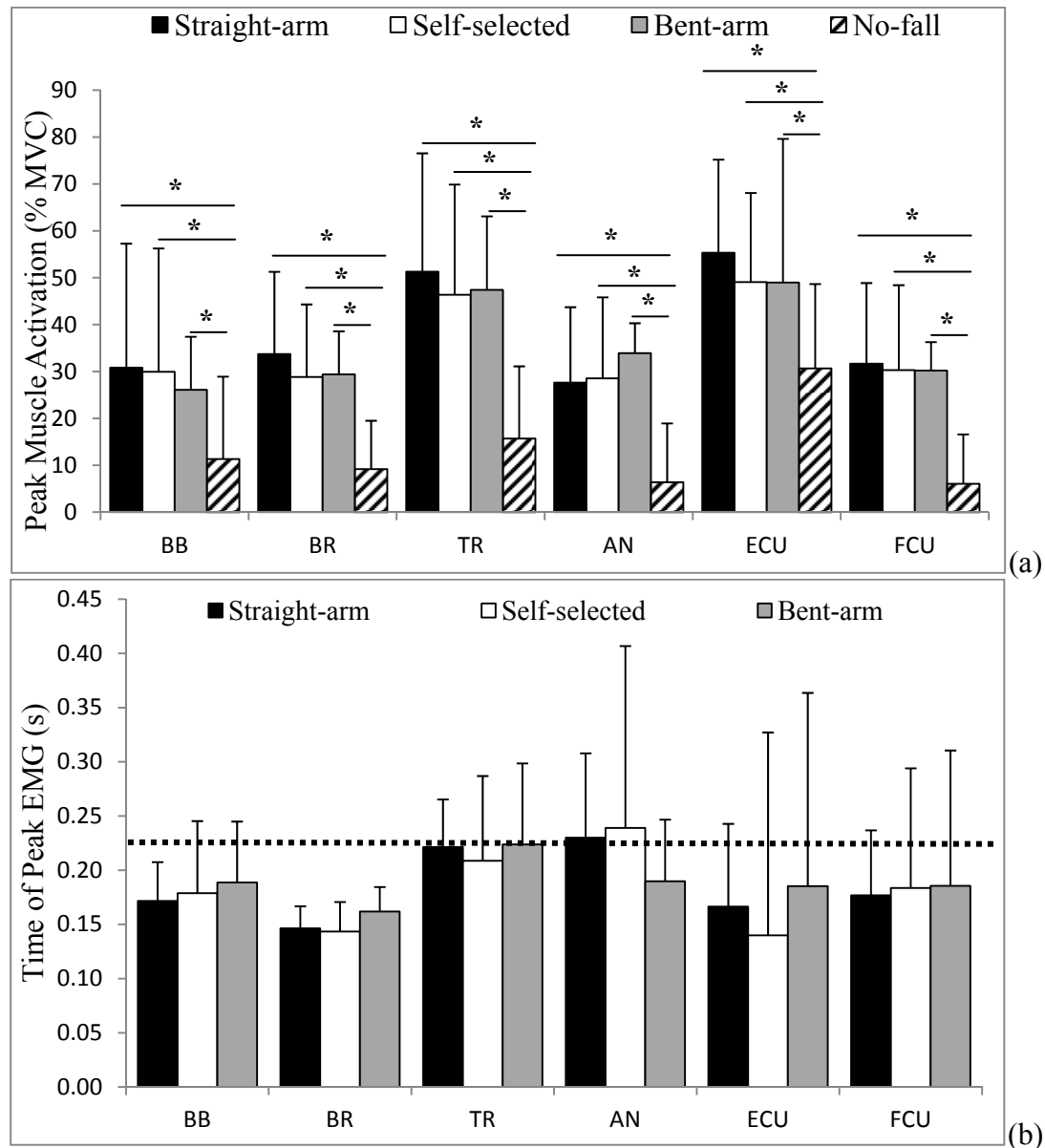
Figure 3.11: Peak EMG and Time of Peak EMG
Mean (SD) peak muscle activation (a) and the time of peak muscle activation (b), where t_o is the time of quick release, for all muscles across each fall type (*p <0.05). The dotted black line represents the time of the mean peak Fz force.

types (Figure 3.11) by a mean of approximately 17.8 %. No significant time of peak

normalized muscle activation effects were found.

For all muscles, the average EMG was significantly different between all fall

phases, such that the average muscle activation increased from start-release to release-

impact and from release-impact to impact-peak, followed by a decrease during the

impact-end fall phase (Figure 3.12a-f). With respect to the fall phase windowed EMG,

a fall height main effect was found during the release-impact phase, with the mean (SD)

FCU level of muscle activation increasing from 16.0 (9.5) % MVC during the straight-

arm falls to 19.1 (10.6) % MVC during the bent-arm falls. Excluding the FCU, all

muscles during the start-release phase were affected by fall type (Figure 3.12a-f), with

the biggest differences (6.1 % MVC) between the straight-arm and self-selected falls for

the ECU. Biceps Brachii (Figure 3.12a) and AN (Figure 3.12d) both increased

significantly between the straight-arm and self-selected falls by 3.0 % MVC and 3.1 %,

respectively, while the ECU (Figure 3.12e) decreased by 6.1 % MVC during release-

impact. Through the impact-peak force phase, AN muscle activation (Figure 3.12d) was

significantly greater during the self-selected falls compared to both the straight- and

bent-arm falls by a mean of 8.8 % MVC. The level of ECU activation during the

impact-peak phase was also significantly affected by fall type, such that the level of

activation decreased from 51.8 (19.8) % MVC during the straight-arm falls to 45.1

(19.5) % MVC during the bent-arm falls (Figure 3.12e).

The wrist experienced a significantly more extended posture during the 0.10 m

(-22.9 (4.1) $^\circ$) compared to the 0.05 m falls (19.5 (4.1) $^\circ$). However, the

flexion/extension angle of the wrist did not change significantly between the fall phases
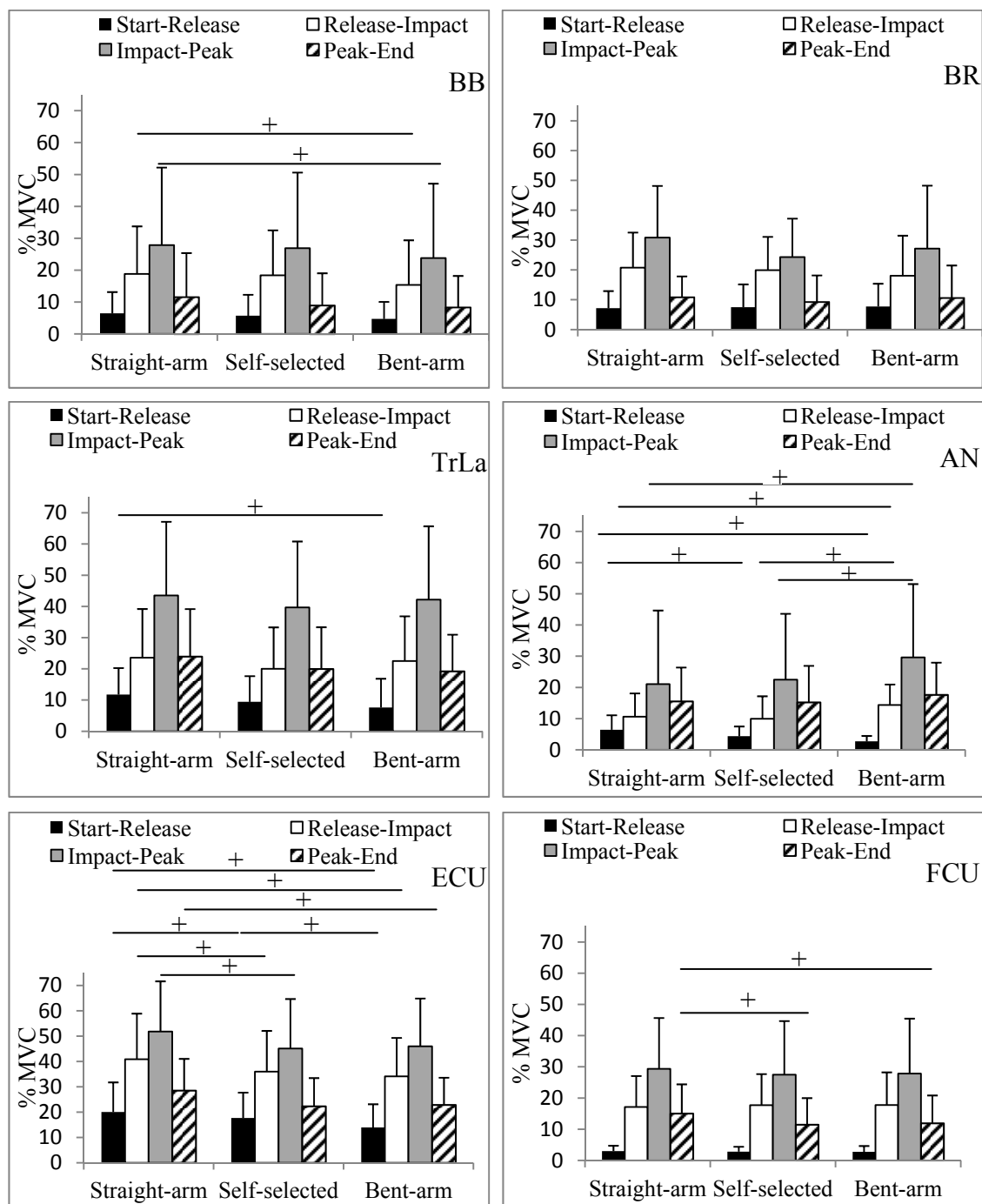
Figure 3.12: EMG across the Fall Phases
Comparison of average fall phase windowed muscle activation levels between fall types for the BB (a) BR (b), TrLa (c), AN (d), ECU (e), and FCU (f) ($^+$represents a significant fall phase by fall type interaction at $p < 0.05$). Although not shown here, the interaction also revealed a significant difference between all fall phases at all fall types for all muscles.

(Figure 3.13a). The mean (SD) ulnar deviation angle was 53.8 (2.3)^o when participants were asked to self-select their arm posture, which was significantly greater than the 48.5 (2.4)^o of ulnar deviation when falling onto a straight arm (Figure 3.13b).

The mean (SD) elbow flexion angle was also significantly affected by a fall phase by fall type interaction. The elbow flexion angle was approximately 7° greater during the self-selected falls compared to the bent-arm falls during the release-impact fall phase (Figure 3.14a). No significant elbow pronation/supination differences were found across the fall heights, phases or types (Figure 3.14b).

The overall mean (SD) shoulder plane of elevation was 36.8 (4.0)^o, suggesting that the humerus was positioned approximately mid-way between the frontal and sagittal planes. The plane of elevation was significantly affected by a fall phase by fall type interaction. During the bent-arm fall trials, the plane of elevation during the peak-end phase was significantly less than all other fall phases by a mean of 19.2^o. Similarly, for the self-selected fall type, the mean (SD) plane of elevation decreased from 39.5 (4.5)^o to 25.2 (5.4)^o from the impact-peak to the peak-end phases, respectively (Figure 3.15a). Finally, the mean (SD) shoulder elevation angle was 16.1 (2.3)^o, but was not significantly affected by the all height, fall type or fall phase (Figure 3.15b).

3.2.4 Discussion

A number of past studies have investigated the effect of different fall types and heights on the kinetics, kinematics and muscle activation patterns of the upper extremity following a simulated forward fall. However, these variables have traditionally been looked at in isolation, the simulated falls have been limited to a single direction of motion, muscle activation has only been analysed for a few select muscles, and only
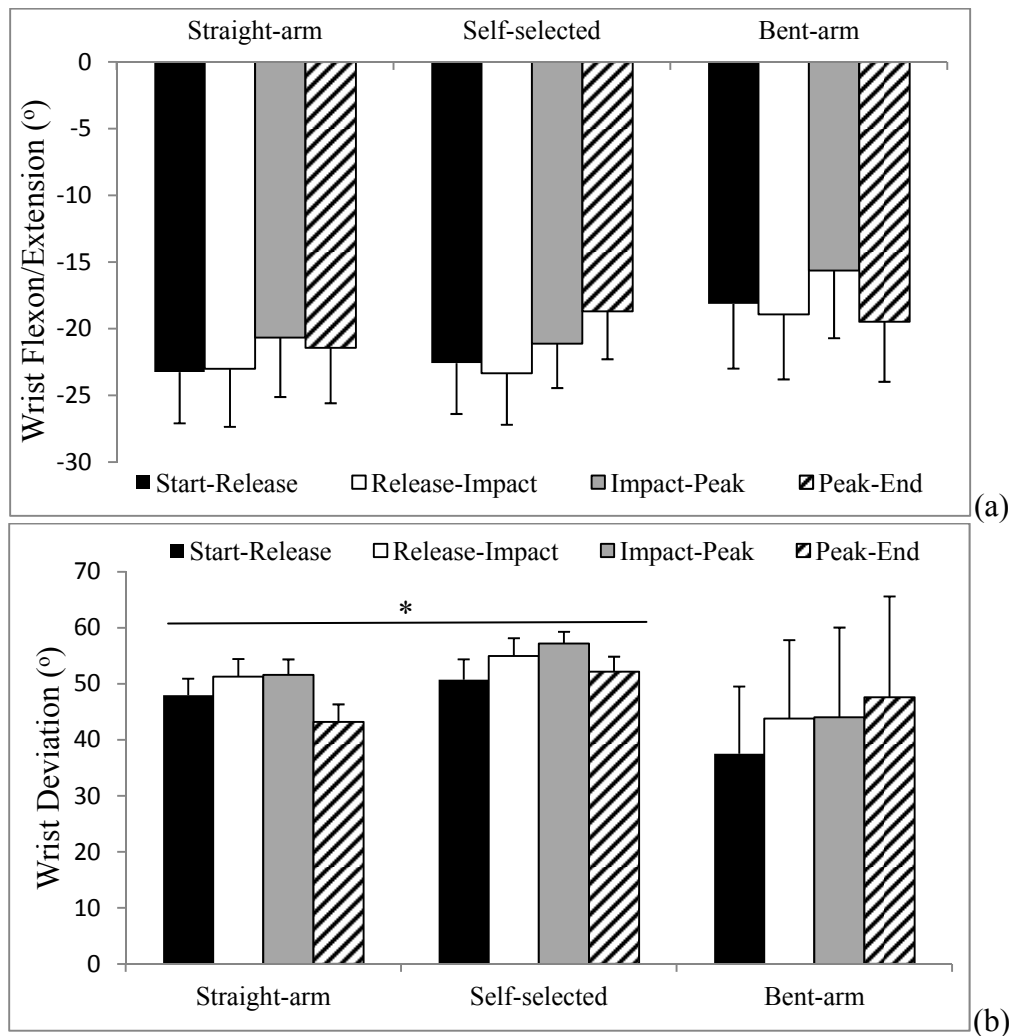
Figure 3.13: Wrist Angles
Comparison of wrist flexion (+)/extension (-) (a) and ulnar (+)/radial (-) deviation (b) angles between fall phases and fall types (* represents a significant main effect between fall types at $p < 0.05$).
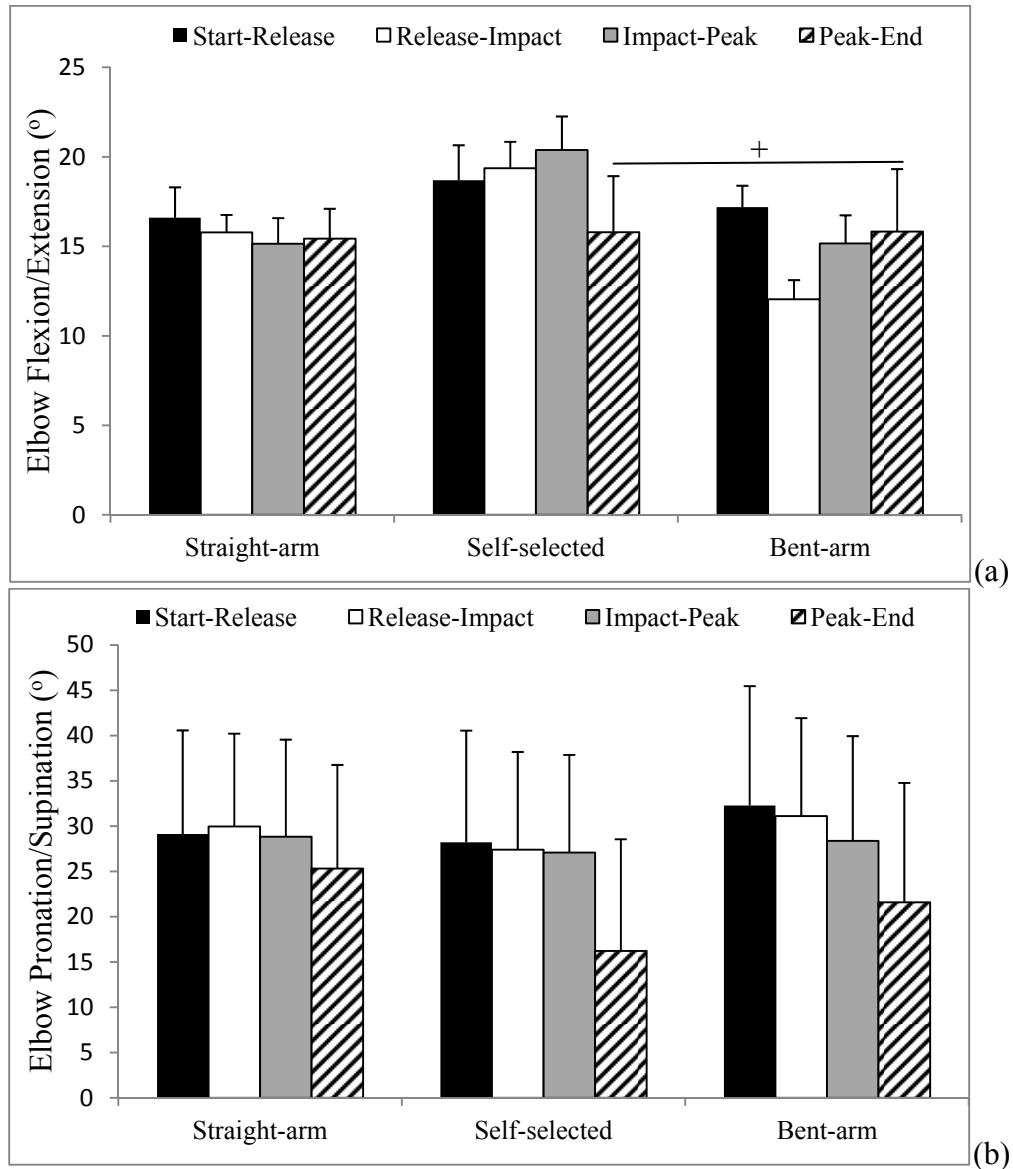
Figure 3.14: Elbow Angles
Comparison of elbow flexion (+)/extension (-) (a) and pronation
(-)/supination (+) (b) angles between fall phases and fall types (+ represents a
significant fall phase by fall type interaction at p<0.05).
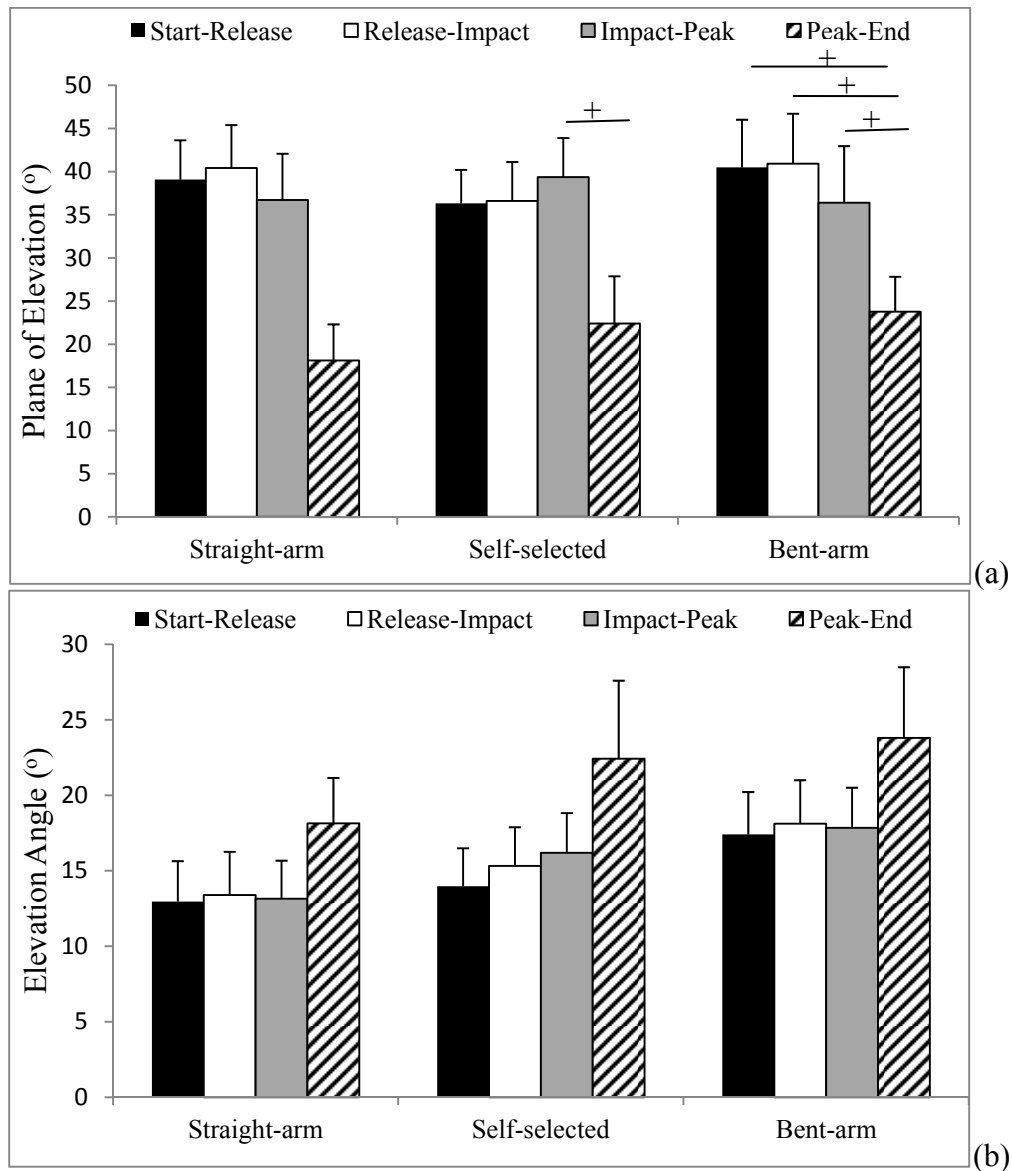
Figure 3.15: Shoulder Angles
Comparison of shoulder plane of elevation (0° = abduction; 90° = flexion) (a), and the elevation angles (b) between fall phases and fall types ([+] represents a significant fall phase by fall type interaction at $p<0.05$).

over a short period (i.e. 50 ms prior to impact), which is not representative of the entire flight and impact phases of a forward fall. The current investigation aimed to address these limitations and present forward fall response data in multiple directions, for all of the main muscle groups of the upper extremity, and over the entire duration of a simulated forward fall (i.e. from fall commencement to the end of the impact force impulse).

The wrist velocity components reported here agree well with previously reported wrist velocities during catch trial forward falls (Troy & Grabiner, 2007), and are approximately 50 % of the magnitude of the resultant velocity found following standing height falls onto padded surfaces (Hsiao & Robinovitch, 1998; Tan et. al., 2006). This suggests that the novel fall simulation method used here is an adequate representation of actual forward falls. Overall, the peak velocity vectors recorded here suggest that, prior to impact, the wrist was moving anteriorly and downwards towards the force platforms and with minimal medial-lateral movement; a consistent pattern across all fall types. At impact, the x- and z-velocity components decreased by a factor of four, while the y-velocity component remained relatively constant. This suggests that the wrist continued to move across the force platform after impact. However, it is unclear if this was a protective mechanism, or a result of the low friction between the surface of the force platform and the hand, combined with the initial forward movement of the simulated fall.

While the type and height of the fall had little effect on the resultant peak force, impulse, and impulse duration, an analysis of the force vector components did reveal significant height and type differences. In general, the straight-arm falls resulted in the

greatest magnitudes along all three force axes and among all force variables, excluding impulse duration. These findings appear to support the well documented theory that a straight-arm fall represents a worst-case scenario (Chiu & Robinovitch, 1998; DeGoede & Ashton-Miller, 2002; DeGoede & Ashton-Miller, 2003; Lo et al., 2003). However, although participants were instructed to maintain a straight arm (i.e. 0° elbow flexion), the elbow flexion/extension angle results suggest that participants approached and initially impacted the force platforms with an elbow angle similar to the other fall types, which is also consistent with the findings of DeGoede & Ashton-Miller (2002).

Between release-impact and impact-peak, the change in elbow flexion angle was greater during the self-selected and bent-arm trials; a pattern also seen in the wrist flexion/extension and shoulder elevation angles. Therefore, it is likely that it was the change in joint angles over the duration of the impact that determined the magnitude and effect of the impact force variables. Of special importance is the significant decrease in the Fy impulse and Fz load rate experienced during the self-selected and bent-arm falls, compared to the straight-arm falls. In Section 2.3, it was shown that these variables exhibit a positive relationship with the probability of crack and fracture events in human radii. This confirms that healthy young adults are capable of consciously selecting an impact minimising fall strategy with limited training and instructions (Lo et al., 2003). Although, as suggested by DeGoede & Ashton-Miller (2003), older or pathological adults may not possess the muscular strength to react to the rapid and often times unknown nature of the fall and subsequent impact.

The visco-elastic properties of a pre-activated muscle have been shown to be adequate to quickly compensate for external load changes (Dietz et al., 1981), and it has

been suggested that the muscles exhibit this preparatory activation in anticipation of an impact (Dietz et al., 1981; Boyer & Nigg, 2004; Santello, 2005). This is an important mechanism as it allows the body to prepare for impacts, whose forces, impulses and load rates can be highly variable (Nigg et al., 2003; Santello, 2005). Dietz et al. (1981) found that the activation level of triceps brachii increases steadily during the pre-impact (flight) and impact phases of forward falls, and peaked subsequent to the peak force.

The muscles that were tested in the current study were all found to exhibit this pre-impact preparatory response that is evident in the large increases in the average muscle activation between the start-release and release-impact phases. This suggests that muscle activation begins to ramp up before the onset of the impulse. Also, the majority of the muscles tested here peaked before or simultaneously with the peak force; another indication of the muscle's preparation for impact.

During the impulse-peak phase (i.e. the application of the force to the upper extremity), the average muscle activation of AN was significantly greater during the bent-arm falls compared to the straight-arm and self-selected falls, while the ECU activation was significantly greater during the straight-arm than the self-selected falls. Although the muscle forces themselves were not calculated here, it appears that these three muscles are important contributors to the stability of the elbow and wrist respectively, when attempting to arrest the forward motion of a fall and minimize the effects of the impact. Furthermore, the TrLa also appears to be an important muscle for arresting the motion of a forward fall. However, given the relative size and level of activation, it is likely that, while TrLa is a contributor to joint stability, it is also the primary muscle involved in controlling the motion about the joint. However, these

levels of muscle activation also explain why the accelerations at the wrist and elbow were greater during the bent-arm and self-selected conditions. While increased muscle activation allows for control of joint stability (Bergmark 1989; Dunning et al. 2001; Potvin & Brown, 2005), it also increases the stiffness within the segment as a whole (Cholewicki & McGill, 1995; Holmes & Andrews, 2006; Lee et al., 2006; Burkhart & Andrews 2010a). Burkhart & Andrews (2010a) found that the acceleration response at the wrist and elbow increased in response to increased ECU and FCU muscle activation. While the accelerations reported here are smaller than those described by Burkhart & Andrews (2010a), this is likely a result of the multi-directional motion used in the current investigation compared to the uni-directional motion used previously.

In the current investigation there was no difference in the impact forces between the 0.05 m and 0.10 m fall heights. The closeness of the hands to the force platforms, combined with the relatively small physical difference between the two heights, could have led to the lack of significant results, and the inability to make any conclusions regarding fall height. Also, the relatively close proximity of the hands to the force platforms, suggests that there may not have been enough time available for the participants to react naturally during the 0.5 m falls. It takes the upper extremity approximately 200 ms - 250 ms to react to a visual stimulus, upwards of 1.5 times longer than the 100 ms it would take the hand to reach the force platform during the 0.05 m falls (Moisello et al. 2009). Therefore, reactions to the fall at this height most likely occur as a result of passive motions as opposed to participant controlled strategies. This may also explain the absence of significant fall type differences with respect to the muscle activation levels and joint angles. While these heights were

chosen to ensure the safety of the participants, the relatively low force variables

achieved during the 0.10 m falls suggest that future work could explore falls from

slightly greater heights without injury (Section 2.2 and Section 2.3). Also, to ensure

that the height of the hands above the force platforms remained consistent during each

trial, participants were instructed to maintain the appropriate postures throughout the

fall phases, including starting the self-selected falls from a straight arm position. This

could account for the relatively small changes in joint angles and impact forces.

Finally, another limitation of the current study is the lag between the torso and

leg quick releases. To ensure that the hands impacted the force platforms prior to the

legs contacting the ground, the lag was set at 150 ms. It is possible that the hands could

have contacted the force platforms slightly before the legs were released, and therefore

the hands would be responsible for arresting the momentum of the body as well as the

residual momentum of the PULARIS before the legs were released. However, the

effect of this would be consistent across trials, thereby not influencing the results

differentially. Regardless, future work will be conducted to examining the effect of

different time lags between torso and leg release.

To date, this is the first investigation of the kinematics and kinetics of the upper

extremity following simulated forward falls using PULARIS. Also presented here were

the activation levels of six muscles of the upper extremity during these simulated

events. The results of this study suggest that, to some extent, individuals are capable of

selecting an upper extremity posture that allows them to minimize the effects of an

impact. This study has also confirmed the presence of a preparatory muscle activation

and has identified the AN, ECU and TrLa as two potentially important muscles in

preparing for and reacting to a forward fall. Future work will continue to explore the role of joint angles (i.e. body orientation) and muscle activation patterns in an attempt to develop successful fall landing interventions.

3.2.5 References

Anglin C, Wyss UP. 2000. Review of arm motion analyses. Journal of Engineering in Medicine. 214, 541-555.

Bergmark A. 1989. Stability of the lumbar spine: a study in mechanical engineering. Acta Orthopaedica Scandinavia. 230, 1-54.

Boyer KA, Nigg BM. 2004. Muscle activity in the leg is tuned in response to impact force characteristics. Journal of Biomechanics. 37, 1583-1588.

Burkhart TA, Andrews DM. 2010a. Activation level of extensor carpi ulnaris affects wrist and elbow acceleration responses following simulated forward falls. Journal of Electromyography Kinesiology. 20, 1203-1210.

Burkhart TA. Andrews DM. 2010b. The effectiveness of wrist guards for reducing wrist and elbow accelerations resulting from simulated forward falls. Journal of Applied Biomechanics. 26, 281-289.

Burkhart TA, Dunning CE, Andrews DM. 2011. Determining the optimal system-specific cut-off frequencies for filtering *in vitro* upper extremity impact force and acceleration data through residual analysis. 44, 2728-2731.

Chiu, J., Robinovitch, S. N. 1998. Prediction of upper extremity impact forces during falls on the outstretched hand. Journal of Biomechanics. 31, 1169-1176.

Cholewicki J, McGill SM. 1995. Relationship between muscle force and stiffness in the whole mammalian muscle: a simulation study. Journal of Biomechanical Engineering. 117, 339-342.

Coburn J, Crisco JJ. 2005. Interpolating three-dimensional kinematic data using quaternion splines and hermite curves. Journal of Biomechanical Engineering. 127, 311-317.

Chou P-H, Lou S-Z, Chen H-C, Chiu C-F, Chou Y-L. 2009. Effect of various forearm axially rotated postures on elbow load and elbow flexion angle in one-armed arrest of a forward fall. Clinical Biomechanics. 24, 632-636.

Chu ML, Yazdanni-Ardakani S, Gradisar IA, Askew MJ. 1986. An *in vitro* simulation study of impulsive force transmission along the lower skeletal extremity. Journal of Biomechanics, 19, 979-987.

Derrik TR, Hamill J, Caldwell GE. 1998. Energy absorption of impacts during running at various stride lengths. Medicine and Science in Sports and Exercise. 30, 128-135.

DeGoede KM, Ashton-Miller JA, Schultz AB, Alexander NB. 2002. Biomechanical factors affecting the peak hand reaction force during the bimanual arrest of a moving mass. Journal of Biomechanical Engineering. 124, 107-112.

DeGoede KM, Ashton-Milller JA. 2002. Fall arrest strategy affects peak hand impact force in a forward fall. Journal of Biomechanics. 35, 843-848.

DeGoede KM, Ashton-Miller JA. 2003. Biomechanical simulations of forward fall arrests: effects of upper extremity strategy, gender and aging-related declines in muscle strength. Journal of Biomechanics. 36, 413-420.

Dietz V, Noth, J, Schmidtbleicher D. 1981. Interaction between pre-activity and stretch reflex in human triceps brachii during landing from forward falls. Journal of Physiology. 311, 113-125.

Dunning CE, Zarzour ZDS, Patterson SD, Johnson JA, King GJW. 2001. Muscle forces and pronation stabilize the lateral ligament deficient elbow. Clinical Orthopaedics and Related Research. 388, 118-124.

Elftman H. 1939. The function of muscles in locomotion. American Journal of Physiology. 125, 357-366.

Flynn, J. M., Holmes, J. D., Andrews, D. M. 2004. The effect of localized leg muscle fatigue on tibial impact acceleration. Clinical Biomechanics. 19, 726-732.

Grood ES, Suntay WJ. 1983. A joint coordinate system for the clinical description of three-dimensional motions: Application to the knee. Journal of Biomechanical Engineering. 105, 136-144.

Gruber K, Ruder H, Denoth J, Schneider K. 1998. A comparative study of impact dynamics: wobbling mass model versus rigid body models. Journal of Biomechanics. 31, 439-444.

Holmes AM, Andrews DM. 2006. The effect of leg muscle activation state and localized muscle fatigue on tibial response during impact. Journal of Applied Biomechanics. 22, 275-284.

Howarth SJ, Callaghan JP. 2010. Quantitative assessment of the accuracy for three interpolation techniques in kinematic analysis of human movement. Computer Methods in Biomechanics and Biomedical Engineering. 13, 847-855.

Hsiao, E. T. Robinovitch, S. N. 1998. Common protective movements govern unexpected falls from standing height. Journal of Biomechanics. 31, 1-9.

Hsu H-H, Chou Y-L, Lou S-Z, Huang M-J, Chou PP-H. 2011. Effect of forearm axially rotated posture in shoulder load and shoulder abduction/flexion angles in one-armed arrest forward falls. Clinical Biomechanics. 26, 245-249.

Lee PJ, Rogers EL, Granata KP. 2006. Active trunk stiffness increases with co-contraction. Journal of Electromyography and Kinesiology. 16, 51-57.

Light LH, McLellan GE, Klenerman L. 1980. Skeletal transients on heel strike in normal walking with different footwear. Journal of Biomechanics. 13, 477-480.

Lo J, McCabe GN, DeGoede KM, Okuizumi H, Ashton-Miller JA. 2003. On reducing hand impact force in forward falls: results of a brief intervention in young males. Clinical Biomechanics. 18, 730-736.

Moisello C, Crupi D, Tunik E, Quartarone A, Bove M, Tononi G, Ghilardi MF. 2009. The serial reaction time task revisited: a study on motor sequence learning with an arm-reaching task. Experimental Brain Research. 194, 143-155.

Nigg, B. M., Liu, W. 1999. The effect of muscle stiffness and damping on simulated impact force peaks during running. Journal of Biomechanics. 32, 849-856.

Nigg BM, Stefannyshyn D, Cole G, Stergiou P, Miller J. 2003. The effect of material characteristics of shoe soles on muscle activation and energy aspects during running. Journal of Biomechanics. 36, 569-575.

Pain MT, Challis JH. 2001. The role of the heel pad and shank soft tissue during impacts: a further resolution to the paradox. Journal of Biomechanics. 34, 327-333.

Potvin JR, Brown SHM. 2005. An equation to calculate individual muscle contributions to joint stability. Journal of Biomechanics. 38, 973-980.

Santello M. 2005. Review of motor control mechanism underlying impact absorption from falls. Gait and Posture. 21, 85-94.

Schinkel-Ivy, A., Burkhart, T. A., Andrews, D. M. 2011. Leg tissue mass composition affects tibial acceleration response following impact. Journal of Applied Biomechanics. Available online at ttp://journals.humankinetics.com/AcuCustom/SiteName/Documents/DocumentItem/Burkhart_jab_2009_0189-in-press.pdf

Schmidt R, Disselhorst-Klug C, Silny J, Rau G. 1999. A marker-based measurement procedure for unconstrained wrist and elbow motions. Journal of Biomechanics. 32, 615-621.

Shrout PE, Fleiss JL. 1979. Intraclass Correlations: Uses in Assessing Rater Reliability. Psychological Bulletins. 2, 420-428.

Tan J-S, Eng JJ, Robinovitch SN, Warnick B. 2006. Wrist impact velocities are smaller in forward falls than backward falls from standing. Journal of Biomechanics. 39, 1804-1811.

Troy, K. L., Grabiner, M. D. 2007. Asymmetrical ground impact of the hands after a trip-induced fall: experimental kinematics and kinetics. Clinical Biomechanics. 22, 1088-1095.

Wu G, van der Helm FCT, Veeger HEJ, Makhsous M, Roy PV, Anglin C, Nagels J, Karduna AR, McQuade K, Wang X, Werner FW, Bucholz, B. 2005. ISB recommendations on definitions of joint coordinate systems of the various joints for the reporting of human joint motions-Part II: shoulder, elbow, wrist. Journal of Biomechanics. 38, 981-992.

van Andel CJ, Wolterbeek N, Doornbosch CAM, Veeger D, Harlaar J. 2008. Complete 3D kinematics of upper extremity functional tasks. Gait & Posture. 27, 120-127.

Van der Woude LHV, Veeger D-J, Rozendal RH, Sargeant TJ. 1989. Seat height in hand rim wheelchair propulsion. Journal of Rehabilitation Research. 26, 31-50.

Winter, D. A. 2005. Three dimensional kinematics and kinetics. In Biomechanics and Motor Control of Human Movement (pp180-202). Hoboken, NJ: John Wiley & Sons Inc.

Wosk J, Voloshin A. 1981. Wave attenuation in skeletons of young healthy persons. Journal of Biomechanics. 14, 261-267.

CHAPTER 4 – A NUMERICAL INVESTIGATION OF THE DISTAL RADIUS DURING IMPACT.

4.1 Development and Quality Measurements of a Finite Element Mesh of the Distal Radius.

4.1.1 Introduction

While experimental testing on human participants and cadaveric specimens provides the most realistic response of the human body and the most accurate injury patterns, these types of testing are not always the most feasible (Quennevile et al., 2010). For example, the safety of participants limits *in vivo* testing to sub-maximal loads, and the destructive nature of damage tests on cadaveric specimens can become costly (Rogge et al., 2002). Finite element models (FEM), on the other hand, provide a feasible alternative for calculating the stress and strain response of bone under a variety of loading conditions.

Obtaining accurate outputs from a finite element model is dependent on the development of a high quality mesh. Given the complex geometry of the radius bone, elements with large distortions often occur and are potential sources of low accuracy or instability of a solution (Valle & Ray, 2005). It has also been suggested that a model composed entirely of hexahedral elements will lead to more accurate results, is more computationally efficient, and mimics the geometry better than a model meshed with shell, tetrahedral, or voxel based meshes (Tautges, 2001; Fyllingen et al., 2009).

While several studies have developed finite element meshes of the distal radius (Ulrich et al., 1999; Pistoia et al., 2002; Rogge et al., 2002; Carrigan et al., 2003; Pistoia et al., 2003; Pistoia et al., 2004; Anderson et al., 2005; Troy & Grabiner, 2007; Boutroy

et al., 2008; MacNeil & Boyd, 2008; Buchanan & Ural, 2010; Edwards & Troy, 2010), none have included measurements of the mesh quality. Furthermore, only two of these models (Rogge et al., 2002; Edwards et al., 2010) are composed of all hexahedral meshes and many represent the geometry of only a very small portion of the radius (Ulrich et al., 1999; Pistoia et al., 2002; Rogge et al., 2002; Pistoia et al., 2003; Pistoia et al., 2004; Boutroy et al., 2008; MacNeil & Boyd, 2008; Buchanan & Ural, 2010). Thus, these limitations raise concerns regarding the validity and applicability of past radius bone finite element models to dynamic impact loading.

Therefore, the purpose of this chapter is to describe the development and assessment of a hexahedral mesh that accurately represents the geometry of the distal radius. A step by step process is provided outlining the protocol for developing a mesh based on images obtained from Computed Tomography (CT) scans.

4.1.2 Methods

4.1.2.1 Surface Geometry Extraction

Eight intact cadaveric radius specimens (Section 2.2) were potted in dental cement at15° to the vertical and were scanned using a GE LightSpeed VCT (General electric Healthcare, Chalfont St. Giles, United Kingdom) at120 kVp, 100 mA, with a 0.625 mm slice thickness. A section of hydroxyapatite and a tube of water were included in the scan region during the CT scans to act as reference materials to be used during the image registration phase. From the eight CT scans, one was chosen as a representative sample from which to build a finite element model. Selection of the most representative sample was based on ranking the specimens according to donor age, bone

mineral density of the distal third of the radius, the fracture force and the Frykman score. Each specimen was ranked on each of these variables according to how well they agreed with the mean values of each variable (Quenneville & Dunning, 2011) (Table 4.1).

The CT scan files of the representative specimen were imported into Mimics® (Materialise, Leuven, Belgium) medical imaging software to build solid models of the cortical, cancellous and marrow regions of the bone. A full description of the mesh development protocol can be found in Appendix H. First, a series of masks (Figure 4.1a) were applied to the scan images to threshold the bone, based on the Hounsfield units (HU) of each voxel. The threshold of the densest region of bone (i.e. the cortical bone) was determined in comparison to the piece of hydroxyapatite that was included in the scan. This resulted in HU from 621 - 2693 for the cortical bone and < 621 for the cancellous bone. These values compare well with previously reported data (Troy & Grabiner, 2007). Polylines (Figure 4.1b) were generated based on the cortical mask, defining the interior and exterior boundaries of the cortical bone. The solid cortical model was created by filling a cavity defined by the interior and exterior polylines with 3D solids. The solid cancellous model was created by filling the space bounded on the edges by the interior polylines and proximally by the marrow region. The transition from cancellous bone to bone marrow is not clearly defined, with sections of cancellous bone found throughout the intermedullary canal. Therefore, as an assumption, this transition was identified as the axial location where the cavity was not entirely occupied by cancellous bone. The solid models were then smoothed (Figure 4.2a and 4.2b) and exported as Stereolithography (STL) files. Surfaces were exported as STL files as they

Table 4.1: Specimen Ranking
A summary of the ranking system that was used to select the most representative
specimen. The bone mineral density (BMD) is taken from the distal third of the radius
determined from the DXA scans.

Specimen	Age	Rank	BMD	Rank	Frykman Score	Rank	Fracture Force	Rank	Sum	Overall Rank
07017L	76	7	0.39	8	7	1	2021	2	26	7
07030R	54	3	0.58	7	7	1	4340	8	23	5
08007L	60	1	0.48	1	7	1	1493	6	9	1
07043L	68	3	0.42	6	7	1	2519	1	15	3
08010L	46	7	0.47	2	7	1	1941	4	22	4
07007R	57	2	0.47	3	7	1	1980	3	11	2
04011R	54	3	0.53	4	3	7	3848	7	25	6
07004L	73	6	0.54	5	3	7	1627	5	29	8
Mean	61		0.48		6		2471			
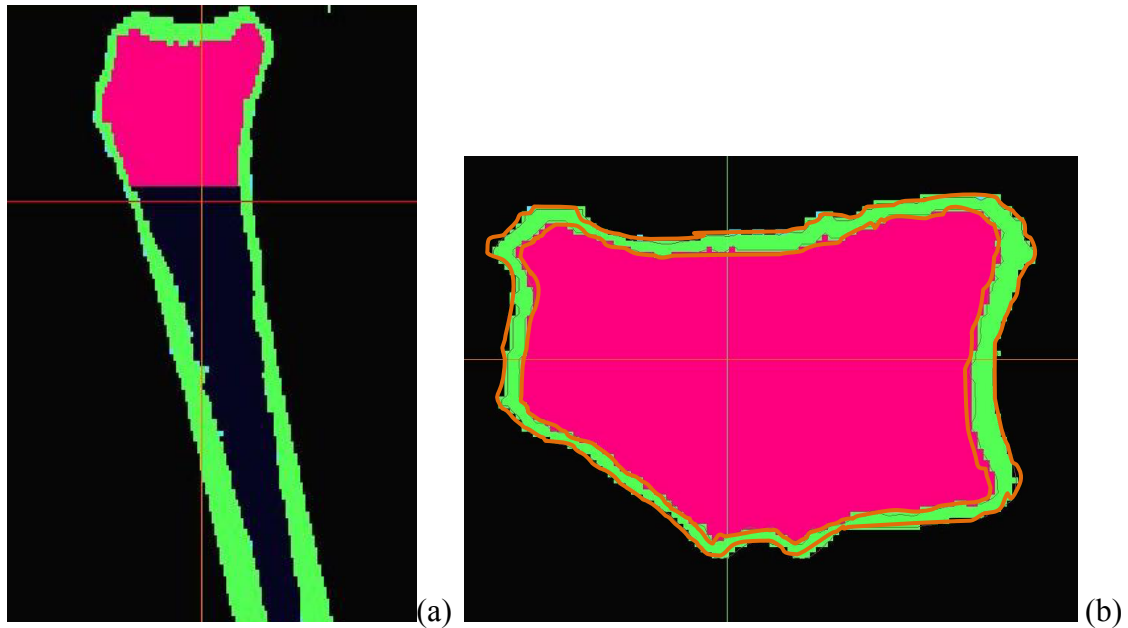
Figure 4.1: Masks and Polylines
Example of the three masks (a) (in the sagittal plane) created from thresholding the bone according to the Hounsfield Units (HU), and the polylines (b) (in the horizontal plane) used to build the solid model. The cortical, cancellous and marrow regions are represented by the green, pink and blue masks, respectively, while the polylines are represented in orange.
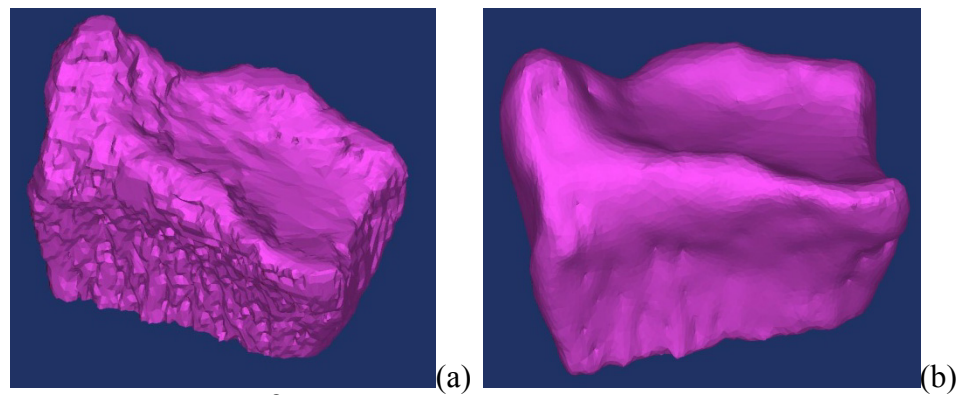
Figure 4.2: Mimics® Solid Models
Comparison of the cancellous bone solid models, before (a) and after (b) the application of smoothing algorithms in Mimics®.

provide the best representation of the surfaces without artificially smoothing the curvature.

To compare the strains developed in the FEM to those experienced experimentally, the location of the strain gauges were first identified on the specimens by digitizing (Microscribe G2X, Immersion corporation san Jose, CA) the four corners and the center of each strain gauge and accelerometer from the experimental testing described in Section 2.2. Three screw holes placed in the PVC potting were also digitized (and were visible in the CT scans) to create a local co-ordinate system. Transformations were conducted and the x-y-z coordinates of the center of each strain gauge was located on the solid model and were exported to a text (.txt) file.

4.1.2.2 Mesh Generation

The mesh of the distal radius bone was created using TrueGrid[®] mesh generator (XYZ Scientific Inc., Livermore, CA, USA). TrueGrid[®] is a high quality, parametrically based meshing program that allows the user to create the mesh using curves and surfaces. The mesh is generated by first creating blocks of mesh that can be moved and manipulated prior to being "projected" onto a surface. Each block is composed of six faces which are connected by edges that join at the corners to form vertices. Many blocks, separated by partitions, are used in the creation of a mesh and the partitions allow each block to be assigned a different number of elements, as well as different material properties. The block structure is created in the computational domain of the TrueGrid[®] user interface, while the physical structure of the mesh shows

the position and shapes of the elements (Figure 4.3). Within the computation view, partitions can be added and blocks can be deleted, while projections, movement of edges and vertices, and the creation of curves occur in the physical view.

Selecting the appropriate topology for the mesh is an important consideration given the highly complex geometry (i.e. high curvature) of the distal radius. Applying a hexahedral mesh to a circular cross section can result in elements that are exceedingly distorted with angles up to 180° at the corners. Therefore, multiple blocks can be combined in what is known as the "butterfly technique", reducing the distortion at the edges. A butterfly is generated by creating a grid of blocks (usually a 3 x 3 grid), deleting the corner blocks and manually moving the corner edges to 45° angles. Following the initial positioning of the edges, the faces are "glued" together at the interior faces (i.e. the faces where the corner blocks were removed) using a block boundary command. This technique greatly improves the most distorted elements (Figure 4.4).

4.1.2.3 Radius Bone Meshing

The STLs created in Mimics® were imported into TrueGrid® as surfaces (Figure 4.5). The interior cancellous and marrow bone sections were meshed first, followed by the cortical bone. Beginning with the cancellous bone, a butterfly structure was created using a 3 x 3 block arrangement. Three dimensional splines were generated around the outside and inside of the distal articular surface, the base and tip of the styloid process, and the proximal surface of the cancellous region (Figure 4.5). Edges of the block structure were attached to these splines and the faces were projected onto the cancellous
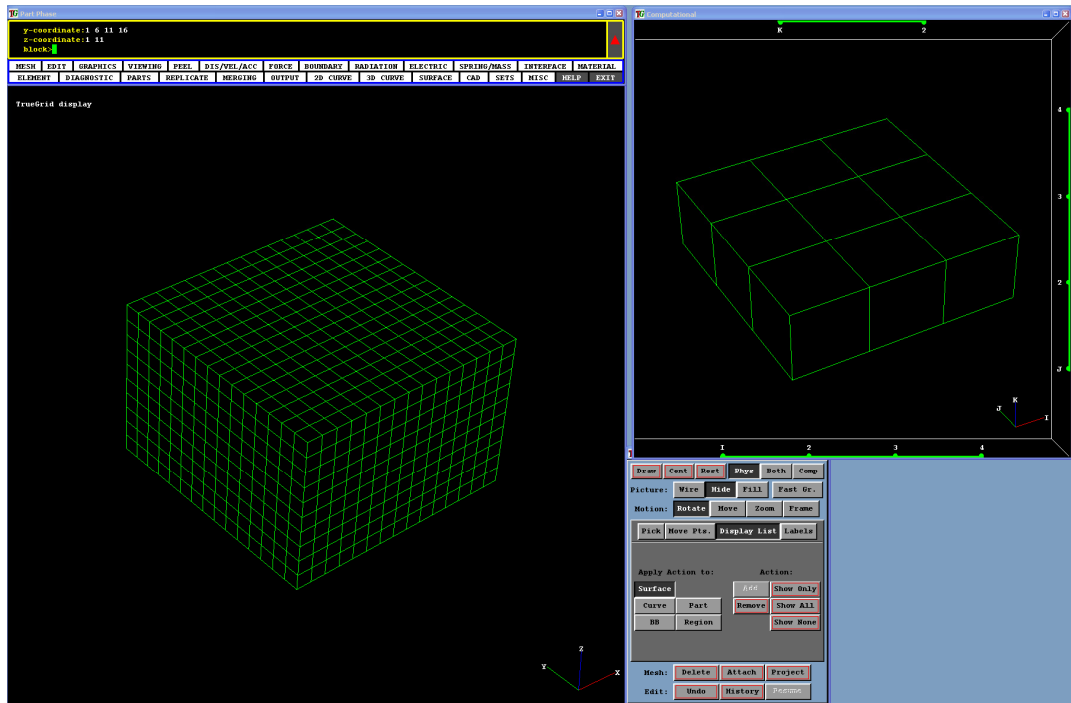
Figure 4.3: TrueGrid® Working Environment
The working environment of TrueGrid®. The physical view is on the left while the computational view is on the right.
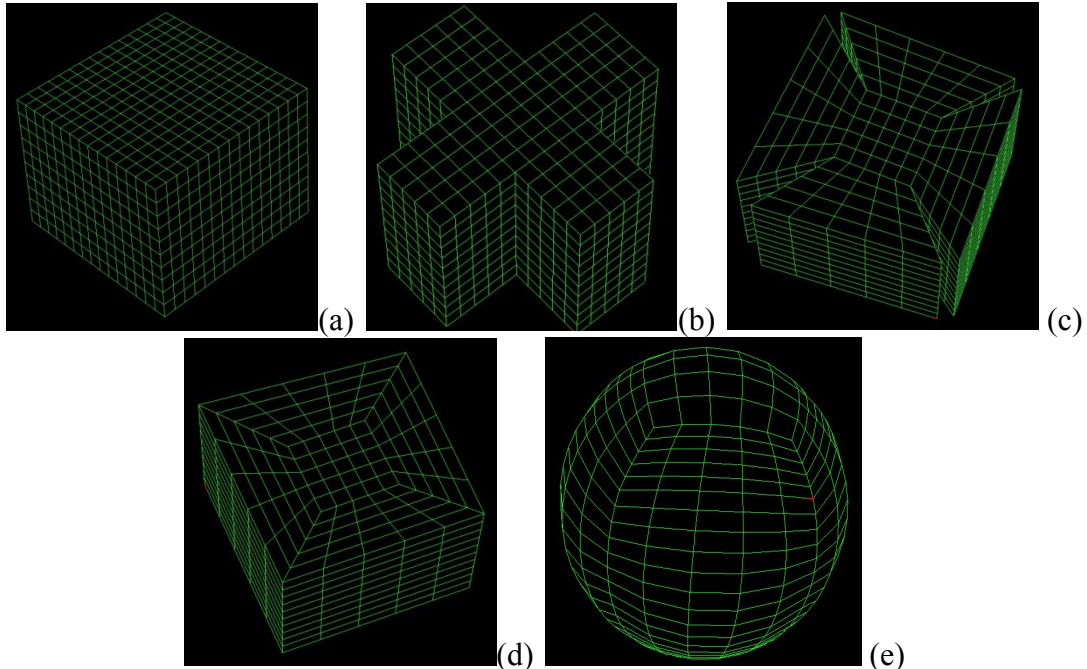
Figure 4.4: Butterfly Method
Process of creating a butterfly structure to accommodate surfaces with large curvatures. Shown here is the process of developing a general spherical surface.

(a)　　　(b)
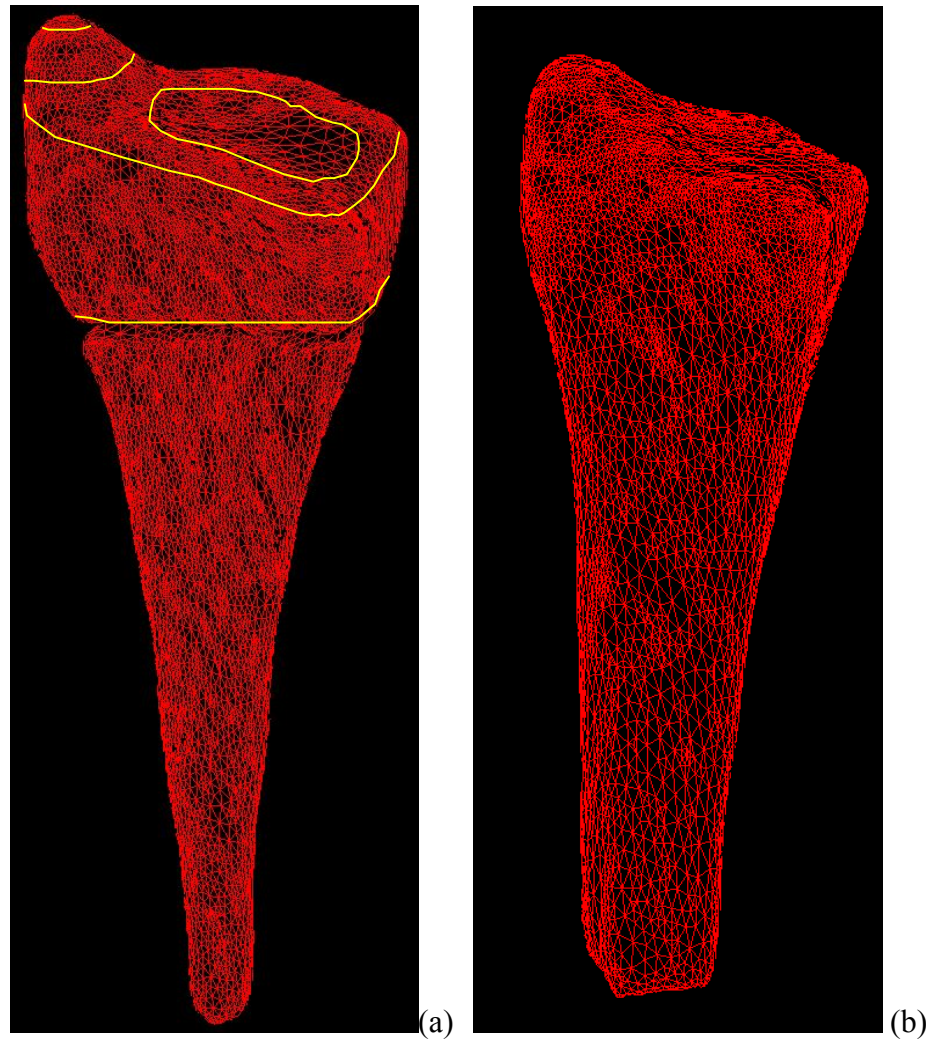
Figure 4.5: STL Bone Surfaces and 3D Splines
The cancellous and marrow (a) and the cortical (b) STL files imported
into TrueGrid® as a surface definition. Also shown in (a) are the cubic
splines generated around the tip and base of the styloid process the
interior and exterior articular surface and the proximal cancellous
region.

surface. As a result of smoothing the surfaces in Mimics®, a small gap was created between the marrow and cancellous sections. A block of elements was included to bridge the space between these surfaces. Therefore, two partitions were added to the bottom of the cancellous block structure to form the bridge and marrow block structures. Similar to the cancellous bone, splines were created and the faces of the blocks were projected onto the appropriate surfaces. To improve the quality of the mesh, density was increased and smoothing algorithms were applied to the faces and volumes.

The cortical bone mesh was created from a 5 x 5 x 4 block grid; the number of elements in the middle blocks, along the i, j, k, directions, corresponded to the number of elements in each block in the cancellous and marrow regions, and the outer blocks were two elements think to represent the cortical layer. The interior and corner blocks were deleted and the corners glued together, forming a hollow cortical layer mesh. Block boundaries were defined such that the interior nodes of the cortical mesh were forced (mapped) onto the corresponding regions of the cancellous and marrow meshes. The exterior faces were then projected onto the cortical surface. Smoothing algorithms were applied to improve the quality of the mesh as before.

4.1.2.4 Impact System Components Mesh

Experimentally (Section 2.2), the applied impact loads were transferred from the projectile through a foam covered distal bracket, a load cell, a model lunate and scaphoid, and onto the distal articular surface of the radius. The load was then terminated at a second bracket located at the proximal end of the radius (Figure 4.6b).

A 3D white light scan (Inspect X Inc. Windsor Ontario, Canada) of the

Projectile Foam Distal Bracket Load Cell Lunate/Scaphoid Specimen Pot/Cement Proximal Bracket
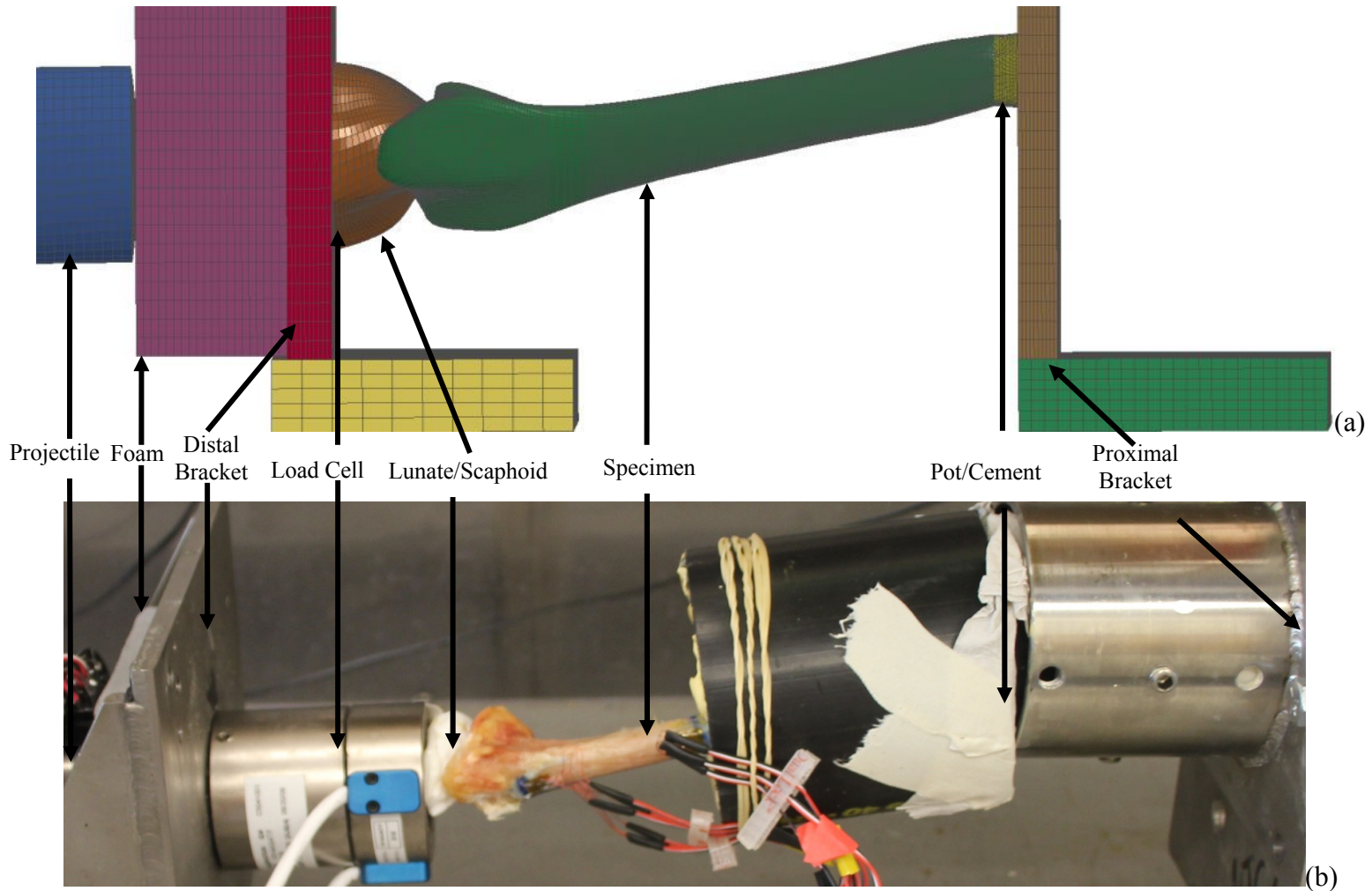
Figure 4.6: Experimental Set-up and Model Components
Radius bone mesh (a) and the components of the impactor (b). The yellow and green blocks (not labelled) represent the distal and proximal rails, respectively.

lunate/scaphoid was imported into TrueGrid® as a binary STL surface. While the surface of the lunate/scaphoid was extremely detailed, it also contained gaps as a result of the lunate/scaphoid position during the white light scan. Based on this observation, it was decided that a less detailed version of the lunate/scaphoid would still provide an accurate representation of the bones and would improve the quality of the mesh. Therefore, a series of curves were placed over the lunate/scaphoid and four new surfaces were created between the intersections of these curves. These four surfaces were then combined, generating a smoother surface of the lunate/scaphoid while maintaining the significant curvatures. Similar to the other bone components, a series of smoothing algorithms were applied. Without contact occurring (i.e. within 0.1 mm), the lunate/scaphoid was visually aligned with the articular surface of the radius (similar to the experimental set-up) (Figure 4.6a).

The distal bracket was attached directly to the lunate/scaphoid and the specific geometry of the distal bracket was not modelled, as the deformations in it were assumed to be negligible. Therefore, only a block was constructed to represent the mass of the distal bracket and the load cell (Figure 4.6a). Off of the distal bracket (25.4 mm), a fourth part was built representing the urethane foam that was used in testing to control the duration of the impulse. Finally, just off of the surface (but not touching) of the urethane foam mesh was another part representing the projectile (with the same front curvature as the projectile that was used experimentally). Similar to the components at the distal end of the radius, the pot (including the cement) was modelled as a single block off of the proximal radius. The proximal bracket was subsequently meshed off the pot with the same geometry as the distal bracket. Finally, two simple blocks were

meshed to represent the proximal and distal linear rails, to which the proximal and distal brackets were attached. All of the mesh components are shown in Figure 4.6, alongside the experimental set-up.

4.1.2.5 Mesh Diagnostics

Several mesh quality assessment techniques were used to evaluate the quality of the mesh prior to analysis. Element Jacobians provide a measure of distortion from an ideally shaped element and represent the determinant of the Jacobian matrix that defines the mapping of vertices from the ideally shaped element to the actual element (Figure 4.7a). The Jacobian of an extremely distorted (i.e. inverted) element is negative and will prevent analysis from continuing (Zhang et al., 2007). Therefore, the criterion for a Jacobian in this study was that it be a positive value and preferably greater than 0.2 (Untaroiu et al., 2005).

Elements whose interior angles deviate too far from 90° can produce unrealistic deformation responses. Therefore, the orthogonality of the mesh was also assessed by measuring the three angles and their deviations at each of the 8 nodes for all elements (Figure 4.7b). The aim of this analysis was to avoid absolute deviations greater than 70° (Quenneville & Dunning, 2011).

Finally, the last method of mesh quality assessment was calculation of the aspect ratios (Figure 4.7c). In TrueGrid®, the aspect ratio is calculated as the ratio of the longest diagonal to the shortest diagonal. The most numerically accurate solution is found when the edges of the elements are equal in length. Therefore, the goal was to achieve aspect ratios as close to one as possible while avoiding ratios greater than 10 (Untaroiu et al., 2005; Quenneville & Dunning, 2011).
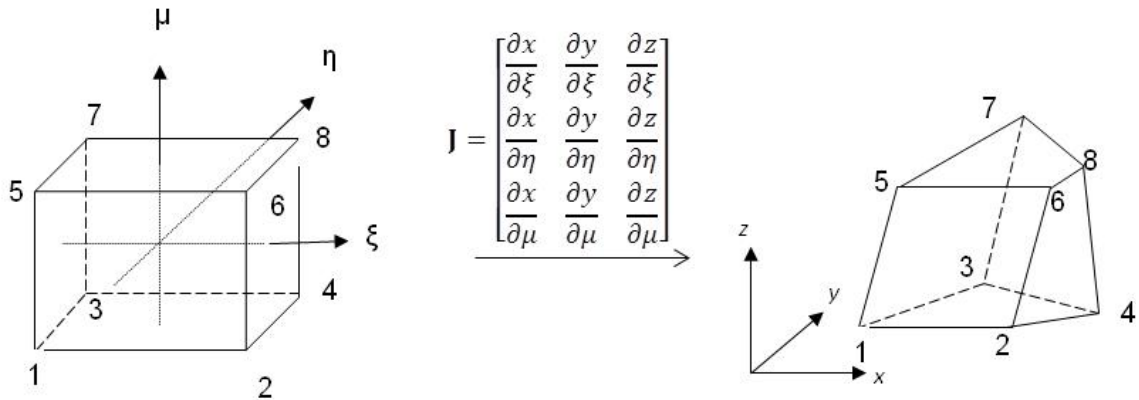
(a) Elemental Jacobian = det (**J**); where J is the Jacobian matrix representing the transformation from an ideal unit cube to the hexahedral element.
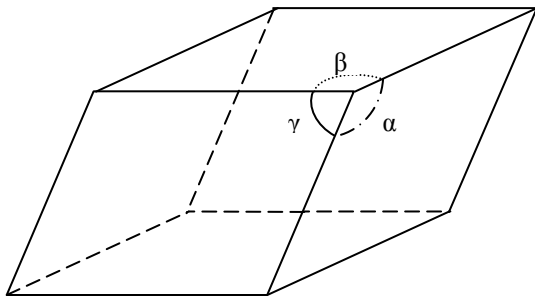
(b) Orthogonality is a measure of the three angles α, β, and γ at each of the eight vertices.

$$Aspect\ ratio = \frac{Min.}{Max.}$$
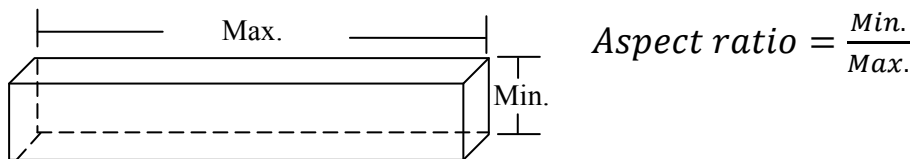
(c) The aspect ratio is the ratio of the longest side to the shortest side. Ideal elements have aspect ratios close to one.

Figure 4.7: Mesh Quality Metrics
A description of the element Jacobian (a), orthogonality (b) and aspect ratio (c) measures used to assess the quality of each element in the mesh.

4.1.3 Results

The Jacobians of the radius mesh ranged from 0.08 to 12 and 0.18 to 8 in the interior (cancellous and marrow regions) and the exterior (cortical region), respectively (Figure 4.8).

The deviation in the cancellous marrow mesh ranged from -70° to 85° (corresponding to absolute interior angles of 20° to 175°) (Figure 4.9a), while the cortical mesh had deviations ranging from -70° to 80° (corresponding to absolute interior angles of 20° to 170° (Figure 4.9b). While some angles were found to deviate more than 70°, the mean deviation was zero in all of the meshes and less than 50 (out of more than 900 000 elements) elements were found to violate this rule.

The aspect ratios for the cancellous and marrow mesh section ranged from 1.2 to 12.4 (Figure 4.10a). Aspect ratios between 1.1 and 26 were found for the cancellous mesh (Figure 4.10b). While the maximum aspect ratio for the cortical bone was far greater than the cut-off value of 10, only one element was shown to have this value and it was located away from the area of interest. The remaining elements had aspect ratios that ranging from 1.1 to 15.

4.1.4 Discussion

To the authors' knowledge, this is the first finite element mesh accurately representing the distal third of the radius that is composed entirely of solid hexahedral elements. The mesh presented here includes components for the cortical, cancellous and marrow sections of the radius bone and all of the structures of the impact apparatus.

While previous studies have used finite element models of the radius to predict
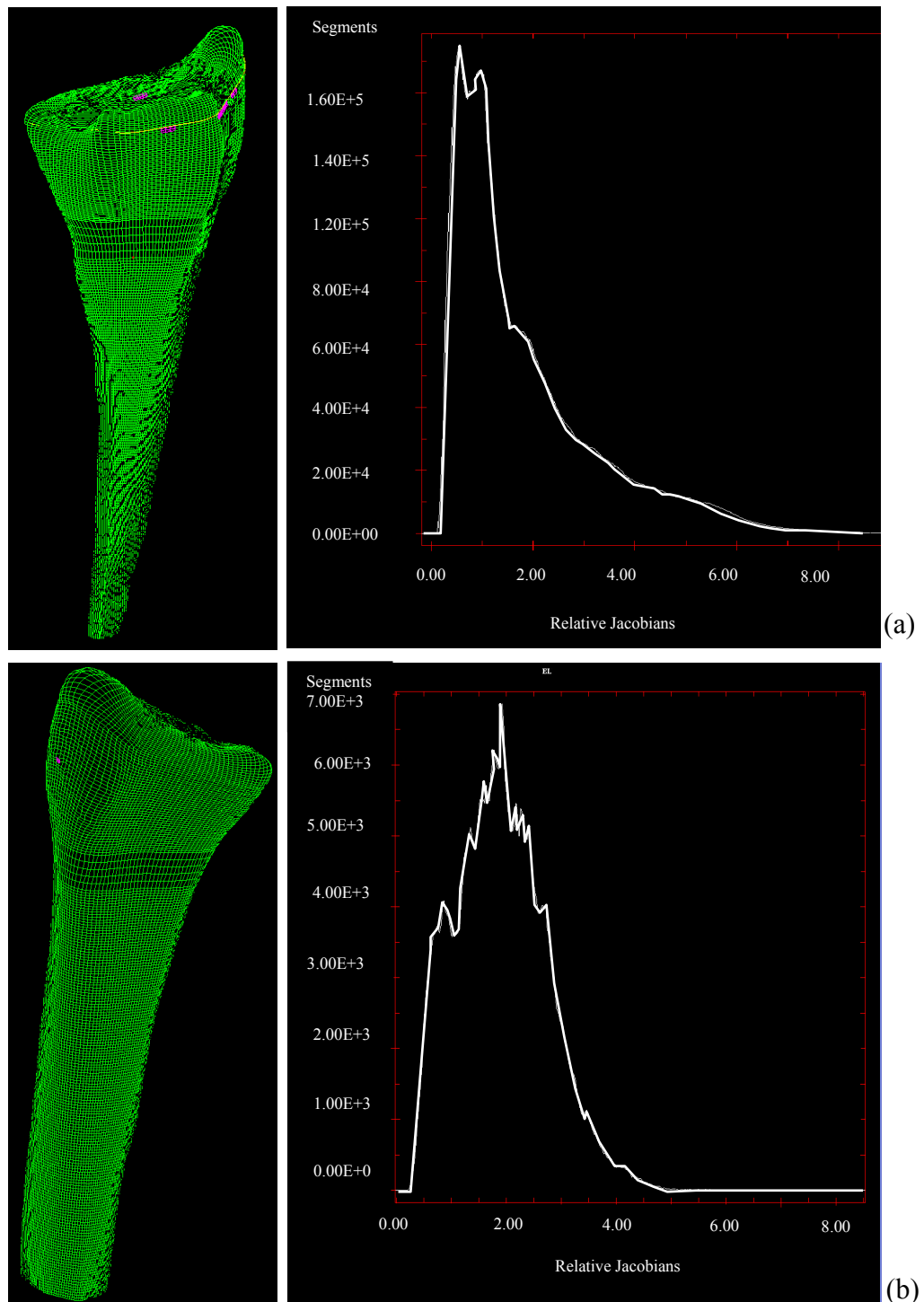
Figure 4.8: Element Jacobians
Element Jacobians of the cancellous and marrow (a) and the cortical (b) mesh
sections. Elements with Jacobians less than 0.2 are highlighted pink.

(a)

(b)
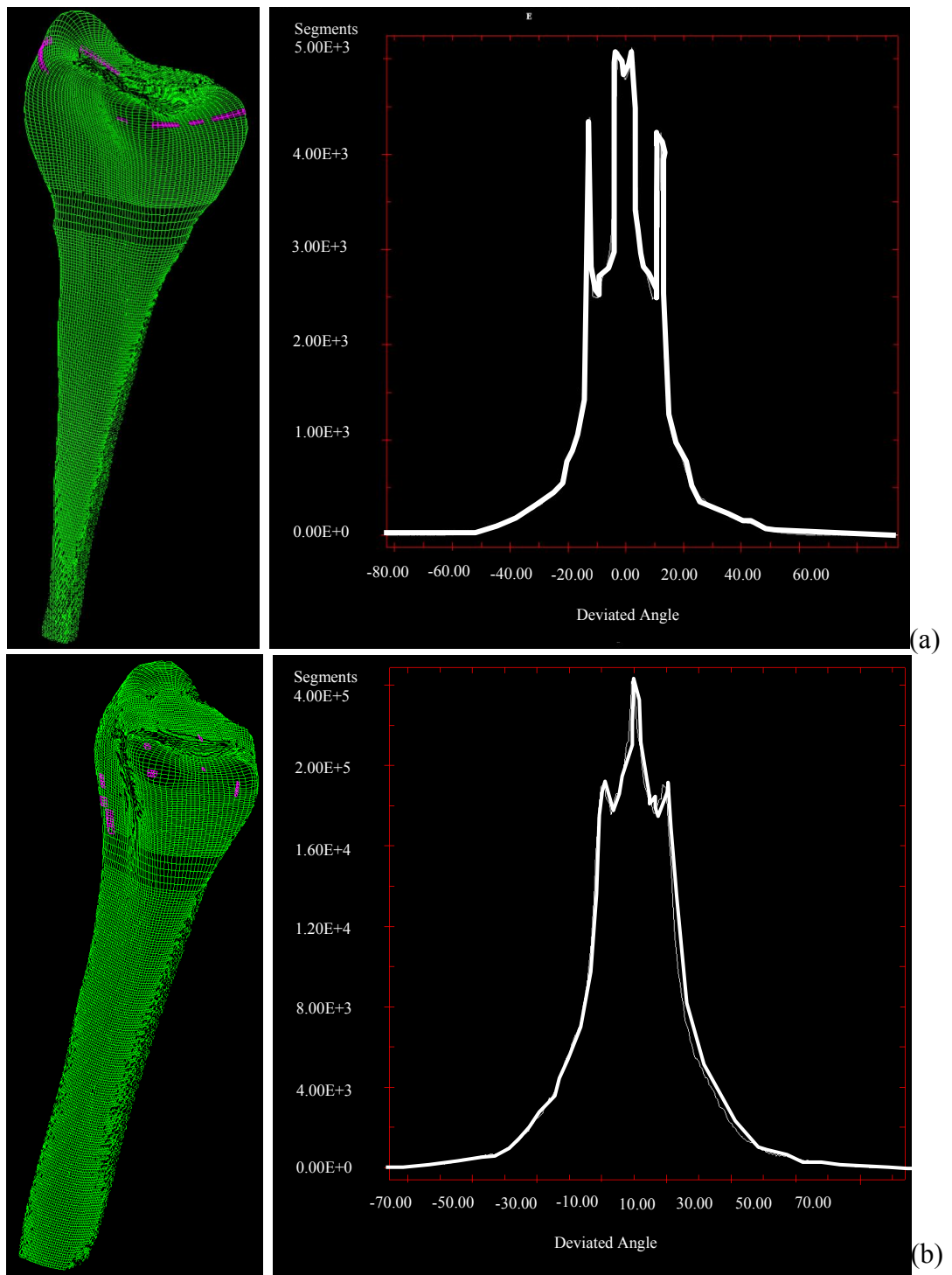
Figure 4.9: Element Orthogonality
Element orthogonality of the cancellous and marrow (a) and cortical (b) mesh
sections. Elements with absolute deviations greater than 75° are highlighted pink.
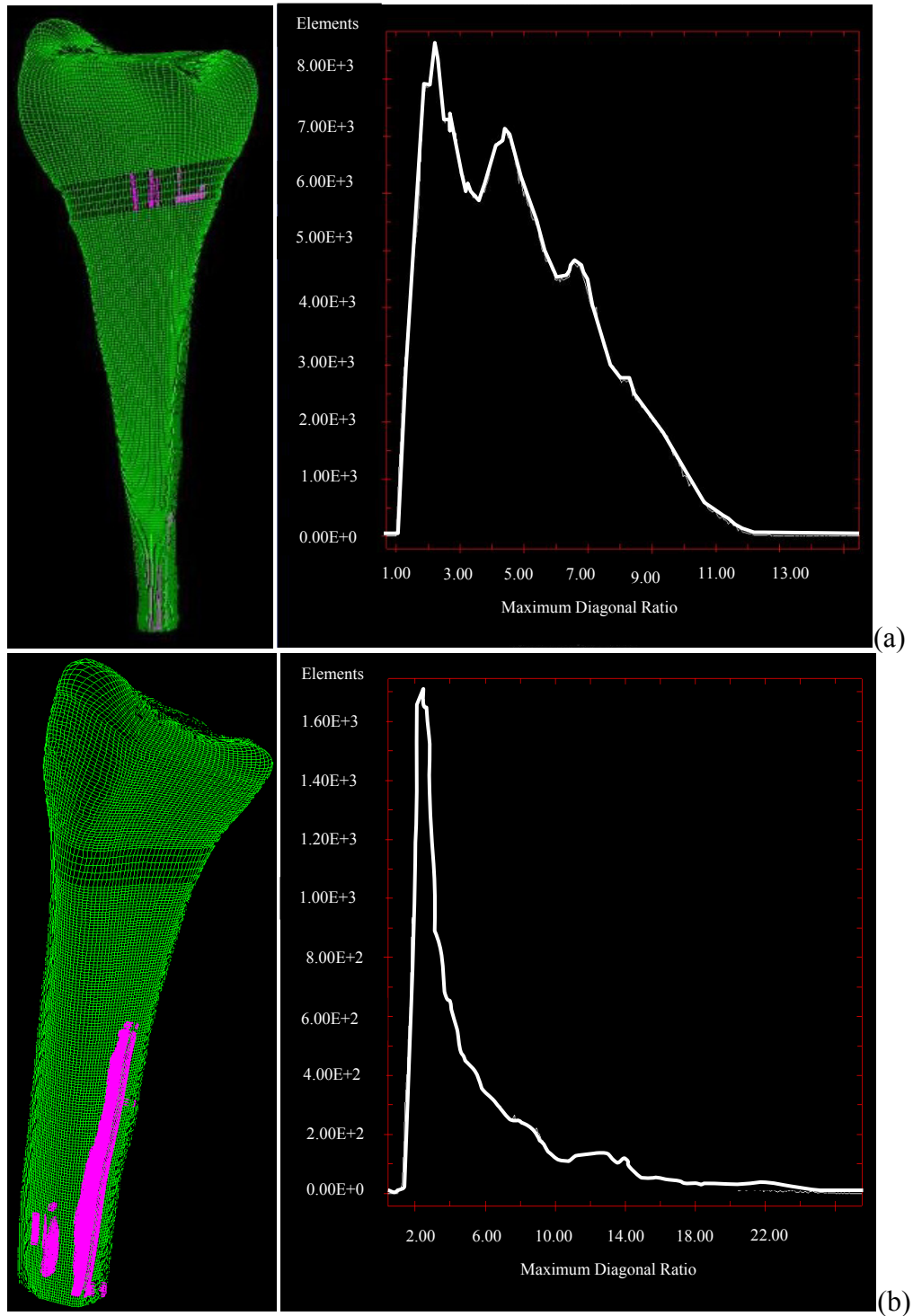
Figure 4.10: Element Aspect Ratios
Aspect ratios for the elements in the cancellous and marrow (a) and the
cortical (b) mesh sections. Elements with aspect ratios between 10 and 20 are
highlighted in pink.

the response to loading, none have included an assessment of the mesh quality. The mesh diagnostics presented here suggest that this is a relatively high quality mesh appropriate for the development of a finite element model.

With respect to the majority of past models, only small sections of the radius were represented and not all types of bone (cortical, cancellous, marrow) have been included. Therefore, an accurate representation of the geometry of the distal third of the radius and all of the bone types was the top priority in developing this mesh. In the current model, the geometry of the entire distal third of the radius (the region most commonly injured) was extracted directly from CT scans of the radius. This method of geometry extraction allowed all three bone types to be expressed in the mesh. The mesh itself was created by generating control curves (i.e. 3D splines) and projecting the mesh block structure onto the surfaces created in Mimics®, a method unique to the TrueGrid® software.

The final bone meshes were highly descritized, consisting of over 900 000 elements. However, a sensitivity analysis was not conducted and therefore it is possible that a coarser mesh would have performed as well and would have decreased the computational costs of the model. The vast majority of the elements met the diagnostic criteria of a high quality mesh (Untaroiu et al., 2005). While there were some elements that did not meet these parameters, they were not located in areas of high interest (i.e. the articular surface of the radius and the distal radial diaphysis) and were generally less than 0.5 % of all the mesh elements. This mesh will be used in Section 4.3 to simulate experimental impacts to the distal radius, addressing the validation of this model.

4.1.5 References

Anderson DD, Deshpande BR, Daniel TE, Baratz ME. 2005. A three-dimensional finite element model of the radiocarpal joint: distal radius fracture step-off and stress transfer. The Iowa Orthopaedic Journal. 25, 108-107.

Boutroy S, van Rietbergen B, Sornay-Rendu E, Munoz F, Bouxsein ML, Delmas PD. 2008. Finite element analysis based on *in vivo* HR-pQCT images of the distal radius is associated with wrist fracture in postmenopausal women. Journal of Bone and Mineral Research. 23, 392-399.

Buchanan D, Ural A. 2010. Finite element modeling of the influence of hand position and bone properties on the colles' fracture load during a fall. Journal of Biomechanical Engineering. 132, 081007-1 - 081007-8.

Carrigan SD, Whiteside RA, Pichora DR, Small CF. 2003. Development of a three-dimensional finite element model for carpal load transmission in a static neutral posture. Annals of Biomedical Engineering. 31, 718-725.

Edwards WB, Troy KL. 2010. Finite element predictions of surface strain and failure load at the distal radius using simplified boundary conditions. Proceedings of the American Society of Biomechanics Conference, Providence Rhode Island.

Fyllingen, O., Hopperstad, O. S., Hanssen, A. G., Langseth, M. 2009. Brick elements versus shell elements in simulations of aluminum extrusions subjected to axial crushing. 7th European LS-DYNA conference, Salzburg, Austria.

MacNeil JA, Boyd SK. 2008. Bone strength at the distal radius can be estimated from high resolution peripheral quantitative tomography and the finite element method. Bone. 42, 1203-1213.

Pistoia W van Rietbergen B, Lochmuller E-M, Lill CA, Eckstein, F., Ruegsegger, P. 2002. Estimation of distal radius failure load with micro-finite element analysis models based on the three-dimensional peripheral quantitative computed tomography images. Bone. 30, 842-848.

Pistoia W, van Rietbergen B, Lochmuller E-M, Lill CA, Eckstein F, Ruegsegger P. 2004. Image-based micro-finite-element modeling for improved distal radius strength diagnosis: moving from "bench" to "bedside". Journal of Clinical Densitometry. 7, 153-160.

Pistoia W, van Rietbergen B, Ruegsegger P. 2003. Mechanical consequences of different scenarios for simulated bone atrophy and recovery in the distal radius. Bone. 33, 937-945.

Quenneville CE, Dunning CE. 2011. Development o a finite element model of the tibia for short-duration high-force axial impact loading. Computer Methods in Biomechanics and Biomedical Engineering. 14, 205-212.

Rogge RD, Adams BD, Goel VK. 2002. An analysis of bone stresses and fixation stability using a finite element model of simulated distal radius fractures. Journal of Hand Surgery. 27A, 86-92.

Tautges TJ. 2001. The generation of hexahedral meshes for assemble geometry: survey and progress. International Journal for Numerical Methods in Engineering. 50, 2617-2642.

Troy KL, Grabiner, M.D. 2007. Off-axis loads cause failure of the distal radius at lower magnitudes than axial loads: a finite element analysis. Journal of Biomechanics. 40. 1670-1675.

Ulrich D, van Rietbergen B, Laib A, Ruegsegger P. 1999. Load transfer analysis of the distal radius from *in vivo* high resolution CT-imaging. Journal of Biomechanics. 32, 821-828.

Valle L, Ray MH. (2005). Development and validation of a 50th percentile male human femur: Attachment A. Worchester Polytechnique Institute. Worchester, MA, National Highway Traffic Safety Administration.

Untaroiu C, Darvish K., Crandall J, Deng B, Wang T-W. 2005. A finite element model of the lower limb for simulating pedestrian impacts. Stapp Car Crash Journal. 49, 157-181.

Zhang Y, Hughes TJR, Bajaj CL. 2007. Automatic 3D mesh generation for a domain with multiple materials. Proceedings of the 16th International Meshing Roundtable, Seattle, Washington, 367-386.

4.2 Development and Validation of a Finite Element Model to Simulate Dynamic Impacts to the Distal Radius.

4.2.1 Introduction

Numerical models (i.e. finite element models) provide a practical approach to measuring the response of a bone (i.e. stresses and strains) to a variety of loading protocols (Cristolfolini et al., 2010). They provide a particularly good alternative to cadaveric testing of a bone's response to impact loading, given the relatively destructive nature of *in vitro* impact testing (Quenneville, et al., 2011).

A number of finite element models of the distal radius have been developed to test a range of loading conditions and bone material properties. For example, Pistoia et al. (2002, 2003, 2004) and MacNeil et al. (2008) developed finite element models to test the effect of bone mineral density on the overall strength of the radius. Troy & Grabiner (2007) and Buchanan et al. (2010) used their models to determine how loading direction affects the fracture force of the distal radius. While these models have been successful in providing valuable information regarding the general strength of bone, the static loading conditions used in these studies do not make them applicable to situations where dynamic impact loading occurs. These models have also not considered the kinematics of a forward fall, such as the angle the forearm makes with the ground or the angle of the wrist at impact. Furthermore, the distribution of the load through the carpals and onto the articular surface of the radius has been applied through boundary conditions taken from past radius loading studies. As such, it is inappropriate to these models to assess the risk of injury to the distal radius following a forward fall.

Finally, past radius finite element models have provided little to no information about how they were validated. Validation of a model's performance against experimental data allows the researcher to assess the credibility of their model (Oberkampf & Trucano, 2002, 2008). This is especially true when the model has human and biological applications such as injury prediction. Oberkampf & Trucano (2002, 2008) suggest that, while graphical validation (i.e. visually comparing time domain data between experimental and numerical situations) can provide a measure of the agreement between experimental and numerical data, a more empirical method should also be included.

Therefore, the purpose of this study was twofold: i) to develop a finite element model (based on the radius mesh presented in Section 4.1) designed to simulate dynamic impacts, and ii) to validate the model using empirically-based validation methods.

4.2.2 Methods

4.2.2.1 Software Overview

The finite element software used in the study was LS-DYNA® (LSTC, Livermore, CA, USA). LS-DYNA® is capable of handling large strain dynamic simulations making it a good solver for assessing the effects of dynamic impact loading. LS-DYNA® is accompanied by a complimentary model editor known as LS-PrePost®, that is used for initial model setup and plotting the outputs of the simulation.

The LS-DYNA® solver runs text based input files, which follow a specific "keyword" format. Keywords with similar functions are grouped together in cards (e.g., material definitions, part definitions, boundary conditions, etc.) and have a predefined

structure for parameter input. LS-DYNA$^®$ contains over 150 material models and their

descriptions can be found in the LS-DYNA$^®$ Keyword Users Manual (LSTC, 2007). A

number of element formulations also exist for each material that affect how the stress is

computed through an element. For example, three element formulations exist for solid

elements: the default constant stress solid (ELMFORM 1), which has a single

integration point; the fully integrated selective reduced solid (ELMFORM 2), which has

eight integration points; and the fully integrated quadratic 8 node element with nodal

rotations (ELMFORM 3), which has 14 integration points. These element formulations

are listed in order of precision and computational cost.

4.2.2.2 Input File Creation

The mesh that was developed in Section 4.1 and output in LS-DYNA$^®$ format

was used for the finite element analysis described here (Appendix H). Each of the

components (cortical bone, cancellous bone, marrow bone, carpals, projectile,

pot/cement proximal and distal brackets, and proximal and distal bearings) were

assigned separate part, section and material identifications that corresponded to the node

and element data generated in TrueGrid$^®$. A number of commands had to be manually

written into the deck for proper functioning and the units were selected as mm, ms, kg

and kN. The duration of the simulation was time controlled and set to 25 ms; long

enough to allow for full application of the impulse that was calculated from the

experimental impacts described in Chapter 2.

Contact definitions (automatic surface-to-surface) were required to prevent the

nodes of contacting parts from penetrating one another. Specifically, the automatic

surface-to-surface contact definition was used between the projectile and the foam

(static and dynamic coefficient of friction of 0.3), the carpals and the distal aspect of the cortical bone (static and dynamic coefficient of friction of 0.01), the proximal bracket and proximal bearing and the distal bracket and the distal bearing (static and dynamic coefficient of friction of 0.5). Since the nodes between the foam/distal bracket, distal bracket/carpals and the proximal cortical bone/proximal bracket were coincident and merged (i.e. forming a continuous mesh) no contact parameters between these parts were required. To ensure rigid contact between the pot/cement and the proximal bracket, the *CONSTRAINED_RIGID_BODIES command was implemented to merge the two parts together.

Finally, boundary conditions are also required and had to be written into the deck. To constrain the motion of the distal bracket within the x-y plane, a planar joint was defined between the distal bracket and the distal bearing. This required creating a set of nodes from both parts that is used to define the direction of the normal. Two separate three node sets were then used to form the coordinate systems within each of the parts. A force was applied to the distal bracket, simulating the frictional force between the distal bracket and linear rail that results from the large bending moment resisted by the bearings. A coefficient of friction of 0.5 was used based on the data from a previous experimental investigation using the impactor described in Chapter 2 (Quenneville, 2009; Quenneville et al., 2011). The motion of the projectile and the proximal bracket were also constrained to the z-direction. An initial velocity was applied to the projectile that was varied to mimic the pre-fracture (2.1 m/s), crack (2.7m/s) and the fracture (3.3 m/s) impact events.

The impact forces were calculated at a cross-section that was defined through the second layer of elements of the carpal bones (DATABASE_CROSS_SECTION_SET). This location was chosen given its close proximity to the experimental load cell. A node set is formed that defines the nodes through the cross section and an element set is then constructed that includes all of the elements to one side of the cross-section node set. Element sets of the elements representing the corners and centers of the strain gauges were also created. Lastly, given the angle of the bone within the impactor and the orientation of the accelerometers experimentally, it was necessary to define local coordinate systems within the model at the locations of the accelerometers (Figure 4.11). This ensured that the accelerations from the model were calculated along axes that corresponded to the experimental accelerometers. Outputs were written to record the forces, strains, and accelerations of the node, element and cross-section sets, that were used to validate the model against the experimental data collected in Chapter 2.

4.2.2.3 Impactor Components

The components used in the experimental investigation (Chapter 2) were defined based on their known material properties.

4.2.2.3.1 Rigid Components

There were five stainlesss steel components used in the current model: the projectile, the proximal and distal brackets and the proximal and distal rails. The stainless steel components were modelled as rigid materials (LS-DYNA$^®$ material model MAT_20), as it was determnined that the stainless components would undergo

Figure 4.11: Model Accelerometer Locations
Radius and carpal finite element model showing the local coordinate systems of the
distal and proximal accelerometer locations and the force axes created within the carpal
cross-section.

minimal deformations compared to bone (i.e. stainless steel is approximtaley 10 times as stiffer than bone). Modelling these components as rigid reduces the computational complexity of the model, as the nodes do not move relative to one another. The masses of the model stainless steel components were matched to the corresponding experimental components by calculating the volumes of each "block" of rigid material (measured in LS-PrePost®) and adjusting the densities assigned to each (Table 4.2).

4.2.2.3.2 Polyurethane Foam

Foams can contain highly variable material properties and often experience large deformations, making it difficult to simulate their behaviours. LS-DYNA® also contains approximately 15 different foam material models. Sambamoorthy & Halder (2001) recommended a low density foam material model as it has shown good correlation with experimental results and is appropriate for simulating highly compressible foams (i.e. a foam that is typically used to simulate seat cushion foams (LSTC, 2007)). To avoid unrealistically large deformations compared to what was seen experimentally, an internal contact was included in the definition of the foam material. The modulus of the foam (Table 4.2) was determined previously from experimental compression tests using an Instron® materials testing machine (Instron® 8872, Canton, MA, USA) (Quenneville, 2009).

4.2.2.3.3 Polyethylene Carpals

The carpal bones, specifically the lunate and scaphoid, were composed of high-density polyethylene (SawBones®, Pacific Research Laboratories Inc., Vashon Washington). While polyethylene undergoes relatively small deformations

Table 4.2: Model Bone Material Properties
Material properties assigned to each of the model components.

Part	Mass Density (kg/m^3)	Rigid Part Volume (mm^3)	Elastic Modulus (GPa)	Plastic Modulus (GPa)	Poisson's Ratio	Yield Stress (GPa)	C[b] (/s)	p[b]
Cortical Bone	1150	-	25.1	1.255	0.3	0.124	64.7	6.4
Cancellous Bone	970	-	1.8	0.090	0.3	0.0010	64.7	6.4
Marrow	1070[a]	-	0.02	-	0.499	-	-	-
Lunate/Scaphoid	1060	-	3.0	-	0.38	-	-	-
Projectile	930	7302.0	210.0	-	0.3	-	-	-
Pot/Cement	1.0E+4	253.9	210.0	-	0.3	-	-	-
Proximal Bracket	205	20945.1	210.0	-	0.3	-	-	-
Distal Bracket	220	19489	210.0	-	0.3	-	-	-
Foam	52	-	0.008	-	0.3	-	-	-
Rear Bearing	5.0E+6	-	210.0	-	0.3	-	-	-
Front Bearing	5.0E+6	-	210.0	-	0.3	-	-	-

[a]Interpolated from a linear relationship between Hounsfield Units and density presented by Peng et al. (2006).
[b]Calculated from the McElaney (1966) data set.

(Quenneville, 2009), it was modelled as an elastic material (LS-DYNA® material MAT_001) so that three force components (Fx: medial-lateral; Fy: inferior-superior; Fz: axial (Figure 4.11) could be calculated for the node set representing the load cell.

4.2.2.4 Bone Components

The complexities of cortical and cancellous bone often make it difficult to select the proper modeling parameters (Figure 4.12). This includes selecting the proper material models (e.g., elastic, elastic-plastic), element formulations (e.g., fully integrated, constant stress), strain rate forms (e.g., family of curves), and failure criteria (von-Mises stresses). It is important that care be taken in selecting the appropriate parameters, as these can significantly influence the behaviour of the model.

4.2.2.4.1 Material Models

Traditionally, bone has been modelled as a linear elastic material (Troy & Grabiner, 2007; Anderson et al., 2008; Boutroy et al., 2008), but this type of model does not account for yielding, plastic deformations or strain rate effects. Two elastic-plastic material models, with (Kim et al., 2005) and without (Untaroiu et al., 2005) damage (which incorporate the von-Mises stress criteria to indicate transition into the plastic region), have been used previously to overcome the limitations of an elastic model. Both the elastic-plastic with and without damage material models consist of a bi-linear modulus curve with the option of including strain rate effects (LSTC, 2007). However, the elastic-plastic with damage material model also incorporates continuum mechanics and deletes an element when a failure strain is experienced (LSTC, 2007). It is hypothesized that this mimics the fracture process, such that the deleted element is no

| Elastic-Plastic (MAT 24) | Elastic-Plastic with Damage (MAT 81/105) | | Constant Stress (1) | Fully Integrated Quadratic (3) |

```
   Elastic-Plastic        Elastic-Plastic                Constant         Fully
     (MAT 24)              with Damage                    Stress (1)       Integrated
                           (MAT 81/105)                                    Quadratic (3)

              Material Model                                   Element Formulation

                              Bone Properties

         Strain Rate Formulation                          Failure Criteria

   Cowper-        Family of                      von-Mises        Maximum
   Symonds        Curves                         Stress           Principal
                                                                  Strain
```

Figure 4.12: Model Properties Summary
A summary of the properties that are needed to define the behaviour of the bone model in LS-DYNA® (modified from Quenneville (2009)). The boxes with the dashed outline highlight those properties that were adopted in the distal radius model described here (Note: The bone marrow was modelled strictly as an elastic material).

longer able to bear a load, but results in unrealistically low impact forces (Quenneville, 2009).

4.2.2.4.2 Element Formulations

With respect to the element formulations, a constant stress (ELFORM 1) and fully integrated (ELFORM 3) solution are available. In the constant stress element formulation the stresses are calculated at only one integration point at the center of the element. While this offers the most computationally efficient formulation, it can be at risk of experiencing a phenomenon called hourglassing (i.e. deformations that occur in a state of zero stress). The fully integrated element formulation, with 14 integration points, is not prone to hourglassing and is more accurate, but is much more computationally expensive (Valle & Ray, 2005).

4.2.2.4.3 Strain Rate Formulations

The viscoelastic properties of bone make its response to loading dependent on the strain rate (Nordin & Frankel, 2001) and LS-DYNA® provides two approaches for incorporating these effects into the model. The first is the Cowper-Symonds model (Jones, 1989), which scales the static yield stress (Figure 4.13) according to the factor:

$$1 + \left(\frac{\dot{\varepsilon}}{C}\right)^{\frac{1}{p}} \qquad \text{(Eq. 4.1)}$$

Where $\dot{\varepsilon}$ is the strain rate, and C and p are material-specific parameters that are determined experimentally. The second strain rate formulation uses a family of strain rate dependent stress-strain curves (Figure 4.14) (Untaroiu et al., 2004).
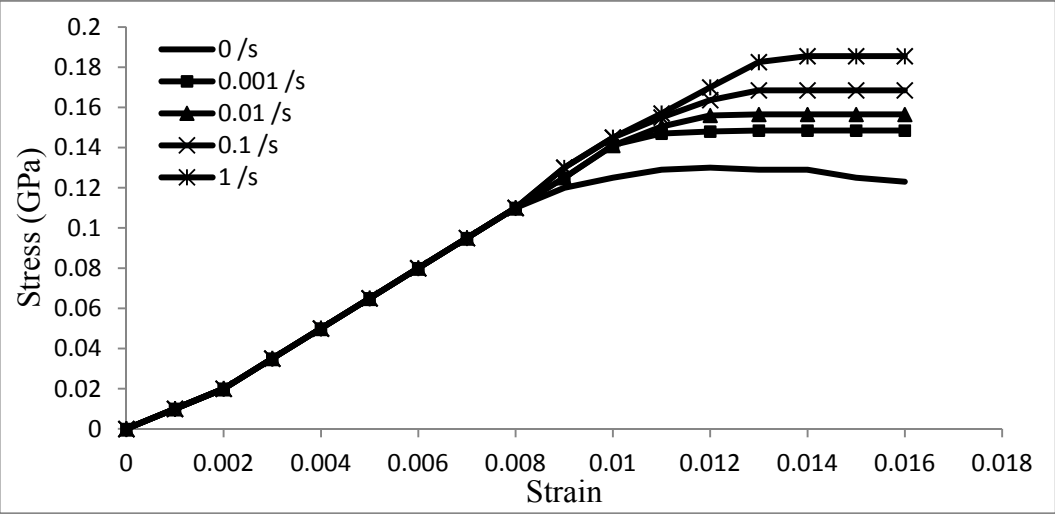
Figure 4.13: Cowper-Symonds Strain Rate Effects
A series of strain rate (/s) dependent stress-strain curves calculated using the
Cowper-Symonds strain rate effect model. This method scales the yield stress
only.
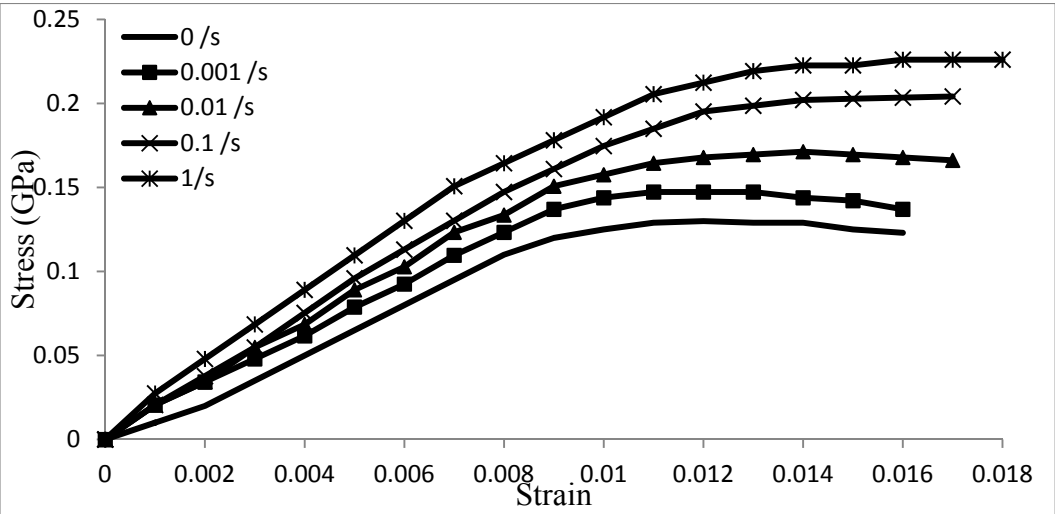
Figure 4.14: Family of Curves Strain Rate Effects
An example of a series of strain rate (s^{-1}) dependent stress-strain curves (Untaroiu,
et al., 2004). In this method, both the modulus and the yield stress are scaled.

4.2.2.5 Selection of Optimal Bone Parameters

To date, only one study (Quenneville, 2009) has investigated the effect of each of the above variables on the validity of the presented model. With respect to the material models, Quenneville (2009) found that the elastic-plastic with and without damage material models underestimated and overestimated the peak fracture force by approximately 200 % and 35 %, respectively. The underestimation of the material model with damage can be attributed to the erosion of elements and their inability to bear a load (Quenneville, 2009).

For the element formulations, the fully integrated form predicted the peak experimental impact force better than the constant stress formulations by approximately 200 N, but required more than 10 times the computing time to run the simulations.

While the Cowper-Symonds strain rate formulation predicted the peak force better than the family of curves, it performed less well in predicting the impulse, impulse duration and velocity. Currently however, a family of curves does not exist specifically for the upper extremity.

Finally, the von-Mises stress failure criteria performed better than the maximum principal strain, as the maximum principal strain method was unable to predict failure in the cancellous region during the fracture trials, but tended to predict failure in the cortical region during the non-fracture impacts. However, Quenneville (2009) also tested an injury criteria model (similar to those developed in Section 2.3) and found that these models were successful in predicting injury.

The bone parameters in the current study were based on the results presented by Quenneville (2009) and discussed above. An elastic-plastic (LS-DYNA®MAT_124)

material model was selected for the cortical and cancellous bone, while an elastic model was chosen to represent the bone marrow. Given the savings in computation time, the constant stress element formulation was chosen (ELFORM1) for all bone types. The constant strain element formulation is especially prone to hourglassing, therefore hourglass control was implemented as stiffness form of type 3. The Cowper-Symonds strain rate formulation was also selected for the three types of bone, as there are currently no family of curves that exist specifically for the distal radius. Finally, the von-Mises stresses and the injury criteria model developed in Chapter 3 was used to assess the probability and location of injury during the crack and fracture events for the simulations presented here. The critical stress levels were set to 134 MPa and 5.3 MPa for the cortical and cancellous bone, respectively (Untaroiu et al., 2005).

4.2.2.6 Bone Material Properties

The properties required to define the cortical bone were density, elastic modulus, Poisson's ratio, yield stress and tangent (plastic) modulus. The cortical bone densities reported in the literature have ranged from 902 kg/m^3 (Boutroy et al., 2005) to 2288 kg/m^3 (Troy & Grabiner, 2007). A value of 1150 kg/m^3 was selected for the cortical bone based on sex-specific and age-adjusted densities (Schonenau et al., 2002).

To date, no radius-specific elastic modulus has been presented; therefore, an elastic modulus of 25.1 GPa was selected based on an age-specific relationship presented by Burstein et al. (1976). The Poisson's ratio used in previous finite element models (Lengsfeld et al., 1998; Pistoia et al., 2004; Boutroy et al., 2008) has consistently been reported at 0.3 and was used in the current model as well. Similar to the elastic modulus, the yield stress was also based on the age of the specimen and was

determined to be approximately 0.124 GPa (Burstein, 1976). A plastic modulus of 1.25

GPa was used based on the findings of Imai et al. (2006), who found that the plastic

modulus is approximately 5 % of the elastic modulus. Finally, given that the Cowper-

Symonds model (Eq. 4.1) was used to scale the yield stress in response to the strain rate,

bone-specific C and p parameters were defined based on the experimental data set

presented by McElhaney (1966). The Cowper-Symonds model (Eq. 4.1) can be re-

written as:

$$\dot{\varepsilon} = C \left(\frac{\sigma_o'}{\sigma_o} - 1 \right)^p \qquad \text{(Eq. 4.2)}$$

Where, C and p are the material-specific parameters, $\dot{\varepsilon}$ is the strain rate, σ_o' is the

dynamic strain rate-specific yield stress and σ_o is the static yield stress.

Equation 4.2 can be written as:

$$ln\dot{\varepsilon} = p \; ln \left(\frac{\sigma_o'}{\sigma_o} - 1 \right) + ln \, C \qquad \text{(Eq. 4.3)}$$

which represents the equation of a straight line. The above forms of the yield stress and

strain rates are then plotted against each other (Figure 4.15) and the C and p parameters

can be determined, such that ln C is the intercept and p is the slope of the regression line

describing the above relationship. Based on this data set: ln C = 4.176, C = 65.1/s and p

= 6.4.

The properties that are needed to describe the cortical bone are also required for

the cancellous bone material. An element-specific cancellous bone density (976 kg/m^3)

was described by Troy & Grabiner (2007) based on the Hounsfield values of a CT

scanned distal radius (Lotz et al., 1990). Values for the elastic modulus vary greatly in
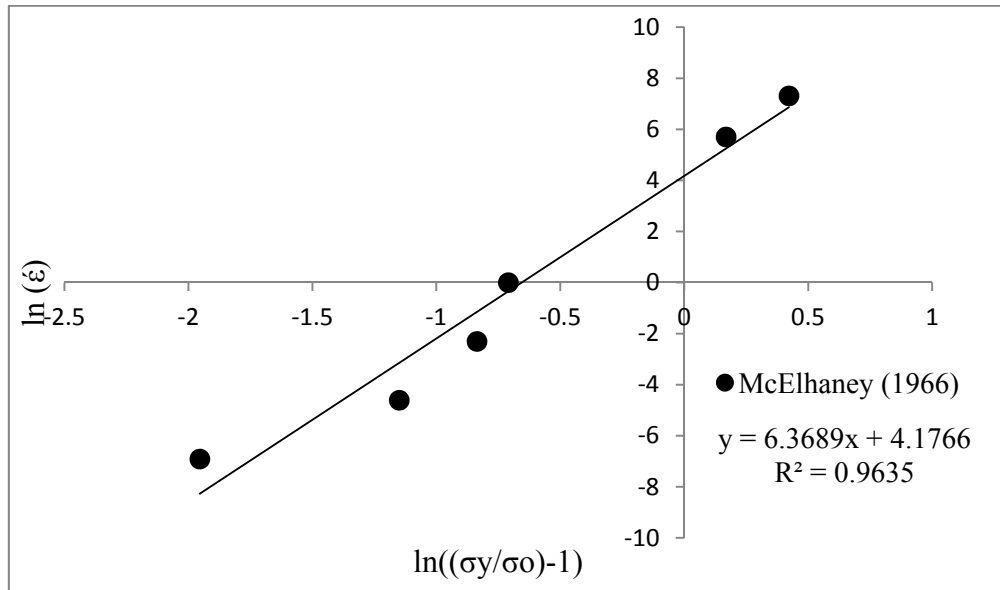
Figure 4.15: Cowper-Symonds Parameters
The transformed McElhaney (1966) data plotted to determine the *C* and *p* parameters of the Cowper-Symonds strain rate effects model.

the literature, ranging from 0.1 GPa to 18.1 GPa, and appear to be segment specific (i.e. femur vs. radius). Only Troy & Grabiner (2007) have provided radius-specific elastic moduli (1.8 GPa) and their values are based on the cancellous bone density just described (Wirtz et al., 2000). The tangent (plastic) modulus for cancellous bone is also assumed to be 5 % of the elastic modulus (Imai et al., 2006). According to this relationship, a plastic modulus of 0.09 was assigned to the cancellous bone. The yield stress of cancellous bone was adopted from Kim et al. (2005) and set at 0.01 GPa. The values for Poisson's ratio (0.3), and the C (65.1 /s) and p (6.4) Cowper-Symonds parameters were identical to those used to describe the cortical bone.

To date, no finite element models of the radius and only a few lower extremity models (Quenneville et al., 2011) have included the bone marrow. The bone marrow has generally been neglected due to its limited ability to transmit load. However, Carter & Hayes (1977) suggested that the bone marrow is capable of transmitting a load at strain rates above 10 /s. While the strain rates reported in Chapter 2 were on the order of 1/s, the marrow was still included here in order to more accurately represent the distal radius. The marrow was defined as an elastic material and therefore, only the density, elastic modulus, and Poisson's ratio are required. The density of the bone marrow was interpolated from the linear relationship between Hounsfield Units (HU) and density (R^2=1) (Peng et al., 2006) (Figure 4.16) determined from water (HU = 0, density = 1000 kg/m^3) and cortical bone (HU = 1500, density = 2000/m^3). In Peng et al. (2006), bone marrow was assigned a HU of 100, resulting in a density of approximately 1067 kg/m^3.
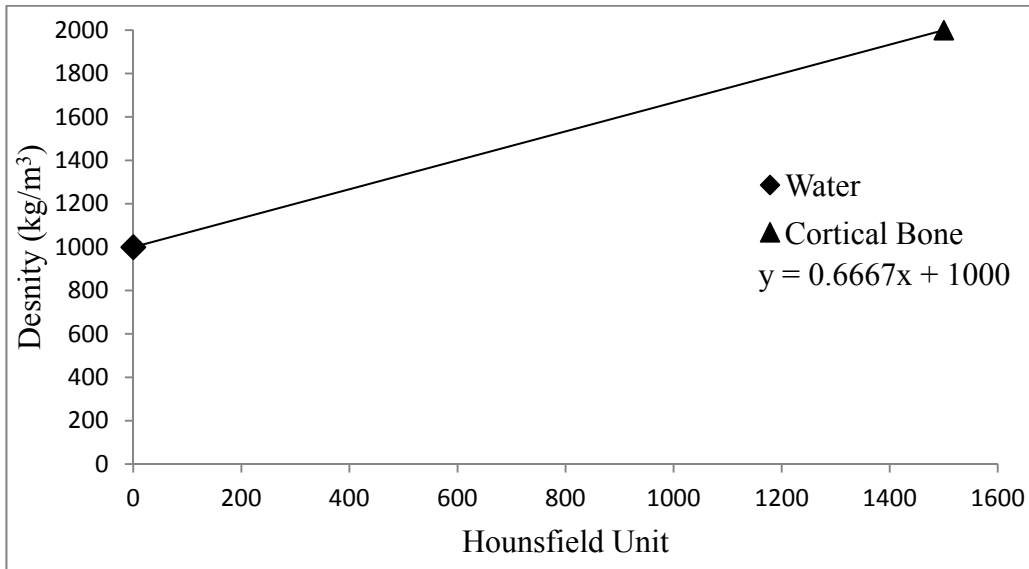
Figure 4.16: Hounsfield Unit Density Relationship
Relationship between Hounsfield units and density (Peng et al., 2006). This
relationship was used to calculate the density of bone marrow at a Hounsfield
unit of 100.

The elastic modulus and Poisson's ratios were assigned values of 0.02 GPa (Peng et al.,

2006) and 0.499 (Pitzen et al., 2002; Peng et al., 2006), respectively.

4.2.2.7 Model Validation

The methods used to validate past finite element models have varied greatly

(Andersson et al., 2007). The confidence in a model to accurately predict real world

phenomena depends on a critical evaluation of the model's results against experimental

data (Oberkampf & Trucano, 2002; Rebba et al., 2006) in the form of numerical

validation. Validation is especially important when the goal of the model is a clinical

application (Viceconti et al., 2005; Cristofolini et al., 2010).

Verification of the model involved an analysis of the energies associated with

the model. Specifically, the global energy balance of the model was analysed to make

certain that there were no major inconsistencies in the energy of the system. This was

achieved by ensuring that the total energy equals the sum of internal, kinetic, sliding,

hourglass, system damping, and rigid wall energies (Schinkel-Ivy, 2010). Since

hourglass control was implemented, a specific analysis of the hourglass energy was

conducted to confirm that the hourglass energy did not contribute more than 10 % of the

total energy (LSTC, 1998; Brewer, 2001, Cheng et al., 2001). Similarly, the sliding

energy was also investigated, as negative sliding energies are undesirable. The

agreement between the experimental and model force, acceleration and strain data was

assessed over the entire impact time interval (~0.2 s) using a validation metric proposed

by Oberkampf & Trucano (2002). The validation metric is computed using:

$$V = 1 - \frac{1}{N} \sum_{n=0}^{N} tanh \left| \frac{y(t_n) - Y(t_n)}{Y(t_n)} \right|$$ (Eq. 4.4)

Where, V is the validation metric, N represents the total number of samples, *tanh* is the hyperbolic tangent trigonometric function, $y(t_n)$ is the numerical measurement of the dependent variable at time t and $Y(t_n)$ is the experimental measurement of the dependent variable at time t. The major advantage of this metric is that it measures the agreement between experimental and numerical results in a way that positive and negative errors cannot cancel each other out. The validation metric produces a value of 1 when there is perfect agreement between experimental and numerical results and approaches 0 as the differences increase (Jin et al., 2010) (Figure 4.17). When calculating the validation metric, the model and experimental signals were aligned according to time of the impulse onset.

The percentage difference between the model and experimental results, was also calculated for the peak force, load rate, impulse and impulse duration for all three force components, peak acceleration and acceleration rate (measured as the slope of the line between 30 % and 70 % of the peak acceleration (Duquette & Andrews, 2010)) in the axial and off-axis directions (Figure 4.11), for both the distal and proximal accelerometer, and the maximum and minimum principal strains at all three strain gauge locations. The percentage differences were calculated for all three impact events (pre-fracture, crack and fracture). Finally, as force is the most commonly presented validation variable, and to assess the generalizability of the model results, ensemble averages of the Fx, Fy and Fz forces were created (all signals were aligned according to the time of impulse onset) and the mean +/- 2 SD was used to assess the validity of the model results.
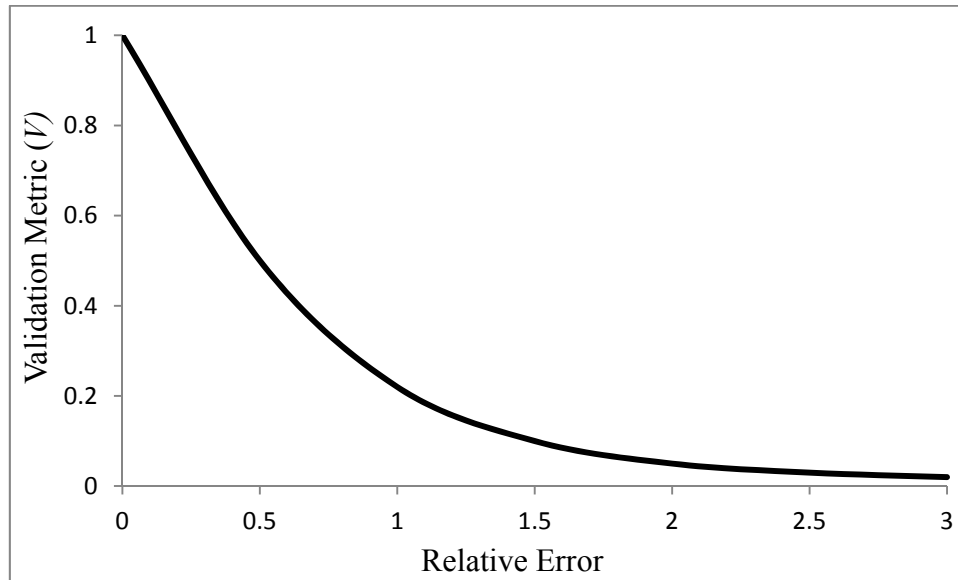
Figure 4.17: Validation Metric
The validation metric as a function of the relative error between the
model and experimental data (Adapted from Oberkampf &Trucano,
2002; Jin et al., 2010).

4.2.3 Results

Overall, the model was composed of approximately 1.04 million elements and 1.13 million nodes (Table 4.3). Both the total global and hourglass energies increased across the three impact simulations (pre-fracture, crack and fracture). However, the hourglass energy only accounted for a maximum of 8.3 % of the total energy (fracture simulation) (Table 4.4). Across all three impact events, the sum of the total energy was balanced by the individual energy contributions. Similarly, while mass scaling was included, the maximum added mass (3.0 kg) accounted for a very small proportion of the total mass (1.4E-03 %) (Table 4.3) and only 3 % of this was added to the bone components.

The validation metrics found here ranged from 0.10 (Fx pre-fracture) to 0.67 (strain gauge 2 and 3 minimum principal strain) (Table 4.3). Overall, the strain gauge and force data resulted in the highest (0.46 (0.12)) and lowest (0.28 (0.13)) mean (SD) validation metrics, respectively. The greatest differences between the model and experimental peak forces were consistently found for the peak forces along the x-axis, such that the model tended to overestimate the peak force by a maximum of approximately 197 % (Figure 4.18a-c).

While the model also overestimated peak forces along the y- and z-axis, they tended to agree relatively well with the experimental peak forces. The estimated peak forces along the y-axis were approximately 4.8 %, 3.5 % and 58.9 % greater than the experimental y-axis forces and the peak model forces along the z-axis were found to be 19.1 %, 28.5 % and 27.1 % greater than the peak forces determined from the experimental testing for pre-fracture, crack and fracture events, respectively (Figure

Table 4.3: Model Summary
A summary of the number of elements and nodes
composing each of the modelled parts

Part	Number of Elements	Number of Nodes
Cortical Bone	55800	187001
Cancellous Bone	180000	83883
Marrow	697500	711516
Lunate/Scaphoid	40000	42861
Pot and Cement	37800	42251
Proximal Bracket	6400	7854
Proximal Bearing	2688	3400
Distal Bracket	36000	40051
Distal Bearing	1000	1386
Foam	8000	9261
Projectile	5000	5731
Total	1037788	1135195

Table 4.4: Energy Balance and Validation Metrics
Energy balances and validation metrics of the radius model across the three impact
simulations.

	Pre-Fracture	Crack	Fracture
Energy Balance (J)			
Total Energy	15.2	25.8	38.5
Hourglass Energy (% total energy)	1.1 (7.2)	2.1 (8.1)	3.2 (8.3)
Kinetic Energy	12.5	22.1	29.9
Internal Energy	1.2	2.0	3.3
Damping	0	0	0
Sliding Energy	0.22	0.45	2.2
Total Mass Added (% of total mass)	2.3	2.7	3.0
	(1.2E-03)	(1.3E-03)	(1.4E-03)
Validation Metrics			
Force			
Fx	0.10	0.21	0.22
Fy	0.34	0.22	0.24
Fz	0.43	0.54	0.23
Acceleration			
Distal Axial	0.40	0.37	0.40
Distal Off-axis	0.42	0.35	0.32
Proximal Axial	0.37	0.30	0.37
Proximal Off-Axis	0.36	0.36	0.39
Strain			
Gauge 1			
Max Principal	0.56	0.58	0.34
Min Principal	0.34	0.48	0.39
Gauge 2			
Max Principal	0.63	0.42	0.35
Min Principal	0.67	0.41	0.39
Gauge 3			
Max Principal	0.63	0.42	0.35
Min Principal	0.67	0.41	0.39
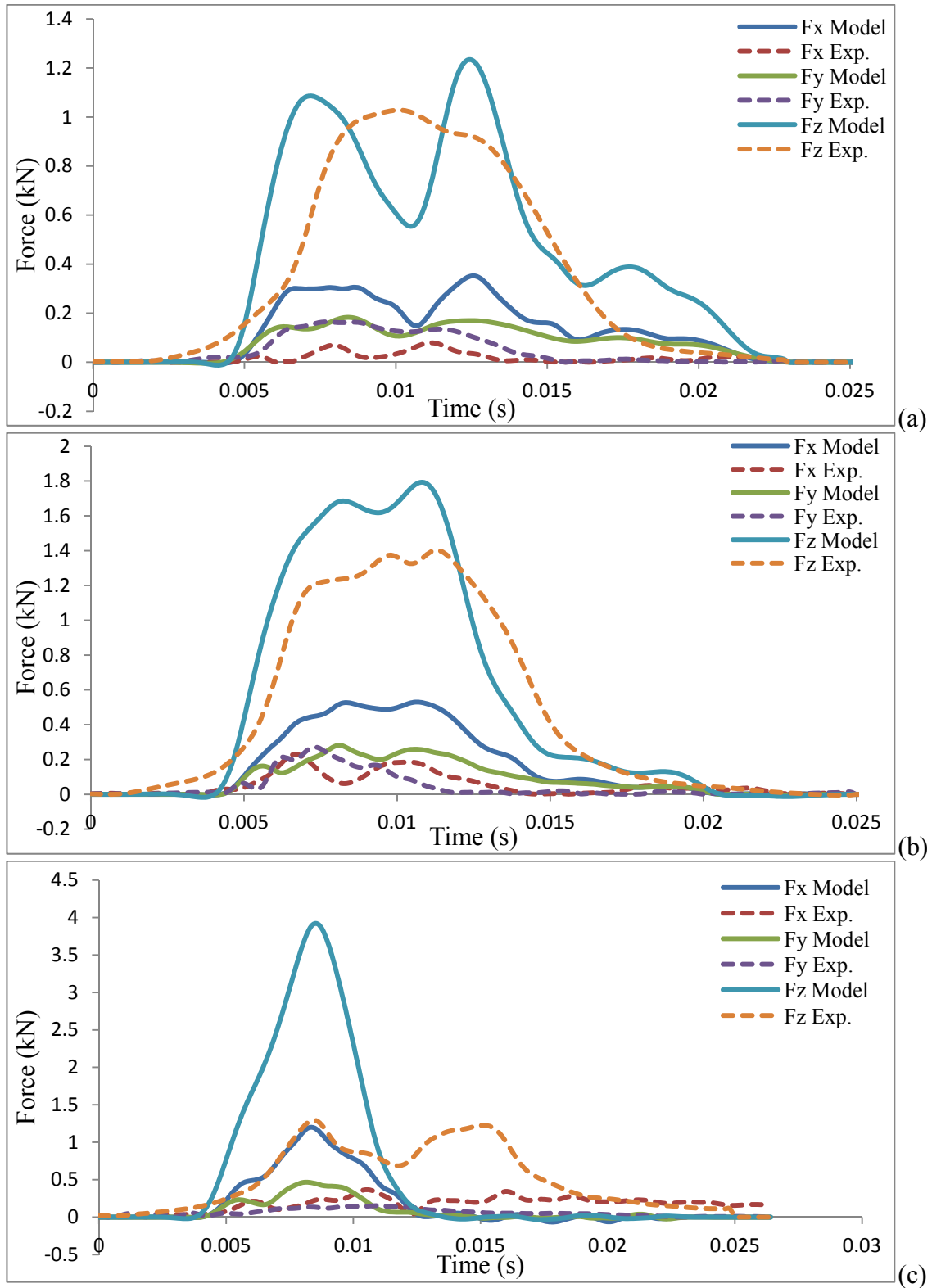
Figure 4.18: Model and Experimental Forces
Comparison of the model and experimental force components for the pre-fracture (a), crack (b) and fracture (c) impact simulations.

4.18 a-c). While the model Fx impulse overestimated the experimental impulse by a maximum of 170 %, relatively good agreement was found for the Fy (maximum: 63.6 %, pre-fracture) and Fz (maximum: 24.8 %, fracture) impulses. Finally, small differences were found for the duration of the impulse across all three force axes and impact events (maximum: 38 %, Fx, fracture). A comparison of the model forces to the mean experimental forces (an ensemble average calculated across all eight specimens) suggests a relatively good relationship, with the model forces falling consistently within plus or minus two standard deviations in both the Fy and Fz directions across the pre-fracture and crack impact events (Figure 4.19). Across all the force axes the model fracture event forces fell outside of two standard deviations of the experimental ensemble averages and therefore are not shown here.

Overall, the model was capable of predicting the peak accelerations within a relatively small degree of error. Distally, the peak acceleration differences ranged from 1.8 % (Off-axis, crack) to -31.7 % (Off-axis, pre-fracture) (Figure 4.20), while the differences in the peak proximal accelerations ranged from -2.4 % (Off-axis, fracture) to -62.9 % (Axial, crack). When the model and experimental acceleration rates were compared, a range of 3.9 % (distal Off-axis, pre-fracture) to 102.8 % (distal axial, crack) was found.

The maximum and minimum principal strains measured from the site of gauge 1 (radial styloid) and gauge 2 (ulnar side of radius) in the model were found to differ by a mean of approximately 33 % across all impact events, when compared to the strains recorded experimentally (Figure 4.21). The smallest strain differences occurred at the
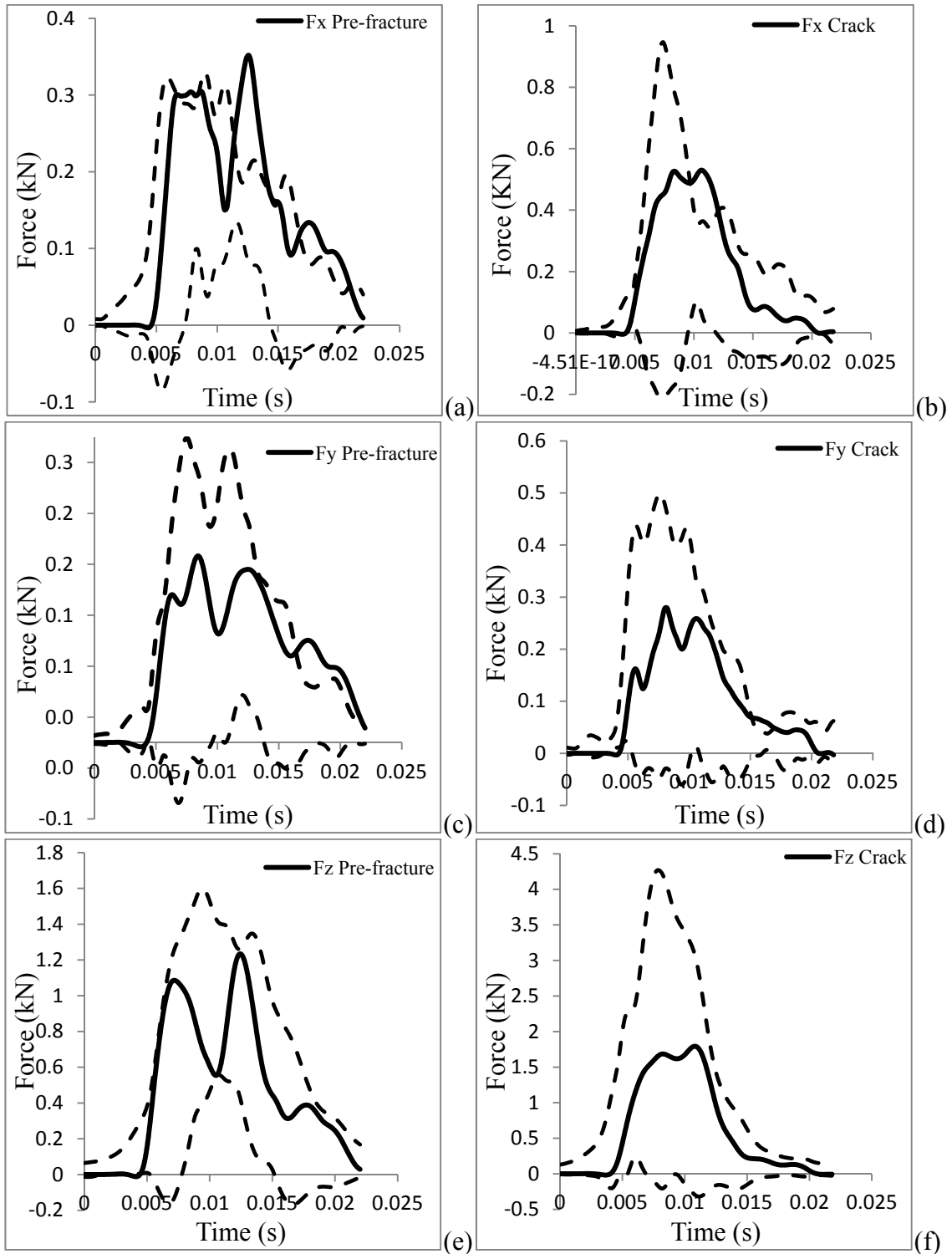
Figure 4.19: Force Ensemble Averages
Comparison of the model Fx (a, b), Fy (c, d,), and Fz (e, f) forces (solid black line) to
the mean +/- 2 SD (dotted black lines) for the pre-fracture (a, c, e) and crack (b, d, f)
experimental impact events. Data from the fracture impact events are not shown here.
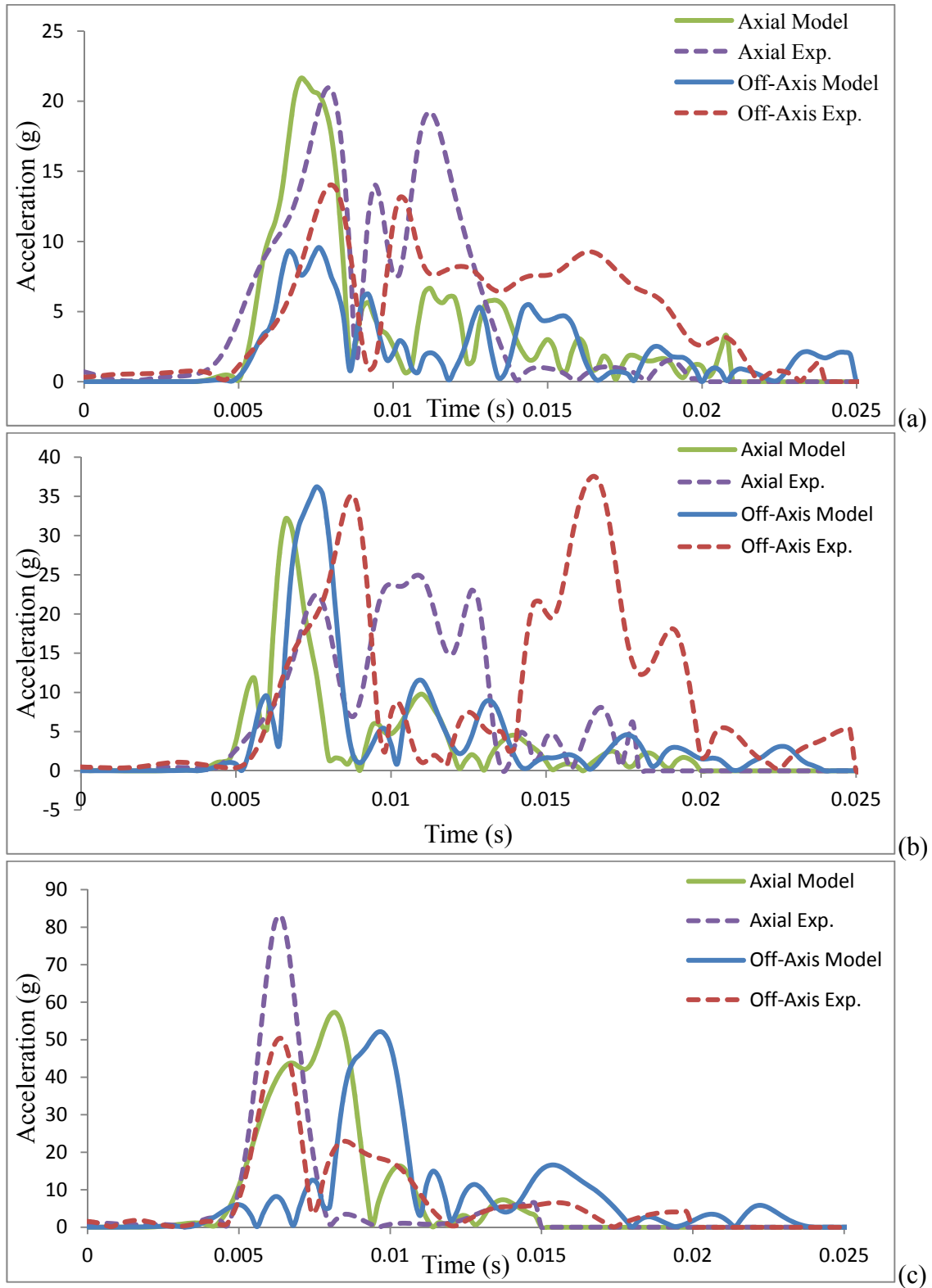
Figure 4.20: Model and Experimental Accelerations
Comparison of the model and experimental distal acceleration components for the pre-fracture (a), crack (b) and fracture(c) impact simulations.
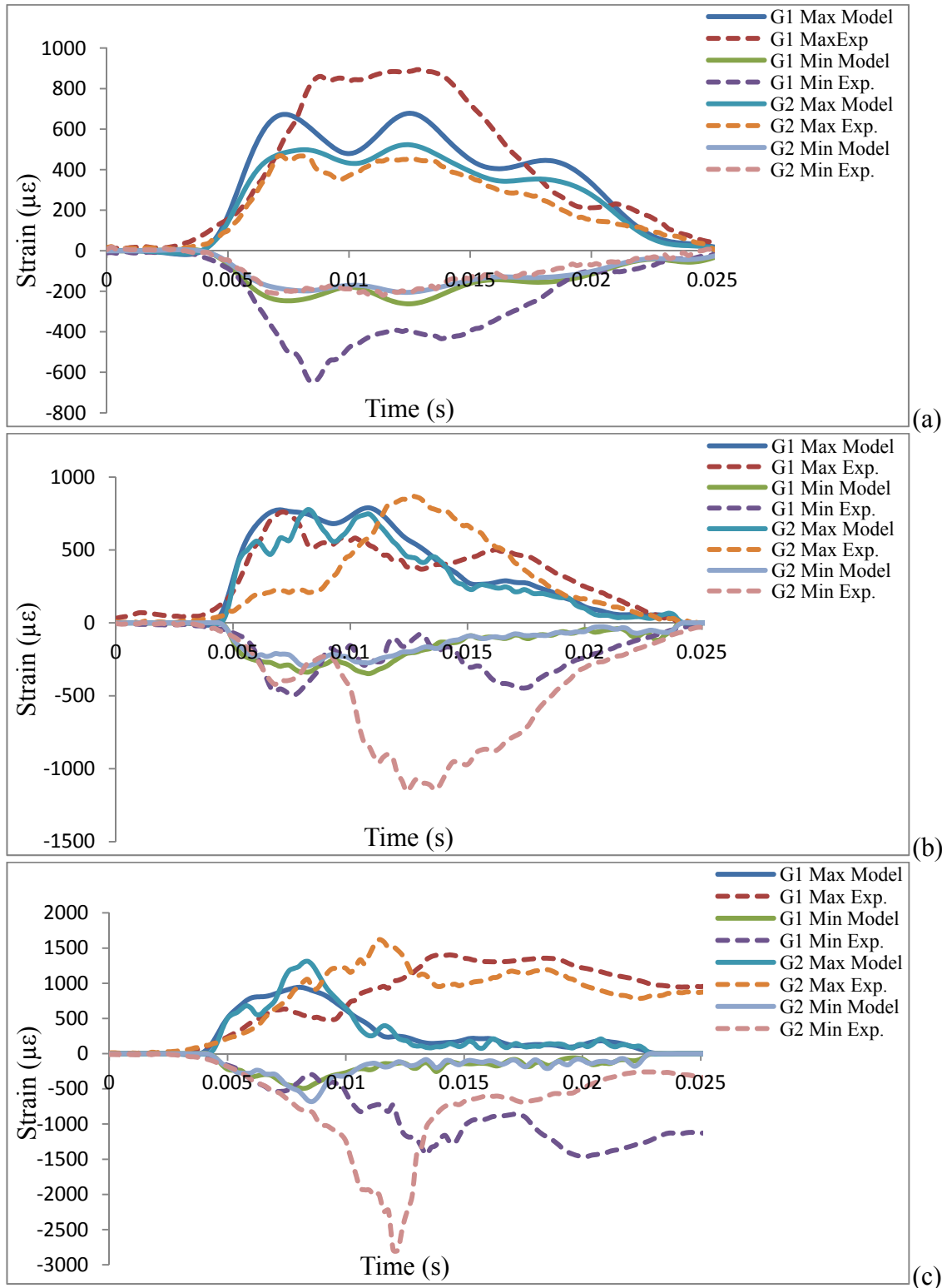
Figure 4.21: Model and Experimental Strains
Comparison of the model and experimental strain components for the pre-fracture (a), crack (b) and fracture impact simulations (c) (G1= gauge 1; G2 = gauge 2)

site of gauge 1 during the crack event (3.0 %), while the largest differences were recorded at the site of gauge 2 during the fracture event (75 %). Relatively large differences were found at the site of gauge 3 (proximal), ranging from 29.6 % (max principal strain, pre-fracture) - 430 % (min principal strain, fracture).

Finally, the von-Mises stress criteria were used to determine if damage had occurred to the bone, and to what extent, in both the cortical and cancellous bone structures (Figure 4.22). During the pre-fracture impact event there were no elements in the cortical bone that exceeded the critical limit (134 MPa (Untaroiu et al., 2005)), while a cluster of cancellous elements located in the volar region on the ulnar side of the radius indicated that "damage" had occurred (>5.3 MPa (Untaroiu et al., 2005)) (Figure 4.22 a-b). Similarly, no cortical "damage" was noted during the crack event, while there was an increase in the volume of elements in the cancellous bone that exceeded the critical limit (Figure 4.22 c-d). However, during the fracture event, the cortical bone showed areas of "damage" on the volar aspect of the intra-articular surface on the ulnar side of the radius as well as into the sigmoid fossa (Figure 4.23a). The cancellous bone also showed significant signs of "damage" during the fracture event (Figure 4.23b). The pattern of "damage" seen during the fracture event for the cortical bone and during all events for the cancellous bone, corresponded very well with the damage that was reported experimentally (Figure 4.23 c-d). Using the multi-variate fracture risk equations developed in Section 2.2, there was a less than 1 % probability of a fracture occurring (risk score = 0.20) when the variables from the pre-fracture impact event were analysed and a 35 % probability of injury (risk score = 0.90) using the fracture event variables (Figure 4.24).
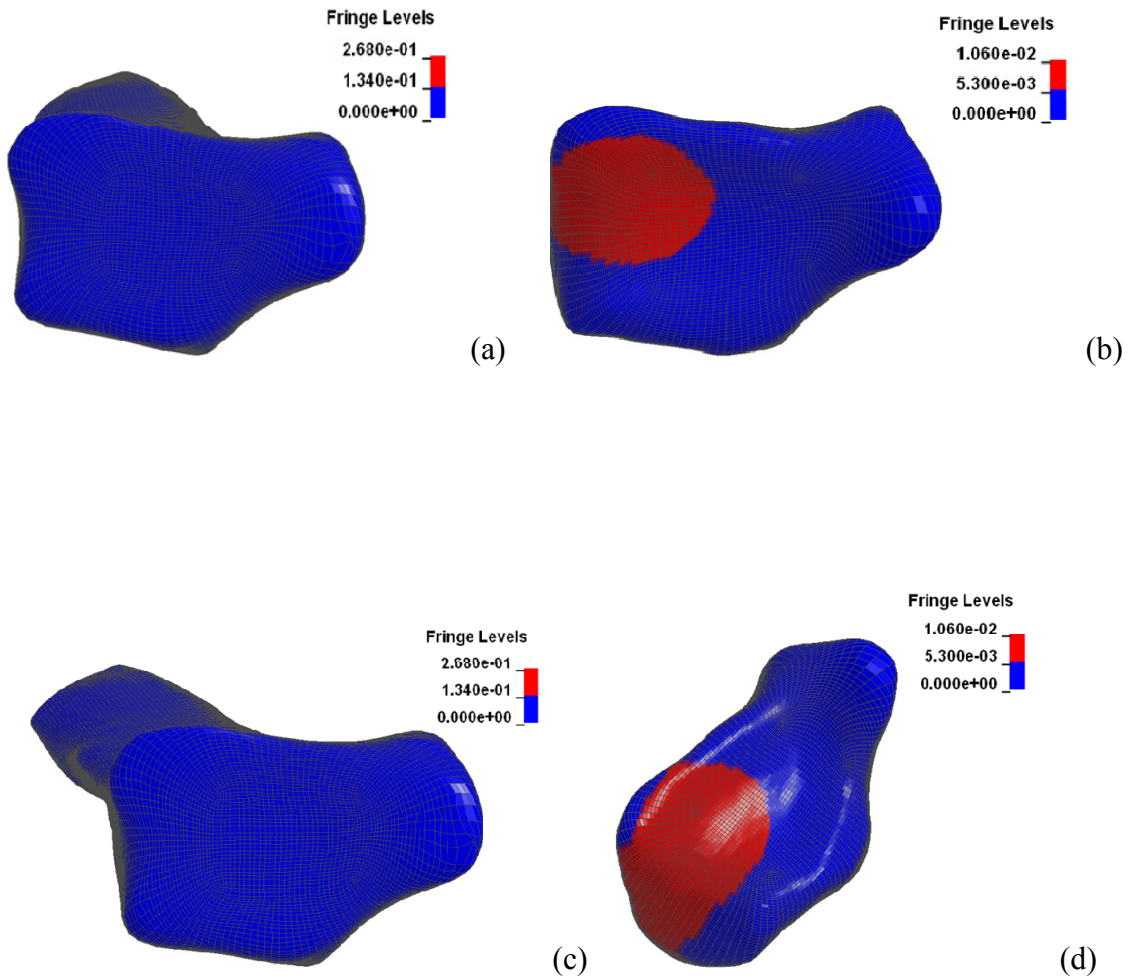
Figure 4.22: Pre-Fracture and Crack von-Mises Stresses
Maximum von-Mises stresses that exceeded the critical level (cortical,1.34 MPa; cancellous, 5.3 MPa) indicated the location and extent of bone damage. Cortical pre-fracture (a), cancellous pre-fracture (b), cortical crack (c), cancellous crack (d).
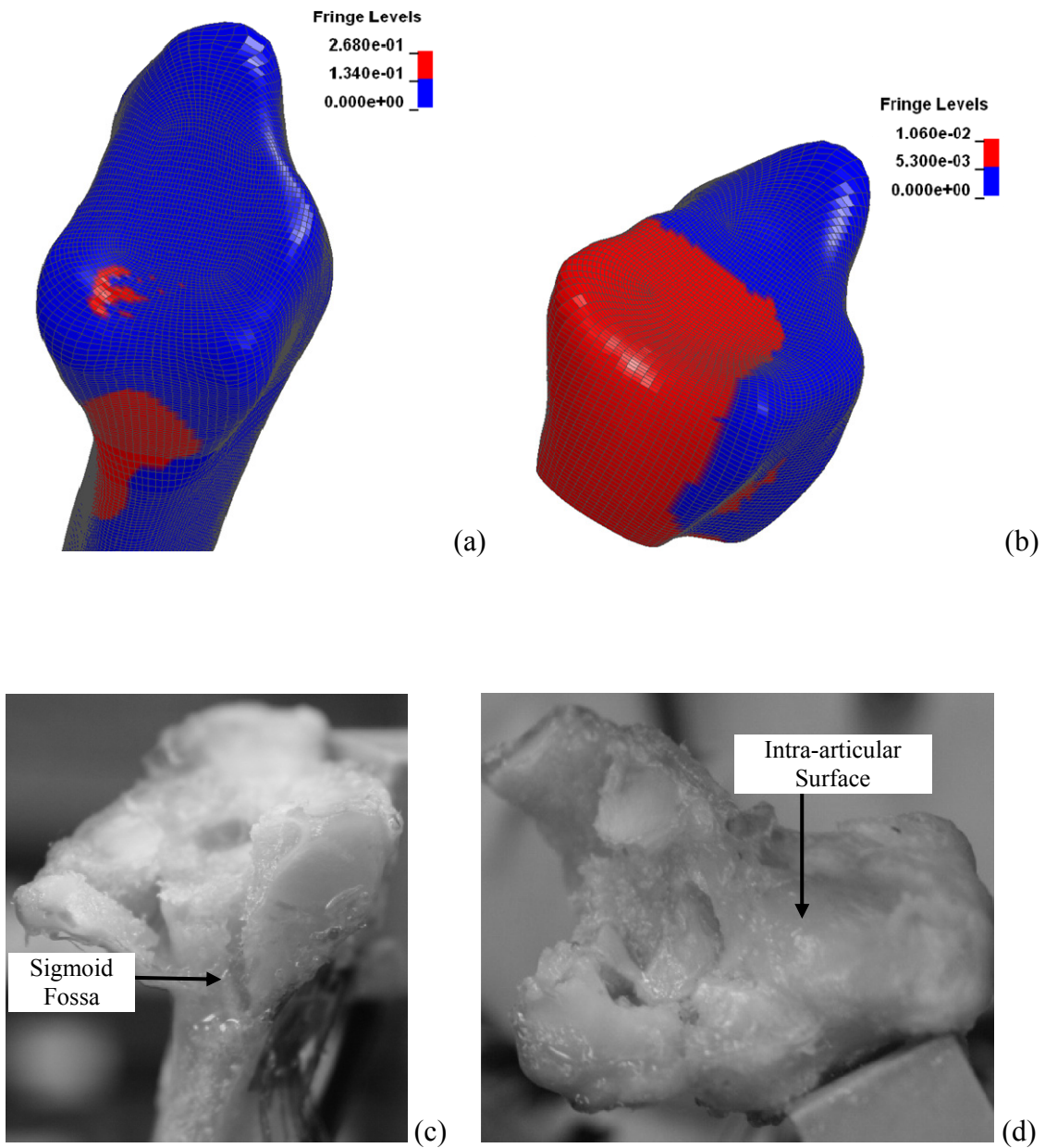
Figure 4.23: Model and Experimental Fracture Patterns
Maximum von-Mises stresses that exceeded the critical level during the fracture event in the cortical (a) and cancellous (b) bone regions and a comparison of the sigmoid fossa (c) and intra-articular (d) damage reported from the experimental testing.
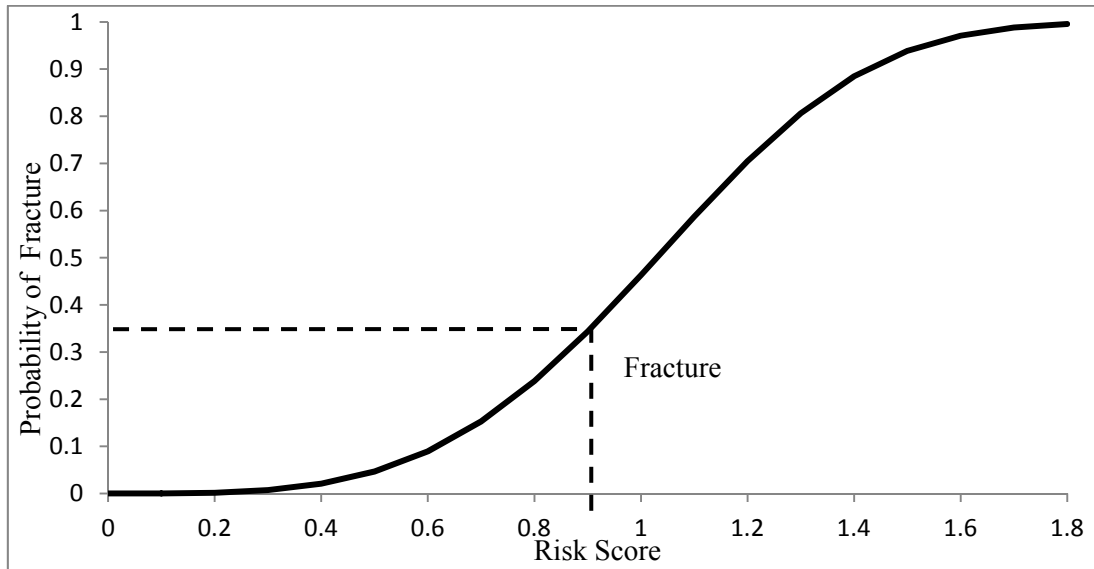
Figure 4.24: Model Injury Risk
Determination of the probability of injury during the fracure event using the multi-variate fracture risk equations developed in Section 2.3.

4.2.4 Discussion

To date, this is the first finite element model of the distal radius composed entirely of hexahedral elements that has simulated dynamic impact loading. Taking into consideration all of the validation results, including the validation metrics, the comparison to specimen-specific experimental results, mean experimental results and comparisons of fracture patterns, the model presented here is a valid representation of the distal radius.

In finite element simulations, a phenomenon known as hourglassing can occur where an element undergoes a deformation in the absence of strain. Hourglassing can lead to inaccurate results and, in severe cases, can result in negative volume elements. Initial simulations were run without controlling for hourglassing that resulted in negative volume elements. To overcome hourglassing, a stiffness form hourglass control was implemented in which a small elastic stiffness was added, allowing the elements to resist hourglassing. However, inaccuracies can also result from the addition of too much hourglass energy. In the simulations reported here, the hourglass energy increased across the three impact events, but remained below the recommended 10 % of total global energy (Brewer, 2001; Cheng et al., 2001; LSTC, 2007). This, combined with the energy balance findings and the small percentage of added mass (including only a small increase in the mass of the bone components), suggests that the results of the model were not affected by the inclusion of hourglass control and provides a verification of the model.

Overall, the model presented here is a good representation of the distal radius, and the impact loads applied also agreed relatively well with the experimental findings.

The Fy and Fz loads predicited by the model during the pre-fracture and crack events agreed well with both the specimen-specific experimental loads. The differences between the model and experimental findings can be attributed to the selection of the material properties. The elastic modulus of cortical and cancellous bone used here were taken from previous work (Burstein et al., 1976; Schonenau et al., 2002; Imai et al., 2006; Troy et al., 2007), and while care was taken in selecting these values (i.e. values were selected to match the age and sex of the specimen donor), they are still estimates of the material properties of the specific bone used here. Furthemore, the model impulse durations in the Fy and Fz directions were greater than those measured experimentally and the Fz force tended to exhibit a more pronounced bi-phasic force pattern compared to the experimentally determined force patterns. This most likely resulted from differences in the masses of the proximal pot and bracket and the friction coefficients between the proximal bracket and the proximal bearing.

The greatest errors were found when the forces along the x-axis were compared. The peak Fx experimental forces were negligible when compared to the model, most likely a result of mis-alignment of the model lunate/scaphoid with the intra-articular surface of the radius. The lunate/scaphoid was visually aligned with the intra-articluar surface, both during the experiment as well as during the proccess of creating the model. Also, the mesh of the model lunate/scaphoid was created based on a highly smoothed version of the scanned lunate/scaphoid.While this resulted in a continuous mesh (i.e. void of any holes that were present from the scanning), this may have altered the surface geometry enough to lose some of the detailed morphology that is helpful in aligning the lunate/scaphoid with the radius. The use of a surrogate lunate/scaphoid,

combined with mis-alignment may have resulted in a greater medial-lateral shift of the carpals on the intra-articular surface, resulting in greater model Fx forces. During the experimental impact testing, the forces (along all axes) tended to decrease between the crack and fracture impact events, and was attributed to a change in the material properties of the bone (i.e. decreased bone stiffness) as a result of the repeated impacts and the damage incurred during the crack event (Martin et al., 1997; Reilly & Currey, 2000; Gupta & Zioupos, 2008) (Section 2.2). However, in the current model the changes in material properties were not simulated, thus the stiffness of the bone was maintained and the impact forces continued to increase.

While the model and experimental acceleration data agree relatively well, the variation between the model and experimental accelerations is most likely a result of where the accelerations were calculated from. The model accelerations were calculated at a single node directly on the surface of the bone, while the experimental accelerations were calculated from external sensors whose centers were located approximately 0.5 cm away from the bone surface. These differences are analogous to the differences that exist between bone-mounted and skin-mounted accelerometers (Lafortune et al., 1995). Furthemore, although care was taken to clear the bone of all surrounding tissues, the experimental accelerations could be affected by underlying residual tissue. Differences between the experimental and model strains might also be explained by differences in the locations where the strains were measured. While the numerical strains were measured from an element that corresponds to a location within the surface layer of the bone, the experimental strains by contrast were offset from the bone by the thickness of the strain gauge and strain gauge glue.

A number of different methods have been proposed to simulate bone fracture in finite element models. However, no validated theory is currently available (Keyak & Rossi, 2000). The Coulumb-Mohr criteria (Keyak & Rossi, 2000; Troy & Grabiner, 2007), cohesive elements with a fracture plane (Ural, 2009), von-Mises stresses and maximum principal strains (Quenneville et al., 2011), have been used previously. Quennville et al. (2011) found that the von-Mises stress criteria accurately predicted the location of fracture, and as such, this method was used in the current study. Despite the differences that were found between the model and experimental results, the model accurately predicted the location and magnitude of the damage inflicted by the impacts. The elements in the cortical bone that exceeded the critical von-Mises stresses, indicating fracture, were primarily located on the intra-articular surface and into the sigmoid fossa. The failed elements in the cancellous bone exhibited the same pattern as those in the cortical bone, but over a larger area. While there were no failed cortical elements in the space between the volar, ulnar aspect of the intra-articular surface and the sigmoid fossa, the volume of failed elements in these regions (~200 mm^3-400 mm^3) suggests that propagation of the failure would have occured (Troy & Grabiner, 2007).

This study presents a finite element model of the distal radius in response to dynamic impact loading. A number of different validation techniques were used, and when reviewed collectively, they suggest that this model is a good representation of the distal radius and simulate the impact response well. Most importantly, the model was succesful in predicting the location and severity of fracture.

4.2.5 References

Anderson DD, Deshpande BR, Daniel TE, Baratz ME. 2008. A three dimensional finite element model of the radiocarpal joint: distal radius fracture step-off and stress transfer. The Iowa Orthopaedic Journal. 25, 108-117.

Anderson DD, Goldsworthy JK, Wendy L, Rudert MJ, Tochigi Y, Brown TD. 2007. Physical validation of a patient-specific contact finite element model of the ankle. Journal of Biomechanics. 40, 1662-1669.

Boutroy S, van Rietbergen B, Sornay-Rendu E, Munoz F, Bouxsein ML, Delmas PD. 2008. Finite element analysis based on *in vivo* HR-pQCT images of the distal radius is associated with wrist fracture in post-menopausal women. Journal of Bone and Mineral Research. 23, 392-399.

Brewer JC. 2001 Effects of angles and offsets in crash simulation of automobiles with light trucks. Society of Automotive Engineers, Technical Paper. Paper Number: 2001-06-0077.

Buchanan D, Ural A. 2010. Finite element modeling of the influence of hand position and bone properties on the colles' fracture load during a fall. Journal of Biomechanical Engineering. 132, 081007-1 - 081007-8.

Burstein A, Reilly DT, Martens M. 1976. Aging of bone tissue: Mechanical properties. Journal of Bone and Joint Surgery. 58, 82-86.

Carter DR, Hayes WC. 1977. The compressive behaviour of bone as a two-phase porous structure. Journal of Bone and Joint Surgery. 59, 954-962.

Cheng ZQ, Thaker JG, Pilkey WD, Hollowell WT, Reagan SW, Sieveka EM. 2001. Experiences in reverse-engineering of a finite element automobile crash model. Finite Elements in Analysis and Design. 37, 843-860.

Cristolfolini L, Schileo E, Juszczyk M, Taddei F, Martelli S, Viceconti M. 2010. Mechanical testing if bones: the positive synergy of finite-element models and *in vitro* experiments. Philosophical Transactions of The Royal Society, A: Mathematical, Physical and Engineering Sciences. 368, 2725-2763.

Duquette AM, Andrews DM. 2010. Comparing methods of quantifying tibial acceleration slope. Journal of Applied Biomechanics. 26, 229-233.

Gupta HS, Zioupos P. 2008. Fracture of bone tissue: the "hows" and "whys". Medical Physics and Engineering. 30, 109-114.

Imai K, Ohnish I, Bessho M, Nakamura K. 2006. Nonlinear finite element model predicts vertebral bone strength and fracture site. Spine. 31, 1789-1794.

Jin SY, Majumder A, Altenhof W, Green D. 2010. Axial cutting of AA6061-T6 circular extrusion under impact using single- and dual-cutter configurations. International Journal of Impact Engineering. 37, 735-753.

Jones N. 1989. Strain rate sensitive behaviour of materials. In Structural Impact (pp 333-384). New York, NY: Cambridge University Press.

Keyak JH, Rossi SA. 2000. Prediction of femoral fracture load using finite element models: an examination of stress- and strain-based failure theories. Journal of Biomechanics. 33, 209-214.

Kim YS, Choi HH, Cho YN, Park TJ, Lee JB, Yang KH, King AI. 2005. Numerical investigations of interactions between the knee-thigh-hip complex with vehicle interior structures. Stapp Car Crash Journal, 49, 85-115.

Lafortune MA, Henning E, Valiant GA. 1995 Tibial shock measured with bone and skin mounted transducers. Journal of Biomechanics. 28, 989-993.

Lengsfeld M, Schmitt J, Alter P, Kaminsky J, Leppek R. 1998. Comparison of geometry-based and voxel-based finite element modeling and experimental validation. Medical Engineering and Physics. 20, 515-522.

Lotz JC, Gerhart TN, Hayes WC. 1990. Mechanical properties of trabecular bone from the proximal femur: a quantitative CT study. Journal of Computer Assisted Tomography. 14, 107-114.

LSTC. 1998. LS-DYNA Theoretical Manual. Livermore, CA, USA.

LSTC. 2007. LS-DYNA User's Manual, V.971. Livermore, CA, USA.

McElhaney JH. 1966. Dynamic response of bone and muscle tissue. Journal of Applied Physiology. 21, 1231-1236.

MacNeil, J. A., Boyd, S. K. 2008. Bone strength at the distal radius can be estimated from high resolution peripheral quantitative tomography and the finite element method. Bone. 42, 1203-1213.

Martin RB, Gibson VA, Stover SM, Gibeling JC, Griffin LV. 1997. Residual strength of equine bone is not reduced by intense fatigue loading: implications for stress fracture. Journal of Biomechanics. 30, 109-114.

Nordin M, Frankel VH. 2001. Biomechanics of bone. In Basic Biomechanics of the Musculoskeletal System (pp. 26-59). Philadelphia, PA: Lippincott Williams & Wilkins.

Oberkampf WL, Trucano TG. 2002. Verification and validation in computational fluid dynamics. Progress in Aerospace Sciences. 38, 209-272.

Oberkampf W L, Trucano TG. 2008. Verification and validation benchmarks. Nuclear Engineering and Design. 238, 716-743.

Peng L, Bai J, Zeng X, Zhou Y. 2006. Comparison of isotropic and orthotropic material property assignments on femoral finite element models under two loading conditions. Medical Engineering and Physics. 28, 227-233.

Pistoia W, van Rietbergen B, Lochmuller E-M, Lill CA, Eckstein F, Ruegsegger P. 2002. Estimation of distal radius failure load with micro-finite element analysis models based on the three-dimensional peripheral quantitative computed tomography images. Bone. 30, 842-848.

Pistoia W, van Rietbergen B, Lochmuller E-M, Lill CA, Eckstein F, Ruegsegger P. 2004. Image-based micro-finite-element modeling for improved distal radius strength diagnosis: moving from "bench" to "bedside". Journal of Clinical Densitometry. 7, 153-160.

Pistoia W, van Rietbergen B, Ruegsegger P. 2003. Mechanical consequences of different scenarios for simulated bone atrophy and recovery in the distal radius. Bone. 33, 937-945.

Pitzen T, Geisler F, Matthis D, Muller-Storz H, Barbier D, Steudel W-I, Feldges A. 2002. A finite element model for predicting the biomechanical behaviour of the human lumbar spine. Control Engineering Practice. 10, 83-90.

Quenneville CE, Dunning CE. 2011. Development of a finite element model of the tibia for short-duration high-force axial impact loading. Computer Methods in Biomechanics and Biomedical Engineering. 14, 205-212.

Quenneville CE, 2009. *Experimental and numerical assessments of injury criteria for short-duration, high-force impact loading of the tibia* (Doctoral Dissertation). The University of Western Ontario, London, Ontario, Canada.

Rebba R, Mahadevan S, Huang S. 2006. Validation and error estimation of computational models. Reliability Engineering and System Safety. 91, 1390-1397.

Reilly GC, Currey JD. 2000. The effects of damage and micro-cracking on the impact strength of bone. Journal of Biomechanics. 33, 337-343.

Sambamoorthy B, Halder T. 2001. Characterization and component level correlation of energy absorbing (EA) polyurethane foams (PU) using LS-DYNA material models. 3rd European LS-DYNA User's Conference, Paris, France.

Schinkel-Ivy A. (2010). *An investigation of shock wave propagation and attenuation in the lower extremity using finite element analysis* (Masters Thesis). University of Windsor, Windsor, Ontario, Canada.

Schonenau E, Neu CM, Rauch F, Manz F. 2002. Gender-specific pubertal changes in volumetric cortical bone mineral density at the proximal radius. Bone. 31, 110-113

Takahashi Y, Kikuchi Y, Konosu A, Ishikawa H. 2000. Development and validation of the finite element model for the human lower limb of pedestrians. Stapp Car Crash Journal. 44.

Troy KL, Grabiner MD. 2007. Off-axis loads cause failure of the distal radius at lower magnitudes than axial loads: a finite element analysis. Journal of Biomechanics. 40, 1670-1675.

Untaroiu C, Darvish K, Crandall J. 2004. Development and validation of a finite element model of the lower limb. ASME, Anaheim, California, USA.

Untaroiu C, Darvish K, Crandall J, Deng B, Wang, J.T. 2005. A finite element model of the lower limb for simulating pedestrian impacts. Stapp Car Crash Journal. 49**,** 157-181.

Ural A. (2009). Prediction of Colles' fracture load in human radius using cohesive finite element modeling. Journal of Biomechanics. 42, 22-28.

Valle L, Ray MH. 2005. Development and validation of a 50th percentile male human femur: Attachment A. Worcester Polytechnic Institute. Worcester, MA, USA. National Highway Traffic Safety Administration.

Viceconti M, Olson S, Nolte LP, Burton K. 2005. Extracting clinically relevant data from finite element simulations. Clinical Biomechanics. 20, 451-454.

Wirtz DC, Schiffers N, Pandorf T, Radermacher K, Weichert D, Forst R. 2000. Critical evaluation of known bone material properties to realize anisotropic FE-simulation of the proximal femur. Journal of Biomechanics. 33, 1325-1330

CHAPTER 5 – GENERAL DISCUSION

5.1 Summary

Distal radius fractures that commonly occur as result of a forward fall are injuries with potentially devastating consequences. As the population continues to age, and as sports participation continues to rise it is projected that these preventable injuries will continue to stress burdened health care systems world-wide. A thorough and accurate understanding of the injury mechanisms, combined with the knowledge on how to minimise the harmful impact-related variables, will allow adequate injury prevention interventions to be developed. While there are standards and injury limits that exist for other areas of the body (i.e. leg, head, and torso), there is currently no injury standard for the distal upper extremity. Therefore, the overall purpose of this work was to determine the fracture mechanisms of the distal radius in response to a dynamic impact and to develop multi-variate injury risk criteria and to determine the kinematics associated with minimising these variables using *in vitro*, *in vivo*, and numerical methods.

The first section of this research was designed to determine the capacity of the distal radius (Objective # 1, Section 2.1) in response to systematically applied dynamic impacts *in vitro*. The cadaveric specimens were positioned to match the posture of the forearm during a forward fall and the mean (SD) resultant fracture force was 2142.1 (1228.7) N. This mean force was found to be more conservative than reported values (Hypothesis #1 accepted) and was attributed to the systematic application of energy controlled impacts. Injury risk equations were developed (Objective # 1, Section 2.2)

and it was found that the multi-variate models that included dynamic variables better predicted the risk of a crack or fracture event occurring to the distal radius (Hypothesis # 2 accepted). Impulse along the Fy axis, Fz load rate, the natural logarithm of Fz and velocity were the variables found to best predict the risk of a crack event. Peak Fz and the Fy impulse and velocity were included in the fracture event prediction model. The inclusion of these variables in distal radius injury risk equations highlights the importance of considering dynamic variables along multiple force axes. Finally, while strain gauges provide the most accurate data regarding the response of a bone, it can become costly and time consuming to use them for *in vitro* failure studies and they are too invasive to be used *in vivo*. Accelerometers are often used as strain gauge surrogates, but to date, there is little evidence to validate them for this use (Objective # 2, Section 2.3). In the current study, it was shown that accelerometers are capable of predicting strains exclusive to the underlying bone (Hypothesis # 3 accepted), and the outputs from them also act as good predictors of bone injury.

The second main component of this research involved the development of a system that was capable of simulating *in vivo* forward falls (Objective # 3, Section 3.1). The result of this work was a Propelled Upper Limb fall ARrest Impact System (PULARIS), which is capable of applying multi-directional motion to participants, to more accurately simulate the flight and impact phases of a forward fall. The hip velocity ratios (horizontal velocity to vertical velocity) were found to agree well with previous *in vivo* fall studies (Hypothesis # 4 accepted). It was also shown that PULARIS was a relatively reliable fall simulation method producing hand force, hip velocity and hip angle Intraclass Correlation Coefficients (ICCs) in the range of 0.48 to

0.95. This system was also designed to be easily adjustable, permitting a variety of fall

heights, torso angles and upper extremity postures which will be tested in future work.

The PULARIS was used in the second *in vivo* study to test the effect of fall types and

fall heights on the kinetics, kinematics and muscle activation levels of the upper

extremity (Objective # 4, Section 3.2). Overall, it was found that, to some extent an

individual could reduce the effect of an impact on the upper extremity when asked to

land as safely as possible. While the peak forces were not significantly different

between the three fall types (straight-arm, self-selected, and bent-arm), the Fy impulse

and Fz load rate were found to be significantly lower during the self-selected falls

compared to the straight-arm (worst-case scenario) falls (Hypotheses # 5 accepted).

Furthermore, the muscle activation patterns suggest that the majority of the muscles

tested in the current investigation displayed a pre-impact anticipatory response that has

been shown to prepare the joints for the often varied impact loads and load durations

possible during forward fall arrest.

The third component of this dissertation aimed to develop a finite element model

of the distal radius, simulate dynamic load applications and validate the model against

the experimental data collected in Chapter 2 (Objective # 5, Chapter 4). A hexahedral

mesh was generated from a CT scan of a radius bone, including the cortical, cancellous

and marrow sections. A number of mesh verification metrics (element Jacobians,

aspect ratios and orthogonality) were used to assess the quality of the mesh prior to

performing the simulations. The mesh was imported into LS-DYNA® where the

appropriate material models, material properties and boundary conditions were applied

to the mesh. Three separate velocity controlled impacts were simulated, such that the

velocity of the model projectile matched that of the experimental projectile described in Chapter 2. The validation metric, error calculations and comparison of fracture patterns suggest that this was a valid model capable of simulating dynamic impacts (Hypothesis # 6 accepted). The data obtained from the simulations were also used to assess the risk of a fracture event using the multi-variate injury risk criteria equations from Section 2.2.

5.2 Strengths and Limitations

The strengths and limitations of each specific study are detailed in their respective sections. However, there are some that are applicable to this research project as a whole. The main strength of this work was the combined use of innovative *in vitro*, *in vivo* and numerical methodologies to evaluate dynamic impacts to the distal radius. As is seen throughout the summary, results from the *in vitro* work were used to explain some of the important findings in the *in vivo* work, and were also used to validate the finite element model. Cristofolini et al. (2010) strongly advocate for the use of multiple research methods in this type of work and highlight the importance of the synergy between them.

Another main strength of this work is the thorough evaluation and validation of the finite element model at all stages of its development. A rigorous investigation of the elements during the mesh generation phase ensured a high quality mesh was developed before simulations were run. Similarly, the data generated from the simulations were validated, using up to four different validation measures (validation metric, error evaluation, ensemble averages, and fracture comparisons).

Finally, for the experimental work, effort was taken to ensure that the instrumentation used and the data processing techniques (specifically digital filtering)

were individualized to these studies and supported by statistical data. For example, the

filter cut-off frequencies chosen for the force and acceleration data for both the *in vitro*

and *in vivo* studies were determined by a residual analysis using data specifically related

to the respective studies (Burkhart et al., 2011). With respect to the EMG data, pilot

work was conducted utilizing a cross-correlation analysis to determine the appropriate

muscles to include in the larger study. Similarly, a sub-sample of MVC data was used

to ensure the reliability of the MVC collection methods. These methods not only ensure

the selection of appropriate instrumentation, and the calculation of accurate results, but

also improve the generalizability of the findings.

　　　　While the research presented throughout this dissertation furthers our

understanding of the mechanisms by which the distal radius fractures, this work is not

without its limitations. Isolated cadaveric specimens were used for the *in vitro* impact

study that had all soft tissues and adjacent bony structures (e.g., the ulna) removed. It

has been shown previously that the ulna can bear up to 60 % of the load experienced at

the wrist (May et al., 2002). Furthermore, Nordsletten & Ekeland (1993) found that the

strength of bone is increased when the muscles are activated during rapid loading. The

combination of results from May et al. (2002) and Nordletten & Ekeland (1993) suggest

that the data presented here are an underestimation of the crack and fracture event

variables. Although this may be the case, the results presented in Sections 2.1 and 2.2

would still provide a more conservative approach to distal radius injury prevention.

Finally, only one radius/impact surface angle and one simulated wrist angle were tested

on a relatively small sample (N=8). While these angles correspond to the most common

upper extremity orientation during an *in vivo* forward fall (Greenwald et al., 1998;

Staebler et al., 1999; Troy & Grabiner 2007), the findings presented here may be limited in their generalizability.

As a convenience sample, as well as to ensure the safety of participants during the simulated forward falls (Sections 3.1 and 3.2), only young (university aged) healthy adults were tested, creating a potentially homogenous sample that it is not necessarily indicative of the population at the highest risk of distal radius injuries (i.e. individuals over the age of 50 years). Therefore, while it appears that healthy young adults are capable of self-selecting the most appropriate fall kinematics to minimize the effects of the impact, as DeGoede & Ashton-Miller (2003) clearly point out, it is questionable as to whether an older adult would possess the same level of muscular strength to similarly choose the appropriate fall kinematics. However, the mean BMI of the participants agrees well with the mean BMI of a sample of Canadians over the age of 25 (Langsetmo et al., 2010). This suggests that, to some extent, the general health of the sample tested in the current study is representative of the average Canadian. A final limitation of the *in vivo* work is the fall heights that were chosen. Given the relatively close proximity of the hands to the force platforms during the 0.05 m falls it is likely that most participants did not have enough time available to actively react to the fall, which may have resulted in unrealistic kinematic strategies.

Another limitation of this research pertains specifically to the finite element model (Chapter 4). A number of assumptions and estimations had to be made regarding the material models, material properties, failure criteria, and element formulations. For example, the bone material properties (e.g., modulus, mass densities) were chosen from the literature and while care was taken to use sex-, age- and radius specific values, these

were still approximations of the actual bone that was used. It would be more accurate

to assign specimen-specific material properties to the bone, but this would greatly

increase the computation costs of the model and would require further experimental

testing. Similarly, model bone fracture is based on the assumption that a failed element

(i.e. one whose von-Mises stress exceeded a critical limit) represents an area of fracture.

While this may be true, and although the model results showed good agreement with the

experimental results, modelling fracture propagation through the bone would also

increase the accuracy and validity of the finite element model for studying the dynamic

response of the distal radius to fall related impact scenarios. Furthermore, similar to the

in-vivo impacts, muscle forces were not simulated here, which may alter the reaction of

the bone, and subsequently, the fracture forces.

5.3 Future Directions

The research performed in this dissertation has explored many aspects of injury

to, and injury prevention of the distal radius. However, this work has also highlighted

areas that require further investigation. Continuing to use experimental and numerical

techniques in tandem will lead to the optimization of experimental protocols through

initial numerical testing. For example, by altering the effective mass of the forearm (i.e.

the % of body weight that the upper extremity must bear during a fall), comparisons can

be made between one and two armed falls. An increase in the sample size and the

investigation of different radius/impact surface angles and wrist angles will improve the

generalizability of the findings. Furthermore, the inclusion of opposing muscle forces

and surrounding soft tissues will result in a more accurate investigation of distal radius

failure mechanisms. Further cadaveric testing involving the investigation of different

load types will also be advantageous. For example, load patterns consistent with the impact between the hand and a steering wheel or the hand and an air bag during a car crash, would provide valuable information for car manufacturers and safety engineers. Given that the dynamic *in vitro* radius impact testing device is capable of creating reliable, clinically relevant fracture patterns, the effect of fracture fixation techniques (e.g., volar and dorsal platting and k-wires) on hand kinematics should also be explored.

Related to the finite element model is the improvement of its biofidelity through the inclusion of the surrounding soft tissues (i.e. muscles, and by association muscle forces) and adjacent bone structures (i.e. ulna, carpals). An anatomically improved model will provide more accurate modelling results and will allow researchers to study other forearm fracture patterns. A sensitivity analysis should be conducted so that the descritization of the finite element mesh can be optimized. Also, the strains reported from the FEM are calculated within the bone, in comparison to the strains calculated from the gauges used experimentally. Therefore, techniques to measure strains on the surface of the bone within the model need to be explored. The injury models created in Section 2.2 indicated that the risk of fracture is related, to some extent, to the impulse of the impact force, suggesting that the experimental fracture process might be better modelled with an impulse metric, or erosion criteria that further takes advantage of the von-Mises stress criteria.

While only a small range of fall types were explored in the PULARIS study (Section 4.2), the adjustability and flexibility of this system suggest that a much larger range of conditions could be tested. This includes changes in torso angles, upper extremity angles, approach angles (i.e. symmetric vs. asymmetric falls) and fall

directions (forward, backward, and sideways). This adjustability also creates the possibility of studying the most effective fall interventions, whether through fall training or prophylactic devices such as wrist guards. Finally, the muscle activation results suggest that some muscles are more involved in the fall arrest than others. Determining the involvement of and role played by specific muscles during impact events should remain a research priority, and would likely also lead to improved fall outcomes.

5.4 Impact of Research

This compilation of research has furthered the understanding of the capacity of the distal radius under dynamic impact loading conditions indicative of a forward fall, and has provided insight into the role of joint kinematics and muscle involvement in reducing the risk of forward fall-related fracture. The multi-variate injury risk models are the first to be developed for the distal radius. Along with the multi-variate models are recommendations of acceptable injury probability levels (calculated from the injury risk models). The combination of this information will allow, for the first time, an evidence-based recommendation to be made regarding the efficacy of a distal radius fracture prevention intervention. The development of a validated distal radius finite element will also provide another valuable tool capable of testing the effectiveness of different fall scenarios and fall interventions.

The multi-disciplinary approach adopted for this dissertation makes the findings attractive to engineers, clinicians, kinesiologists and public health officials. While the data presented throughout this dissertation apply to a specific type of loading (i.e. a fall onto the outstretched upper extremity in which the forearm makes a 75° angle with the

impact surface and the wrist is extended 45°), and to a specific demographic (i.e.

healthy young adults), the results of this preliminary work provide valuable information

to the existing literature and highlight area of future research. It is hoped that the body

of work presented here will be used to develop distal radius fracture prevention methods

in an attempt to improve the health and well being of those individuals currently at the

highest risk of sustaining these injuries.

5.5 References

Burkhart TA, Dunning CE, Andrews DM. 2011. Determining the optimal system-specific cut-off frequencies for filtering *in vitro* upper extremity impact force and acceleration data through residual analysis. Journal of Biomechanics. 44, 2728-2731.

Cristolfolini, L., Schileo, E., Juszczyk, M., Taddei, F., Martelli, S., Viceconti, M. 2010. Mechanical testing if bones: the positive synergy of finite-element models and *in vitro* experiments. Philosophical Transactions of The Royal Society, A: Mathematical, Physical and Engineering Sciences. 368, 2725-2763.

DeGoede KM, Ashton-Miller JA. 2003. Biomechanical simulations of forward fall arrests: effects of upper extremity strategy, gender and aging-related declines in muscle strength. Journal of Biomechanics. 36, 413-420.

Greenwald RM, Janes PC, Swanson SC, McDonald TR. 1998. Dynamic impact response of human cadaveric forearms using a wrist brace. The American Journal of Sports Medicine. 26, 825-830.

Langstemo L, Poliquin S., Hanley DA, Prior JC, Barr S, Anastassiades, T, Towheed T, Goltzman D, Kreiger N. 2010. Dietary patterns in Canadian men and women ages 25 and older: relationship to demographics, body mass index, and bone mineral density. BMC Musculoskeletal Disorders. doi:10.1186/1471-2474-11-20

May MM, Lawton JN, Blazar PE. 2002. Ulnar styloid fractures associated with distal radius fractures: incidence and implications for distal radioulnar joint instability. Journal of Hand Surgery [American Edition]. 27A, 965-971.

Nordsletten L, Ekeland A. 1993. Muscle contribution to tibial fracture strength in rats. Acta Orthopaedica Scandinavia. 64, 157-160.

Staebler MP, Moore DC, Akelman E,Weiss AP, Fadale PD, Crisco JJ III. 1999. The effect of wrist guards on bone strain in the distal forearm. The Amercian Journal of Sports Medicine. 27, 500-506.

CHAPTER 6 - CONCLUSIONS

The findings described throughout this dissertation are a result of three research methods (*in vitro, in vivo,* and numerical) that further the understanding of distal radius injuries in response to impact loading (radius/impact surface angle of 75$^{\rm o}$ and a wrist extension angle of 45$^{\rm o}$) that occurs during a forward fall. The results presented throughout apply to a specific loading application and demographic (healthy young adults). While each of these methods on their own provide valuable information with respect to these injuries (Section 6.1), the combined effect provides a better perspective on how these injuries occur and the fall strategies that can be employed to reduce their occurrence.

Specific conclusions for each of the three thematic areas within the dissertation are outlined in separate sections below.

6.1 *In vitro*

➢ The radius fractures at a mean impact velocity of 3.4 m/s corresponding to mean energy and resultant force levels of 40 J and 2285 N, respectively.

➢ Multi-variate injury models were been developed that highlight the multi-directional dynamic nature of fractures to the distal radius that result from a forward fall.

➢ Accelerometers are a valid strain gauge surrogate for measuring the response of the underlying bone to impacts.

6.2 *In vivo*

➢ The Propelled Upper Limb fall ARrest Impact System (PULARIS) accurately and reliably simulates the kinematics and kinetics associated with a forward fall from low heights.

➢ Individuals are capable of selecting a safe landing strategy when given minimal instruction.

➢ The muscles of the upper extremity display a preparatory response in anticipation of a distal upper extremity impact.

6.3 Numerical

➢ A high quality hexahedral finite element mesh of the distal radius was developed and used to create a distal radius finite element model.

➢ The distal radius finite element model accurately predicts the reaction of the radius in response to dynamic loading.

➢ The location and severity of fracture patterns was highly agreeable between the experimental and numerical testing.

APPENDICES

APPENDIX A - Specimen Preparation Protocol

1. Potting the specimen

a. Remove specimen from freezer and let thaw over night wrapped in saline soaked paper towels.
b. Cut a 5 cm length of PVC pipe
c. Place paper towel in bottom of jig and insert the PVC pipe. The jig is the component that houses the PVC pipe and attaches to posterior impact plate within the impactor (Figure A.1)
d. Tighten the jig set screws around PVC pipe (Figure A.1)
e. Set bone in place to determine where bone screws will need to be placed to stabilize the bone within the cement. Remove the bone and place 3-4 screws in the proper locations.
f. Align the impactor mock-up that included the model lunate and scaphoid such that the center of the mock-up is in-line with the center of the potting jig (Figure A.2).
g. Place the bone in the potting jig and adjust the lunate and scaphoid to a predetermined height that matches the distance from the posterior impact plate to the model lunate scaphoid within the impactor (Figure A.2).
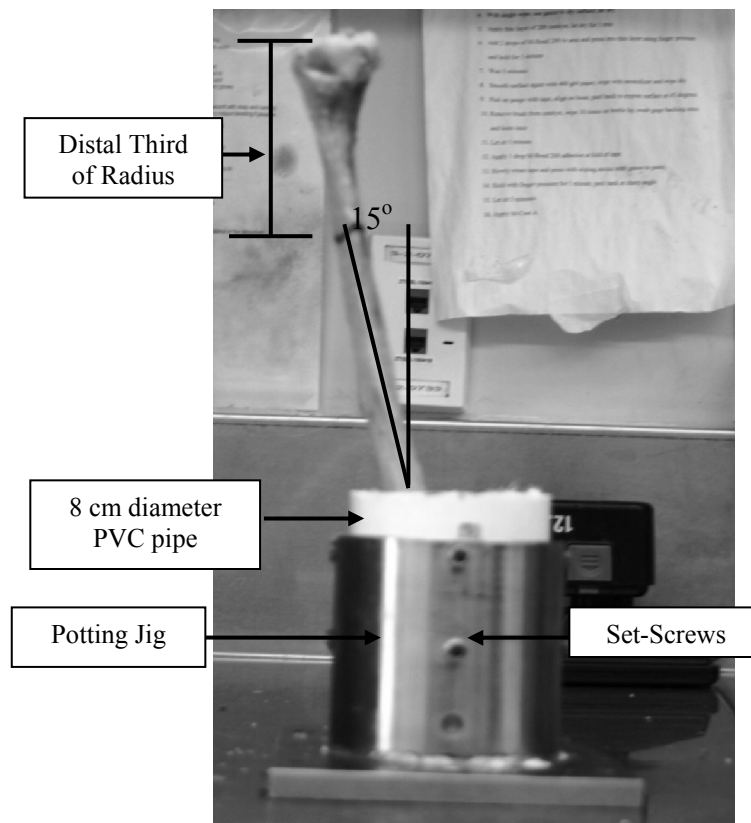
Figure A.1: Potted Specimen
The potted specimen within the jig before
the second PVC is added.
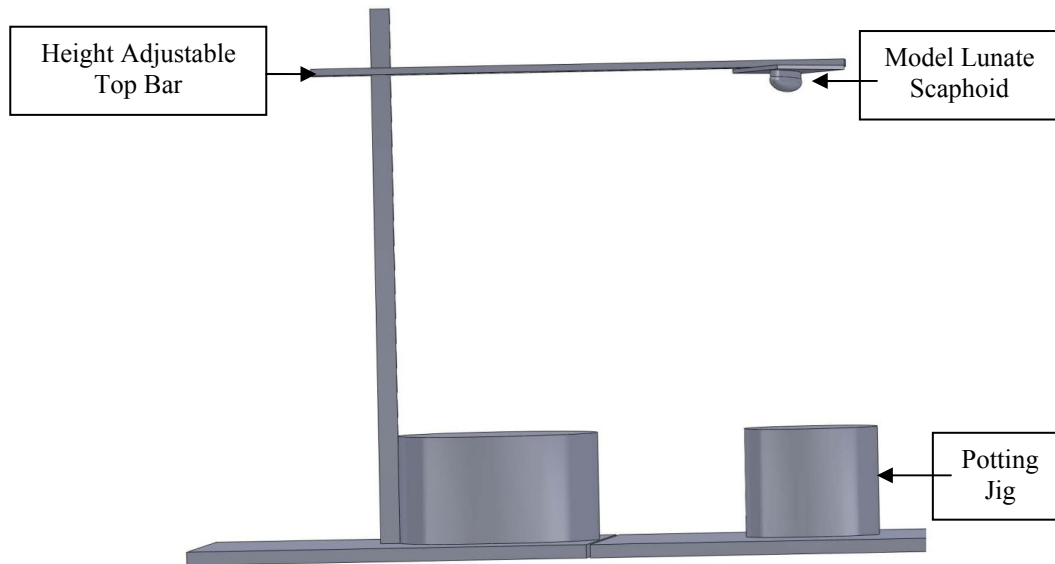
Figure A.2: Potting Mock-up
A schematic of the mock-up jig that was used to pot the specimens and
set the appropriate sagital and frontal plane angles.

h. Place the bone back in the jig and PVC pipe and align the distal end of the radius
with the model lunate scaphoid so that the intraartuicular surface is in contact with the
model lunate and scaphoid (Figure A.1).
i. Adjust the position of the proximal radius until 15° sagital plane and 0° frontal plane
angles are achieved (Figure A.1).

2. Cementing the Bone

a. In a Ziploc bag add 250 ml of cement to ~1.5 syringes of water (may need to add
more water to get to the right consistency).
b. Mix thoroughly to ensure that there are no lumps and the mixture is smooth.
c. Cut the corner off of the Ziploc bag and pour the cement into the PVC pipe while
patting down with a popsicle stick (do not over work the cement or air bubbles will
form).
d. Let the cement dry for 20-30 minutes, keeping the specimen wrapped in saline
soaked paper towel.
e. Add three screws to the set cement leaving approximately 2.5-5.0 cm of the screws
exposed.
f. Cut a piece of 12.7 cm diameter PVC pipe such that when it is added to the top of the
jig the distal third of the radius remains exposed (Figure A.3).
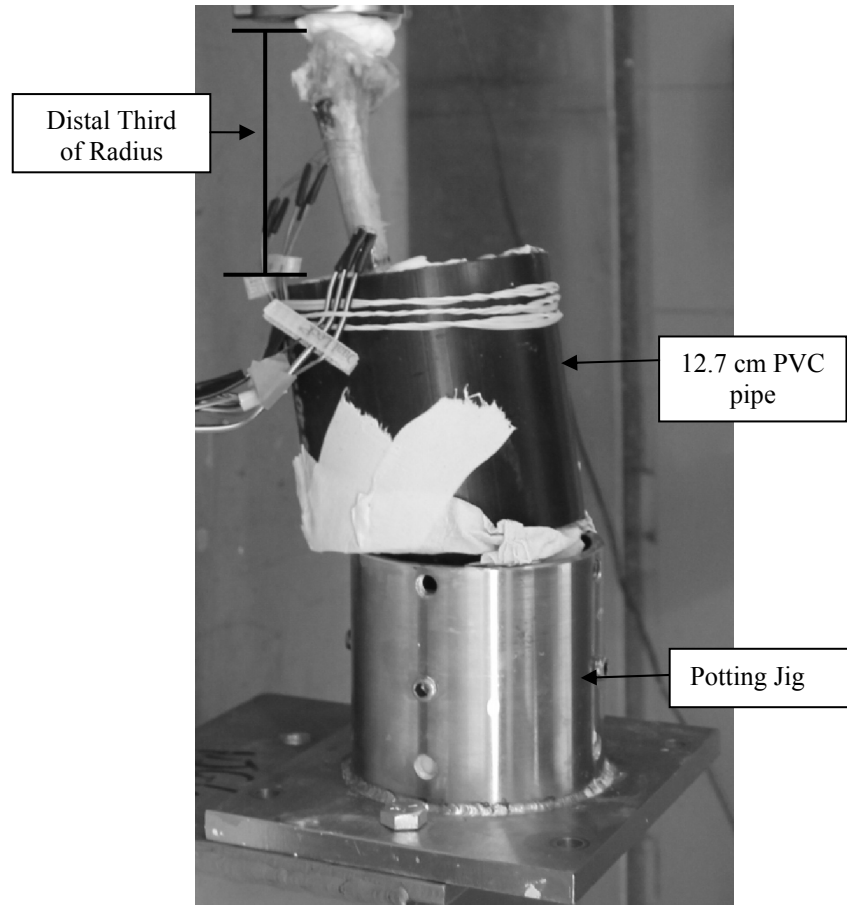
Figure A.3: Final Potted Specimen
The final potted specimen resting against the
model lunate scaphoid of the mock-up jig. Also
shown here is with the additional PVC pipe.

g. Place the second PVC pipe on top of the potting jig and secure in place with tape.
Tape layers of paper towel in areas where there are holes between the potted specimen
and the second piece of PVC pipe (Figure A.3).
h. Mix the cement and add it to potted specimen. Bring the cement to the appropriate
level leaving only the distal third of the radius exposed (Figure A.3).

3. Attaching Strain gauges
a. Sand the surface of the bone where the gauge is to be laid with 400 grit sandpaper,
rub with alcohol pad to degrease.
b. Apply a thin layer of M-Bond 200 catalyst, let dry for 1 min.
c. Add 2 drops of M-Bond to the area and press into a thin layer using tape and finger
pressure. Hold for 1 min.
d. Wait 5 minutes.
e. Remove the tape, sand lightly to even surface. Wipe again with alcohol pad.
f. Place the strain gauge on a clean surface, and press a piece of installation tape on top.
Pick up the gauge using tape.

g. Apply a thin layer of M-Bon catalyst to both the back surface of gauge and the surface of the bone.

h. Align the grid of the gauge with the laser line, and apply 1 drop of M-Bond 200 adhesive to the attachment site. Press down evenly, hold with finger pressure for 1 minute pressing on all corners of the gauge.

i. Let sit for 5 minutes, remove tape.

j. Apply M-Coat, a polyurethane coating to gauge and lead wire attachment points.

k. Let sit for 5-minutes.

4. Impact Protocol

a. Mount the specimen on the proximal bracket, ensure alignment is correct with the scaphoid/lunate impactor and tighten all set screws.

b. Wire instrumentation into electronics boxes (note: the 10th and 11th pair of terminals are to be skipped). Tighten screw-down terminals tightly.

c. Open Measurement and Automation Explorer using task "radius impact"

d. Calibrate instrumentation **(turn shunt calibration OFF).**

e. Recalibrate the load cell and determine the off-set values.

f. Open vi that controls the solenoid (solenoid.vi) and set solenoid control box to automatic and set the solenoid vi to activate for 0.3 s Make sure air tank pressure is zero and cycle a few times to make sure it is running smoothly.

g. Open vi that controls the regulator (regulator vi), open valve to wall air, open valve next to tank, and select AO1 from drop down menu and set the voltage and hit run.

h. Open MotionScope camera software and set appropriate parameters (1000 fps).

i. Turn on the pressure gauge under the counter and track the pressure using the camera while adjusting the voltage to the regulator. Once pressure is stabilized, stop the camera acquisition.

j. Push the projectile to the appropriate distance, apply foam to the distal bracket, push distal bracket in contact with the end cap, and adjust the proximal bracket so that the specimen is sandwiched.

k. Trigger the camera.

l. Trigger the data collection program.

m. Trigger the solenoid.

References

Quenneville CE, 2009. *Experimental and numerical assessments of injury criteria for short-duration, high-force impact loading of the tibia*. PhD Dissertation, The University of Western Ontario.

Finlay JB, Bourn RB, McLean J. 1982. A technique for the *in vitro* measurement of principal strains in the human tibia. Journal of Biomechanics. 15, 72-729.

Wright TM, Hayes WC. 1979. Strain gauge application on compact bone. Journal of Biomechanics, 12, 471-475.

APPENDIX B - Definition of Fracture Classification Systems

Table B.1: AO Fracture Classification
Description of the AO distal radius fracture classification system.

Classification	Description
A	Extra-articular Fractures
A1	Ulna Fractured, radius intact
A2	Radius, simple and impacted
A3	Radius, multi-fragmentary
B	Partial articular fracture of radius
B1	Sagittal
B2	Coronal, dorsal rim
B3	Coronal, palmar rim
C	Complete articular fracture of radius
C1	Articular simple, metaphyseal simple
C2	Articular simple, metaphyseal multi-fragmentary
C3	Articular multi-fragmentary

Table B.2: Frykman Fracture Classifications
Description of the Frykman fracture classification system.

| Description | Classification | |
	Ulna Fracture Absent	Ulna Fracture Present
Extra-articular	I	II
Intra-articular	III	IV
Intra-articular involving distal radial ulnar joint	V	VI
Intra-articular involving both radiocarpal and distal radioulnar joints	VI	VIII

References

Frykman G. 1967. Fracture of the distal radius including sequelae-shoulder-hand-finger syndrome: disturbance in the distal radio-ulnar joint and impairment of nerve function. Acta Orthopaedica Scandinavia, 108, 1-135.

Mueller ME, Nazarian S, Koch P, Schatzker J. 1990. The AO classification of fractures of long bones. Berlin, Germany: Springer-Verlag.

APPENDIX C - Fracture Patterns and Classifications

Table C.1: Fracture Patterns and Classifications

Summary of the fracture patterns for all eight specimens. The letter after the specimen number indicates whether the specimen was from the left (L) or the right (R) side. The sagittal view pictures are taken from the medial (ulnar) aspect to show the damage into the sigmoid fossa and the pictures are labelled to orient the specimens with respect to the medial (M), lateral (L), volar (V) and dorsal (D) directions.
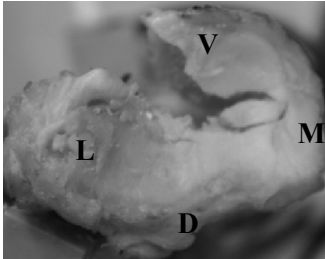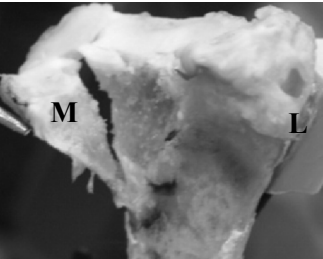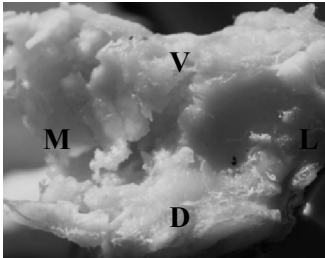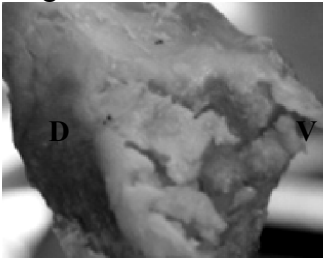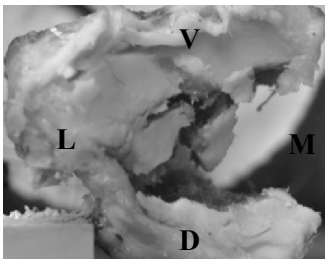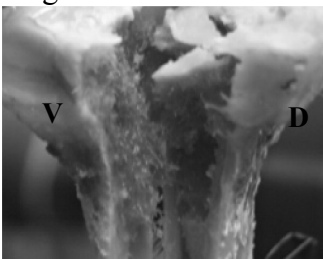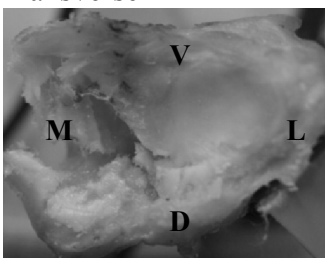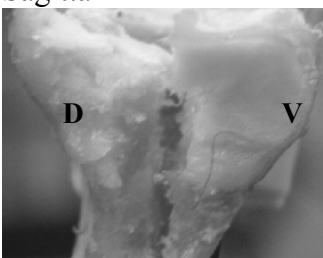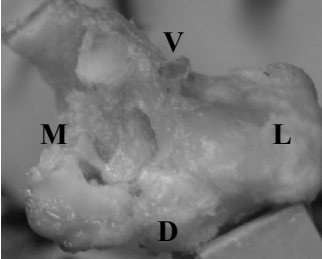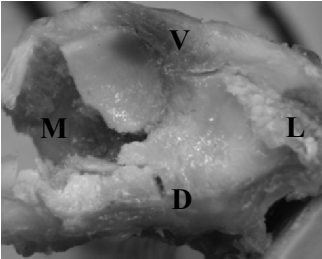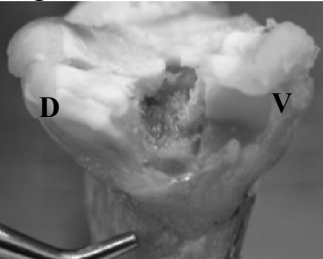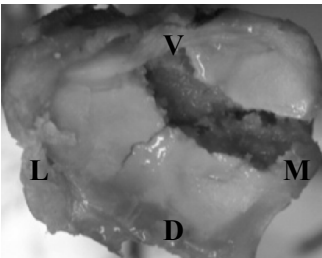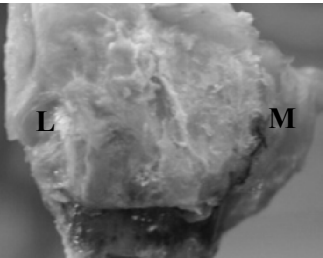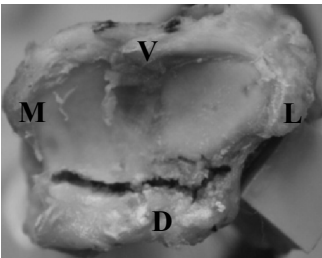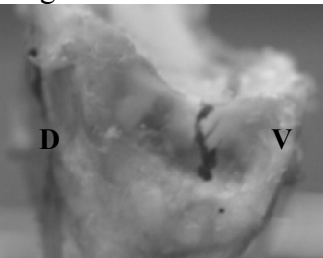
Specimen	Fracture Pattern		Fracture Classification	
			Frykman	AO
04011R	Transverse	Frontal	III (Barton's)	B3
07017L	Transverse	Sagittal	VII	B3
07030R	Transverse	Sagittal	VII	C3
07043L	Transverse	Sagittal	VII	B2

Table C.1 Con't

Specimen	Fracture patterns		Fracture Classification	
			Frykman	AO
08007L	Transverse	Sagittal	VII	B3
08010L	Transverse	Sagittal	VII	C1
07007R	Transverse	Dorsal	VII (Colles)	C1
07004L	Transverse	Sagittal	III (Colles)	B2

APPENDIX D - Comparison of *In vivo* Fall Methods

Table D.1: *In vitro* Fall Studies
Summary of the different fall methods and protocols.

Author	Set-up	Protocol/conditions	Impact Velocity	Impact force
Chiu et al. (1998)	Kneeling One handed	1 cm, 3 cm & 5 cm falls	N.S.	Fz^a 1 cm: 400 N 3cm: 600 N 5 cm: 800 N
Chou et al. (2001)	Not described	3 cm and 6 cm Bent arm and straight arm	N.S.	Fz 3 cm : ~390 N 6 cm: ~401 N
DeGoede et al. (2002)	Sitting Weighted pendulum used to induce impact	3 elbow angles	1.8 m/s 2.3 m/s 3.0 m/s	Fz 100-300N
DeGoede et al. (2002)	Standing bent at waist Supported by a tether	3 fall types Shoulders 1 m off ground	2.1 m/s	Fz 500 N -1000N
Kim et al. (2003)	Standing on a block hands at side Vertically mounted force platform	4 fall distances	N.S.	Fz 0.2 BW (203 N) 0.4 BW (278 N)
Lo et al. (2003)	Standing bent at waist Supported by a tether	Fall intervention Shoulders 1 m off ground		Fz 750 N
Troy et al. (2008)	Kneeling Hand s relaxed at sides	Two force platforms with four targets each. Impacts at different combinations of targets.	N.S.	92 % of Fr^b Fz: ~602 N
Burkhart et al. (2010)	Seated human pendulum 5 cm fall	3 elbow angles 4 muscle activation levels Guarded vs. Unguarded	1 m/s	Fz ~ 0.5BW 360 N
Chou et al. (2009) Hsu et al. (2011)	Sling assisted drop Kneeling Hand 5cm	3 arm rotations	N.S.	Fz 65.5 % BW (~430 N)

[a]Fz is the vertical force component, perpendicular with the force platform
[b]Fr is the resultant impact force

APPENDIX E - Determination of Optimal Filter Cut-off Frequencies by Residual Analysis

Introduction[4]

The fundamental nature of impact testing requires a cautious approach to signal processing, to minimize noise while preserving important signal information. However, few recommendations exist regarding the most suitable filter frequency cut-offs to achieve these goals. Therefore, the purpose of this investigation was twofold: to illustrate how residual analysis can be utilized to quantify optimal system-specific filter cut-off frequencies for force, moment, and acceleration data resulting from *in vitro* upper extremity impacts, and to show how optimum cut-off frequencies can vary based on impact condition intensity. Eight human cadaver radii specimens were impacted with a pneumatic impact testing device at impact energies that increased from 20 J, in 10 J increments, until fracture occurred. The optimal filter cut-off frequency for pre-fracture and fracture trials was determined with a residual analysis (performed on all force and acceleration waveforms). Force and acceleration data were filtered with a dual pass, 4th order Butterworth filter at each of 14 different cut-off values ranging from 60 Hz-1500 Hz.

Residual Analysis Theory

A residual analysis calculates a residual (root mean square error (RMSE) at each frequency cut-off between the un-filtered and the filtered signal (Eq. E.1) and are graphed against each respective frequency cut-off (Winter, 2005) (Figure E.1).

---

[4]A Version of this work has been published. Burkhart TA, Dunning CE, Andrews DM. 2011. Determining the optimal system-specific cut-off frequencies for filtering in-vitro upper extremity impact force and acceleration data by residual analysis. Journal of Biomechaics. 44, 2728-2731. This work is also the result of joint research

$$R(f)_c = \sqrt{\frac{1}{N}\sum_{i=1}^{N}(X_i - \widehat{X_i})^2}$$
(E.1)

Where X_i = the original signal at i^{th} sample and $\widehat{X_i}$ = fitered data at the ith sample. If the

data were to contain no signal and were comprised only of noise, the residual plot

would be a straight line decreasing from the intercept at 0 HZ (note: the y-axis intercept
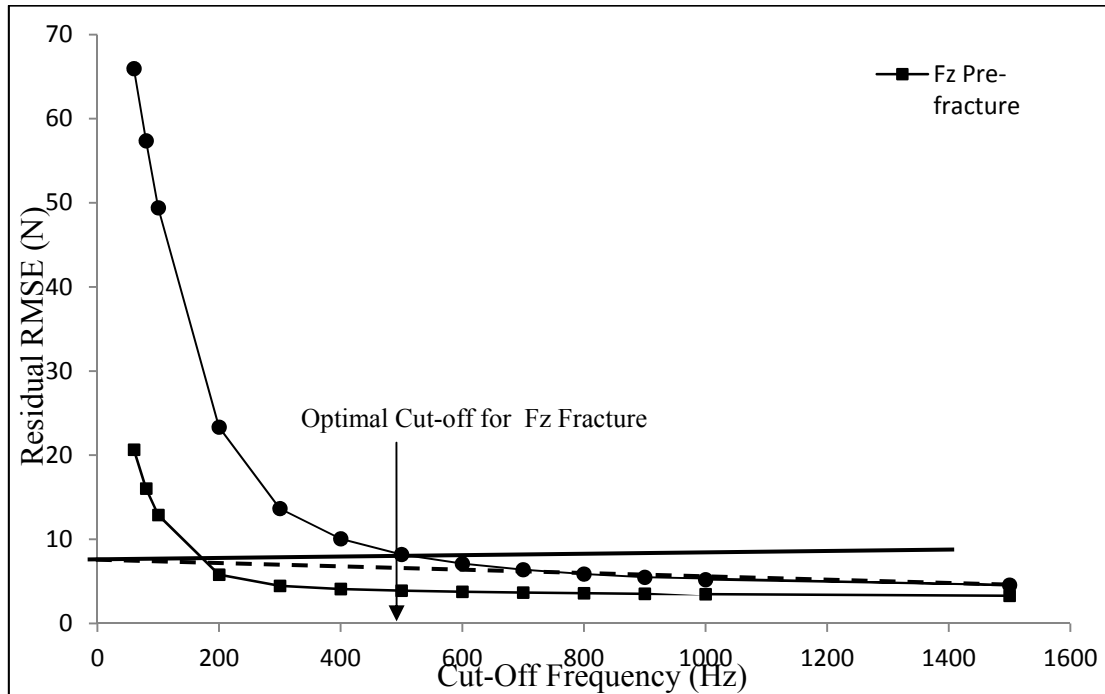
Figure E.1: Residual Analysis
Typical, axial force (Fz) results of the residual analysis comparing a pre-fracture and
fracture trial for a selected specimen. (Reproduced with permission from Journal of
Biomechanics, Elsevier Publishing).

represents the RMS value of the noise) to the Nyquist frequency (x-axis intercept)

(dashed line in Figure E.1). However, when the data consists of the true signal plus the

noise the residuals increase above the straight line as the frequency cut-offs decrease.

When choosing the optimal cut-off, a decision must be made so that the amount of

signal distortion and the noise allowed through is balanced. In many cases it is adequate

to assume that these will be equal and as such a horizontal (solid line in Figure E.1) is

drawn to intersect the residual curve from the y-axis intercept. This intersection

represents the optimal filter cut-off frequency and the amount of noise passed through

and the magnitude of signal distortion (line a-b Figure E.1) can be visualized.

Results

The mean (SD) optimal cut-off frequencies for all force and moment variables

were greater for the fracture trials (605.8 (82.7) Hz) than the pre-fracture trials (513.9

(79.5) Hz), with an average difference of approximately 100 Hz (range of 73 Hz -131

Hz) (Table E.1). Conversely, the optimal cut-off frequencies for the acceleration

variables were lower on average by approximately 17 Hz for the fracture trials (624.7

(94.0) Hz) compared to the pre-fracture trials (641.9 (108.1) Hz) (Table E.1).

Table E.1: *In vitro* Filter Cut-off Frequencies
Mean (SD) optimal cut-off frequencies calculated from the residual analyses and the
rounded (actual) cut-off frequencies that were used to evaluate peak forces and
accelerations. (Reproduced with permission from Journal of Biomechanics, Elsevier)

| Variable | Pre-fracture | | Fracture | |
	Residual (Hz)	Actual (Hz)	Residual (Hz)	Actual (Hz)
Force				
Fx	493.5 (55.9)*	500	588.3 (87.4)	600
Fy	575.7 (84.4)*	600	661.2 (73.4)	700
Fz	396.2 (64.7)	400	469.5 (81.2)	500
Moment				
Mx	598.2 (69.6)	600	672.3 (74.0)	700
My	505.7 (61.2)*	500	637.7 (93.8)	600
Acceleration				
Impact Plate	452.8 (80.8)	500	459.2 (78.2)	500
Distal Axial	716.2 (42.6)*	700	654.5 (31.2)	700
Distal Off-Axis	658.3 (96.1)	700	657.6 (51.8)	700
Proximal Axial	703.9 (33.6)	700	694.8 (29.5)	700
Proximal Off-Axis	678.4 (21.5)	700	657.6 (23.0)	700

*Significant ($p \leq 0.05$) difference in the optimal cut-off frequency between the pre-
fracture and fracture trials.

APPENDIX F - Summary of the Best Subsets Regression

Table F.1: Crack Event Best Subsets

Summary of all of the best subsets crack event regression models including the criteria (Variance Inflation Factor (VIF), p-value (p) and adjusted R^2 (Adj. R^2)) that were used to select the best model. Each column represents a different subset. The variables that were included in each model are represented by their p- and VIF value.

	Crack Event Model Number											
	1		2		3		4		5		6	
Variable	p	VIF	p	VIF	p	VIF	p	VIF	p	VIF	p	VIF
Weight												
Height												
UDBMD												
Peak												
Fr												
Fy										0.18	3	0.09	6
Fz					0.01	6						
My												
Impulse												
Fx												
Fy			0.01	1			0.01	1	0.01	2	0.01	6
Fz	0.001	1			0.001	4						
Load Rate												
Fr												
Fz			0.001	1	0.001	3	0.01	3	0.01	3	0.01	3
Imp. Dur.												
Fr												
Fx												
Fy											0.26	6
Velocity							0.02	4	0.01	7	0.01	12
LnFz							0.05	5	0.02	9	0.01	9
Age												
Adj R^2	0.38		0.53		0.60		0.63		0.65		0.66	

Table F.1: Con't

	Crack Event Model Number											
	7		8		9		10		11		12	
Variable	p	VIF	p	VIF	p	VIF	p	VIF	p	VIF	p	VIF
Weight					0.01	3	0.001	3	0.001	4	0.001	4
Height	0.001	5	0.001	5	0.01	15	0.001	17	0.001	17	0.001	20
UDBMD	0.01	2	0.01	2								
Peak												
Fr			0.05	28								
Fy									0.17	13	0.15	13
Fz	0.02	27									0.26	38
My			0.09	2			0.09	2	0.01	4	0.02	5
Impulse												
Fx					0.06	4	0.02	4	0.03	6	0.02	6
Fy	0.001	3	0.001	3								
Fz					0.001	23	0.001	27	0.00	34	0.001	35
Load Rate												
Fr												
Fz					0.03	3	0.08	3				
Imp. Dur.									0.06	2	0.16	2
Fr												
Fx	0.03	3	0.02	3	0.01	3	0.01	3	0.02	6	0.01	8
Fy												
Velocity	0.001	10	0.001	11	0.001	15	0.001	18	0.001	15	0.001	17
LnFz	0.001	42	0.001	42	0.001	35	0.001	48	0.00	52	0.001	105
Age					0.001	3	0.001	3	0.03	5	0.02	6
Adj R^2	0.72		0.76		0.80		0.83		0.85		0.86	

Table F.1: Con't

Variable	13 p	13 VIF	14 p	14 VIF	15 p	15 VIF	16 p	16 VIF	17 p	17 VIF
					Crack Event Model Number					
Weight	0.02	5	0.001	4	0.001	5	0.02	16	0.12	42
Height	0.001	24	0.001	28	0.001	28	0.001	38	0.01	65
UDBMD					0.19	8	0.24	24	0.30	30
Peak										
Fr	0.06	14253	0.09	50	0.18	57	0.46	86	0.81	222
Fy			0.03	19	0.02	21	0.04	32	0.10	54
Fz	0.07	15249								
My	0.04	3	0.01	7	0.01	8	0.01	8	0.02	8
Impulse										
Fx	0.01	6	0.01	9	0.01	9	0.02	9	0.04	10
Fy							0.54	22	0.65	104
Fz	0.001	37	0.001	37	0.001	38	0.01	107	0.04	237
Load Rate										
Fr	0.07	20841	0.04	14986	0.03	26271	0.04	32932	0.08	37483
Fz	0.07	21022	0.04	14697	0.03	26243	0.04	33191	0.08	37509
Imp. Dur.										
Fr			0.04	4	0.04	4	0.05	4	0.09	5
Fx	0.01	4	0.01	8	0.01	8	0.01	9	0.03	9
Fy									0.82	39
Velocity	0.001	29	0.001	32	0.001	32	0.001	32	0.02	75
LnFz	0.001	138	0.001	141	0.001	141	0.001	152	0.001	157
Age	0.001	9	0.01	9	0.001	11	0.01	8	0.03	20
Adj R^2	0.87		0.90		0.91		0.91		0.88	

Table F.2: Fracture Event Best Subsets
Summary of all of the best subsets Fracture event regression models including the criteria (Variance Inflation Factor (VIF), p-value (p) and adjusted R^2 (Adj. R^2)) that were used to select the best model. Each column represents a different subset. The variables that were included in each model are represented by their p- and VIF value.

| | Fracture Event Model Number | | | | | | | | | |
| | 1 | | 2 | | 3 | | 4 | | 5 | |
Variable	P	VIF	P	VIF	P	VIF	P	VIF	P	VIF
Weight										
Height										
UDBMD										
Peak										
Fr										
Fz					0.015	2	0.001	92	0.01	113
Impulse										
Fy			0.05	1	0.005	1			0.02	2
Fz										
Load Rate										
Fr										
Imp. Dur.										
Fz							0.01	8	0.01	8
Fr										
Fy										
Velocity	0.001	1			0.001	2	0.001	3	0.001	3
Ln Fz							0.002	55	0.02	73
Age										
Adj. R2	0.64		0.71		0.82		0.83		0.90	

Table F.2: Con't

| Variable | Fracture Event Model Number | | | | | | | | | |
| | 6 | | 7 | | 8 | | 9 | | 10 | |
	P	VIF	P	VIF	P	VIF	P	VIF	P	VIF
Weight	0.18	1	0.03	2	0.04	2	0.10	2		
Height									0.11	15
UDBMD			0.2	3	0.18	3				
Peak										
Fr			0.001	98	0.02	142				
Fz	0.003	116					0.01	147	0.01	279
Impulse										
Fy	0.04	2			0.21	3	0.31	4	0.29	7.1
Fz									0.23	56
Load Rate										
Fr			0.001	9	0.01	17	0.48	8980		
Imp. Dur.										
Fz	0.01	8					0.57	8902	0.02	19
Fr					0.22	4			0.37	14
Fy			0.05	2			0.26	5	0.31	11
Velocity	0.001	3	0.001	5	0.001	6	0.01	9	0.002	8
Ln Fz	0.01	76			0.01	84	0.01	95	0.02	310
Age			0.001	53			0.19	3	0.11	11
Adj. R2	0.90		0.91		0.92		0.91		0.90	

Table F.2: Con't

Variable								
				Fracture Event Model Number				
	11		12		13		14	
	p	VIF	p	VIF	p	VIF	p	VIF
Weight							0.96	34
Height	0.15	17	0.15	28	0.46	6	0.77	254
UDBMD			0.62	6	0.80	9	0.90	12
Peak								
Fr			0.06	490	0.82	20388	0.92	25989
Fz	0.02	305			0.91	16139	0.93	28852
Impulse								
Fy	0.33	11	0.36	11	0.48	11	0.74	30
Fz	0.26	74	0.20	101	0.51	205	0.77	634
Load Rate								
Fr	0.70	13367	0.60	21886	0.72	24256	0.87	87601
Imp. Dur.								
Fz	0.62	13180	0.60	21886	0.68	24546	0.85	88225
Fr	0.38	16	0.55	21999	0.563	20	0.83	129
Fy	0.42	12	0.36	17	0.64	13	0.80	23
Velocity	0.03	23	0.57	12	0.20	53	0.59	199
Ln Fz	0.04	354	0.07	40	0.26	962	0.64	3254
Age	0.14	12	0.08	550	0.35	17	0.74	89
Adj. R2	0.90		0.84		0.80		0.54	

APPENDIX G - Protocol for Performing a Weibull Analysis in Excel

1. Calculating and transforming risk scores

a. After determining the multivariate model that best predicts the fracture event, place the values of these variables for each respective specimen across the top of the spreadsheet. Include both the pre-fracture and fracture values (Figure G.1; Cells B1:J11).

b. Using the prediction model calculate the risk of failure for both the pre-fracture and fracture events.

c. Start a new table by ranking (1-8; D22:D29) the risk of failures calculated in step 2, in ascending order (Figure G.1; C22:C29).

d. Calculate the median ranks (Eq.G.1) (Figure G.1; E22:E29), that is, the proportion of the population that will fail at the risk score calculated from the failure prediction equation (Figure G.1; C22:C29).

$$\frac{Risk\ Order - 0.3}{N + 0.4}$$

(Eq. G.1)

e. For each median rank calculate (Figure G.1; F22:F29):

$$\frac{1}{(1 - Median\ Rank)}$$

(Eq. G.2)

f. Lineralize the previously calculated values with Eq. G.3) (Figure G.1; G22:G29):

$$\ln\left(\ln\left(\frac{1}{(1 - Median\ Rank)}\right)\right)$$

(Eq. G.3)

g. Transform the failure risk values (Figure G.1; C22:C29) by taking the natural logarithm of each value (Eq. G.4) (Figure G.1; H22:H29):

$$\ln(failure\ risk\ score)$$

(Eq. G.4)

2. Fitting a line to the data

a. Perform a regression analysis to fit a line to the data and calculate the Weibull Coefficients: Under the "Data" tab select "Data Analysis" and regression.

b. The input Y range will be the data in cells G22:G29 (Figure G.1), and the input X-range will be H22:H29 (Figure G.1), and select labels.

c. Under the output options, select "New Worksheet Ply:" and hit "OK". This will place the results of the regression analysis (Figure G.2) in a new worksheet. Note: this regression analysis is not unique to Excel and could be performed with alternate statistical software.

	A	B	C	D	E	F	G	H	I	J
1										
2				PreFracture			Fracture			
3		Specimen	FzPeak	FyImpulse	Velocity	FzPeak	FyImpulse	Velocity	Risk at Fail	Risk at Prefail
4		10-07017L	1343.917947	0.3054392	2.2	3797.564852	3.7389718	4.3226802	1.311064488	-0.046254461
5		10-07030R	1123.195489	1.7056138	2.1692991	953.0525951	1.4246665	3.3606177	1.034114329	0.245838822
6		10-08007L	1388.611619	1.4427285	2.1278248	3930.303029	1.2921458	4.273768	0.801738934	0.098215039
7		10-07043L	1330.336083	1.1992785	2.1355362	2350.317682	2.7549283	3.3549821	0.886963146	0.075489616
8		10-08010L	1035.290419	1.125503	2.1	1335.452119	1.9773292	3.3	0.988505375	0.119420965
9		10-07007R	1080.78119	0.7614036	2.058406	1859.740157	3.1292643	3.3502179	1.085593675	0.013758592
10		10-04011R	1512.297734	0.2962801	2.13184435	837.269441	0.2615086	3.2138761	0.758887328	-0.139362668
11		10-07004L	1165.746352	1.7962975	2.1262113	1640.964249	4.2554513	3.596591714	1.512090520	0.221849564
12										
13										
14									Failure predictions	
15										
16					Model					
17		Variables	Constant	FzPeak	FyImpulse	Velocity		Prediction model Coefficients		
18		Coef.	-1.196	-0.000274	0.18	6.65E-01				
19										
20		WEIBULL	A	B	C	D	E	F		
21		Specimen	Risk	Risk order	Median Ranks	1/(1-Median Rank)	ln(ln(1/(1-Median Rank)))	ln(Risk)		
22		10-04011R	0.758887328	1	0.083333333	1.090909091	-2.441716399	-0.275901961		
23		10-08007L	0.801738934	2	0.202380952	1.253731343	-1.486670964	-0.220972243		
24		10-07043L	0.886963146	3	0.321428571	1.473684211	-0.947354424	-0.119951847		
25		10-08010L	0.988505375	4	0.44047619	1.787234043	-0.543574052	-0.011561198		
26		10-07030R	1.034114329	5	0.55952381	2.27027027	-0.198574256	0.03354534		
27		10-07007R	1.085593675	6	0.678571429	3.111111111	0.12661497	0.082127003		
28		10-07017L	1.311064488	7	0.797619048	4.941176471	0.468504666	0.270839393		
29		10-07004L	1.51209052	8	0.916666667	12	0.910235093	0.413493143		
30										

Ranked Failure Risks

Figure G.1: Weibull Data Preparation
Preparation of the failure data for determining the Weibull parameters

3. Calculating the Weibull Parameters

a. Label cells B19 and B20 Beta and Alpha, respectively.
b. The beta coefficient is simply the coefficient of the ln(failure risk) determined from the regression analysis. Transfer this value to cell C19.
c. The alpha coefficient can be calculated in cell C20 (Figure G.2) using Eq.G.5.

$$\overline{}$$

(Eq. G.5)

Where b = the intercept coefficient (Figure G.2; C17) (Figure G.2; C18).

	A	B	C	D	E	F	G	H	I	J
1		SUMMARY OUTPUT								
2										
3		*Regression Statistics*								
4		Multiple R	0.978422376							
5		R Square	0.957310346							
6		Adjusted R Square	0.948772416							
7		Standard Error	0.187276094							
8		Observations	7							
9										
10		ANOVA								
11			*df*	*SS*	*MS*	*F*	*Significance F*			
12		Regression	1	3.932464519	3.932464519	112.1243986	0.000129845			
13		Residual	5	0.175361677	0.035072335					
14		Total	6	4.107826197						
15										
16	b		*Coefficients*	*Standard Error*	*t Stat*	*P-value*	*Lower 95%*	*Upper 95%*	*Lower 95.0%*	*Upper 95.0%*
17		Intercept	-0.475362191	0.074228754	-6.404016813	0.00137653	-0.666173278	-0.284551103	-0.666173278	-0.284551103
18		ln (Failure Risk)	3.701997412	0.349611772	10.58888089	0.000129845	2.803291742	4.600703082	2.803291742	4.600703082
19	β	Beta	3.701997412							
20		Alpha	1.137015615		Alpha and Beta Coefficients					
21										
22		RESIDUAL OUTPUT								
23										
24		*Observation*	Predicted -2.44171639888146	*Residuals*						
25		1	-1.293400861	-0.193270103						
26		2	-0.919423618	-0.027930806						
27		3	-0.518161718	-0.025412335						
28		4	-0.351177429	0.152603173						
29		5	-0.171328239	0.297943209						
30		6	0.527284542	-0.058779876						
31		7	1.055388356	-0.145153263						
32										

Figure G.2: Weibull Regression Results
Results of the regression analysis.

4. Creating a Weibull Cumulative Distribution Function (CDF)

a. To the side of the regression analysis data create a column of random data (Figure G.3; N3:N18) starting at zero and increasing until you reach a value greater than the highest failure prediction.
b. In the next column calculate the probability of failure using the Excel command:

=WEIBULL (Risk, Alpha, beta, True)

Where Risk = the risk score in column N (Figure G.3), alpha is the alpha parameter (Figure G.2; C20), beta is the beta parameters (Figure G.2; C19) and TRUE displays the data as a cumulative distribution function (CDF).
c. To display the CDF curve create an x-y scatter where risk is on the x-axis and probability is on the y-axis (Figure G.3).

	N	O	P	Q	R	S	T	U
1	CDF				Data			
2	Risk	p			Risk at Prefail	Risk at Fail		
3	0	0		0	-0.046254461	1.311064488	1	
4	0.1	0.000123461		0	0.245838822	1.034114329	1	
5	0.2	0.001605531		0	0.098215039	0.801738934	1	
6	0.3	0.007182781		0	0.075489616	0.886963146	1	
7	0.4	0.020694123		0	0.119420965	0.988505375	1	
8	0.5	0.046645427		0	0.013758592	1.085593675	1	
9	0.6	0.089548238		0	-0.139362668	0.758887328	1	
10	0.7	0.152953144		0	0.221849564	1.51209052	1	
11	0.8	0.238252308						
12	0.9	0.343531396						
13	1	0.462947732						
14	1.1	0.58715561						
15	1.2	0.705036663						
16	1.3	0.806405822						
17	1.4	0.884711976						
18	1.5	0.938514845						
19	1.6	0.971034229						
20	1.7	0.988118339						
21	1.8	0.995819632						

Figure G.3: Cumulative Distribution Function Data
Data used to create the CDF.

References

Dorner WW. 1999. Using Microsoft Excel for Weibull analysis. Quality Digest. Downloaded from http://www.qualitydigest.com/jan99/html/body_weibull.html

APPENDIX H - Procedure for Developing a Radius Bone Model

Step 1: Solid model development in Mimics[®]

1. Defining bone regions

a. Import images from the CT scan by creating a new project, selecting "Import Images, and navigating to the folder where the scan is located, then select "convert". Assign a "top" and "bottom" to the model.

b. The model appears in three views with a 3D rendering in the fourth quadrant (Figure H.1). Adjust the contrast sliders (lower right corner of the screen) until the detail in the models is best visible.
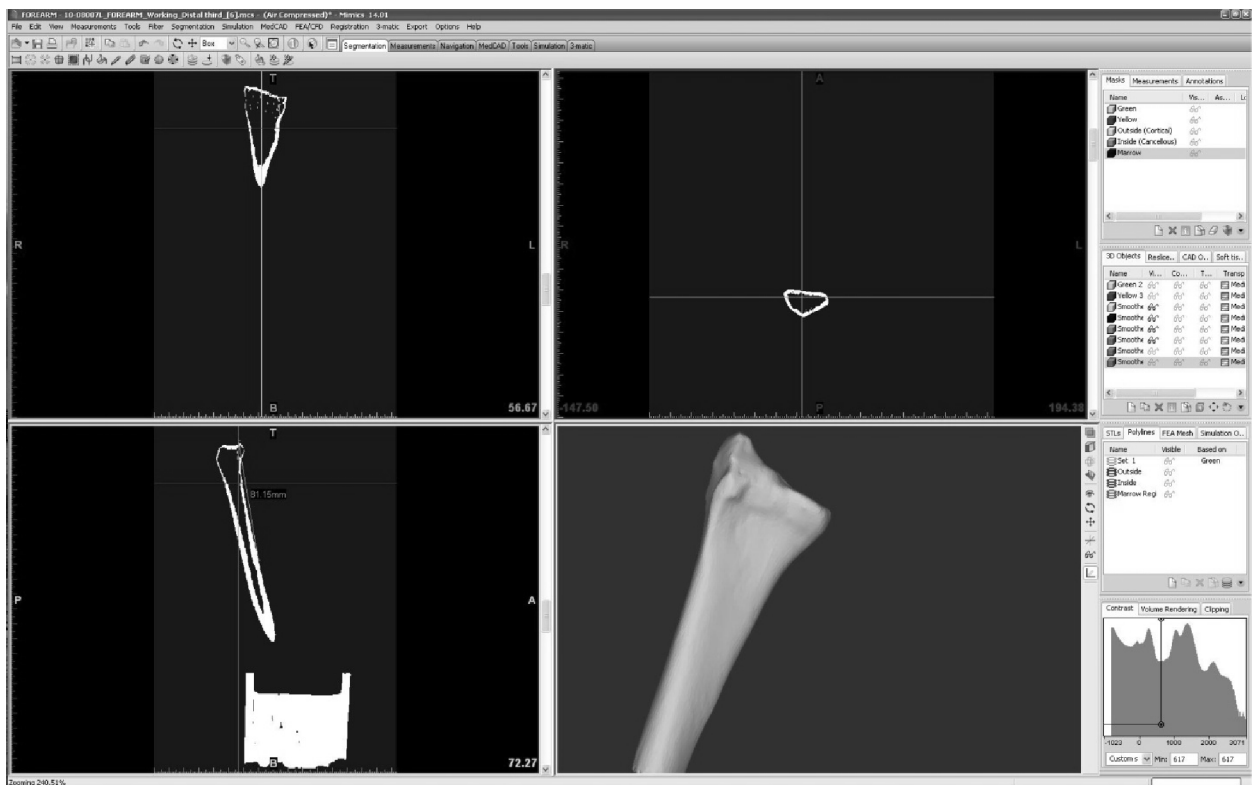
Figure H.1: Mimics[®] Environment
The CT scans in the Mimics[®] environment.

c. Scroll through the axial plane until the hydroxyapatite is visible. Select the

"Thresholding" tool ⬜ (upper left corner of the screen) to create a new mask based on the Hounsfield values in the model. Adjust the slider bars, such that the upper and lower

boundaries allow the hydroxyapatite to be highlighted (this should also highlight the cortical bone) and select "Apply". This will segment the bone with a coloured mask.

Select the "Crop Mask" tool ▦ and adjust cropping mask in all directions to leave only the distal third of the radius (this can be determined from the digitization of the level of the potting cement).

Adjust the slider bars so that the upper and lower boundaries highlight only the cancellous bone and select "Apply".
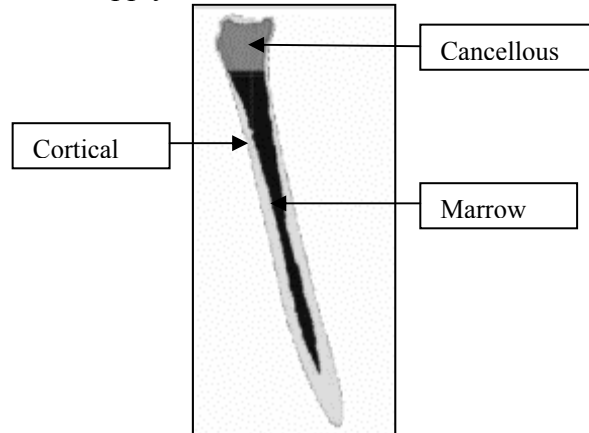
Figure H.2: Bone Thresholding
Thresholded bone with cortical (light grey), cancellous (dark grey) and marrow (Black) mask.

d. Zoom in on the axial slices and use the "Edit Mask" tool ✎ to remove extra pixels from the mask and fill in any holes in the mask, such that the cortical bone is one continuous region.
e. Once the bone is thresholded (Figure H.2), polylines need to be generated to define the outer and inner surfaces of the bone. On the "Polylines" tab select "New" and select the cortical mask generated in the previous step (d).

(a) (b)
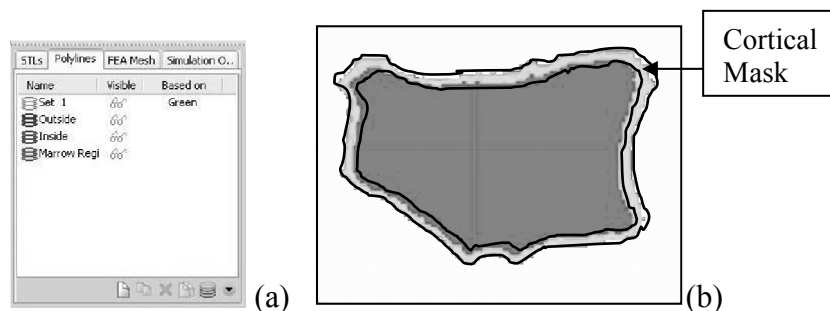
Figure H.3: Polylines
Polylines tab (a) and the polylines (b) based on the cortical mask created previously.

f. Select the "Polyline Growing" tool ![icon] to move the exterior polylines to a unique set and the interior polylines to a second unique set (Figure H.3). This involves selecting the polylines, which will also auto multi-select, but as the geometry changes, several polylines may be needed to be selected in order to capture all of the required polylines.

g. To define the transition from cancellous bone to marrow, scan through the axial slices until a hole larger than a few pixels is present. This will define the level where the transition occurs. Copy the interior polylines from this region (transition to the end of the bone) to a separate set.

h. Select the "Cavity Fill" tool ![icon] and generate a mask for each set of polylines: outside, inside, and marrow.

i. Generate 3D models by selecting the "Calculate 3D" ![icon] tool. Select the masks created previously, set the quality to optimal and select calculate (Figure H.4).
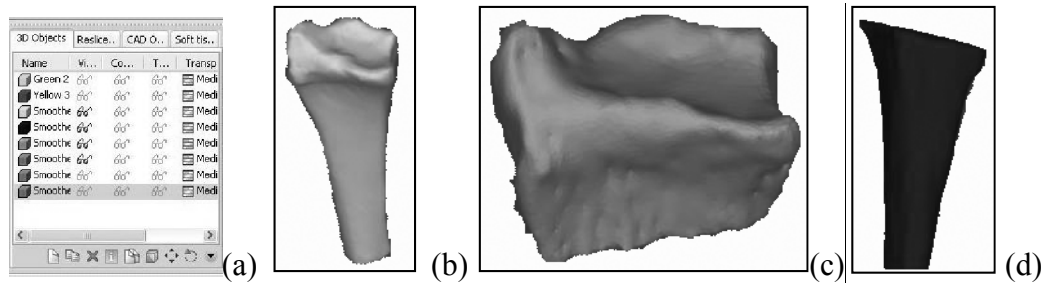
Figure H.4: Solid Model Development
The 3D objects tab (a) and the resulting 3D cortical (b), cancellous (c) and marrow (d) models.

j. Apply smoothing algorithms to the geometry by selecting the "more options" tool ![icon] in the 3D objects tab and select "smoothing" tool ![icon]. Set the number of iterations to 10 and the smoothing factor to 1. Repeat this process until the desired geometry is achieved.

k. To output these models so that they can be imported into TrueGrid® for mesh development, select the "STL+ Module" tool ![icon] and create an ASCII STL file for each of the models created in the previous step (i, j). Use "High Quality" settings.

2. Strain gauge and accelerometer identification

a. To compare strains in the finite element model with those measured experimentally, the locations of the strain gauges need to be identified. On the "CAD objects" tab select "New", "Point", and "Draw". Locate the position of the four corners and center of each strain gauge and accelerometer on the model from the transformed digitized points.

b. On the "CAD objects" tab select "Export txt" and all points. This file will include the x-y-z coordinates of each point.

Step 2: Mesh Development in TrueGrid®

1. Building the Cancellous and Marrow Regions

a. Import and number the three surfaces: cancellous, marrow, cortical (command: *sd surface number_surface type_file path.stl*).
b. Create a part that is 3 blocks (5x5x5 elements) by 3 blocks (5x5x5elements) by (1 block 10 elements) (Command: *block* i-index 1 6 11 16; j-index 1 6 11 16; k-index 1 11;) and delete the corner blocks (command: *dei*).
c. Create a butterfly by moving the vertices to approximate 45° angles and glue the faces together (Command: *Interface, bb*). Note: Each block boundary consists of defining a master and slave face with the same block boundary number (Figure H.5).

(a)

(b)
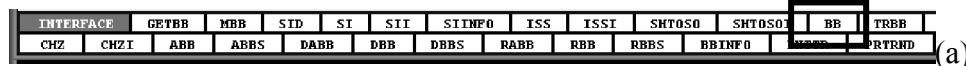
Figure H.5: TrueGrid® Interface Menu
Interface menu (a) and block boundary dialogue (b).

d. Position the part in the center of the cancellous surface (Figure H.6).
e. Create 3D splines on the inner and outer surface of the articular surface (Figure H.6), the base and tip of the styloid and the bottom of the cancellous section. Select the 3D curve menu and select splines (Figure H.7). On the control window select z-buffer and manually create the spline by picking points on the surface. To close the curve select "Prepend", "Accept", "Save" (enter a curve number) "Accept" and "Quit" (Command: *3D curve, spline*).
f. Create surfaces which describe the proximal and distal level of the transition zone and the most proximal region of the marrow by offsetting the x-y plane (command: *sd xyplane_surface number_axis of traslation_coordinate*).
g. Move the block edges towards the appropriate cancellous curves, attach the edges of the part by highlighting each edge and selecting "Attach" in the command window

(Command: *curs*) and project the block faces onto the cancellous surface by highlighting the appropriate face and selecting "Project" (Command: *sfi*).

h. Increase the mesh density in each direction as needed (Command: *Mesh, mseq*) and apply smoothing algorithms to the faces (Command: *Mesh, relax*) and the volumes of the mesh (Command: *Mesh, unifrm*).

i. To create the mesh that will bridge the gap between the cancellous and marrow sections, add a 5 element block in the proximal z direction (Command: *Mesh, insrprt*) and attach the bottom edges to a curve created at the interface of the marrow and the x-y plane surface.

j. Insert a 100 element block in the proximal z direction, attach the proximal edges to a curve created at the interface of the proximal marrow and the proximal x-y plane and project the faces onto the marrow surface. Increase the mesh density as needed and apply smoothing algorithms to the surfaces and volumes.
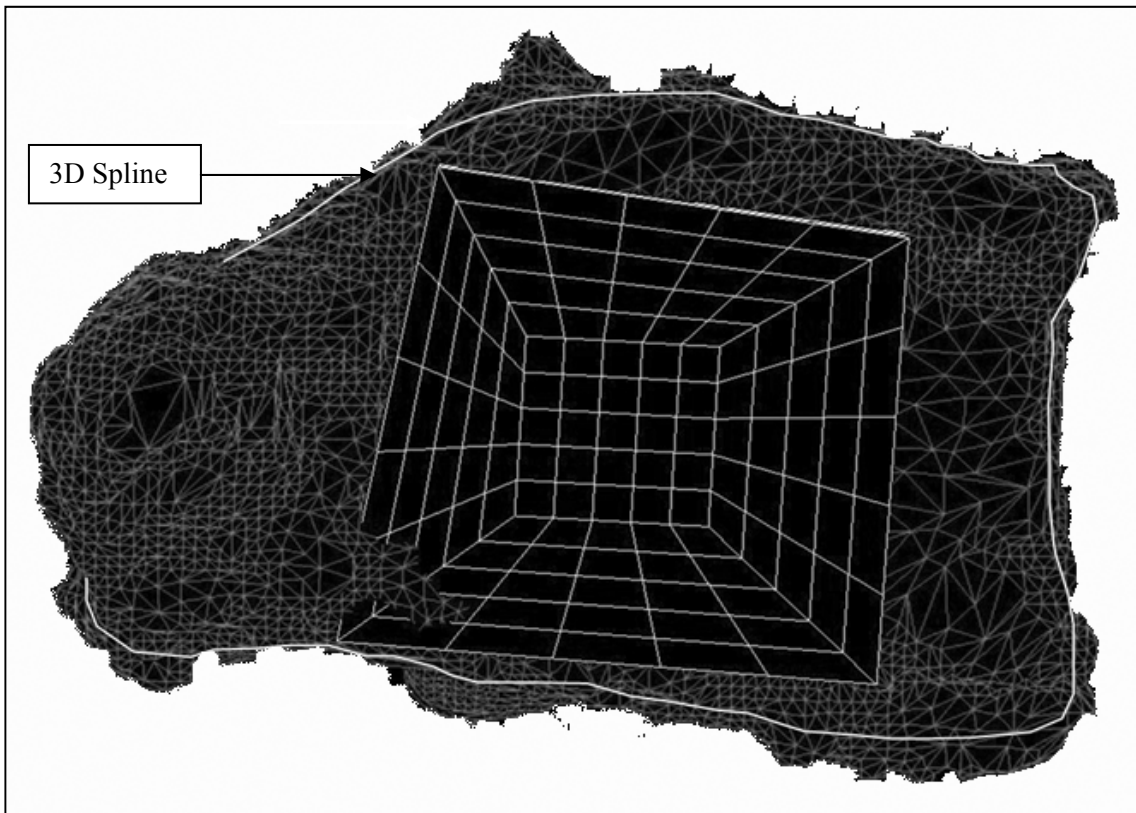
Figure H.6: TrueGrid® Parameter Definitions

A butterfly block structure positioned within the .STL surface definition and a 3D spline (yellow outline) used to position the edges of the block.

| 3D CURVE | CURD | APCURD | LP3 | TWSURF | SPLINE | COEDG | RMSEG |
| LACD | CDINFO | DCD | DCDS | DACD | ACD | ACDS | RCD | RCDS | RACD |

(a)

(b)
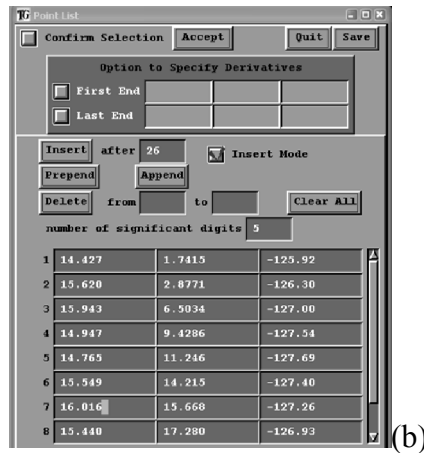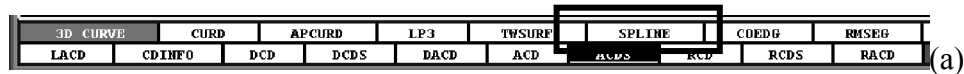
Figure H.7: TrueGrid® Curve Menu
3D curve menu (a) and curve
definition dialogue (b).

k. Assign material properties to individual blocks: Cancellous blocks are material 1, marrow and bridge blocks are material 2 (Command: *Material, mt*). Assign individual, master block boundaries to the faces of each block (Command: *interface, bb*), and merge the interior nodes of the block boundaries that were formed previously (c).
l. Close out the cancellous and marrow parts (Commands: *Merge, Merging, Quit*) (Figure H.8).

Cancellous

Marrow

(a)   (b)
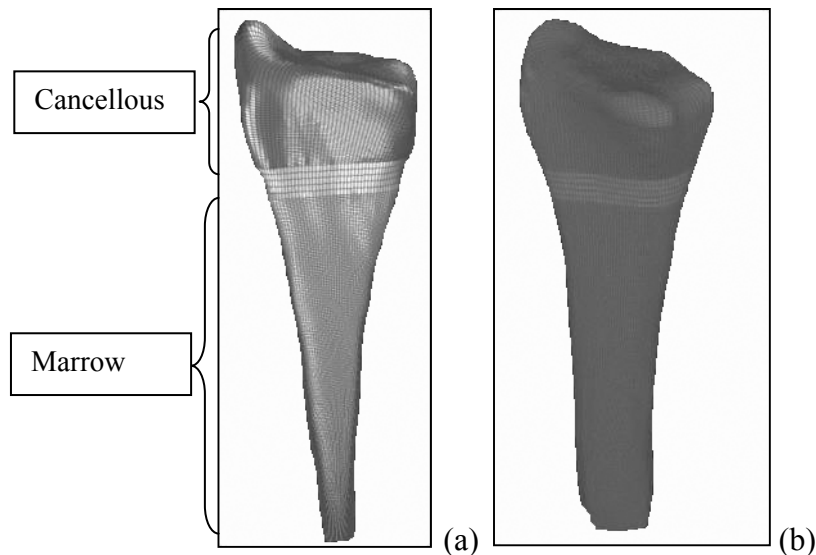
Figure H.8: TrueGrid® Bone Meshes
The cancellous and marrow (a) and cortical
(b) mesh after "closing out" the block
structure.

2. Building the cortical bone region

a. Create a new part to represent the cortical bone that is 5 blocks by 5 blocks by 4 blocks. The exterior blocks are 2 elements thick and the number of elements in the interior blocks correspond to the same number of blocks in the i, j, k directions as the cancellous and marrow sections. (Command: *block*).

b. Delete the corner and interior blocks (Command: *dei*), move the vertices to 45° angles and glue the interior faces together (Figure H.9) (Command: *bb)*.
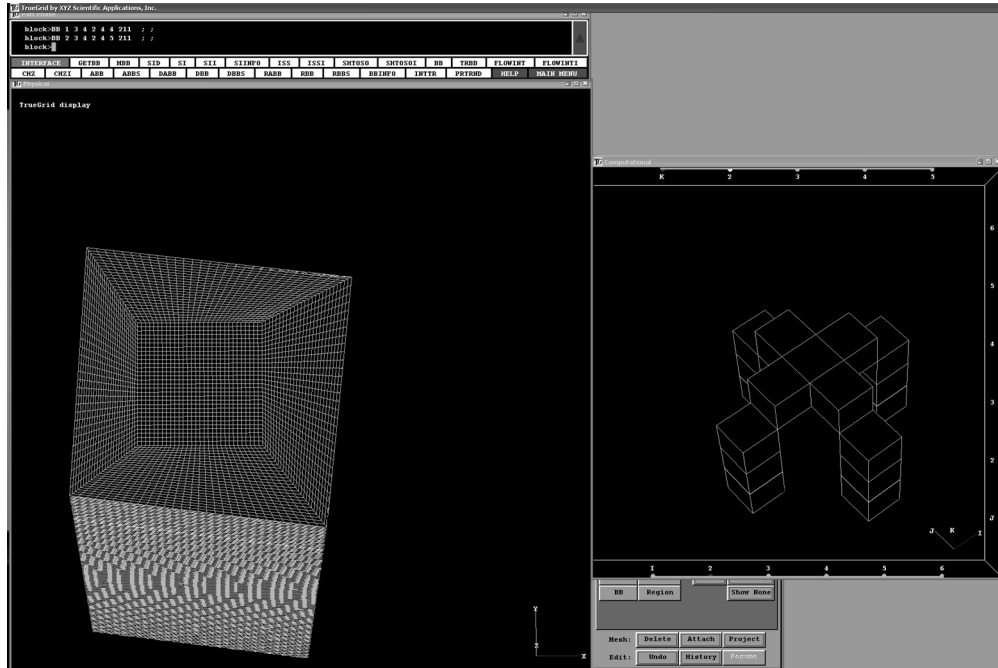
Figure H.9: Cortical Bone Block Structure
Cortical bone block structure (right) and the resulting butterfly (left).

c. Attach the interior surfaces of the cortical structure to the appropriate surfaces of the cancellous and marrow structures using the "Interface" and "bb". In this case the cortical surfaces will be the slave sides of the boundary conditions defined previously (Step 2; k). Set the "forced slaved to master boundary mapping" to 1.

d. Attach the edges of the cortical structure to the cortical curves and project the faces onto the cortical surface as before. Apply smoothing algorithms, define material properties (cortical blocks will be material 3) and merge the interior nodes as before.

e. Create a master block boundary on the proximal faces of the cortical bone and close out the cortical bone part (Figure H.8)

3. Building the other components

The proximal bracket

a. Create a part to represent the proximal bracket that is 3x3x1 blocks and form a butterfly. Attach the face of the newly formed face onto the proximal end of the cortical

bone. Define a surface in the x-y plane that is located approximately 2 cm off the end of the bone. Project the free face of the block structure onto the surface. Register the part as a separate material, and merge the nodes to close out the part.

The carpals

a. Import the carpals surface created from the white light scan (Figure H.10).
b. To smooth the scanned surface and to fill in gaps, create a series of splines on the outside of the carpals surface such that they create four sections. The splines should be generated such that they follow the relevant curvature of the carpals surface.
c. Surfaces can be defined within four bounding splines. Therefore, four new surfaces can be generated covering the original carpals surface (Commands: *sd, blend4*)
d. Complete the new surface by joining the edges of the surfaces created in "c." (Commands*: sd, sds*).
e. Generate a part that is 3x3x1 blocks and form a butterfly. Create 3D splines around the top and bottom curvature of the new carpals surface. Attach the top and bottom edges of the part to the respective curves and project the faces onto the surface. Using the interface and block boundary commands, create master block boundaries on the distal surface of the carpals.
f. Increase the mesh density, apply smoothing algorithms, register the carpals as a separate part and merge the nodes to close out the part.
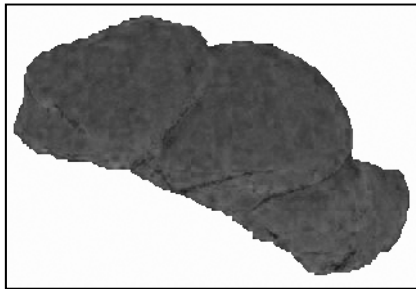
Figure H.10: Carpal STL
Original .STL carpals surface
from the white light scan.

The distal bracket and foam

a. Create a part that is 5x5x1blocks. Glue the inner six blocks (three in the i, and three in the j, directions), to the master interfaces generated on the distal carpals surface.
b. Define a surface from the x-y plane that is located 1 cm (approximately the thickness of the distal bracket) from the distal edge of the carpals. Project the distal faces of the part onto the x-y plane surface. Increase the mesh density, apply smoothing algorithms as necessary, and insert a partition to the distal end.
c. To form the mesh of the foam create another surface from the x-y plane located 0.5 cm off of the distal end of the bracket. Project the face of the inserted part onto the surface and apply smoothing algorithms as needed.
d. Register the distal bracket and the foam as separate parts and merge the nodes to close out the part.

The projectile

a. Define a spherical surface that has the same radius of curvature as the projectile used experimentally (~10 cm). Place the proximal end of the sphere so that is located approximately 0.1 cm from the distal edge of the foam surface (commands*: sd, sphere; sd, cyr3*).

b. Define an x-y plane surface located 5 cm distal to the apex of the sphere.

c. Create two 3D splines; one at the top of the sphere and the second at the bottom of the sphere where it intersects with x-y plane surface.

d. Define a cylindrical surface with a radius equal to the radius of the second spline created in "c."

e. Create a part that is 3x3x1 blocks and form a butterfly. Attach the top and bottom edges to the respective splines.

f. Project the top face onto the spherical surface the bottom face onto the x-y plane surface and the side faces onto the cylindrical surface. Increase the mesh density, apply smoothing algorithms as necessary, register the part as a separate material and merge the nodes to close out the part.

g. Write the output file containing the node, element and part information in Ls-DYNA keyword format (Commands: *output, lsdyna keyword, write*).
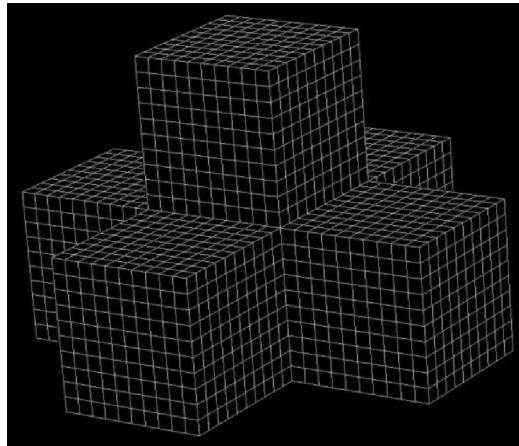
Figure H.11: Projectile Block Structure

Step 3: Writing the Deck in LS-DYNA®

a. Start writing a deck in notepad. Use *KEYWORD to define this as a keyword-written deck, *TITLE to define the title of the study. Use *CONTROL_TERMINATION to set the simulated duration.

b. Write *DATABASE cards to output node data (*DATABASE_HISTORY_NODE) for specific nodes on components, force data for the set where the load cell was located (*DATABASE_NODAL_FORCE_GROUP) and element data for elements located underneath the strain gauges (DATABASE_HISTORY_SOLID_SET) (Figure H.12).

c. Write a *PART card, a *SECTION card and a *MAT card for each component.

d. In LS-PrePost® , import the keyword file of the bone and impact components from TrueGrid®. Locate the elements closest to the x-y-z locations of the strain gauges (*LS-PrePost: Page 1, Ident, element*).

d. Write a *INITIAL_VELOCITY_RIGID_BODY card to specify the velocity of the projectile.

e. Define *CONTACT_AUTOMATIC_SURFACE_TO_SURFACE cards between all components that will come into contact (projectile-foam, carpals-cortical bone).

f. Conclude with *END.
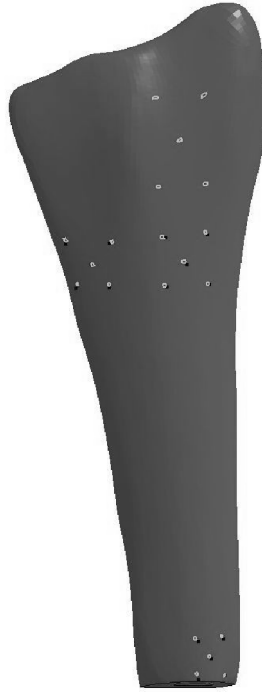
Figure H.12: Model Strain Gauge Identification
Location of the elements that represent the
strain gauges and the distal accelerometer.

APPENDIX I - Input Deck for LS-DYNA[®]

```
$This program takes a Radius bone mesh as output from TrueGrid, applies
material $properties and creates a simulation of the experimental impact using
projectile mass $and velocity inputs and modelling of the bracket and foam.
The load applied to the $distal radius strain and $acceleration at specific
sets corresponding to strain $gauge and accelerometer locations are used for
validation purposes.
$This program was written on August 31st, 2011 by Timothy A. Burkhart
$UNITS: millimetre, millisecond, Kilogram, kilo Newton
$
*KEYWORD memory=150000000
$deck is written in keyword format
$
$
*Title
Fracture_Impact.
$
$---+----1----+----2----+----3----+CONTROL CARDS-5----+----6----+----7----+---
*CONTROL_TERMINATION
$    ENDTIM    ENDCYC     DTMIN    ENDENG    ENDMAS
       30.0
$
*CONTROL_TIMESTEP
$    DTINIT    TSSFAC      ISDO    TSLIMT     DT2MS      LCTM     ERODE
MS1ST
         0       0.8         0         0    -2.0E-4         0         0
0
$
*HOURGLASS
$     HGID       IHQ        QM       IBQ        Q1        Q2     QB/VDC
QW
         1         3      0.25
$     HGID       IHQ        QM       IBQ        Q1        Q2     QB/VDC
QW
         2         4       0.1
$
*CONTROL_ACCURACY
$      OSU       INN    PIDOSU
         0         1         0
$
*CONTROL_ENERGY
$     HGEN      RWEN    SLNTEN     RYLEN
         2         2         2         2
$
*CONTROL_SOLID
$    ESORT    FMATRX   NIPTETS    SWLOCL    PSFAIL
         1         0         0         0         0
$      PM1       PM2       PM3       PM4       PM5       PM6       PM7
PM8       PM9      PM10
         0         0         0         0         0         0         0
0         0         0
$CONTROL_CONTACT
$   SLSFAC
$      0.1
$   USRSTR    USRFRC     NSBCS    INTERM     XPENE
$
$---+----1----+----2----+----3----DATABASE CARDS-5----+----6----+----7----+---
*DATABASE_JNTFORC
$       DT    BINARY      LCUR     IOOPT     DTHFF     BINHF
      0.001
$
*DATABASE_BINARY_INTFOR
$  DT/CYCL   LCFT/NR      BEAM     NPLTC    PSETID
       0.01
$
*DATABASE_EXTENT_BINARY
```

```
$     NEIPH     NEIPS    MAXINT    STRFLG    SIGFLG    EPSFLG    RLTFLG
                                      1
$    CMPFLG    IEVERP    BEAMIP     DCOMP      SHGE     STSSZ    N3THDT
                                      1
$
*DATABASE_HISTORY_NODE
$DISTBRACK PROXBRACK   PROJECT
  1047820    971972   1089859
$
*DATABASE_HISTORY_NODE_LOCAL_ID
$        ID       CID       REF       HF0
    904765        50         0
$  HEADING
   DISTAL ACCELEROMTER
$
*DEFINE_COORDINATE_NODES
$       CID        N1        N2        N3      FLAG       DIR
        50    904806    904756    904558         0         Z
$
*DATABASE_HISTORY_NODE_LOCAL_ID
$        ID       CID       REF       HF0
    910402        51         0         0
$  HEADING
   PROXIMAL ACCELEROMTER
$
*DEFINE_COORDINATE_NODES
$       CID        N1        N2        N3      FLAG       DIR
        51    910102    910094    911606         0         Z
$
$---+----1----+----2----+----3----DATABASE CARDS-5----+----6----+----7----+---
$
*DATABASE_BINARY_D3PLOT
$ DT/CYCL    LCDT/NR      BEAM     NPLTC    PSETID
     0.05
$
*DATABASE_NCFORC
$        DT    BINARY      LCUR     IOOPT     DTHFF     BINHF
      0.05         3
$
*DATABASE_HISTORY_SOLID_SET
$ strain Gauges
$ RADGAUGE  ULNGAUGE PROXGAUGE  DISACCEL PROXACCEL
        20        21        22        23        24
$
$---+----1----+----2----+----3----DATABASE CARDS-5----+----6----+----7----+---
$
*DATABASE_NODOUT
$        DT    BINARY      LCUR     IOOPT     DTHFF     BINHF
      0.05         3
$
*DATABASE_NODFOR
$        DT    BINARY      LCUR     IOOPT     DTHFF     BINHF
      0.05         3
$
*DATABASE_NODAL_FORCE_GROUP
$Distal aspect of the carpals representing the load cell
$     NSID
         2
$
*DATABASE_ELOUT
$        DT    BINARY      LCUR     IOOPT     DTHFF     BINHF
      0.05         3
$
*DATABASE_GLSTAT
$        DT    BINARY      LCUR     IOOPT     DTHFF     BINHF
      0.05         3
$
*DATABASE_CROSS_SECTION_SET
$     NSID      HSID      BSID      SSID      TSID      DSID        ID
         2         1
```

```
$
*DATABASE_SECFORC
$        DT    BINARY     LCUR     IOOPT     DTHFF     BINHF
      0.05         3
$---+----1----+----2----+----3----PARTS CARDS----5----+----6----+----7----+---
*PART
CANCELOUS BONE
$       PID     SECID       MID     EOSID      HGID      GRAV    ADPOPT
TMID
          1         1         1                   2
$
*PART
MARROW
$       PID     SECID       MID     EOSID      HGID      GRAV    ADPOPT
TMID
          2         2         2                   2
$
*PART
CORTICAL
$       PID     SECID       MID     EOSID      HGID      GRAV    ADPOPT
TMID
          3         3         3                   2
$
*PART
Pot
$       PID     SECID       MID     EOSID      HGID      GRAV    ADPOPT
TMID
          4         4         4
$
*PART
CARPALS
$       PID     SECID       MID     EOSID      HGID      GRAV    ADPOPT
TMID
          5         5         5                   2
$
*PART
DISTBRACKET
$       PID     SECID       MID     EOSID      HGID      GRAV    ADPOPT
TMID
          6         6         6
$
*PART
FOAM
$       PID     SECID       MID     EOSID      HGID      GRAV    ADPOPT
TMID
         11        11        11                   1
$
*PART
PROJECTILE
$       PID     SECID       MID     EOSID      HGID      GRAV    ADPOPT
TMID
          7         7         7
$
*PART
PROXIMAL BEARING
$       PID     SECID       MID     EOSID      HGID      GRAV    ADPOPT
TMID
          8         8         8
$
*PART
DISTAL BEARING
$       PID     SECID       MID     EOSID      HGID      GRAV    ADPOPT
TMID
          9         9         9
$
*PART
PROXIMAL BRACKET
$       PID     SECID       MID     EOSID      HGID      GRAV    ADPOPT
TMID
         10        10        10
```

```
$
$---+----1----+----2----+----3----+----4---+----5----+----6----+----7----+---
*LOAD_BODY_Y
$      LCID        SF    LCIDDR        XC        YC        ZC       CID
         1  -0.00981
$
*DEFINE_CURVE
$      LCID      SIDR       SFA       SFO      OFFA      OFFO    DATTYP
         1
$           ABSICCA              ORDINATE
               0.0                  1.00
            1000.00                  1.00
$
$---+----1----+----2----+----3--SECCTION CARDS---5----+----6----+----7----+---
*SECTION_SOLID
$CANCELLOUS SECTION
$     SECID    ELFORM       AET
         1         1
$
*SECTION_SOLID
$MARROW
$     SECID    ELFORM       AET
         2         1
$
*SECTION_SOLID
$CORTICAL
$     SECID    ELFORM       AET
         3         1
$
*SECTION_SOLID
$POT
$     SECID    ELFORM       AET
         4         1
$
*SECTION_SOLID
$CARPALS
$     SECID    ELFORM       AET
         5         1
$
*SECTION_SOLID
$DISTALBRACKET
$     SECID    ELFORM       AET
         6         1
$
*SECTION_SOLID
$FOAM
$     SECID    ELFORM       AET
        11         1
$
*SECTION_SOLID
$PROJECTILE
$     SECID    ELFORM       AET
         7         1
$
*SECTION_SOLID
$PROXIMAL BEARING
$     SECID    ELFORM       AET
         8         1
$
*SECTION_SOLID
$DISTAL BEARING
$     SECID    ELFORM       AET
         9         1
*SECTION_SOLID
$PROXIMAL BRACKET
$     SECID    ELFORM       AET
        10         1
$---+----1----+----2----+----3---MATERIAL CARDS--5----+----6----+----7----+---
```

```
*MAT_PIECEWISE_LINEAR_PLASTICITY
$CANCELLOUS BONE
$      MID         RO          E          PR        SIGY        ETAN        FAIL
TDEL
        10.00000097        1.8        0.3        0.01        0.09
$        C          P        LCSS        LCSR          VP
    0.0651       6.4
$      EPS1       EPS2        EPS3        EPS4        EPS5        EPS6        EPS7

$       ES1        ES2         ES3         ES4         ES5         ES6         ES7
$
$
*MAT_PIECEWISE_LINEAR_PLASTICITY
$CORTICAL BONE
$      MID         RO          E          PR        SIGY        ETAN        FAIL
        30.00000115       25.1        0.3       0.124       1.255
$        C          P
    0.0651       6.4
$      EPS1       EPS2        EPS3        EPS4        EPS5        EPS6        EPS7

$       ES1        ES2         ES3         ES4         ES5         ES6         ES7


$
$
*MAT_ELASTIC
$MARROW
$      MID         RO          E          PR
         2  0.000001        0.02       0.499
$
*MAT_ELASTIC
$LUNATE/SCAPHOID
$      MID         RO          E          PR
        50.00000106       10.0        0.38
$
*MAT_RIGID
$PROJECTILE - MEASURED PROJECTILE VOLUME AS 7302.03mm3
$projectile with density set based on volume (rho=6.8 kg/7302.03mm3 =0.00093)
$      MID         RO          E          PR
         7   0.00093        210         0.3
$      CMO       CON1        CON2
         1          4          7
$  LCOorA1         A2          A3          V1          V2          V3

$
*MAT_RIGID
$POT-MEASURED VOLUME AS 253.93 mm3
$Proximal bracket with density set based on volume (rho= 2.68 kg/253.93 mm3
=0.01055)
$      MID         RO          E          PR
         4   0.01055        210         0.3
$      CMO       CON1        CON2
         1          4          7
$  LCOorA1         A2          A3          V1          V2          V3

$
*MAT_RIGID
$DISTAL BRACKET - MEASURED VOLUME AS 19489 mm3
$distal bracket with density set based on volume (rho = 4.314kg/19489 mm3 =
0.00022)
$      MID         RO          E          PR
         6   0.00022        210         0.3
$      CMO       CON1        CON2
         1          4          7
$  LCOorA1         A2          A3          V1          V2          V3

$
```

```
*MAT_LOW_DENSITY_FOAM_TITLE
Polyurethane foam
$Polyurethane foam (52 kg/m3 = 5.2e-8, 8 MPa)
$        MID         RO          E        LCID         TC         HU       BETA
          110.00000005      0.008           2        0.1          0        0.5
$      SHAPE
          10
$
*DEFINE_CURVE_TITLE
foam_stress-strain
$      LCID        SIDR        SFA         SFO       OFFA       OFFO     DATTYP
          2           0          1        1E-3          0
$CURVE       ABCISSA              ORDINATE
                0              0.009201
         0.011525              0.024810
         0.022673              0.038370
         0.033607              0.050733
         0.043744              0.060938
         0.053709              0.070829
         0.063514              0.080311
         0.073369              0.089906
         0.083186              0.100483
         0.092955              0.109865
         0.102773              0.120033
         0.112759              0.130432
         0.122501              0.140888
         0.132364              0.151994
         0.142378              0.163223
         0.152486              0.174794
         0.162530              0.186495
         0.172389              0.197816
         0.182303              0.211105
         0.192389              0.223370
         0.202398              0.235819
         0.212392              0.248871
         0.222465              0.261523
         0.232367              0.275491
         0.242345              0.289471
         0.252294              0.304056
         0.262130              0.318766
         0.272267              0.333332
         0.282250              0.349557
         0.292323              0.365175
         0.302353              0.382515
         0.312310              0.398674
         0.322315              0.415940
         0.332396              0.434461
         0.342264              0.452135
         0.352316              0.471777
         0.362252              0.491416
         0.372267              0.511982
         0.382212              0.533448
         0.392061              0.555440
         0.402091              0.578719
         0.412077              0.602601
         0.422034              0.627253
         0.431974              0.653450
         0.441964              0.681166
         0.452033              0.709879
         0.461984              0.739738
         0.471937              0.770881
         0.482063              0.804153
         0.491995              0.838552
         0.501988              0.875237
         0.512100              0.914160
         0.522060              0.954676
         0.531960              0.998122
         0.541828              1.043707
         0.551907              1.093506
         0.561816              1.146145
```

```
                0.571736                 1.202105
                0.581741                 1.262803
                0.591673                 1.328974
                0.601670                 1.401435
                0.611665                 1.479815
                0.621649                 1.568052
                0.631561                 1.665895
                0.641554                 1.774604
                0.651587                 1.897351
                0.661554                 2.035150
                0.671424                 2.195556
                0.681414                 2.381222
                0.691407                 2.598219
                0.701248                 2.859995
                0.711299                 3.173293
                0.721150                 3.553004
                0.731164                 4.013932
                0.740901                 4.541521
                    0.75                        5
                    0.76                        6
                    0.77                        8
                    0.78                     10.5
                    0.79                       14
                     0.8                       19
                    0.81                       26
                    0.82                       35
                    0.83                       45
                    0.84                       56
                    0.85                       68
                    0.86                       81
                    0.87                       95
                    0.88                      119
                    0.89                      137
                     0.9                    160.0
                    0.91                    270.0
                    0.92                    420.0
                    0.93                    550.0
                    0.94                    980.0
                    0.95                   1700.0
                    0.96                   2800.0
                    0.97                   5000.0
                    0.98                  10000.0
$
*MAT_RIGID
$DISTAL BEARING
$        MID        RO         E         PR
           9         5       210        0.3
$        CMO      CON1      CON2
           1         7         7
$  LCOorA1        A2        A3         V1        V2        V3


$
*MAT_RIGID
$PROXIMAL BEARING
$        MID        RO         E         PR
           8         5       210        0.3
$        CMO      CON1      CON2
           1         7         7
$  LCOorA1        A2        A3         V1        V2        V3


$
*MAT_RIGID
$PROXIMAL BRACKET
$proximal bracket with density set based on volume (rho = 4.314kg/20945.1 mm3
=0.00020596)
$        MID        RO         E         PR
          10  0.000206       210        0.3
$        CMO      CON1      CON2
           1         4         7
$  LCOorA1        A2        A3         V1        V2        V3
```

```
$
$---+----1----+----2----+----3--CONSTRAINT CARDS-5----+----6----+----7----+--
*INITIAL_VELOCITY_RIGID_BODY
$initial velocity of 2.1mm/ms; crack velocity of 2.7 mm/ms; fracture velocity
of 3.3 mm/ms in the z-direction
$       PID        Vx        Vy        Vz       VxR       VyR       VzR
          7       0.0       0.0      -3.3       0.0       0.0       0.0
$
*CONSTRAINED_RIGID_BODIES
$RIGIDLY ATTACHES THE POT TO THE PROXIMAL BRACKET
$      PIDM      PIDS
          4        10
*CONSTRAINED_EXTRA_NODES_SET
$       PID      NSID
          6         6
$
$---+----1----+----2----+----3---CONTACT CARDS---5----+----6----+----7----+---
*CONTACT_AUTOMATIC_SURFACE_TO_SURFACE_ID
$Contact between the projectile and the foam
$       CID    HEADING
          1  PROJECTILE TO FOAM
$      SSID      MSID     SSTYP     MSTYP
          7        11         3         3
$        FS        FD        DC        VC       VDC    PENCHK        BT        DT
        0.3       0.3         0         0         0         0         0 1.0E+20
$       SFS       SFM       SST       MST      SFST      SFMT       FSF       VSF
          1         1         0         0         1         1         1         1
$OPTIONAL CARD A
$      SOFT
          2
$
*CONTACT_AUTOMATIC_SURFACE_TO_SURFACE_ID
$Contact between the carpals and the bone
$       CID    HEADING
          2  CARPALS TO BONE
$      SSID      MSID     SSTYP     MSTYP    SBOXID    MBOXID       SPR       MPR
          1         2         0         0                             1         0
$        FS        FD        DC        VC       VDC    PENCHK        BT        DT
       0.01      0.01         0         0         0         0         0      0E+20
$       SFS       SFM       SST       MST      SFST      SFMT       FSF       VSF
          1         1         0         0         1         1         1         1
$
*CONSTRAINED_JOINT_PLANAR
$ Define a joint between the bracket and the rail
$ Nodes 1034459  and 1034239 are on the bracket rigid body (Body A)
$ Nodes 1081637  and 1099881  are on the rail rigid body   (Body B)
$       NA1       NB1       NA2       NB2
   1034459   1081637   1034239   1099881
*NODE
$#   nid               x               y               z       tc       rc
 1099881     -20.0000000        -13.9119        -111.148        0        0
$
*CONSTRAINED_EXTRA_NODES_SET
$       PID  NID/NSID
          9         8
$
*CONSTRAINED_JOINT_STIFFNESS_TRANSLATIONAL
$      JSID      PIDA      PIDB      CIDA      CIDB       JID
          1        10         6         5         6
 
$Next 3 cards are required for translational stiffness
$     LCIDX     LCIDY     LCIDZ    DLCIDX    DLCIDY    DLCIDZ
          0         0         3         0         0         0
$       ESX       FFX       ESY       FFY       ESZ       FFZ
          0         0         0         0         0         0
$      NSDX      PSDX      NSDY      PSDY      NSDZ      PSDZ
          0         0         0         0         0         0
$
*DEFINE_CURVE
```

```
$Load curve ID for z-force vsz-translational relative displacement
$between origins of CIDA and CIDB (Ff =0.4*9.81*4.314/100000 = 0.0169 kN)
$      LCID      SIDR       SFA
          3
$    ABISCA  ORDINATE
          0         5
        100         5
$
*DEFINE_COORDINATE_NODES
$       CID        N1        N2        N3      FLAG
          5   1081380   1081758   1081782         0
$
*DEFINE_COORDINATE_NODES
$       CID        N1        N2        N3      FLAG
          6   1034467   1034461   1060080         0
$
*SET_NODE_LIST
$       SID
          8
$        N1
    1099881
$
*CONTACT_AUTOMATIC_SURFACE_TO_SURFACE_ID
$       CID   HEADING
          3   Distal bracket to distal BEARING
$      SSID      MSID     SSTYP     MSTYP
          6         4         0         0
$        FS        FD        DC        VC       VDC    PENCHK        BT        DT
  0.000000  0.000000     0.100     0.000     0.000         0    0.0001   1.0E+20
$       SFS       SFM       SST       MST      SFST      SFMT       FSF       VSF
          1         1         0         0         1         1         1         1
$
*CONTACT_AUTOMATIC_SURFACE_TO_SURFACE_ID
$       CID   HEADING
         11   Proximal bracket to proximal BEARING
$      SSID      MSID     SSTYP     MSTYP
          7         5         0         0
$        FS        FD        DC        VC       VDC    PENCHK        BT        DT
    0.4000     0.400     0.100     0.000     0.000         0    0.0001   1.0E+20
$       SFS       SFM       SST       MST      SFST      SFMT       FSF       VSF
          1         1         0         0         1         1         1         1
$
*CONTACT_INTERIOR
$      PSID
         30
*CONTACT_AUTOMATIC_SURFACE_TO_SURFACE_ID
$       CID   HEADING
         20   FOAM TO DISTAL BRACKET
$      SSID      MSID     SSTYP     MSTYP
         11         6         3         3
$        FS        FD        DC        VC       VDC    PENCHK        BT        DT
       0.3       0.3         0         0         0         0         0   1.0E+20
$       SFS       SFM       SST       MST      SFST      SFMT       FSF       VSF
          1         1         0         0         1         1         1         1
$
$---+----1----+----2----+----3-----SET CARDS-----5----+----6----+----7----+---
*SET_SOLID_TITLE
RADIAL GAUGE
$       SID
         20
$        UR        UU        LR        LU         C
    886363    916954    885399    915995    885895
$
*SET_SOLID_TITLE
ULNAR GAUGE
$       SID
         21
$        UR        UU        LR        LU         C
    916911    930468    916013    929566    916560
*SET_SOLID_TITLE
```

```
PROXIMAL GAUGE
$      SID
        22
$       UR         UU         LR         LU          C
    878453     908978     877731     908260     908614
$
*SET_SOLID_TITLE
DIST ACCEL
$      SID
        23
$       UR         UU         LR         LU          C
    888829     919537     886721     917253     887815
*SET_SOLID_TITLE
$
PROX ACCEL
$      SID
        24
$       UR         UU         LR         LU          C
    892322     892392     891421     891313     891970
$
*SET_PART
$      SID        DA1        DA2        DA3        DA4
        30        1.1        0.1                   2.0
$     PID1       PID2       PID3
         5          3
$---+----1----+----2----+----3----+Boundary Card-5----+----6----+----7----+---
*BOUNDARY_SPC_SET
$Bottom Proximal Bracket
$ NID/NSID       CID       DOFX       DOFY       DOFZ      DOFRX      DOFRY      DOFRZ
         1                    1          1          0          1          1          1
*BOUNDARY_SPC_SET
$Bottom Proximal Bearing
$ NID/NSID       CID       DOFX       DOFY       DOFZ      DOFRX      DOFRY      DOFRZ
         3                    1          1          1          1          1          1
$---+----1----+----2----+----3----+----4----+----5----+----6----+----7----+---
*END
```

APPENDIX J - Letters of Permission

This Appendix includes the letter of permission for the material presented in Section 2.1 and Appendix E

Order Completed	
Thank you very much for your order. This is a License Agreement between Timothy A Burkhart ("You") and Elsevier ("Elsevier"). The license consists of your order details, the terms and conditions provided by Elsevier, and the	
License Number	2810920875664
License date	Dec 16, 2011
Licensed content publisher	Elsevier
Licensed content publication	Journal of Biomechanics
Licensed content title	Determining the optimal system-specific cut-off frequencies for filtering *in-vitro* upper extremity impact force and acceleration data by residual analysis
Licensed content author	Timothy A. Burkhart, Cynthia E. Dunning, David M. Andrews
Licensed content date	13 October 2011
Licensed content volume number	44
Licensed content issue number	15
Number of pages	4
Type of Use	reuse in a thesis/dissertation
Portion	full article
Format	both print and electronic
Are you the author of this Elsevier article?	Yes
Will you be translating?	No

Order Completed	
Thank you very much for your order. This is a License Agreement between Timothy A Burkhart ("You") and John Wiley and Sons ("John Wiley and Sons"). The license consists of your order details, the terms and conditions provided by John Wiley and Sons.	
License Number	2810921392447
License date	Dec 16, 2011
Licensed content publisher	John Wiley and Sons
Licensed content publication	Journal of Orthopaedic Research
Licensed content title	Failure characteristics of the isolated distal radius in response to dynamic impact loading
Licensed content author	Timothy A. Burkhart, David M. Andrews, Cynthia E. Dunning
Licensed content date	Jan 1, 2011
Start page	n/a
End page	n/a
Type of use	Dissertation/Thesis
Requestor type	Author of this Wiley article
Format	Print and electronic
Portion	Full article
Will you be translating?	No

APPENDIX K - Ethics Approval

Office of the Research Ethics Board

University of Windsor

thinking forward

Today's Date: December 4, 2009
Principal Investigator: Tim Burkhart
Department/School: Kinesiology
REB Number: 09-225
Research Project Title: Individual Muscle Contributions to Elbow and Wrist Joint Stability: The Response to Dynamic Upper Extremity Impact Loading Indicative of a Forward Fall.
Clearance Date: December 4, 2009
Project End Date: August 31, 2010

Progress Report Due:
Final Report Due: August 31, 2010

This is to inform you that the University of Windsor Research Ethics Board (REB), which is organized and operated according to the *Tri-Council Policy Statement* and the University of Windsor *Guidelines for Research Involving Human Subjects*, has granted approval to your research project on the date noted above. This approval is valid only until the Project End Date.

A Progress Report or Final Report is due by the date noted above. The REB may ask for monitoring information at some time during the project's approval period.

During the course of the research, no deviations from, or changes to, the protocol or consent form may be initiated without prior written approval from the REB. Minor change(s) in ongoing studies will be considered when submitted on the Request to Revise form.

Investigators must also report promptly to the REB:
a) changes increasing the risk to the participant(s) and/or affecting significantly the conduct of the study;
b) all adverse and unexpected experiences or events that are both serious and unexpected;
c) new information that may adversely affect the safety of the subjects or the conduct of the study.

Forms for submissions, notifications, or changes are available on the REB website: www.uwindsor.ca/reb. If your data is going to be used for another project, it is necessary to submit another application to the REB.

We wish you every success in your research.

Pierre Boulos, Ph.D.
Chair, Research Ethics Board

cc: Dr. David Andrews, Kinesiology
        Mark Curran, Research Ethics Coordinator

This is an official document. Please retain the original in your files.

VITA AUCTORIS

NAME: Timothy A. Burkhart

PLACE OF BIRTH: Brantford, Ontario, Canada

YEAR OF BIRTH: 1981

EDUCATION: Paris District High School, Paris ON
1995-2000
University of Windsor, Windsor ON
2000-2004 BHK
University of Windsor, Windsor ON
2005-2007 MHK